ULTRASOUND DRIVEN SYNTHESIS OF BIO-FUNCTIONAL NANOSTRUCTURES

By

Sukhvir Kaur Bhangu

ORCID ID: 0000-0002-9810-4304

Submitted in total fulfilment of the requirements of the degree of Doctor of Philosophy

August 2019

School of Chemistry
Faculty of Science
The University of Melbourne
Parkville, Vic 3010, Australia

Abstract/Scope of Thesis

Polyphenolic-, amino acids- and doxorubicin-based nanostructures are of great interest due to their multifarious applications in biomedical field as antibiotics, antioxidants, antimicrobial and anti-cancer agents.

Most of the research on the polyphenolic and amino acids based nanostructures adhere to the formation of coordination complexes with metals, self-assembly techniques or chemical functionalization and crosslinking reactions. To improve the efficacy of therapeutic agents, a variety of nanoparticles have been developed for the controlled and targeted delivery of doxorubicin. These include biopolymers-based nano/microcapsules, carbon-based nanoparticles, polymer-drug conjugate, dendrimers, liposomes, micelles, inorganic nanoparticles and nucleic acids nanostructures.

The development of simple, one pot and effective synthesis routes to fabricate bio-nanomaterials is in high demand. In particular, the use of polyphenols, doxorubicin and single amino acids as building blocks to fabricate nanostructured materials is still unexplored. In this PhD work, I have used ultrasound-based technologies to synthesize phenolic, amino acid and doxorubicin based micro and nanoparticles for different biomedical applications.

Chapter 1 provides an overview on the structural and bio-functional properties of nanoparticles and methods to synthesize nanoparticles for biomedical use, including the ultrasonic techniques have been discussed. Furthermore, fundamentals of ultrasound are also provided.

In the literature review (Chapter 2), several studies dealing with the polyphenol, doxorubicin and amino acid molecules have been summarised. In the last section of this chapter, numerous investigations on synthesis of diverse types of nanostructures using ultrasound are reviewed. In Chapter 3 materials and methods, equipment and all other experimental details used are described.

Chapter 4 provides a fundamental understanding on the ultrasonic coupling of simple phenolic molecules, where acoustic bubble acts as a catalytic binding site for the generation of bioactive oligomers without the need for utilizing any enzymes, catalysts (organic or inorganic) and other toxic reagents. It has been observed that the extent of oligomerization and nanoparticles formation depends on the ultrasonic frequency, concentration and physiochemical properties of the phenolic building blocks.

Chapter 5 demonstrates that cavitation bubbles are simple micro-reactors with reactive surfaces to perform one-pot multiple reactions on complex polyphenolic molecules to convert tannic acid to ellagic acid, namely (i) hydrolysis of an ester linkage, (ii) C–C coupling reactions, (iii) condensation reactions and (iv) crystallization of the product into regularly shaped particles. The size and shape of the crystals can be controlled by ultrasonic frequency, power and time. The synthesized particles exhibit fluorescence properties, anticancer and antioxidant activity and could be further used for drug loading and delivery.

In Chapters 6 and 7, the role of the acoustic field in the formation of supramolecular nanoaggregates using tryptophan and phenylalanine as building blocks was investigated. It has been demonstrated that the acoustic bubbles driven at high frequency standing wave, in addition to provide a reactive surface for the dimerization of biomolecules, can also provide an energy source to fuel and refuel the dissipative out of equilibrium assembly of these molecules below the critical aggregation concentration. Furthermore, the unique optical and bio-functional properties of nanoparticles for bioimaging and probing the intracellular trafficking of a drug have also been studied.

In Chapter 8 the sound-driven self-assembly of the anticancer drug doxorubicin was investigated to generate nanoparticles solely made of drug molecules. The newly developed nanoparticles were tested on different types of cancer cells and the drug was found to be active in drug resistant cell lines. In addition, the mechanism of action of drug nanoparticles was investigated.

Chapter 9 provides a summary of the entire PhD work.

Declaration of Authorship

This is to certify that:

I. the thesis comprises only my original work except where indicated in the preface,

II. due acknowledgement has been made in the text to all other material used,

III. and the thesis is fewer than the 100,000 words in length, exclusive of tables, maps, bibliographies and appendices.

Sukhvir Kaur Bhangu

Preface

Work carried out in collaboration (Chapter 4, Chapter 5, Chapter 6, Chapter 7, Chapter 8) indicates the nature and proportion of the contribution of others and in general terms the portions of the work which the student claims as original.

For the part of thesis represented in its published form (Chapter 4, Chapter 5) a statement prepared by the candidate explaining the contributions of all involved is provided. A signed copy of co-author authorization form by all the authors who contributed to the publication is submitted to the Melbourne School of Graduate Research along with the thesis.

Chapter 4: ***A simple one-step ultrasonic route to synthesise antioxidant molecules and fluorescent nanoparticles from phenol and phenol- like molecules***

Sukhvir Kaur Bhangu, Muthupandian Ashokkumar and Francesca Cavalieri, ACS Sustainable Chemistry and engineering 2017, 5, 6081-6089

The candidate is the primary author and contributed to more than 75 % of the content in this publication. The candidate reviewed the literature, planned and carried out the experimental work. The candidate analysed the experimental data and prepared the manuscript under the supervision of Prof. Ashokkumar and Dr. Cavalieri

Chapter 5: ***Sono-transformation of tannic acid into bio-functional ellagic acid micro/nanocrystals with distinct morphologies***

Sukhvir Kaur Bhangu, Enrico Colombo, Ritu Singla, Muthupandian Ashokkumar, Francesca Cavalieri, Green Chemistry 2018, 20, 4, 816-821

The candidate is the primary author and contributed to more than 75 % of the content in this publication. The candidate reviewed the literature, planned and carried out the experimental work. The candidate analysed the experimental data and prepared the manuscript under the supervision of Prof. Ashokkumar and Dr. Cavalieri. Dr. Enrico Colombo and Dr. Ritu Singla provided assistance with the SEM and mass spectrometry and discussion on experimental data.

Chapter 6: ***Sound-driven dissipative self-assembly of aromatic biomolecules into nanoparticles***

Sukhvir Kaur Bhangu, Gianfranco Bocchinfuso, Muthupandian Ashokkumar, Francesca Cavalieri. (In revision following peer review by Nanoscale Horizon)

The candidate is the primary author and contributed to more than 75 % of the content in this publication. The candidate reviewed the literature, planned and carried out the experimental work. The candidate analysed the experimental data and prepared the manuscript under the supervision of Prof. Ashokkumar and Dr. Cavalieri. Molecular dynamic simulations were carried out by Gianfranco Bocchinfuso.

Chapter 7: ***Synthesis of bio-functional nanoparticles from sono-responsive amino acids using high frequency ultrasound. (****Manuscript submitted to Ultrasonics sonochemistry****)***

Sukhvir Kaur Bhangu, Francesca Cavalieri, Muthupandian Ashokkumar

The candidate is the primary author and contributed to more than 75 % of the content in this publication. The candidate reviewed the literature, planned and carried out the experimental work. The candidate analysed the experimental data and prepared the manuscript under the supervision of Prof. Ashokkumar and Dr. Cavalieri.

Chapter 8: ***A Sono-drug to Combat Drug Resistance in Cancer Therapy***. ***(Manuscript in preparation)***

Sukhvir Kaur Bhangu, Giovanni Luca Beretta, Nadia Zaffaroni, Marcin Wojnilowicz, Muthupandian Ashokkumar, and Francesca Cavalieri

The candidate was the primary author and contributed to more than 75 % of the content in this publication. The candidate reviewed the literature, planned and carried out the experimental work. The candidate analysed the experimental data and prepared the manuscript under the supervision of Prof. Ashokkumar and Dr. Cavalieri. Giovanni Luca Beretta and Nadia Zaffaroni carried out and discussed the experimental studies on drug resistant cell lines. Marcin Wojnilowicz provided assistance with the use of flow cytometry and immunostaining of cells.

Student Signature .....

(Sukhvir Kaur Bhangu)

Supervisor Signature 1) .....

(Muthupandian Ashokkumar)

2) .....

(Francesca Cavalieri)

Publications (2016-2019)

Ph.D. Project

Publications

1. ***A simple one-step ultrasonic route to synthesise antioxidant molecules and fluorescent nanoparticles from phenol and phenol- like molecules***
   Sukhvir Kaur Bhangu, Muthupandian Ashokkumar and Francesca Cavalieri, ACS *Sustainable Chemistry and engineering* **2017**, 5,6081-6089

2. ***Sono-transformation of tannic acid into bio-functional ellagic acid micro/nanocrystals with distinct morphologies***
   Sukhvir Kaur Bhangu, Muthupandian Ashokkumar, Francesca Cavalieri *Green Chemistry* **2018,**4,816-821

3. ***Sound-driven dissipative self-assembly of aromatic biomolecules into nanoparticles***
   Sukhvir Kaur Bhangu, Muthupandian Ashokkumar, Francesca Cavalieri (In revision following peer review by Nanoscale Horizon)

4. ***Synthesis of bio-functional nanoparticles from sono-responsive amino acids using high frequency ultrasound***
   Sukhvir Kaur Bhangu, Francesca Cavalieri, Muthupandian Ashokkumar (Manuscript submitted to Ultrasonics sonochemistry)

5. ***A Sonodrug to combat drug resistance in cancer therapy***.
   Sukhvir Kaur Bhangu, Giovanni Luca Beretta, Nadia Zaffaroni, Marcin Wojnilowicz, Muthupandian Ashokkumar, and Francesca Cavalieri.
   (Manuscript in preparation)

Book Chapters

6. ***Theory of Sonochemistry***
   Sukhvir Kaur Bhangu, Muthupandian Ashokkumar Topics in Current Chemistry, 2016, 374, 56 (***Review work – part of this has been used in Chapter 1 of the thesis***)

7. ***Ultrasound assisted recovering of lactose from whey***,
   Yanira García, Sukhvir Kaur Bhangu, Muthupandian Ashokkumar and Néstor Gutiérrez-Méndez. Novel Applications in Dairy Food Processing, 2018

8. Contributed to the ***Synthesis of Micro-Nanoparticles Using Ultrasound-Responsive Biomolecules*** in Sonochemical Production of Nanomaterials.
   Kenji Okitsu, Francesca Cavalieri, Springer, 2018, 39-62.

Other Projects

9. ***Ultrasound Assisted Crystallization of Paracetamol: Crystal Size Distribution and Polymorph Control***
   Sukhvir Kaur Bhangu, Muthupandian Ashokkumar, and Judy Lee Crystal growth & design 2016, 16, 1934 -1941.

10. ***Ultrasonic enhancement of lipase-catalysed transesterification for biodiesel synthesis***
    Sukhvir Kaur Bhangu, Shweta Gupta, Muthupandian Ashokkumar Ultrasonic Sonochemistry, 2017, 34, 305-309.

11. ***Chitosan microspheres as a template for TiO_2 and ZnO microparticles: studies on mechanism, functionalization and applications in photocatalysis and H2S removal***
    Enrico Colombo, Wu Li, Sukhvir Kaur Bhangu and Muthupandian Ashokkumar, *RSC Advances 2017*, 7(31), 19373-19383.

Conference Presentations

1. Sukhvir Kaur Bhangu, Muthupandian Ashokkumar, and Judy Lee "*A Sound Method of Crystallising Paracetamol* "48th BACG 27- 30 June 2017

2. Sukhvir Kaur Bhangu, Muthupandian Ashokkumar, Francesca Cavalieri "*A simple route to synthesize antioxidant fluorescent nanoparticles from phenolic molecules"*, AOSS-3 Conference India 14-16 September 2017

3. Sukhvir Kaur Bhangu, Muthupandian Ashokkumar, Francesca Cavalieri "*Ultrasonic transformation of tannic acid into bio-functional ellagic acid micro/nanocrystals with distinct morphologies"* 16th European Society of Sonochemistry, France 15-19 April 2018

4. Sukhvir Kaur Bhangu, Muthupandian Ashokkumar, Francesca Cavalieri "*Ultrasonic processing as a nonthermal technology: potential applications"*, International Nonthermal Food Processing Symposium (2018 INFPS) September 26–28, Hangzhou, China 2018

5. Sukhvir Kaur Bhangu, Muthupandian Ashokkumar, Francesca Cavalieri "*Ultrasonic transformation of tannic acid into bio-functional ellagic acid micro/nanocrystals with distinct morphologies"* Euro Biomaterials and Stem cells Conference, Prague 4-6 June 2018

6. Sukhvir Kaur Bhangu, Giovanni Luca Beretta, Nadia Zaffaroni, Marcin Wojnilowicz, Muthupandian Ashokkumar, and Francesca Cavalieri "*Nano-formulation of Doxorubicin using High Frequency Ultrasound"* 10th International nanomedicine conference, Sydney, 24-26 June 2019

Acknowledgements

I would like to express my deepest gratitude to the people without whom the completion of this work would not have been possible.

My sincere gratitude to Prof Muthupandian Ashokkumar, for his immense support and guidance throughout this work. I would like to thank you for encouraging my research. Your advice on both research as well as on my career have been invaluable.

I would like to extend my sincere appreciation and gratitude to Dr. Francesca Cavalieri for her enormous help, guidance and for shaping me as a researcher that I am today. I cannot thank her enough for the time, patience and encouragement she has provided me through these years. Without her eternal guiding and creative ideas my PhD would not have been possible. She helped me learn the skills that I am going to pursue for my life and Thank you for allowing me to grow as a research scientist.

My sincere thanks to Marcin Wojnilowicz for teaching and guided me with the cell biology work. Thanks to Prof. Gianfranco Bocchinfuso from University of Rome, Tor vergata for carrying out Molecular Dynamic Simulations and helping me improve the quality of my work. My sincere appreciation for Giovanni Luca Beretta from Department of Applied Research and Technological Development, Fondazione IRCCS Istituto Nazionale dei Tumori di Milano for their great contribution in cellular studies. Thanks to Prof Frank Caruso for providing access to all the facilities and equipment in NIMS laboratory. Thanks to Dr. Kristin Brown from Peter MacCallum Cancer Centre for providing me with the cell lines. Thanks to Dr Giancarlo Forte for hosting me in their research group in Brno at the Center for Translational Research at St Anne's Hospital.

I would like to extend my gratitude to all the past and present group members of the Sonochemistry and NIMS group. Enrico, Haiyan, Gisya, Stan, Rachana, Charitha, Pooja, Joydip, Rita and Masooma for sharing my frustration when things didn't work and cheering me up. Thanks to Ritu Singla who has always motivated and helped me become a confident individual. Special thanks to Parv (Parvinder Sidhu) for being there as a friend and for helping me with most of the Bio21 facilities I have used during my PhD.

Finally, my parents and family who decided to send me to Australia. My parents for not just being parents but friends for most of the times, giving me courage to stand for myself, for supporting me financially, emotionally, for putting their trust in me. There is nothing more I can ask from them. Thank you for believing in me for more than I believed myself.

I gratefully acknowledge and appreciate the support from School of Chemistry and the University of Melbourne in providing me this wonderful opportunity to be a part this prestigious institution and all the financial support recurring towards my PhD. I would extend my acknowledgement to Nanosupremi grant, John Hodgson Scholarship (Science), T.W Healy award and Norma Hilda Schuster Scholarship for their support to study abroad at the Center for Translational Research at St Anne's Hospital in Czech Republic and for attending various conferences.

This Thesis is dedicated to my Tayaji.

Table of contents

Lists of Figures and Tables

Chapter 1

Chapter 2

Chapter 3

Chapter 6

Chapter 7:

Chapter 8

Chapter 7

Chapter 1

Introduction

This chapter furbishes with a general overview on importance of nanoparticles, their biomedical applications and importance of controlling their physiochemical properties. In particular, different applications of polyphenol, amino acid and doxorubcin based nanostructures and fundamentals of ultrasound are discussed.

1.1. Nanoparticles for biomedical applications

Colloidal particles in the size range of 1-1000 nm are generally referred to as nanoparticles and sub-microparticles [1]. Biologically active nanoparticles have been attracting substantial attention because of their unique physiochemical and bio-functional properties. Nanomedicines are therapeutical or diagnostic agents with nanoscale structures and functionalities which can furbish us with simultaneous transport and delivery of drugs for both treatment and prevention of different types of diseases [2]. The specific and unspecific interactions of nanoparticles with biological environments at cellular or sub-cellular level are affected by different physical properties of the nanoparticles such as geometry (size, shape), chemical composition, surface charge and functionality. Since the physiochemical properties of the nanoparticles are critical factor for controlling their bioactivity, the procedures to synthesize uniform, different shape and different biomolecules nanostructures are of greatest interest.

Potential benefits offered by the nanoparticles include: (1) the ability to carry drugs and improving their pharmacological properties without doing any alteration to the drug itself and preventing the premature degradation of drugs, (2) more efficient delivery of drugs and active ingredients to targeted sites using both active and passive targeting mechanisms, (3) sustained delivery of payload across a range of biological barriers (epithelial and endothelial) by stimuli-responsive processes, (4) the ability to deliver multiple therapeutics agents to suppress drug resistance, (5) delivery of therapeutics agents in combination with the imaging (theranostics) for the real-time monitoring of therapy efficacy [3]. Generally, drug molecules are loaded onto the nanocarriers through electrostatic interactions, π-π stacking interactions, H-bonding interactions, or conjugation.

Figure 1.1 shows schematics of nanoparticle-mediated drug delivery to solid tumours. The passive tissue targeting was achieved by enhanced retention and permeability (ERP) effect and active targeting shown in insert was achieved by functionalisation of the nanoparticle surface with targeting ligands which can recognize the cell membrane receptors. Subsequently the nanoparticles can either release the pay load in extracellular matrix or be internalized into the cell by different endocytic processes

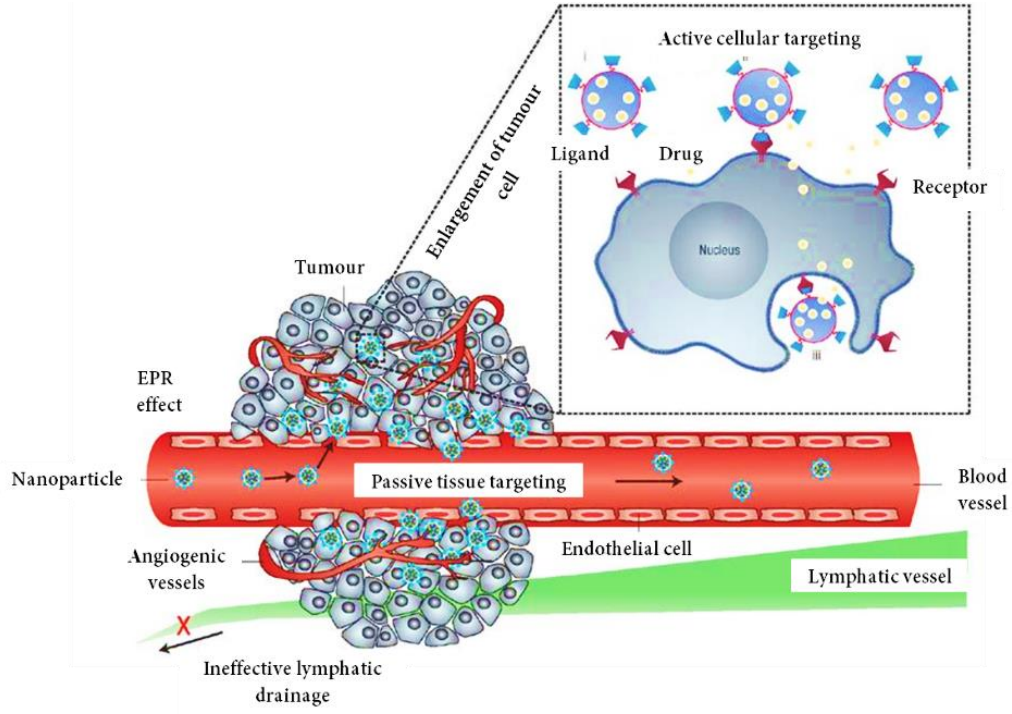

Figure 1.1: **Schematic representation of different mechanisms by which nanocarriers can deliver drugs to tumours. Adapted from [3]**

Physical and chemical properties of nanocarriers can affect their internalization pathways. After endocytosis, nanoparticles are typically transported through the endosomal and lysosomal vesicles. The endocytic vesicles recruit Rab 5 signalling proteins which mediate the fusion of the endocytic vesicles with early endosomes by interaction with early endosome antigen 1 (EEA1). Early endosomes due to adenosine triphosphate-dependent pump activity can mature to late endosomes undergoing acidification (changing the pH from 6.3 to 5.5). The maturation of endocytic vesicles leads to loss of

Rab5 and recruitment of Rab7 marker, characteristic for late endosome. Subsequently late endosome can merge with lysosome (changing the pH from 5.5 to 4.7) where different hydrolytic enzymes are present which are responsible for degradation of the cargo and the exocytosis pathway. Therefore, it is essential to synthesize particles which can trigger the endosomal escape and release the functional payload. A variety of nanomedicine platforms have been developed for various biomedical applications such as diagnosis/monitoring (devices and labelling), drug delivery (therapy) and gene delivery (transfection), detection (imaging) and tissue engineering. These include dendrimers, protein nano/microcapsules, immuno-toxin/drug fusion proteins, carbon-based nanoparticles, polymer-drug conjugates, liposomes, micelles, Metal organic frameworks (MOFs), inorganic nanoparticles (Au, Ag, Fe_3O_4, Pt, Si, ZnO), DNA, RNA, etc [4]. Figure 1.2 summarises some examples of the materials used to synthesize nanoparticles along with different factors affecting the bioactivity of these nanostructures.

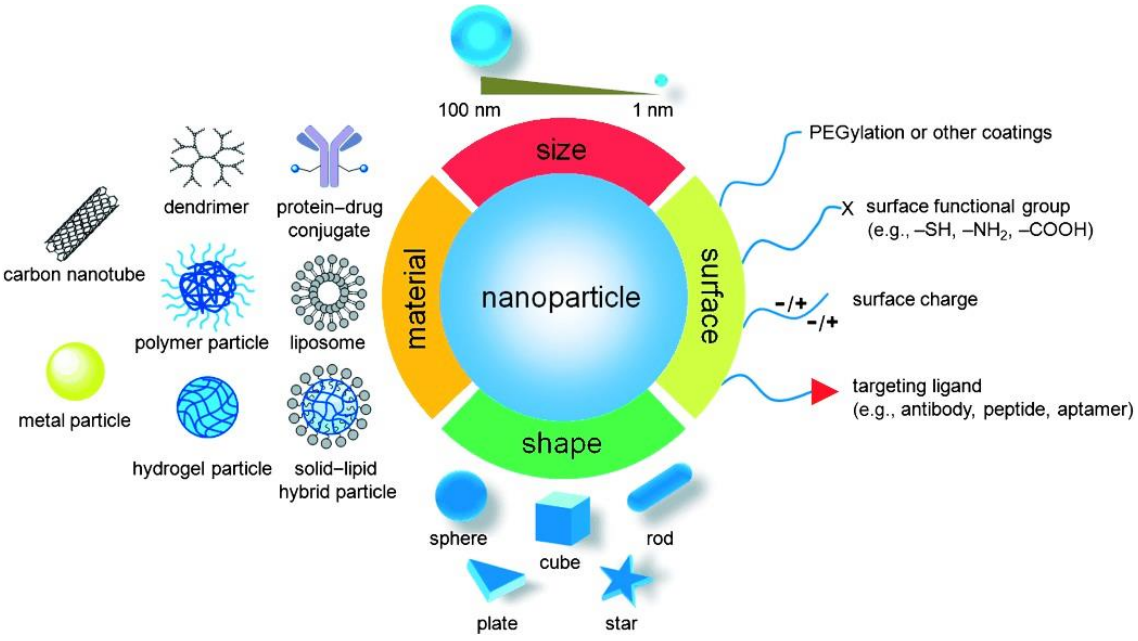

Figure 1.2: Schematic showing a summary and structure of nanocarriers used in biomedical applications and illustrating the biophysiochemical properties of the nanocarriers which can affect their bio- activity. Adapted from [4].

Before going into a detailed discussion on different types of nanomaterials studied in the current *Ph.D.* work, the following section aims to shed light on how physical properties of nanoparticles can affect the bioactivity. The shape, size and surface charge of the nanocarriers can significantly alter their biodistribution upon intravenous administration. The following discussion briefly elucidates how these parameters can affect the bioactivity of nanoplatforms.

1.1.1. Effect of nanocarrier size

The size of nanocarriers is one of key parameters to be tailored since the cellular interaction and uptake of the nanoparticles depends on the size. The two major endocytosis mechanisms involved in the cellular uptake of different particles are phagocytosis and pinocytosis [5, 6]. Phagocytosis mostly occurs in macrophages, neutrophils and dendritic cell [7]. Particles larger than 1 μm are usually internalized by this mechanism [7]. On the other hand, pinocytosis is more relevant for small size nanocarriers and occurs in majority of cell types. Pinocytosis can primarily occur through further four types of mechanisms, i.e., caveolae-mediated endocytosis, clathrin mediated endocytosis, macropinocytosis and caveolin-independent endocytosis [6-8].

Apart from uptake mechanism, the clearance and biodistribution of nanocarriers also depends upon their size. For instance, it was reported that particles <5 nm can undergo renal clearance rapidly when administrated intravenously [9]. In contrast, larger nanoparticle can also undergo clearance through sinusoids in spleen, Kupffer cells in liver [9, 10]. Particles of 2-5 μm have a propensity to accurately reside in the liver and can be often beneficial for metastatic diseases. It has been reported that particles in the range of 10-100 nm exhibit maximum uptake in vitro and are accepted for the biomedical applications depending upon their rate of clearance and biodistribution in-vivo as shown in Figure 1.3. These nanoparticles can overcome the rapid renal and lymphatic clearance.

It has also been reported that particles in the size range 100-400 nm can offer long circulation periods in blood stream which in turns enhance the tendency of the nanocarriers to penetrate and effectively accumulate into solid tumours [11]. However, the effectiveness of these particles based on their size, depends also on the type and density of tumours as well. For instance Kataoka et al. [12] tested liposomes particles of different sizes (30 nm, 50 nm, 70 nm and 100 nm) and showed that only particles smaller than 50 nm can extravasate and penetrate into poorly permeable hypovascular tumours. Although when the permeability of tumour was increased, the accumulation and penetration of 70 nm particles was also improved. Without a doubt, the size distribution is a crucial factor that influences the cellular uptake and clearance rates of nanoparticles However many contradictory claims can also be found in the literature since the behaviour of nanoparticles also depends on the material and cell type being tested. Therefore, it is important to optimize the size of the nanoparticle for a given cell type and material.

1.1.2. Effect of nanocarrier shape

In addition to the size, recent studies have suggested that particle morphology also play a significant role during cellular uptake, hemorheological dynamics and circulation of the particles *in vivo.* Though most of the nanocarriers are spherical and they show higher uptake as compared to their nanorod counterparts [13]. On the other hand, it was shown that discoidal particles exhibit higher vessel wall interactions and have high circulation half time as compared to spherical particles [14-16]. DeSimone et al. [17] have demonstrated that rod-like particles with higher aspect ratio exhibit faster internalisation towards HeLa cells in comparison with cylindrical particles irrespective of the volume of nanoparticles. They also reported that filamentous polymeric micelles have blood circulation times of >1 week as compared to 2-3 days with spherical particles [15]. It was found that all the constructs with high aspect ratios and minimum regions of curvature

such as ellipsoidal, cylindrical, discoidal and worm like particles could increase the therapeutics within tumours [18, 19]. Figure 1.3 also summarises how different flow characteristics of the particles due to their different architectures can affect the biodistribution in the different organs [20].

1.1.3. Effect of Surface charge and hydrophobicity of nanocarriers

The surface charge of the nanocarrier is another unique parameter that can also affect the cellular uptake, physical stability, and endosomal escape of the particles. Figure 1.3 shows how the biodistribution was affected depending upon the surface charge of the nanocarriers. Since the cell membrane itself is negatively charged, if the surface charge is also negative it can induce repulsions leading to slower uptake. Therefore, it is usually believed that the uptake increases with increasing positive charge. However, excessive positive charge can also pose some disadvantages for instance, toxicity, initiation of immunological reactions and high degree of non- specific uptake. On the other hand neutral and negatively charged particles show less serum protein interactions and provide long circulation [21]. Negatively charged particles show low accumulation in liver and spleen as reported by Katoaka et al. [22].

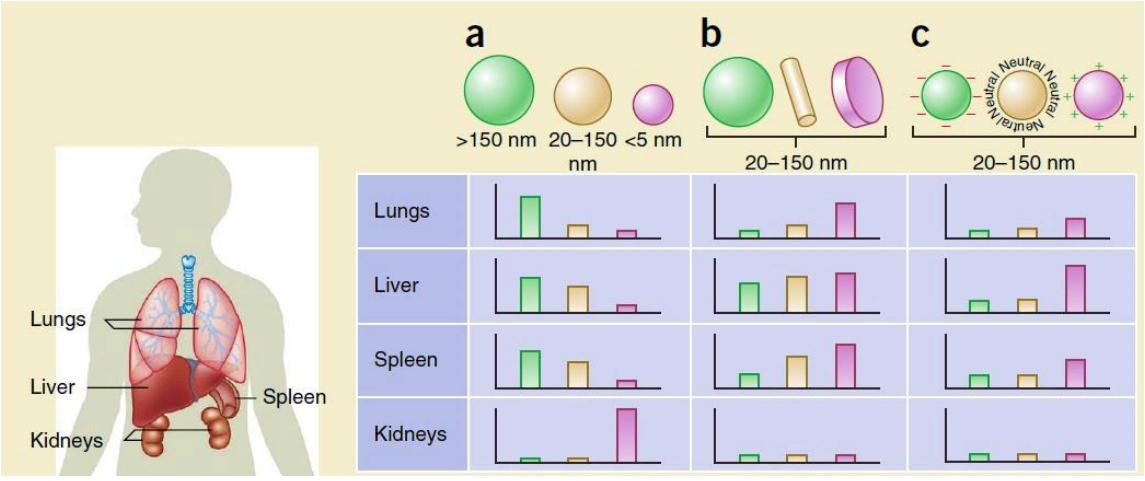

Figure 1.3: ***Summary of biodistribution of the nanocarriers in different organs - lungs, liver, kidneys and spleen in vivo depending on their (a) size [23], (b) shape [20] and (c) surface charge [24]. Figure adapted from [25].***

The hydrophobicity of the nanoparticles is another parameter that can control the uptake. Usually nanoparticles with more hydrophobic surface than cellular membrane are readily taken up by the cells [7]. However, they have higher tendency to interact and adsorb proteins and also IgG (Immunoglobin G) shows higher affinity towards hydrophobic surfaces [26].

1.1.4. Effect of the chemical composition of nanocarriers

As mentioned earlier, upon uptake nanoparticles undergo different intracellular trafficking pathways involving early endosome, late endosome and lysosomes. To deliver the payload to the site of action nanoparticles need to undergo endosomal escape which can be triggered by different mechanisms such as proton sponge effect, membrane fusion and cell membrane disruption due to formation of pores. It was reported that aromatic hydrophobic molecules and acidic endosome environment can rupture the endosomal membrane through fusion of hydrophobic moieties into the lipid bilayer and ultimately leading to escape of the entrapped species [27, 28]. Another mechanism to promote nanoparticles endosomal escape is the proton sponge effect. This is usually mediated by molecular species which have high buffering capacity and have pK_a in the range of endosomal escape (pH 7-5). This buffering capacity can lead to the osmotic swelling of the endosomes or lysosomes due to high influx of protons and ions (to maintain charge balance) leading to the rupture of vesicles membrane. This effect has been demonstrated for the histidine-rich molecules, cationic lipids and polycations such as poly(amido amine), polylysine and polyethyleneimine [29,30]. This is particularly important for delivery of therapeutic nucleic acids and proteins, where the endosomal escape of the nanocarriers is considered the rate limiting step. Therefore, it is essential to synthesize nanoparticles which bear buffering capacity, hydrophobic moieties and can successfully undergo endosomal escape to release the cargo into the cytosol.

The building blocks used for the synthesis of these nanoparticles are usually metals, synthetic polymers, proteins, peptides, inorganic materials etc. Most common methodologies used for the synthesis of inorganic and organic nanoparticles are pyrolysis, electrospray drying, sol-gel synthesis, mechanical milling, microemulsion polymerization technique, self- assembly, chemical vapour deposition, biogenic synthesis using biomolecules as the templates, biogenic synthesis using plant extracts and microorganisms [31]. Then, these nanocarriers are used as platforms for the loading and controlled delivery of synthetic drugs and biological compounds such as proteins, nucleic acids and polyphenols etc. Despite that, these methods are often associated with some drawbacks such as complex reaction procedures, poor control over size, size distribution and shape. This Ph.D. work is focused on the ultrasound mediated modification of simple phenolic, polyphenolic, amino acids and drug molecules to synthesize nanostructured particles with different sizes, shape for miscellaneous biomedical applications. The biological properties and intracellular trafficking of these newly developed particles were investigated using several techniques including confocal and super resolution microscopy. Following section provides a brief overview on why polyphenols, amino acids / peptides and doxorubicin nanostructures have been selected to fabricate these new materials.

1.2. Nanostructured particles based on polyphenols, aromatic amino acids and drugs

1.2.1. Polyphenols and their applications

Polyphenols are a class of naturally occurring compounds found in many plants and products. Over 8000 polyphenolic compounds and their analogues have been discovered from plants [32]. Significant amounts of polyphenols are present in human food which include olive oil, wine, peanuts, cereals, apple dark chocolate, green and black tea, turmeric, etc. [32]. The different types of polyphenols include tannins, phenolic acids,

flavonoids, lignins, etc. Basically, the tannins are classified into (i) Hydrolysable Tannins (which include Gallotannins and Ellagitannins) and (ii) Condensed Tannins. The interest in polyphenol biomolecules has been arising due to the fact that they can prevent neurodegenerative diseases, cardiovascular disease and their role in cancer therapy. Additionally, many types of polyphenols have their applications as antibiotics, antioxidants, antidiarrheal, antimicrobial and anti-inflammatory agents. Moreover, they can be utilized for treatment of hypertension, vascular fragility, allergies and hypercholesterolemia [33-36]. Beyond these biomedical applications, they are also utilized for several industrial applications, for instance in the production of paper, paint, cosmetics, and as a natural colorant and preservatives in food industry [33-36]. The types of polyphenols used and synthesized in this study are as follows.

1.2.1.1. Tannic acid

Tannic acid is a polyphenol which consists of a central glucose and each hydroxyl in glucose is esterified with five digallic acid molecules (Figure 1.4). It can be found in many plants such as hemlock, chestnut, gallnuts, mangrove, bark of oak and fruits. Tannic acid exhibits significant antioxidant, antiviral, antimicrobial effects, and also bears anti-cancer activity [37].

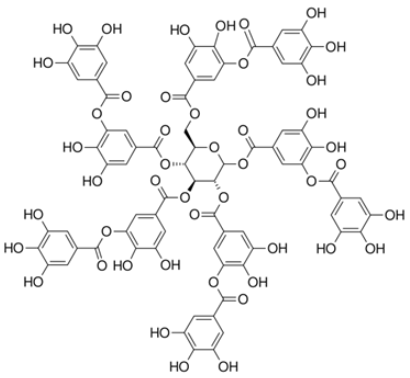

Figure 1. 4: Molecular structure of Tannic acid

1.2.1.2. Ellagic acid

Ellagic acid (structure shown in Figure 1.5) is also a naturally occurring polyphenol, mostly present in ellagitannin obtained from various fruits and vegetables (grapes, green tea, strawberries, etc.). Ellagitannins are the esters of glucose with ellagic acid [38]. Ellagic acid is proven to exert therapeutic effects against several types of cancers such as colon cancer, prostate cancer, breast cancer, skin cancer, etc., which has been proven both in vitro and in vivo [39]. It exerts anticancer effects by inducing antiproliferative and pro-apoptotic actions [40]. It also exhibits high antioxidant, anti-inflammatory activity in both bacterial and mammalian systems [41].

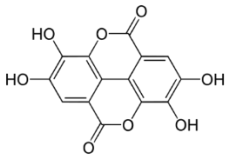

Figure 1. 5: Molecular structure of Ellagic acid

Owing to the benefits of these types of polyphenolic biomolecules in cancer therapy (drug delivery and imaging), modification and synthesis of nanoarchitectures based on specific type of biomolecule and biomacromolecules with controlled size and morphology are of great importance. Previously, polyphenolics delivery has been demonstrated using gold nanoparticles [42], silver nanoparticles [43], solid lipid nanoparticles[44], polyphenol-metal complexes etc. The details on different types of polyphenolic nanostructures are provided in chapter 2. Additionally, the polymerization of phenolic and polyphenolic moieties to generate nanostructures has been carried out to improve their bio-functionality. It can be achieved by different oxidative phenolic coupling processes. Different methods including enzymatic polymerization, coordination complexation with metal ions, etc. have been used for the oxidative coupling of these moieties. Other types

of cross-linking reactions are OH radical mediated. They are usually produced by radiations inducing decomposition of water. This PhD work utilizes ultrasound to perform such reactions without resorting to any enzymes, catalysts or other toxic reagents for the generation OH radicals.

1.2.2. Amino-acid based Nanocarriers

Although different materials and methods have been utilized for the synthesis of different nanocarriers for drug delivery and cellular imaging (Figure 2), these are often associated with various disadvantages. For instance, metal nanoparticles, quantum dots and organic fluorophores which are being used in fluorescent imaging often cause toxicity and are prone to photobleaching [45, 46]. Harnessing different amino acids and peptide-based structures with low toxicity, high biocompatibility and tunability [47] offer several benefits. Different peptides and amino acids with aromatic moieties can form different types of nanoarchitectures such as nanofibrils with solid or hollow core, spheres, which is most typically due to self-assembly processes mediated by the π-π stacking interactions [47, 48]. In addition, these kind of interactions confer optical properties to the self-assembled peptides that can be used for imaging of the targeted cancer cells [49]. The nanoparticles obtained from amino acids and peptides are very versatile nanocarriers due to (i) the small particle size (high uptake by target cells) [50], (ii) facile interactions with the hydrophobic drugs that can be loaded within nanoparticle core during self-assembly [51] and (iii) the presence of carboxyl and amine groups on the surface for further conjugation of targeting moieties [51]. Different methods and techniques used to synthesize nanoparticles based on peptides have been discussed in detail in the next chapter. However, the use of single aromatic amino acid molecules was never reported. The fluorescent nanoparticles based on aromatic amino acids can offer several advantages

such as biocompatibility, bio-imaging, high cellular uptake, drug delivery as well as can be used to probe intracellular trafficking of the drugs

1.2.3. Doxorubicin

Doxorubicin is a chemotherapy drug used to treat different types of cancers such as bladder cancer, breast cancer, leukemia, ovarian carcinoma, etc [52]. It was first isolated in the early 1960s from new strain of *Streptomyces peucetius*. Doxorubicin is known to (i) inhibit many transcription processes by intercalation into DNA duplexes [53, 54], (ii) produce reactive oxygen species (ROS) causing cellular damage (cytotoxicity secondary to lipid peroxidation) ultimately cell death by apoptosis or necrosis [55, 56] , (iii) inhibit topoisomerase II (nuclear DNA transcription enzymes-important for tertiary structure of DNA) activity resulting in DNA breaks [57]. The use of doxorubicin generally causes cardiotoxic effects resulting in severe cardiomyopathy and drug resistance [58, 59]. To mitigate these risks doxorubicin analogues have been synthesized which can be administered orally with minimal acute toxicity along with less cardiomyopathy and drug resistance [58, 60]. A variety of nanomedicine platforms have been developed for the sustained and targeted delivery of doxorubicin in cancer therapy. These include protein-based nano/microcapsules, inorganic porous materials, metal-organic frameworks, mesoporous silica-based materials protein nanoparticles, carbon-based nanoparticles, mesoporous magnetic colloidal nanocrystal clusters, polymer-drug conjugates, liposomes, micelles, inorganic nanoparticles etc [4, 58]. Major drawbacks of these nanoparticles are limited drug loading capacity, and the poor control over release of the doxorubicin. Therefore, innovative nanosystems to maximize the therapeutic effect of doxorubicin as well as to eliminating the use of additional nanocarrier and overcoming drug resistance are desirable.

The PhD study utilized and demonstrated the role of ultrasound and sonochemistry to assist complex reactions and promote assembly processes of the aforementioned biomolecules bearing aromatic moieties. The synthesis of nano-microarchitectures was performed by radical mediated oxidation reactions without the use of any external agents such as metal or inorganic catalysts, any templates, enzymes, etc. The OH radicals were generated in-situ in aqueous solutions by applying high frequency ultrasound.

Sonochemistry has been proven to exhibit a wide range of applications in electrochemistry, food technology, chemical synthesis, materials extraction, nanotechnology, phase separation, surface cleaning, water and sewage treatment, alteration of enzyme activity and the removal of deposits and biofilms from the surfaces of equipment [61, 62]. This study aims to introduce the innovative use of ultrasound to synthesize bio-nanomaterials exploiting a set of hydrophobic, amphiphilic sono-responsive biomolecules.

The following section provides background knowledge on the fundamentals and different physical and chemical effects generated by ultrasound. This section of thesis has been taken from the book chapter ("*Theory of Sonochemistry" in Topics in Current Chemistry*, *2016, 374, 56*) published during the Ph.D.

1.3. Ultrasound

Ultrasound refers to sound waves beyond the frequency that can be detected by the human ear. Sound waves with a frequency of >20 kHz fall under this category. Ultrasound is divided into three main regions: low frequency (20-100 kHz), intermediate frequency (100 kHz-1 MHz) and high frequency (1-10 MHz) [61]; however, intermediate range is also sometime referred as high frequency. Ultrasound interacts with gas bubbles in liquids generating chemical reactions and strong physical forces that could be used for various

processing applications and for promoting chemical reactions. The driving force for the generation of chemical and physical forces is acoustic cavitation. Acoustic cavitation is the phenomenon of formation, growth and violet collapse induced by the pressure fluctuations generated by sound waves in a liquid medium, which generates extreme temperatures and pressures [61].

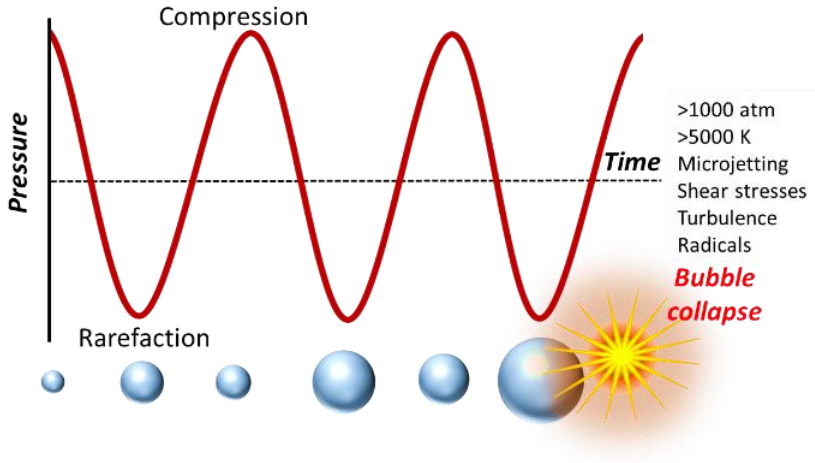

Figure 1.6: Response and size change of acoustic bubbles towards the pressure

1.3.1. Bubble formation

When the intensity of ultrasound is enough to overcome the tensile strength of the medium, there occurs a point where intermolecular forces are not able to hold the molecular structure together. This point leads to the formation of a cavity in the medium. A large amount of energy is required to create a void or cavity. Equation 1 can be used to calculate the critical pressure (P_B) required to create a cavity of radius, R_e.

$$P_B \sim P_h + \frac{0.77\sigma}{R_e} \qquad \text{Equation 1}$$

σ is surface tension of the liquid and P_h is hydrostatic pressure (could be approximated to atmospheric pressure under normal experimental conditions). The equation is valid when $2\sigma/R_e \ll P_h$ [62]. However, free gas bubbles and gas molecules trapped in solid impurities

are inherently present in liquids, which can act as nuclei for cavitation. Hence, the actual pressure required is far less for cavitation to occur. Hence, in practical terms, acoustic cavitation refers to the growth of pre-existing gas nuclei followed by the collapse of "grown" bubbles.

In order to quantify the physical and chemical effects generated during acoustic cavitation, several theoretical models on bubble oscillation dynamics are available. One of the models was developed by Rayleigh, discussed in detail by Leighton [65].

1.3.2. Bubble growth and Collapse

Bubbles inherently present in liquids tend to grow to a critical size (which is influenced by several parameters such as acoustic pressure, ultrasonic power and frequency, viscosity of medium, etc.) in an ultrasonic field. The ultrasound driven growth is due to "rectified diffusion" which is defined as "the slow growth of pulsating gas bubble due to an average flow of mass (dissolved gases and solvent vapour) into the bubble as a function of time. Crum [63] explained this "rectification of mass" in terms of two effects, viz., "area effect" and "shell effect".

Rectified diffusion leads to the growth of the bubble to a critical (resonance) size, at which the natural bubble oscillation frequency matches that of the driving ultrasound frequency. A simple relationship between the frequency of ultrasound and the resonance radius of a bubble is given Minnaert's equation (Equation 2).

$$F \times R \approx 3 \qquad \text{Equation 2}$$

(F = frequency in Hz, R = radius of the bubble in meters)

Once a critical size is reached, the bubble grows to a maximum in a single acoustic cycle and implodes (collapses). The bubble implosion, from a thermodynamic consideration is

important because a large change in bubble volume occurs. Since the bubble collapse happens in a very short time domain (~ 1 µs), the "work done" (PdV) leads to a "near" adiabatic heating of the contents of the bubble, which results in the generation of very high temperatures (> 5000 K) and pressures (> 1000 atm) within the bubble. Rayleigh initially developed the fundamental equation dealing with the collapse of gas cavity in 1917 for an isothermal process, which can be easily extended for an adiabatic process.

1.3.3. Physical & chemical effects generated by acoustic cavitation

The sudden violent collapse of a cavitation bubble gives rise to a number of physical and chemical effects in the liquid such as microstreaming, agitation, turbulence, microjetting, shock waves, generation of radicals, sonoluminescence etc. [62]. Shock waves are produced when the bubble collapse symmetrically [62]. However, when the bubble collapse unsymmetrically (mostly at a boundary), it leads to the formation of a jet in the liquid (Figure 1.7a) [64] due to the uneven acoustic field around the bubble.

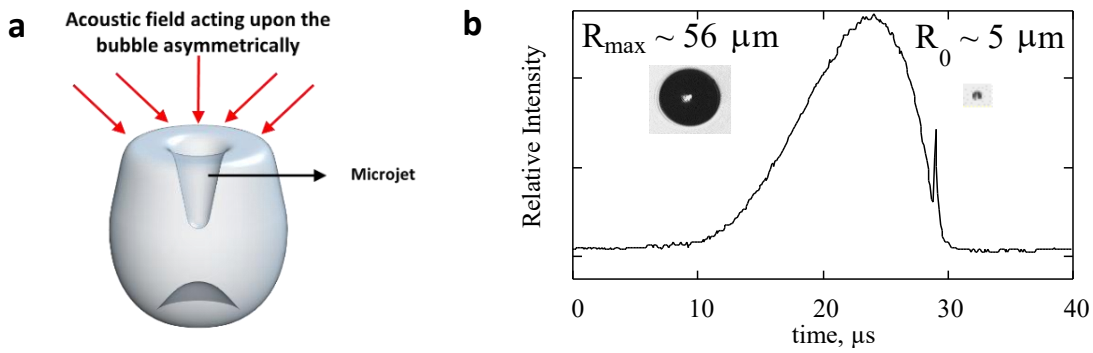

Figure 1. 7: (a) Microjet formation when a bubble collapses near solid surface [65]. (b) Relative scattered light intensity, proportional to the size of the bubble, as a function of time. Bubble growth is a relatively slow process compared to the collapse. The spike observed near end of collapse phase is the SL emission, Adapted from [61].

The microjets have velocities of the order of 100 m/s. The effect of shock waves and microstreaming together with the transition from high to low flow velocities away from

the bubble surface generates extensive amount shear stresses [65]. The generation of very high temperatures on bubble collapse leads to local heating. The heat generated can raise the temperature of the core of the bubbles to thousands of degrees for a short period (micro- to nanoseconds). Such extreme thermal conditions lead to light emission from the bubbles, referred to as sonoluminescence [66]. It was first observed in 1933 by Marinesco and Trillant [67]. Frenzel and Schultes [68] and Griffing and Sette [69] were the first to detect sonoluminescence using photomultipliers with accurate temporal resolution. Sonoluminescence can be divided in to two categories [70]. A large number of cavitation bubbles generates multibubble sonoluminescence (MBSL). Single bubble sonoluminescence (SBSL) refers to emission observed from a stably oscillating single bubble in a liquid. The change in radius of a single bubble within one acoustic cycle is shown in Figure 1.7b [61, 70-72]. The relative scattered intensity is proportional to radius of the bubble. Using a stroboscopic technique, images of an oscillating bubble were recorded and shown in Figure 5b. SL emission could also be observed at the end of bubble collapse. The intensity of SL depends on the nature of liquid medium [73, 74], amount of dissolved gases [75, 76], hydrostatic pressure [77], acoustic pressure amplitude [69, 78], and acoustic frequency [69, 79].

Another consequence of the extreme conditions of ultrasound is that it leads to a variety of chemical reactions (formation of highly reaction radical species). When an argon saturated aqueous solution is sonicated formation of $H^{\cdot}$ and $OH^{\cdot}$ radicals take place as majority of bubble content is water vapour. H radicals are reducing in nature whereas OH radicals are oxidising in nature. Two OH radicals can react leading to the formation of H_2O_2. Several techniques have been used to confirm the formation and quantification of radical species. ESR spin traps and chemical dosimeters have been used for the quantification of the radical produced during sonication [80-82]. Another method is the

reaction between terephthalic acid and $OH^{\cdot}$ radicals which leads to the formation of fluorescent hydroxyterephthalic acid [82, 83]. The intensity of fluorescence can be utilized to quantify the amount of $OH^{\cdot}$ radicals generated during cavitation. A simple method called 'Weissler'' method can be used to quantify OH Radicals, which is based on the oxidation of iodide ions [61, 84]. In this method, $OH^{\cdot}$ radicals react to produce hydrogen peroxide (Reaction 1) which can oxidize iodide ions to molecular iodine (Reaction 2). When excess of iodide ions are present, molecular iodine is converted into the triiodide complex (Reaction 3). Triiodide has absorption maximum at 353 nm which can be used to quantify the amount of iodine, and hence the amount of $OH^{\cdot}$ radicals generated.

$$2OH^{\cdot} \rightarrow H_2O_2 \qquad \text{Reaction 1}$$

$$H_2O_2 + 2I^- \rightarrow 2OH^- + I_2 \qquad \text{Reaction 2}$$

$$I_2 + I^- \rightarrow I_3^- \qquad \text{Reaction 3}$$

In air-saturated water, a variety of radicals and molecular products such as H_2O_2, HO_2, O, O_3, HNO_2, HNO_3 and H_2, are generated.

Due to these strong physical and chemical effects, various applications of acoustic cavitation have been developed for its commercial usage including wastewater treatment [85] and the formation of protein microbubbles which can be used for flavour encapsulation and drug delivery [86].

1.3.4. Effect of ultrasound frequency on sonochemistry

The extent of sonochemical reactions (for example, yield of primary and secondary radicals) and sonoluminescence intensity produced by acoustic cavitation depends on the frequency, power, etc. Various methods have been used to estimate the cavitation yield such as the amount chemical products obtained, T_{max}, SL intensity etc. as a function of acoustic frequency. Yasui et al. [87] have estimated the average temperature and rate of

production of main oxidant OH at different frequencies (20, 100, 300 and 1 MHz) as a function acoustic amplitude. At lower frequencies (20 kHz and 100 kHz), maximum temperature was reached at relatively lower acoustic amplitudes. This is due to bubble expansion to a relatively larger volume caused by the longer acoustic period, resulting in an increase in the amount of water vapour inside a bubble [88]. For a vaporous bubble, which is defined as a bubble with higher molar fraction of vapour than 0.5 at the end of the bubble collapse, the main oxidant created is OH radicals [87].

It has been shown that T_{max} is proportional to R_{max} for the frequencies greater than 16 kHz [89]. It has been observed for a gaseous bubble that when the molar fraction of vapour is less than 0.5, the collapse temperature ranges from 4000 K to 6500 K and the main oxidant is H_2O_2. However, when the bubble temperature is greater than 6500 K in gaseous bubbles, the main oxidant is O atom. The consumption of oxidants took place inside an air bubble by an oxidizing nitrogen when the bubble temperature is higher than 7000 K and the main chemical products are HNO_2, NO, and HNO_3 [87, 90].

While Yasui's [87] calculations on frequency effect are based on a single bubble system, the overall chemical activity in a multibubble system should be looked at with a different approach. While single bubble dynamics calculations provide an avenue to theoretically calculate bubble temperatures, chemical yield, sonoluminescence intensity, etc., such calculations may not provide insight into multibubble systems. Single bubble calculations tend to provide overestimates of bubble temperatures and chemical yields in when multibubble systems are considered. This is due to various factors that include bubble clustering, bubble coalescence, asymmetric collapse of bubbles, inhomogeneous nature of acoustic field, etc.

It is well known that with an increase in frequency, the number of antinodes increase. Hence, the number of cavitation bubbles generated also increase. Figure 1.8 shows the

schematic and photographic images of the standing waves observed at 37 and 440 kHz, which clearly illustrates the increase in the number of standing waves as well as the bubble population. It has been noted that the radical yield increases with an increase in frequency, reaches a maximum value and decreases with further increase in the frequency. The highest sonochemical yield is obtained between 200-800 kHz which is demonstrated in various studies [70, 91-94].

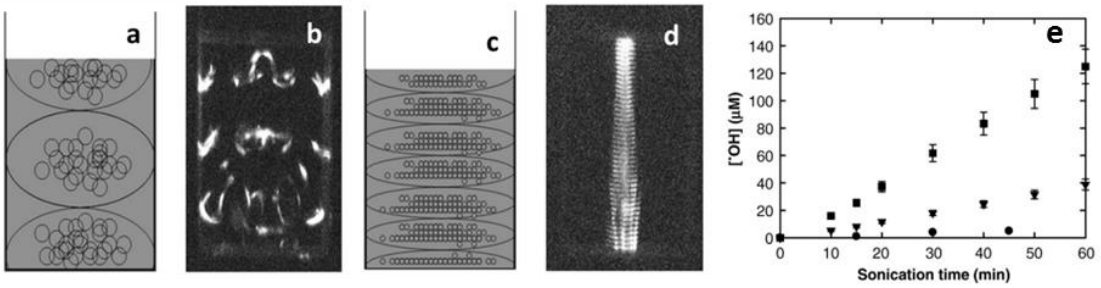

Figure 1. 8. (a) and (c) schematic representation of the standing wave leading to increase in the number of bubbles with increasing frequency, (b) and (d) Images of Sonoluminescence profile at 37 and 440 kHz respectively (Adapted from [62]).(e) OH radicals yield as a function of sonication time for different ultrasonic frequencies (■ 358 kHz, ▼ 1062 kHz, ● 20 kHz) at 0.90 W cm^{-2} (Adapted from [95])

Figure 1.8e represents the OH radical yield as a function of sonication time obtained by sonicating water for different frequencies (20 kHz, 358 kHz and 1062 kHz) at power of 0.90 W/cm^2 [95]. The amount of OH radicals produced was highest at 358 kHz whereas a decrease was observed when the frequency was increased to 1062 kHz.

This is due to a relatively lower bubble temperature generated at higher frequency and a lower amount of water vapour that could evaporate into a bubble during the expansion phase [95].

Using the resonance radius of the bubbles at each frequency, the amount of water molecules in a monolayer on the surface of bubbles could be calculated [95]. As for the evaporation process, a finite time is required. From the time required for evaporation and expansion cycle and the number of molecules at the interface, it can be seen that the mass

that evaporates exceeds the amount present in a monolayer on the bubble surface at lower frequencies. At higher frequencies, the amount that could evaporate is less than a monolayer, which is due to very short expansion time available during bubble oscillations. Though a surge in bubble population occurs at higher frequency, the size of bubble reduces leading to a decrease in the bubble temperature hence the radical yield. Thus, a combination of lower bubble temperature and lower amount of water vapour present inside a collapsing bubble is responsible for a decrease in sonochemical efficiency at very high frequencies.

1.4. References

1. Kreuter, J., *Nanoparticles—a historical perspective.* International journal of pharmaceutics, 2007. **331**(1): p. 1-10.
2. Elsabahy, M. and K.L. Wooley, *Design of polymeric nanoparticles for biomedical delivery applications.* Chemical Society Reviews, 2012. **41**(7): p. 2545-2561.
3. Peer, D., J.M. Karp, S. Hong, O.C. Farokhzad, R. Margalit, and R. Langer, *Nanocarriers as an emerging platform for cancer therapy.* Nature nanotechnology, 2007. **2**(12): p. 751.
4. Sun, T., Y.S. Zhang, B. Pang, D.C. Hyun, M. Yang, and Y. Xia, *Engineered nanoparticles for drug delivery in cancer therapy.* Angewandte Chemie International Edition, 2014. **53**(46): p. 12320-12364.
5. Conner, S.D. and S.L. Schmid, *Regulated portals of entry into the cell.* Nature, 2003. **422**(6927): p. 37.
6. Kamaly, N., Z. Xiao, P.M. Valencia, A.F. Radovic-Moreno, and O.C. Farokhzad, *Targeted polymeric therapeutic nanoparticles: design, development and clinical translation.* Chemical Society Reviews, 2012. **41**(7): p. 2971-3010.
7. Zhao, F., Y. Zhao, Y. Liu, X. Chang, C. Chen, and Y. Zhao, *Cellular uptake, intracellular trafficking, and cytotoxicity of nanomaterials.* Small, 2011. **7**(10): p. 1322-1337.
8. Verma, A. and F. Stellacci, *Effect of surface properties on nanoparticle–cell interactions.* Small, 2010. **6**(1): p. 12-21.
9. Choi, H.S., W. Liu, P. Misra, E. Tanaka, J.P. Zimmer, B.I. Ipe, M.G. Bawendi, and J.V. Frangioni, *Renal clearance of quantum dots.* Nature biotechnology, 2007. **25**(10): p. 1165.
10. Wisse, E., F. Braet, D. Luo, R. De Zanger, D. Jans, E. Crabbe, and A. Vermoesen, *Structure and function of sinusoidal lining cells in the liver.* Toxicologic pathology, 1996. **24**(1): p. 100-111.
11. Torchilin, V.P., *Targeted pharmaceutical nanocarriers for cancer therapy and imaging.* The AAPS journal, 2007. **9**(2): p. E128-E147.
12. Cabral, H., Y. Matsumoto, K. Mizuno, Q. Chen, M. Murakami, M. Kimura, Y. Terada, M. Kano, K. Miyazono, and M. Uesaka, *Accumulation of sub-100 nm polymeric micelles in poorly permeable tumours depends on size.* Nature nanotechnology, 2011. **6**(12): p. 815.
13. Mahmoudi, M., K. Azadmanesh, M.A. Shokrgozar, W.S. Journeay, and S. Laurent, *Effect of nanoparticles on the cell life cycle.* Chemical reviews, 2011. **111**(5): p. 3407-3432.

14. Gentile, F., C. Chiappini, D. Fine, R. Bhavane, M. Peluccio, M.M.-C. Cheng, X. Liu, M. Ferrari, and P. Decuzzi, *The effect of shape on the margination dynamics of non-neutrally buoyant particles in two-dimensional shear flows.* Journal of biomechanics, 2008. **41**(10): p. 2312-2318.
15. Geng, Y., P. Dalhaimer, S. Cai, R. Tsai, M. Tewari, T. Minko, and D.E. Discher, *Shape effects of filaments versus spherical particles in flow and drug delivery.* Nature nanotechnology, 2007. **2**(4): p. 249.
16. Decuzzi, P., B. Godin, T. Tanaka, S.-Y. Lee, C. Chiappini, X. Liu, and M. Ferrari, *Size and shape effects in the biodistribution of intravascularly injected particles.* Journal of Controlled Release, 2010. **141**(3): p. 320-327.
17. Wang, J., J.D. Byrne, M.E. Napier, and J.M. DeSimone, *More effective nanomedicines through particle design.* Small, 2011. **7**(14): p. 1919-1931.
18. Champion, J.A. and S. Mitragotri, *Role of target geometry in phagocytosis.* Proceedings of the National Academy of Sciences, 2006. **103**(13): p. 4930-4934.
19. Champion, J.A. and S. Mitragotri, *Shape induced inhibition of phagocytosis of polymer particles.* Pharmaceutical research, 2009. **26**(1): p. 244-249.
20. Black, K.C., Y. Wang, H.P. Luehmann, X. Cai, W. Xing, B. Pang, Y. Zhao, C.S. Cutler, L.V. Wang, and Y. Liu, *Radioactive 198Au-doped nanostructures with different shapes for in vivo analyses of their biodistribution, tumor uptake, and intratumoral distribution.* ACS nano, 2014. **8**(5): p. 4385-4394.
21. Alexis, F., E. Pridgen, L.K. Molnar, and O.C. Farokhzad, *Factors affecting the clearance and biodistribution of polymeric nanoparticles.* Molecular pharmaceutics, 2008. **5**(4): p. 505-515.
22. Yamamoto, Y., Y. Nagasaki, Y. Kato, Y. Sugiyama, and K. Kataoka, *Long-circulating poly (ethylene glycol)–poly (d, l-lactide) block copolymer micelles with modulated surface charge.* Journal of controlled release, 2001. **77**(1-2): p. 27-38.
23. Longmire, M., P.L. Choyke, and H. Kobayashi, *Clearance properties of nano-sized particles and molecules as imaging agents: considerations and caveats.* 2008.
24. Xiao, K., Y. Li, J. Luo, J.S. Lee, W. Xiao, A.M. Gonik, R.G. Agarwal, and K.S. Lam, *The effect of surface charge on in vivo biodistribution of PEG-oligocholic acid based micellar nanoparticles.* Biomaterials, 2011. **32**(13): p. 3435-3446.
25. Blanco, E., H. Shen, and M. Ferrari, *Principles of nanoparticle design for overcoming biological barriers to drug delivery.* Nature biotechnology, 2015. **33**(9): p. 941.
26. Vonarbourg, A., C. Passirani, P. Saulnier, and J.-P. Benoit, *Parameters influencing the stealthiness of colloidal drug delivery systems.* Biomaterials, 2006. **27**(24): p. 4356-4373.
27. Chen, L., L. Gan, M. Liu, R. Fan, Z. Xu, Z. Hao, and L. Chen, *Destabilization of artificial biomembrane induced by the penetration of tryptophan.* Applied Surface Science, 2011. **257**(11): p. 5070-5076.
28. Lönn, P., A.D. Kacsinta, X.-S. Cui, A.S. Hamil, M. Kaulich, K. Gogoi, and S.F. Dowdy, *Enhancing endosomal escape for intracellular delivery of macromolecular biologic therapeutics.* Scientific reports, 2016. **6**: p. 32301.
29. Pack, D.W., D. Putnam, and R. Langer, *Design of imidazole-containing endosomolytic biopolymers for gene delivery.* Biotechnology and Bioengineering, 2000. **67**(2): p. 217-223.
30. Lin, C. and J.F. Engbersen, *Effect of chemical functionalities in poly (amido amine) s for non-viral gene transfection.* Journal of controlled release, 2008. **132**(3): p. 267-272.
31. Dhand, C., N. Dwivedi, X.J. Loh, A.N.J. Ying, N.K. Verma, R.W. Beuerman, R. Lakshminarayanan, and S. Ramakrishna, *Methods and strategies for the synthesis of diverse nanoparticles and their applications: a comprehensive overview.* Rsc Advances, 2015. **5**(127): p. 105003-105037.
32. Kaur, H. and G. Kaur, *A critical appraisal of solubility enhancement techniques of polyphenols.* Journal of pharmaceutics, 2014. **2014**.
33. Bravo, L., *Polyphenols: chemistry, dietary sources, metabolism, and nutritional significance.* Nutrition reviews, 1998. **56**(11): p. 317-333.

34. Kühnau, J., *The flavonoids. A class of semi-essential food components: their role in human nutrition*, in *World review of nutrition and dietetics*. 1976, Karger Publishers. p. 117-191.
35. Saito, M., H. Hosoyama, T. Ariga, S. Kataoka, and N. Yamaji, *Antiulcer activity of grape seed extract and procyanidins.* Journal of Agricultural and Food Chemistry, 1998. **46**(4): p. 1460-1464.
36. Singleton, V.L., *Naturally occurring food toxicants: phenolic substances of plant origin common in foods.* Advances in food research, 1981. **27**: p. 149-242.
37. Labieniec, M. and T. Gabryelak, *Effects of tannins on Chinese hamster cell line B14.* Mutation Research/Genetic Toxicology and Environmental Mutagenesis, 2003. **539**(1): p. 127-135.
38. Girish, C. and S.C. Pradhan, *Drug development for liver diseases: focus on picroliv, ellagic acid and curcumin.* Fundamental & clinical pharmacology, 2008. **22**(6): p. 623-632.
39. Heber, D., *Multitargeted therapy of cancer by ellagitannins.* Cancer letters, 2008. **269**(2): p. 262-268.
40. Zhang, H.-M., L. Zhao, H. Li, H. Xu, W.-W. Chen, and L. Tao, *Research progress on the anticarcinogenic actions and mechanisms of ellagic acid.* Cancer biology & medicine, 2014. **11**(2): p. 92.
41. Vattem, D. and K. Shetty, *Biological functionality of ellagic acid: a review.* Journal of food biochemistry, 2005. **29**(3): p. 234-266.
42. Sanz, V.C., M.L. Mena, A. González-Cortés, P. Yanez-Sedeno, and J. Pingarrón, *Development of a tyrosinase biosensor based on gold nanoparticles-modified glassy carbon electrodes: Application to the measurement of a bioelectrochemical polyphenols index in wines.* Analytica Chimica Acta, 2005. **528**(1): p. 1-8.
43. Moulton, M.C., L.K. Braydich-Stolle, M.N. Nadagouda, S. Kunzelman, S.M. Hussain, and R.S. Varma, *Synthesis, characterization and biocompatibility of "green" synthesized silver nanoparticles using tea polyphenols.* Nanoscale, 2010. **2**(5): p. 763-770.
44. Pandita, D., S. Kumar, N. Poonia, and V. Lather, *Solid lipid nanoparticles enhance oral bioavailability of resveratrol, a natural polyphenol.* Food research international, 2014. **62**: p. 1165-1174.
45. Gonçalves, M.S.T., *Fluorescent labeling of biomolecules with organic probes.* Chemical reviews, 2008. **109**(1): p. 190-212.
46. Ranjbarvaziri, S., S. Kiani, A. Akhlaghi, A. Vosough, H. Baharvand, and N. Aghdami, *Quantum dot labeling using positive charged peptides in human hematopoetic and mesenchymal stem cells.* Biomaterials, 2011. **32**(22): p. 5195-5205.
47. Ulijn, R.V. and A.M. Smith, *Designing peptide based nanomaterials.* Chemical Society Reviews, 2008. **37**(4): p. 664-675.
48. Chan, K.H., W.H. Lee, S. Zhuo, and M. Ni, *Harnessing supramolecular peptide nanotechnology in biomedical applications.* International journal of nanomedicine, 2017. **12**: p. 1171.
49. Fan, Z., L. Sun, Y. Huang, Y. Wang, and M. Zhang, *Bioinspired fluorescent dipeptide nanoparticles for targeted cancer cell imaging and real-time monitoring of drug release*. Nature nanotechnology, 2016. **11**(4): p. 388.
50. Kogan, M.J., I. Olmedo, L. Hosta, A. R Guerrero, L.J. Cruz, and F. Albericio, *Peptides and metallic nanoparticles for biomedical applications.* 2007.
51. Crombez, L., M.C. Morris, S. Deshayes, F. Heitz, and G. Divita, *Peptide-based nanoparticle for ex vivo and in vivo dug delivery.* Current pharmaceutical design, 2008. **14**(34): p. 3656-3665.
52. Kaushik, D. and G. Bansal, *Four new degradation products of doxorubicin: An application of forced degradation study and hyphenated chromatographic techniques.* Journal of pharmaceutical analysis, 2015. **5**(5): p. 285-295.
53. Agudelo, D., P. Bourassa, G. Bérubé, and H.-A. Tajmir-Riahi, *Intercalation of antitumor drug doxorubicin and its analogue by DNA duplex: structural features and biological implications.* International journal of biological macromolecules, 2014. **66**: p. 144-150.

54. Quach, B., A. Birk, and H. Szeto, *Mechanism of preventing doxorubicin-induced mitochondrial toxicity with cardiolipin-targeted peptide, SS-31 (966.1).* The FASEB Journal, 2014. **28**(1_supplement): p. 966.1.
55. Cheregi, B., C. Timpani, K. Nurgali, A. Hayes, and E. Rybalka, *Chemotherapy-induced mitochondrial respiratory dysfunction, oxidant production and death in healthy skeletal muscle C2C12 myoblast and myotube models.* Neuromuscular Disorders, 2015. **25**: p. S202.
56. Deavall, D.G., E.A. Martin, J.M. Horner, and R. Roberts, *Drug-induced oxidative stress and toxicity.* Journal of toxicology, 2012. **2012**.
57. Sawyer, D.B., X. Peng, B. Chen, L. Pentassuglia, and C.C. Lim, *Mechanisms of anthracycline cardiac injury: can we identify strategies for cardioprotection?* Progress in cardiovascular diseases, 2010. **53**(2): p. 105-113.
58. Shen, S., Y. Wu, Y. Liu, and D. Wu, *High drug-loading nanomedicines: progress, current status, and prospects.* International journal of nanomedicine, 2017. **12**: p. 4085.
59. Abraham, S.A., D.N. Waterhouse, L.D. Mayer, P.R. Cullis, T.D. Madden, and M.B. Bally, *The liposomal formulation of doxorubicin*, in *Methods in enzymology*. 2005, Elsevier. p. 71-97.
60. L Beretta, G. and F. Cavalieri, *Engineering nanomedicines to overcome multidrug resistance in cancer therapy.* Current medicinal chemistry, 2016. **23**(1): p. 3-22.
61. Ashokkumar, M. and T.J. Mason, *Sonochemistry.* Kirk-Othmer Encyclopedia of Chemical Technology, 2007.
62. Ashokkumar, M., *Ultrasonic Synthesis of Functional Materials*, in *Ultrasonic Synthesis of Functional Materials*. 2016, Springer. p. 17-40.
63. Crum, L., *Acoustic cavitation series: part five rectified diffusion.* Ultrasonics, 1984. **22**(5): p. 215-223.
64. Crum, L., *Sonoluminescence, sonochemistry, and sonophysics.* The Journal of the Acoustical Society of America, 1994. **95**(1): p. 559-562.
65. Mason, T.J. and D. Peters, *Practical sonochemistry: Power ultrasound uses and applications*. 2002: Woodhead Publishing.
66. Ashokkumar, M., J. Lee, S. Kentish, and F. Grieser, *Bubbles in an acoustic field: an overview.* Ultrasonics Sonochemistry, 2007. **14**(4): p. 470-475.
67. Trillat, N.M.a.J.J., *Action des ultrasons sur les plaques photographiques.* C.R. Acad. Sci. Paris, 1933. **196**: p. 858.
68. Schultes, H.F.a.H., *Luminescenz im Ultraschallbeschickten Wasser*. Z. Phys. Chem, 1935. **27B**: p. 421.
69. Griffing, V. and D. Sette, *Luminescence produced as a result of intense ultrasonic waves.* The Journal of Chemical Physics, 1955. **23**(3): p. 503-509.
70. Suslick, K.S. and L.A. Crum, *Sonochemistry and sonoluminescence*. 1998: Wiley-Interscience: New York.
71. Yasui, K., *Mechanism of single-bubble sonoluminescence.* Physical Review E, 1999. **60**(2): p. 1754.
72. An, Y., *Mechanism of single-bubble sonoluminescence.* Physical Review E, 2006. **74**(2): p. 026304.
73. JARMAN, P., *SONOLUMINESCENCE.* Science Progress (1933-), 1958. **46**(184): p. 632-639.
74. Crum, L., A. Walton, A. Mortimer, M. Dyson, D. Crawford, and D. Gaitan, *Free radical production in amniotic fluid and blood plasma by medical ultrasound.* Journal of ultrasound in medicine, 1987. **6**(11): p. 643-647.
75. Finch, R., *Sonoluminescence.* Ultrasonics, 1963. **1**(2): p. 87-98.
76. Weissler, A., *Sonochemistry: the production of chemical changes with sound waves.* The Journal of the Acoustical Society of America, 1953. **25**(4): p. 651-657.
77. Chendke, P. and H. Fogler, *Sonoluminescence and sonochemical reactions of aqueous carbon tetrachloride solutions.* The Journal of Physical Chemistry, 1983. **87**(8): p. 1362-1369.

78. Parke, A. and D. Taylor, *855. The chemical action of ultrasonic waves.* Journal of the Chemical Society (Resumed), 1956: p. 4442-4450.
79. Chambers, L.A., *The emission of visible light from cavitated liquids.* The Journal of Chemical Physics, 1937. **5**(5): p. 290-292.
80. Misik, V., N. Miyoshi, and P. Riesz, *EPR spin-trapping study of the sonolysis of H2O/D2O mixtures: probing the temperatures of cavitation regions.* The Journal of Physical Chemistry, 1995. **99**(11): p. 3605-3611.
81. Mišík, V. and P. Riesz, *EPR study of free radicals induced by ultrasound in organic liquids II. Probing the temperatures of cavitation regions.* Ultrasonics sonochemistry, 1996. **3**(1): p. 25-37.
82. Mišík, V. and P. Riesz, *Recent applications of EPR and spin trapping to sonochemical studies of organic liquids and aqueous solutions.* Ultrasonics Sonochemistry, 1996. **3**(3): p. S173-S186.
83. Mason, T., J. Lorimer, D. Bates, and Y. Zhao, *Dosimetry in sonochemistry: the use of aqueous terephthalate ion as a fluorescence monitor.* Ultrasonics Sonochemistry, 1994. **1**(2): p. S91-S95.
84. Ashokkumar, M., T. Niblett, L. Tantiongco, and F. Grieser, *Sonochemical degradation of sodium dodecylbenzene sulfonate in aqueous solutions.* Australian journal of chemistry, 2003. **56**(10): p. 1045-1049.
85. Duckhouse, H., T. Mason, S. Phull, and J. Lorimer, *The effect of sonication on microbial disinfection using hypochlorite.* Ultrasonics sonochemistry, 2004. **11**(3): p. 173-176.
86. Ferrara, K., R. Pollard, and M. Borden, *Ultrasound microbubble contrast agents: fundamentals and application to gene and drug delivery.* Biomedical Engineering, 2007. **9**: p. 415-447.
87. Yasui, K., T. Tuziuti, T. Kozuka, A. Towata, and Y. Iida, *Relationship between the bubble temperature and main oxidant created inside an air bubble under ultrasound.* The Journal of chemical physics, 2007. **127**(15): p. 154502-154502.
88. Yasui, K., *Effect of liquid temperature on sonoluminescence.* Physical Review E, 2001. **64**(1): p. 016310.
89. Toegel, R., B. Gompf, R. Pecha, and D. Lohse, *Does water vapor prevent upscaling sonoluminescence?* Physical Review Letters, 2000. **85**(15): p. 3165.
90. Yasui, K., T. Tuziuti, and Y. Iida, *Optimum bubble temperature for the sonochemical production of oxidants.* Ultrasonics, 2004. **42**(1): p. 579-584.
91. Beckett, M.A. and I. Hua, *Impact of ultrasonic frequency on aqueous sonoluminescence and sonochemistry.* The Journal of Physical Chemistry A, 2001. **105**(15): p. 3796-3802.
92. Capocelli, M., E. Joyce, A. Lancia, T.J. Mason, D. Musmarra, and M. Prisciandaro, *Sonochemical degradation of estradiols: Incidence of ultrasonic frequency.* Chemical engineering journal, 2012. **210**: p. 9-17.
93. Kanthale, P., M. Ashokkumar, and F. Grieser, *Sonoluminescence, sonochemistry (H_2O_2 yield) and bubble dynamics: frequency and power effects.* Ultrasonics sonochemistry, 2008. **15**(2): p. 143-150.
94. Petrier, C., A. Jeunet, J.L. Luche, and G. Reverdy, *Unexpected frequency effects on the rate of oxidative processes induced by ultrasound.* Journal of the American Chemical Society, 1992. **114**(8): p. 3148-3150.
95. Ashokkumar, M., D. Sunartio, S. Kentish, R. Mawson, L. Simons, K. Vilkhu, and C.K. Versteeg, *Modification of food ingredients by ultrasound to improve functionality: a preliminary study on a model system.* Innovative Food Science & Emerging Technologies, 2008. **9**(2): p. 155-160.
96. Leighton, T., *The acoustic bubble*. 2012: Academic press.
97. Plesset, M., *The dynamics of cavitation bubbles.* Journal of applied mechanics, 1949. **16**: p. 277-282.
98. Rayleigh, L., *VIII. On the pressure developed in a liquid during the collapse of a spherical cavity.* The London, Edinburgh, and Dublin Philosophical Magazine and Journal of Science, 1917. **34**(200): p. 94-98.

99. poritsky, p., *The collapse or growth of a spherical bubble or cavity in a viscous fluid.* proceedings of the 1st US National Congress in Applied Mathematics, 1952: p. 813.
100. Tomita, Y. and A. Shima, *Mechanisms of impulsive pressure generation and damage pit formation by bubble collapse.* Journal of Fluid Mechanics, 1986. **169**: p. 535-564.
101. Yasui, K., *Effect of non-equilibrium evaporation and condensation on bubble dynamics near the sonoluminescence threshold.* Ultrasonics, 1998. **36**(1): p. 575-580.

Chapter 2

Literature Review

This chapter reviews various studies dealing with the delivery of polyphenols and doxorubicin using different type of nanocarriers, self-assembly of amino acids, peptides and their applications. Moreover, numerous types of reactions mediated by ultrasound such as synthesis of nanoparticles and ultrasound-induced polymerization reactions were also reviewed.

Previous chapter provides an overview on the importance of nanoparticles in biomedical field along with the knowledge on fundamentals of ultrasound. The main aim of the current study is to investigate the role of ultrasound for the synthesis of nanoarchitectures from phenolic compounds and simple amino acids molecules and extend this study to hydrophobic chemotherapy drugs. Therefore, this chapter provides an insight into the previous reports on different methods to fabricate phenolic and amino acid (through self-assembly) functionalised or based nanostructures along with their biomedical application. Till date several reports dealing with the polyphenolic, drug and amino acid molecules have been published. Most of the research adheres formation of metal-phenol complexes, protein or polysaccharide-polyphenol conjugates and loading or encapsulation of these (drugs, polyphenols) on to other nanoplatforms (metal, liposome, protein nanostructures, etc.). However, negligible amount of work could be found, where polyphenol- modified, single amino acid-modified or doxorubicin-based nanostructures are fabricated. In this chapter, diverse methods and techniques used to manufacture polyphenol-based and doxorubicin-based particles are discussed. Moreover, reports dealing with self-assembly of amino acid and peptides to generate nanoparticles are summarised. The last section of the chapter bestows an overview on the numerous ultrasound mediated reactions used for the synthesis of different nanostructures.

2.1. Synthesis of polyphenol-based nanostructures

The polyphenol functionalised nanostructures and polymerization of phenolic moieties to generate polyphenolic structures have received much attention recently due to their applications in biomedicine, food industry, dyes, formation of biodegradable plastics, etc. [1-5]. The applications of different polyphenolic molecules have already been discussed in the previous chapter. Considering, only phenol itself its oxidized products (catechol,

hydroquinone) have been used in various applications such as in dyes, perfumes, rubber, medicine, etc. [5]. Several methods are used to carry out oxidative coupling reaction among various aromatic phenolic moieties which are listed below.

2.1.1. Enzyme and Metal - Catalysed oxidative coupling

Polymerization of phenol by using peroxidase catalysis has been carried out with different techniques; for example, soybean peroxidase along with H_2O_2 was used to form such reactions [6, 7]. The use of copper ions and copper complexes as catalysts was also employed in the polymerization of phenol [7, 8]. Enzymatic polymerization of phenol using templates like poly (ethylene glycol) and poly-(ethylene glycol) monododecyl ether was performed to synthesize a soluble polyphenol-poly (ethylene glycol) complex [9-11]. Similarly, horseradish peroxidase (HRP) was used to polymerize 3-methylcatechol, which has applications in germanium recovery [2]. The proposed mechanism involved the generation of radicals by HRP and H_2O_2, transfer of radicals to the monomer, polymerization of the monomer, and ultimately precipitation of the polyphenols. Alternatively, oxidative coupling reactions were also studied using pulse radiolysis and Fenton- type reactions [12-14].

Zhenhua et al. [3] performed heat-induced oxidative coupling to assemble green tea polyphenol using copper (II) as a catalyst. They synthesised the biocompatible fluorescent smooth, hollow and porous nanospheres from different green tea polyphenols (epi-catechins and (epi)(gallo)catechins gallates) (Figure 2.1). The polyphenolic moieties were first converted into their corresponding quinones (T') and semiquinones (T). Next, the T-T' combines through nucleophilic addition [15] or by coupling of two semi-quinone radicals [15-17]. The process was controlled by the redox cyclization of Cu^{2+}/Cu^{+} and the coordination of Cu to the polyphenols [16, 18]. The continuation of this process, led to

the formation of oligomeric/polymeric tea polyphenols, which then self-assemble into yellow spherical nanostructures by non-covalent interactions when the temperatures was dropped to the room temperature.

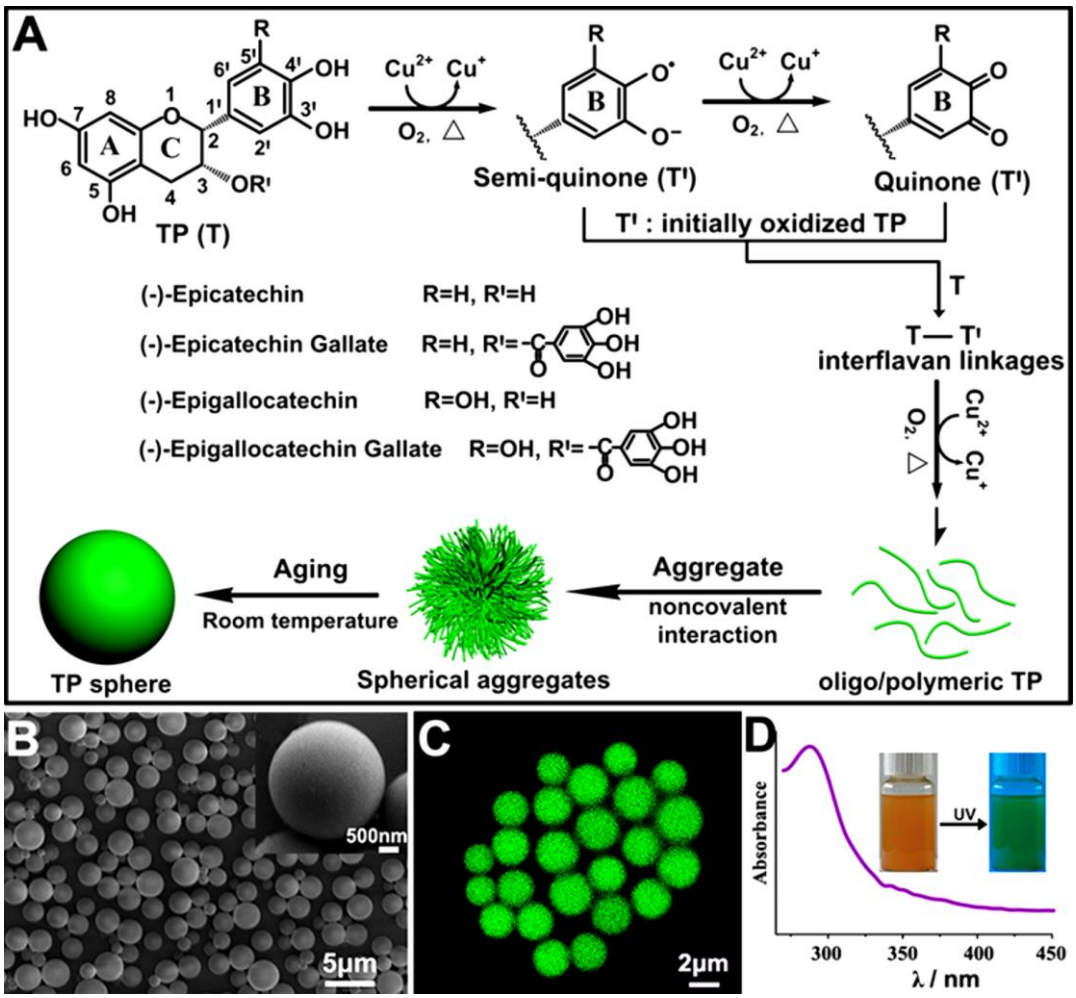

Figure 2. 1: (A) Schematic illustration of temperature and Cu(II) mediated oxidative assembly of Tea polyphenol (TP), and characterization of CT-1 spheres obtained in the presence of 70 mM Cu2+ at 100 °C: (B) SEM, (C) CLSM and (D) UV−vis absorption spectrum and well-dispersed spheres in water. Adapted from [3]

Fei et al. [4] reported an oxidative coupling reaction using $AgNO_3$ under microwave irradiation to synthesize metal−tea polyphenol nanoparticles. They demonstrated a one pot synthesis of tea- polyphenol functionalised Ag/Au core shell nanocomposites with Near InfraRed (NIR) absorption which can be exploited for cancer diagnosis and treatment [4]. In addition to this, different metal-phenol networks (MPN) have also been

explored by Rahim et al. [19]. They have demonstrated the chelation of tannic acid with iron (Fe(III)). It was reported that catechol and galloyl units present in polyphenol molecules chelate with Fe to form mono-tris type coordination complexes, which can self-assembly into core shell nanostructures after core removal. Apart from Fe(III), Guo et al. [20] reported that tannic acid can form coordination complex with other metal ions such as manganese, chromium, aluminium, vanadium, nickel, copper, zinc, etc. (Figure 2.2) [20-22]. The synthesized MPN capsules were applied for the drug delivery, magnetic resonance imaging (MRI) and positron emission tomography applications[20]. Analogously, resorcinol when chelated with Fe(III) formed thin planar films[23].

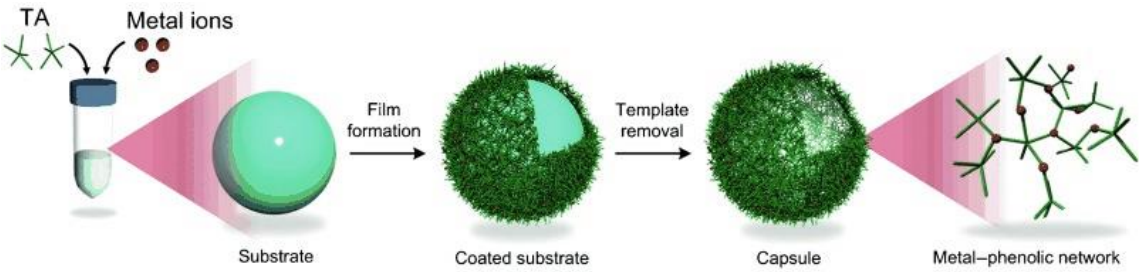

Figure 2. 2: The formation of tannic acid and metal ions film on to the particulate template and removal of template to form Metal phenol networked (MPN) capsules. Adapted from [20].

Jing et al. [24] synthesised metal-coordination complexes with crystalline framework and regular morphology. They reported the formation of Co or Fe tannic acid complex which on hydrothermal treatment was converted to a crystalline framework. They proposed simultaneous self- assembly of Co ion and tannic acid to form coordination complex and oxidative self-polymerisation of tannic acid at alkaline pH and high temperature [24]. Zieschang et al. [25] synthesized the bioactive flavonoids (quercetin, myricetin, luteolin and fisetin) metal (Fe) coordinated thin films and hollow capsules. The synthesised flavonoid films showed higher radical scavenging activity as compared to their parent

molecules. Ju et al.[26] performed template assisted self-assembly to form low-fouling and pH degradable MPNs. They conjugated catechol groups in polyphenol to poly ethylene glycol (PEG) and synthesized PEG-MPN showed higher resistance to non-specific binding to proteins. The MPN were disassembling in physiological conditions (pH=5) providing control release of payload and can be used for intracellular drug delivery. Therefore, range of metals and polyphenols can be used for the synthesis of MPNs.

2.1.2. Protein and Polysaccharide conjugates

It is prominent that polyphenols can be oxidised in alkaline solutions in the presence of oxygen to conjugate with proteins forming protein-polyphenol conjugates [27, 28]. The phenolic moieties are first oxidised to their respective quinones and then react with lysine, tryptophan or other free amino groups in the proteins. Rawel et al.[29, 30] and Rohan et al. [30, 31] have reported the formation of whey proteins-quercetin; whey proteins-rutin; BSA-quercetin; soy or whey proteins- isoflavones conjugates by alkaline treatment which affected the antioxidant properties, solubility and improved the hydrophilicity of polyphenols. Apart from alkaline treatments, enzymatic oxidation of polyphenol using enzymes such as catecholoxidases and laccases in the presence of oxygen was also reported [32, 33]. The enzymatic synthesis of gelation-catechin conjugate was carried out using laccase as catalysed and complex enhanced the activity to inhibit the oxidation of low-density proteins [34].

Likewise, polysaccharide-polyphenol conjugates have been synthesized using free radical grafting method [35, 36]. This method involves firstly, the source which can generate OH radicals; secondly, attack of OH radical on polysaccharide molecules to produce radical species. The radical species react with polyphenol via covalent linkage to form

polysaccharide-polyphenol conjugates [37]. Chitosan-gallic acid; chitosan-catechin; chitosan-protocatechuic acid or -caffeic acid, -p-hydroxybenzoic acid, -vanillic acid; chitosan-caffeic acid, or -ferulic acid, -sinapic acid; chitosan-EGCG (epigallocatechin gallate) were synthesized using free radical grafting methods. Conjugates showed improved physicochemical and biological properties such as antioxidant and antimicrobial activity, solubility, improved α-glucosidase and α-amylase inhibitory activities, foodborne pathogens inhibition, oxidative stress reduction in liver cells, etc. [35, 38-44]. Polysaccharide-polyphenol conjugates were also obtained by coupling reactions mediated by carbodiimide which usually involves the formation of amide linkages [45]. The synthesis of Hyaluronic acid−EGCG conjugates using carbodiimide mediated coupling reaction was performed and resultant conjugates exhibited higher resistance to degradation caused by hyaluronidase, high anticancer and antioxidant activity together with targeted gene delivery [46-48]. Hence, conjugation of phenolic moieties with protein and polysaccharides can be obtained by different enzymatic and non-enzymatic processes which can alter their physiochemical and nutritional properties such as solubility, digestibility, bioavailability, surface and antioxidant activity.

2.1.3. Other Polyphenols based Nano-formulations

Another method utilised to generate polyphenols functionalized nanostructures is micro/nano-encapsulation. The encapsulation would increase the half-life of these molecules along with improving the bioavailability [49]. There are different strategies used to encapsulate bioactive polyphenol molecules such as spray drying, Ionic Gelation, Coacervation, emulsion etc. [49, 50].

Spray drying encapsulation has been widely used in food industry to encapsulate different food ingredients. Maltodextrins has been spray dried as a coating agent with the

carrot juice extract for the loading of anthocyanins [51]. The maltodextrin was also used in combination of Arabic gum for the encapsulation of procyanidins extracted from grape seeds by spray drying [52]. 27% olive leaf extract was loaded into chitosan microspheres using spray drying [53]. It was demonstrated that the fruit fibres can also be used as a coating agent which can provide dual benefits of multifunctional food derivatives [50]. The spray dried particles mostly have spherical morphology and the size range of 10-100 micrometre [50].

Another encapsulation technique is coacervation. The method has been utilised for the generation of yern amate and gallic acid functionalised calcium alginate and calcium alginate-chitosan nanoparticles [54]. The encapsulation in calcium alginate was 30% higher than that of calcium alginate modified with chitosan. The synthesised particles (Figure 2.3) were found to be stable under both oven and freeze drying. It was found that beads coated with chitosan could only maintain 50% polyphenol activity however, when only calcium alginate was used, 85% polyphenolic activity was preserved. They demonstrated that the release kinetics can be altered depending upon type of coating material.

Shutava et al. [55] synthesised protein/polyphenol microcapsules using gelatin and epigallocatechin gallate through layer by layer assembly. $MnCO_3$ particles (dissolved in EDTA) were also used as template to synthesize microcapsules by deposition of epigallocatechin gallate layer. The polyphenol content of these microcapsules was about 30 % w/w [55]. Correspondingly, black current extract functionalised glucan beads were generated by using coacervation technique. The hot glucan gel was mixed with black current extract and subsequently the gel was cooled, cut into cubes and dropped into oil to obtain beads [56].

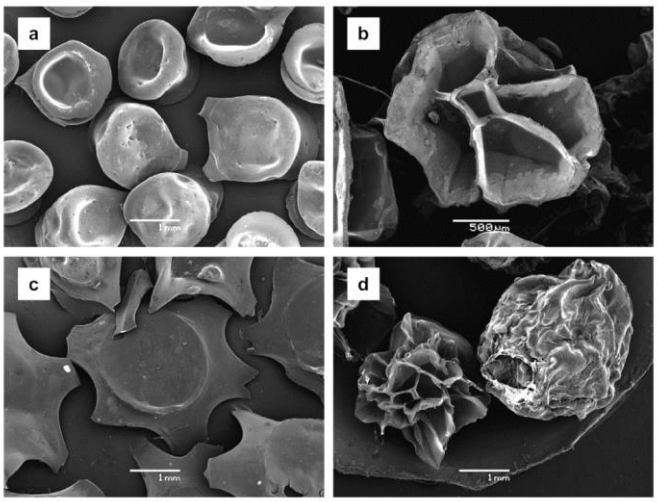

Figure 2.3: SEM images of (a) control after oven drying, (b) control lyophilized beads, (c) alginate–chitosan after oven drying and (d) alginate–chitosan lyophilized beads. Adapted from [54].

Bala et al. [57] used a diffusion evaporation technique for the synthesis of ellagic acid (EA) loaded PLGA nanoparticles with PEG as a co-solvent. Two stabilizers didodecyldimethylammomium bromide (DMAB) and polyvinyl alcohol (PVA) with and without the combination of chitosan were explored. The technique involves dispersion of EA-PLGA-PEG 400 solvent in continuous phase and in equilibrium to form irregular and different size droplets, during which the stabilizer was adsorbed on the surface to create homogenous small size emulsion. Water was then added, and the mixture was heated to destabilize the equilibrium, resulting in fusion of organic phase with aqueous phase ultimately leading to the precipitation of polymer functionalised with EA. The release of ellagic acid from nanoparticles in PBS 7.4 was initially high, followed by the sustained release. The cytotoxic activities and in-situ intestinal permeability of nanoparticles was also estimated. Additionally, resveratrol functionalized amphiphilic copolymers mPEG–PCL (methoxy poly(ethylene glycol)-poly(caprolactone)) particles with greater than 90% loading efficiency were synthesized [58]. Hu et al. [59] demonstrated the ionotropic

gelation method for the formation of tea catechins chitosan- tripolyphosphate (CS-TPP) nanoparticles [59].

In contrast to these methods, loading of EGCG, tannic acid, curcumin and theaflavin was carried out using a multistep method. The nanoparticles prepared by desolvation method were encapsulated with polyelectrolytes using layer by layer assembly technique. Subsequently, adsorption of different polyphenols on nanoparticles was carried out at different pH values. They reported that the compounds with larger amounts of OH groups show higher interaction and loading efficiency. Theaflavin showed highest loading efficiency in contrast to curcumin which should negligible loading [60]. Liang et.al. prepared chitosan structures loaded with tea polyphenol extract [61] and an Elsholtzia splenedens extract [62] using ionic gelation methods. The synthesised particles showed sustained release mediated mostly by diffusion. Catechin and (-)-epigallocatechin which are found to be unstable in alkaline conditions but have many important activities, were immobilized in chitosan tripolyphosphate nanoparticles [63]. About 50% catechin was degraded after 24 hours as compared to 8 hours for the free catechin [63].

There are humongous number of reports on the use of liposomes for encapsulating different bioactive ingredients [49, 50]. For Instance, Takahash et al [64-65] prepared liposome encapsulated curcumin particles (LEC) using lecithins and curcumin. The resulting LEC showed 68 % curcumin encapsulation efficiency. Priprem et al [66] has prepared liposomes from egg phosphatidylcholine/cholesterol for encapsulating quercetin. Likewise, acoustically active lipospheres encapsulating resveratrol were synthesized using soybean phosphatidylcholine, a cholesterol, co-emulsifier [67].

A great deal of work has been carried on encapsulation and delivery of polyphenols using nanocarriers, but negligible amount of work could be found on the nano-formulations of

polyphenols itself. For instance, ellagic acid powder is conventionally obtained either through enzymatic hydrolysis or acid hydrolysis and oxidation of ellagitannins by tannase, polyphenoloxidase and decarboxylase [68, 69] or multistep organic synthesis [70] without any control over size and shape. The synthesis of ellagic acid has never been reported using tannic acid and ultrasound. This study aims to provide one pot ultrasonic strategy for fabricating ellagic acid particles with different size, shape and aspect ratios from tannic acid without utilizing any catalysts, acids, enzymes, etc.

2.2. Self -assembly of peptides and their applications

As mentioned earlier, many reports are available on functionalisation of various nanoplatforms with different peptides, amino acids and proteins. Most of the proteins and peptide can be used as targeting ligands as they can selectively bind to different receptors on the cell membrane for the delivery of nanoparticles to the required site [71, 72]. Apart from this, self-assembly of peptide nanostructures into different geometries such as nanospheres, nanofibrils, nanotubes etc is of considerable interest. The peptide and amino acid building blocks can interact through different non-covalent interactions such as H-bonding, electrostatic, hydrophobic and aromatic interactions [73]. Ghadiri et al. [74, 75] have shown for the first time that alternative arrangement of D and L amino acids into planar cyclic rings can then self- assemble to form elongated and hollow nanotubes. The self-assembly based on the electrostatic interactions among the charged building blocks was studied by Zhang et al. [76]. They have shown when the linear peptide nanostructures were composed of negatively and positively charged amino acids, they can readily self-assemble in aqueous solutions to form ordered charge complementary nanofibrils. Peptides can also form macroscopic assemblies such as hydrogels with nano-scale order. It was demonstrated that the amphiphilic peptides can self-assemble to form

nanostructures in aqueous solution based on the same principle which drives the molecular self-assembly of phospholipids.

Another important type of self-assembly is based on aromatic short peptides to form aromatic nanostructures. For instance, β-amyloid and diphenylalanine polypeptide can spontaneously form discrete rigid and hollow nanotubes upon their dilution from organic solvents into aqueous solutions as well as by heating and cooling of their aqueous solutions [77-79]. On the other hand, the diphenylglycine peptide can form spherical nanostructures in aqueous solutions [80]. It was also shown that introduction of thiol group into diphenylalanine peptide can alter its arrangement from tubular to spherical [71]. These types of nanostructures were extremely stable under high temperature, autoclave treatment, etc. [81]. All these types of nanostructures have been utilised for different applications. For instance, amyloid fibrils are nanofibrils that occur naturally [73] and yeast nanofibrils when genetically modified to contain cystine residue can serve as a site for the metal deposition [82]. These metal coated fibril were found to be conductive and can found there applications in nano-wiring and electronics [82].

Another important class of peptides are antimicrobial cationic peptides which have the capability to fight against multi-drug resistant microbes. Liu et al. [83] have synthesized core-shell nanostructures from the self-assembly of amphiphilic peptide CG_3R_6TAT . They have demonstrated that the antimicrobial activity of self-assembled peptides from yeast, bacteria and fungi was significantly higher than unassembled peptide itself. It was tested using *Staphylococcus aureus* infection in rabbits that the nanoparticles can cross the blood-brain barrier and decrease the growth of bacteria's in the infected brains [83]. Wang et al [84] have recently reported the formation of cationic cholesterol-conjugated G_3R_6TAT (CG_3R_6TAT) nanoparticles through self-assembly. They established that the nanoparticles can be used for the treatment of Cryptococcus

neoformans (yeast)-induced brain infections. They also have a tendency to cross blood brain barrier and decrease yeast growth, inflammatory response and brain parenchyma etc. In addition, they did not cause any damage to the functioning of liver and kidney [84]. Another class of self-assembled peptide nanoparticle was utilized as a vaccine. Burkhard et al. [85] formed the nanoparticles through self-assembly of the peptides with incorporating T-cell and B-cell epitopes which can be useful for vaccination.

It was reported that the efficiency of DNA delivery strongly depends upon the structure of head groups and their ability to condense DNA. Ghosh et al.[86] have shown that lysine-functionalised head groups coated on gold nanoparticle can act as effective delivery vectors. These nanoparticles were found to be biocompatible and responsive to cellular glutathione level which was observed during their in-vitro transfection. These Lysine dendrons functionalized gold nanoparticles showed 28 times higher gene expression than polylysine itself. Apart from enhancement in antimicrobial activity, self-assembled peptide nanoparticles can serve as a platform (after further functionalization) for drug delivery, imaging and drug targeting for cancer treatment.

The use of these peptide nanoparticles in bioimaging has been exploited many times. However, the peptides have limited optical properties in the UV spectral range, which is not suitable for bioimaging in the intracellular and extracellular biological environment [87]. The formation of tryptophan–phenylalanine dipeptide nanoparticles (DNPs) via π-π stacking interaction and Zn(II) coordination was recently reported [88]. The aggregation of this dipeptide induced a shift in the peptide's intrinsic fluorescent signal from the ultraviolet to the visible range. The visible emission signal in the blue region with an emission peak around 420 nm allowed the DNPs to act as imaging and sensing probes. To obtain tryptophan–phenylalanine nanoparticles Zn coordination of indole moieties was exploited whereas neither tryptophan–phenylalanine nor Tryptophan-Tryptophan

dipeptides were able to self-assemble into organized nanoparticles without the addition of Zn ions. In addition, the blue emission exhibited by these nanoparticles is not the optimal spectral region for bioimaging. Nanoparticles emitting in the far- and near-Infrared spectral region emission better suit to the biological environment because of low autofluorescence of biological specimens in this region of the spectrum and deeper tissue penetration [89]. The use of aromatic amino acids as building block for the nanofabrication of multifunctional nanoparticle is desirable and has a great potential for possible use in a biological context.

Besides these studies, negligible research has been carried out based on single amino acid systems. The aim of the study is to carry oxidative coupling reactions among different amino acid molecules and hence the following section discuss the previous reports dealing with the oxidation of tryptophan and phenylalanine molecules by OH radicals. The attack of OH radicals on amino acids has been demonstrated several times using Fenton reaction, pulse radiolysis and γ-radiolysis [90-92]. It was shown that during Fenton's reaction and γ-radiolysis of phenylalanine, the o-, m-, and p-hydroxyphenylalanine together with some 2,4-dihydroxyphenylalanine, 2,3 dihydroxyphenylalanine were formed [91]. Correspondingly, tryptophan's Fenton reaction and γ-radiolysis also led to the formation of hydroxytryptophans, N-formylkynurenine and oxindole3-alanine, [93]. Previous computational and experimental studies have shown that tryptophan bears multiple sites for OH radical attack. It was suggested that hydrogen can be abstracted from either the benzene or pyrrole rings [94]. Then two Trp radicals can react to form dimers [95, 96]. However, none of these studies have explored the formation of any amino acid-based nanoparticles. Therefore, this PhD study will be exploiting the role of ultrasound in oxidative coupling of aromatic amino

acid moieties and its role in mediating self-assembly of their oxidized products to form nanoparticles along with demonstration of their biological applications.

2.3. Nanocarriers for Doxorubicin delivery

As previously mentioned, free doxorubicin is often associated with several disadvantages which can influence the desired effects of the drug. Major drawbacks include short half-life, multidrug resistance, cardiotoxicity, high concentration and uptake by normal tissues, rapid clearance etc [97]. Different nanomedicine platforms such as liposomes, polymer-drug conjugates, quantum dots, nano-emulsions, metal nanoparticles are developed for the loading and delivery of doxorubicin to eliminate the side effects of the drug [72, 98].

It was reported that liposome based nanoformulation of doxorubicin can limit the cardiotoxicity by reducing the accumulation of the drug in heart tissues [99, 100]. Different liposomal based doxorubicin formulations such as Doxil (United States), Caelyx (Canada and Europe) are also clinically approved [100]. In addition to reduction in cardiotoxicity and gastrotoxicity they can improve circulation lifetime [101]. Apart from this, doxorubicin micellar delivery systems by conjugating it to different polymers such as poly(DL-lactic-co-glycolic acid) (PLGA), polyethylene glycol and poly(L-lactic acid) (PLA) have also been synthesised [102]. PEG monomethylether-b-poly(methacrylamide tert-butyl carbazate)-Doxorubcin (MPEG-*b*-Dox) conjugate with 40 wt % loading efficiency was generated by Xu et al. [103]. In this formation, Dox was conjugated to methacrylamide tert-butyl carbazate through an acid-labile hydrazine bond which acted as a hydrophobic part. The hydrophilic part was constituted by MPEG. This conjugate self-assembled to form micelles of 80 nm size and exhibited minimal release at pH 7.4 and high release at pH 5. Additionally, mesoporous carbon nanoparticles

functionalized with hydrophilic cover such as PEG and reagents with phenolic, and -COOH group have been used to doxorubicin by π–π stacking and hydrophobic interactions [104]. Other porous materials as doxorubicin carrier are mesoporous silica-based nanoparticles, magnetic colloidal nanocrystals, metal-organic frameworks, protein nanoparticles [97].

Moreover, metal nanoparticles such as gold (Au) nanorods and Au nanocages have also been used in cancer therapy as their strong absorption in near infrared region allows them to generate local cytotoxicity upon NIR irradiation [105]. Au nanoparticles with surface conjugated to Dox-loaded-poly (lactic-co-glycolic acid) and functionalised with targeting moieties were synthesized by Sun-Mi et al. [106] to overcome the multi drug resistance which offered combined targeting drug delivery and photothermal treatment. Vimala et al. [107] synthesised the doxorubicin loaded zinc oxide porous rod shaped nanoparticles which beared pH responsive release towards breast cancer cells.

Most of these nanoformulation are however accompanied by certain drawbacks such as poor drug loading, posing additional toxicity, uncontrollable release kinetics and endosomal escape. Hence, discovery of new drugs or modification of established drugs to generate nanocarrier free therapeutics would offer several advantages which can be achieved by high frequency ultrasound through oxidative coupling reactions. This PhD study has utilized high frequency ultrasound to chemically modify the doxorubicin and to self-assemble it into nanoparticles.

2.4. Ultrasound mediated reactions

In biomedical field ultrasound was used to induce alteration of gene and protein expressions [108], diagnosis and molecular imaging [109-111], targeted drug and gene delivery [108], thermal tissue ablation [112] and many other therapeutic effects. In terms

of material synthesis, it has been utilized to perform polymerization, self-assembly and oxidative coupling reactions as well as synthesis of metal nanoparticles, polymer/protein shelled nano/microcapsules etc. The following section discusses various types of reactions and nanostructures generated using ultrasound which can be used in various biomedical applications.

2.4.1. Ultrasonic mediated polymerization and self-assembly

Ultrasound has been successfully used for various radical mediated coupling reactions such as free radical emulsion polymerisation reaction. Such reactions are carried out between insoluble monomer dispersed in aqueous phase typically in presence of initiator in the absence of ultrasound. The initiator in presence of ultrasound is replaced with the radicals generated due to the acoustic cavitation. Besides, replacing the initiator, ultrasound reduces the required reaction temperature, effects the rate of polymerization and reaction time [113].

Biggs and Grieser [114] reported the ultrasound assisted polymerisation of styrene in aqueous solutions without the addition of an initiator. Similarly, butyl acrylate/vinyl acetate copolymer latex nanoparticles were synthesized with narrow particle size distribution using ultrasound [115]. Teo et al. [116] reported the formation of temperature responsive polymerization of poly(N-isopropylacrylamide) and poly(N-vinylcaprolactam) with their potential applicability in drug delivery. Teo et al. and Barley et al. [117, 118] also demonstrated the mechanism involved in the ultrasound mediated radical emulsion polymerization (Figure 2.4). It was suggested that H/OH radicals generated as a result of acoustic cavitation, can undergo addition to monomer molecules adsorbed at bubble/solvent interface to form monomer radicals, which can initiate the polymerization reaction in bulk to obtain polymer-based nanoparticles.

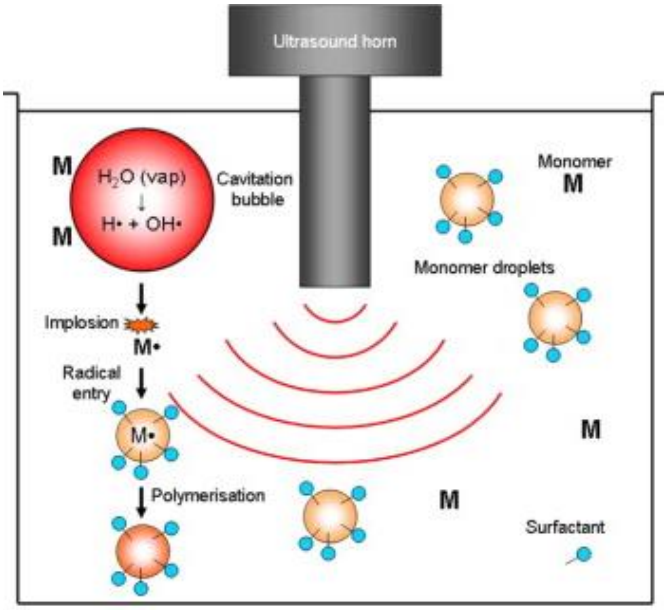

Figure 2.4: Schematic showing the proposed mechanism for the polymerisation induced by ultrasound. Adapted from [117]

A similar approach was followed to synthesize polyethylene glycol (PEG) based nanoparticles with hydrophobic core and hydrophilic shell [119]. The study illustrated the polymerization of oligo (ethylene glycol) methyl ether methacrylate at the water/oil interface with ethylene glycol dimethacrylate cross linker. The particle core can be used to load any hydrophobic drug or contrast agents. Other types of polymerization reactions induced by high frequency ultrasound include RAFT (reversible addition–fragmentation chain transfer) polymerisation. McKenzie et al. [120] demonstrated that ultrasonically generated radicals can initiate the RAFT polymerization and can be used for the polymerization of different monomers such as *N*,*N*′-dimethyl acrylamide, *N*-acryloylmorpholine, oligo(ethylene glycol) methyl ether acrylate), oligo(ethylene glycol) methyl ether methacrylate with high conversion rates.

2.4.2. Metal Nanoparticles and their biological applicability

The synthesis of metal nanoparticles with controlled size and size distribution is another key application of ultrasound. Pyrolysis reactions using acoustic bubbles in organic

solvents to form metal nanostructures were also explored [121, 122]. It was reported that $Fe(CO)_5$ when irradiated with 20 kHz in decane at 0 °C can pyrolysis to Fe atoms which aggregate to form Fe nanoparticles. Mostly amorphous Fe nanoparticles are generated with the size range of 10 nm and surface area of 120 m^2/g that is 120 times more than the conventional Fe nanoparticles. Another report employed ultrasound and the mixture of polyvinylpyrollidone (stabilizer) and octanol solution of $Fe(CO)_5$ that can supress the growth and aggregation of Fe. The size of nanoparticles was reduced to 3-8 nm [123]. Similarly, Fe nanoparticle were prepared in the solution containing silica particles to generate Fe/SiO_2 nanoparticles [124]. However, the yield of nanomaterials synthesized by ultrasound depends on a variety of other factors such as dissolved gas, vapour pressure of the liquid, etc. Madine et al. [125] haves reported the synthesis of Fe_2O_3 nanoparticles on polyester fabric through oxidation of Fe^{2+} to Fe^{3+} by OH radicals. The synthesized particles showed significant antifungal and antibacterial as well as magnetic and catalytic properties.

Apart from pyrolysis, sonochemical reduction of the metal precursor to generate metal nanoparticles in aqueous solution has attained great attention. As explained in the previous chapter, sonication of aqueous solutions would lead to the homolysis of water to generate H and OH radicals. When the solution of $AuCl_4$ is irradiated with high frequency (200 kHz) in noble gas atmosphere different kind of reducing radicals are formed [126-129]. The radicals generated can reduce Au (III) to Au (II), Au (II) to Au (I) and the disproportion reaction can also occur as shown in equations (Reaction 1-6) below. Finally, reduction would lead to the formation of Au nanoparticles.

Au (III) + reducing radical → Au (II) Reaction 1

Au (II) + reducing radical → Au(I) Reaction 2

Au(I) + reducing radical → Au Reaction 3

$2Au\ (II) \rightarrow Au\ (III) + Au(I)$ Reaction 4

$nAu \rightarrow \rightarrow Au_n$ Reaction 5

$Au_n + Au \rightarrow Au_{n+1}$ Reaction 6

Furthermore, ultrasound can also control the size and morphology of these nanostructures. For instance, Okitsu et al. [130] have prepared Au nanorods of different sizes and aspect ratios with ultrasound and seeding of nanorods. Figure 2.5 shows the Au nanorods obtained after the addition of Au nanorod seed at different sonication times [130]. The morphological changes in Au nanostructures can change their optical properties. These particles have found their applications in bioimaging, photothermal cancer therapy, surface-enhanced Raman spectroscopy, etc. [131, 132].

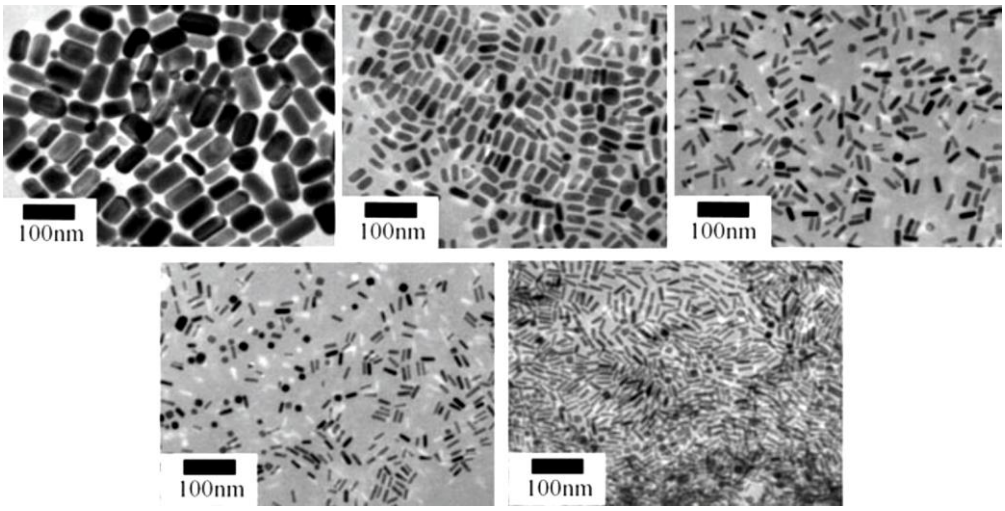

Figure 2.5: TEM images of Au nanorods produced via Au seeds formed after (a) 0.5, (b) 1, (c) 3, (d) 10, or (e) 15 min of ultrasonic irradiation. Adapted from [130]

Similar to Au nanoparticles, the sonochemical reduction technique can also be used to synthesize Ag, Pd, Pt nanoparticles from different metal precursors such as Ag^+, $[PdCl_4]^{2-}$, $[PtCl_4]^{2-}$, $[PtCl_6]^{2-}$, $[AuCl_4]^-$ etc [27, 133-136]. Correspondingly, bimetallic nanoparticles were synthesized using ultrasound. Mizukoshi et al. [136] used SDS aqueous solution of Au and Pd to synthesize Au/Pd bimetallic particles. Mangenese

oxides particle can be used as catalysts, adsorbents and sensors. The physical properties of MnO_2 (size, shape and crystal structure) nanoparticles strongly effects their applications. The MnO_2 nanoparticles with different sizes and morphologies can be sonochemically generated from MnO_4^- by utilizing H_2O_2 and H atoms formed during sonication [27]. Apart from reduction and pyrolysis, other techniques used to synthesize metal nanostructures involve sonoelectrochemical, spray pyrolysis, and metal displacement reduction techniques [121].

Ashima et al. [137] have reported the sonofabrication of L-lysine functionalized luminescent gadolinium oxide nanoparticles. The synthesized nanoparticles showed no toxicity when tested against HaCaT cells. However, significant antimicrobial activity was observed against both Gram negative bacteria E. coli and Gram positive bacteria S. aureus. Similar was the effect on different species such as Candida albicans and Candida glabrata [137]. Correspondingly, CuO nanoparticles functionalized with vitamin B1 were synthesised using ultrasonication and later the particles were used as antimicrobial agents [138]. The reduced Graphene oxide (RGO) nanoparticles were synthesized using ultrasound without any addition of stabilizer [139]. The synthesized RGO nanoparticles were used for the delivery anti-cancer drug paclitaxel. It was found by MTT [3-(4,5-dimethylthiazol-2-yl)-2,5-diphenyltetrazolium bromide] assay that paclitaxel functionalized RGO nanoparticles showed specific cytotoxicity towards HK-1 cancer cells and were biocompatible towards normal MRC-5 cells [139] .

2.4.3. Ultrasonic Synthesis and Assembly of Protein-Shelled Microbubbles

In addition to metal nanoparticles, protein, lipid or surfactant-based microbubbles for biomedical applications have gained much attention. Microspheres consist of a solid shell

surrounding the liquid or gas core. The microspheres can be functionalised with antibodies, vitamins, and peptides to attain the specific targeting. Cavalieri et al. [140-142] have introduced the ultrasonic technique for the synthesis of air-filled lysozyme microbubbles and microcapsules. The disulphide bonds in lysosome were partly denatured using dithiothreitol (DTT). Next, the denatured lysozyme solution was sonicated using 20 kHz high intensity ultrasound and air-filled lysozyme microbubbles were obtained with controlled size. It was found that HO_2 radicals (formed during the sonication) can crosslink the free thiol groups to form stable elastic protein shell. The increase in ultrasonic power lead to an increase in shear forces and radicals. The microbubbles showed more effective crosslinking and higher stability when synthesized at higher powers. Additionally, size and size distribution can also be controlled by post sonication treatment [143]. The synthesized microbubbles showed high antimicrobial activity towards *Staphylococcus aureus* and *Micrococcus luteus* due to the interactions between hydrophobic moieties in lysozyme and membrane of bacteria which disturbed the functioning and integrity of the bacteria.[144]

Perfluorocarbon encapsulated lysozyme microbubbles were synthesized for use as ultrasound contrast agents [145]. Furthermore, microbubbles can be used as ultrasound myocardial perfusion imaging, focal liver lesion diagnosis and detection of focal breast lesions [146]. It was reported that microbubbles can be locally administrated, and drug loaded microbubbles can be disrupted with ultrasound to release the drug at targeted sight. Aside from the formation of nano/microspheres, ultrasound can also be used to rupture the microspheres for initiating the focal release of the payload. It was demonstrated in-vivo that the biological tissue do not have any response towards the ultrasonic waves however, microbubble on application of ultrasound experience nonlinear harmonic oscillations [147, 148]. Therefore, the acoustic signal generated can only be attributed to

the microbubbles. During the microbubble collapse, the gas bubble can fragment into smaller bubbles and this phenomenon can be visualized by using a sonoscanner. Upon ultrasonic treatment, the elastic microbubble shell can undergo sonocracking, fragmentation and microjetting to release the drug loaded into the shell [149].

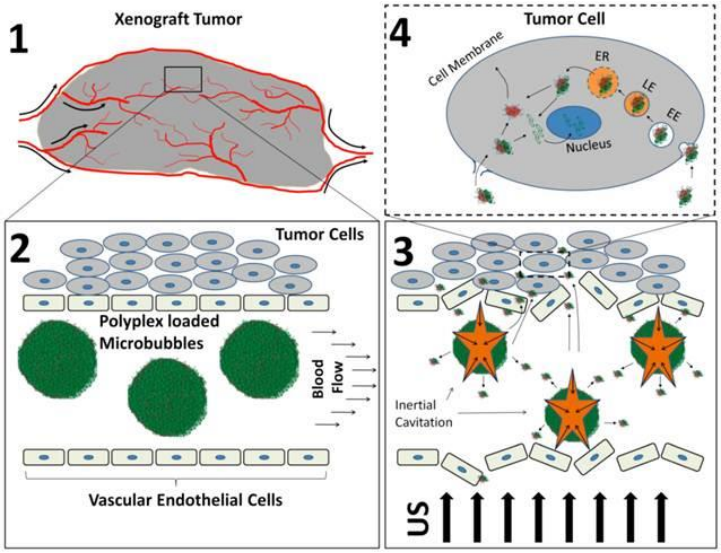

Figure 2.6: (1) Implantation of xenograft tumour in mice tail, (2) Introduction of polyplex-loaded MCA microspheres to deliver plasmid DNA, (3) The ultrasound was applied to facilitate the release of polyplex from microspheres , (4) uptake of the polyplex by tumour cells and delivery of DNA to the cell nucleus. Adapted from [152].

In addition to lysozyme, bovine serum albumin (BSA) microspheres were synthesized and used for the loading (with 90 % loading efficiency) and delivery of taxol to the Mouse Multiple Myeloma cell line MPC-11 [151]. Chen et al. [152] synthesised lipid loaded microbubble ultrasound contrast agents (MCA) for the delivery of DNA to xenograft tumours (Figure 2.6). They reported that Luciferase expression can only be observed in the region where ultrasound was applied.

2.4.4. Ultrasonic mediated oxidative coupling reactions

The interfacial polymerization reactions can also take place at cavitation bubble-water interface to induce manipulation of low molecular weight species (mostly amphiphilic biomolecules with phenolic and thiol groups) to high molecular weight products, which

can enhance their biological applications. Ultrasound can be used to obtain the desired nanostructures with controlled optical and physical properties. Recently, Cavalieri and co-workers reported that the high frequency oscillating surface of acoustic cavitation microbubbles acts as a reactive and catalytic binding site for the coupling of tyrosine moieties into oligomers [153]. In analogy with enzymes and inorganic catalysts, the catalytic coupling of tyrosyl radicals at the bubble-solution interface implies a mechanism whereby the aromatic rings of tyrosyl radicals molecules approach each other at the liquid-gas interface prior to their oxidation and coupling [153]. Furthermore, it was observed that during sonication the obtained amphiphilic oligomers aggregates into nanoparticles with fluorescence properties in the spectral region 400-600 nm. This seminal work paved the way for the engineering of phenolics and amino acid-based nanostructured materials using the one pot, reagent-less and facile ultrasonic approach.

Nevertheless, the role of ultrasound in promoting the self-assembly of the oligomers into nanoparticles remained elusive. To give general applicability to this ultrasonic technology as a universal platform to fabricate nanoparticles from low molecular weight amphiphilic molecules, a general principle on the role of cavitation bubbles in inducing self-aggregation processes must be established. The study suggested that only complex molecules such as hydrophobically modified tyrosine can be used for this process, whereas no oxidative coupling was observed with the more hydrophilic tyrosine.

Therefore, we aimed to explore this phenomenon starting from simplest aromatic moiety with OH group, i.e. phenol. Previously, a significant amount of work has been reported on the sonochemical degradation of phenol [154-157]. None of these reports show the formation of dimers, trimers or oligomers of phenol because focus of these was to study the degradation of phenol. Therefore, only reduction in the concentration of phenol was monitored. The formation of a few intermediate species such as catechol, hydroquinone,

1,4-benzoquinone, 1,2-benzoquinone was however, reported, which were again degraded on continuous sonication [158]. These studies have not focused on the coupling reaction of phenol, mediated by ultrasound irradiation to synthesize new building blocks and nanostructures. Similarly, the polyphenolic, single amino acid and doxorubicin nanoparticles with different size and shapes have never been synthesised before neither with nor without sonication. Ultrasound can offer a green methodology to carry out multidisciplinary homo and heterogeneous reaction without any external agent.

2.5. Research Aims

- The first aim of this PhD study was to develop a fundamental understanding on the ultrasonic coupling of phenolic moieties starting with a simple system, phenol, to identify the critical reaction parameters to obtain nanoparticles. The main scientific questions I aimed to answer were: whether oligomeric structures could be generated with simple molecules containing a phenolic moiety? Should the precursor molecules possess specific properties to form oligomers and subsequently assemble into nanoparticles? In order to answer these questions, the effect of high frequency ultrasound (355 kHz and 1056 kHz) on the simple molecule phenol under different experimental conditions was studied.
- In second part of the PhD, a more complex polyphenolic molecule such as tannic acid was used as substrate The aim of this work was to demonstrate the role of cavitation bubbles as a simple microreactors with reactive surfaces to perform one-pot multiple reactions on complex organic molecules, namely (i) hydrolysis of an ester linkage, (ii) C–C coupling reactions, (iii) condensation reactions and (iv) crystallisation of the tannic acid into regularly shaped ellagic acid particles. As a proof of concept, a sustainable, reagent-less and cost-effective synthetic

methodology to transform amorphous tannic acid into regularly shaped crystalline ellagic acid particles, with tuneable morphologies and functionality was developed. The size and shape of ellagic acid micro-nanocrystals were finely tuned by choosing appropriate ultrasonic parameters such as sonication time, power and frequency.

- The third part of my PhD emphasises on how ultrasound can be used to initiate the self-assembly of amphiphilic amino acid molecules- tryptophan, phenylalanine. The aim was (i) to combine an experimental and computational approach to unveil the role of the acoustic field in the formation of supramolecular nanoaggregates using tryptophan and phenylalanine as building blocks, (ii) to demonstrate that the acoustic bubbles driven at high frequency standing wave, can also provide an energy source to fuel and refuel the dissipative out- of equilibrium assembly of these molecules into nanoparticles below the critical aggregation concentration, (iii) to test the unique optical and bio-functional properties of nanoparticles for bioimaging and probing the intracellular trafficking of a drug.
- In the fourth part of my PhD, the use of high frequency ultrasound for the synthesis of nanodrug from doxorubicin - a chemotherapy drug was investigated. The cytotoxicity and mechanism of action of DOXNP (Doxorubicin nanoparticles) and the native drug towards different cancer cells (both drug resistant and non-resistant) were compared. In addition, the intracellular trafficking of DOXNP using super resolution microscopy - Stochastic Optical reconstruction microscopy (STORM), was performed.

2.6. References

1. Pilato, L., *Phenolic resins: a century of progress*. 2010: Springer.
2. Nozoe, A., M. Abe, K. Ohto, and H. Kawakita, *Germanium recovery using polyphenol microspheres prepared by horseradish peroxidase reaction.* Journal of Chemical Technology & Biotechnology, 2011. **86**(11): p. 1374-1378.

3. Chen, Z., C. Wang, J. Chen, and X. Li, *Biocompatible, functional spheres based on oxidative coupling assembly of green tea polyphenols.* Journal of the American Chemical Society, 2013. **135**(11): p. 4179-4182.
4. Fei, J., J. Zhao, C. Du, A. Wang, H. Zhang, L. Dai, and J. Li, *One-pot ultrafast self-assembly of autofluorescent polyphenol-based core@ shell nanostructures and their selective antibacterial applications.* ACS nano, 2014. **8**(8): p. 8529-8536.
5. Qiao, J.-Q., N. Yuan, C.-J. Tang, J. Yang, J. Zhou, H.-Z. Lian, and L. Dong, *Determination of catalytic oxidation products of phenol by RP-HPLC.* Research on Chemical Intermediates, 2012. **38**(2): p. 549-558.
6. Dubey, S., D. Singh, and R. Misra, *Enzymatic synthesis and various properties of poly (catechol).* Enzyme and microbial technology, 1998. **23**(7-8): p. 432-437.
7. Eker, B., D. Zagorevski, G. Zhu, R.J. Linhardt, and J.S. Dordick, *Enzymatic polymerization of phenols in room-temperature ionic liquids.* Journal of Molecular Catalysis B: Enzymatic, 2009. **59**(1-3): p. 177-184.
8. Kobayashi, S. and H. Higashimura, *Oxidative polymerization of phenols revisited.* Progress in Polymer Science, 2003. **28**(6): p. 1015-1048.
9. Bruno, F.F., R. Nagarajan, J. Kumar, and L.A. Samuelson, *Novel enzymatic polyethylene oxide-polyphenol system for ionic conductivity.* Journal of Macromolecular Science, Part A, 2002. **39**(10): p. 1061-1068.
10. Kim, Y.-J., H. Uyama, and S. Kobayashi, *Regioselective synthesis of poly (phenylene) as a complex with poly (ethylene glycol) by template polymerization of phenol in water.* Macromolecules, 2003. **36**(14): p. 5058-5060.
11. Kim, Y.J., H. Uyama, and S. Kobayashi, *Peroxidase-catalyzed oxidative polymerization of phenol with a nonionic polymer surfactant template in water.* Macromolecular bioscience, 2004. **4**(5): p. 497-502.
12. Heck, T., G. Faccio, M. Richter, and L. Thöny-Meyer, *Enzyme-catalyzed protein crosslinking.* Applied microbiology and biotechnology, 2013. **97**(2): p. 461-475.
13. Cohen, G., S. Yakushin, and D. Dembiec-Cohen, *Proteinl-Dopa as an Index of Hydroxyl Radical Attack on Protein Tyrosine.* Analytical biochemistry, 1998. **263**(2): p. 232-239.
14. Garrison, W.M., *Reaction mechanisms in the radiolysis of peptides, polypeptides, and proteins.* Chemical Reviews, 1987. **87**(2): p. 381-398.
15. Pourcel, L., J.-M. Routaboul, L. Kerhoas, M. Caboche, L. Lepiniec, and I. Debeaujon, *TRANSPARENT TESTA10 encodes a laccase-like enzyme involved in oxidative polymerization of flavonoids in Arabidopsis seed coat.* The Plant Cell, 2005. **17**(11): p. 2966-2980.
16. Mochizuki, M., S.-i. Yamazaki, K. Kano, and T. Ikeda, *Kinetic analysis and mechanistic aspects of autoxidation of catechins.* Biochimica et Biophysica Acta (BBA)-General Subjects, 2002. **1569**(1-3): p. 35-44.
17. Guyot, S., J. Vercauteren, and V. Cheynier, *Structural determination of colourless and yellow dimers resulting from (+)-catechin coupling catalysed by grape polyphenoloxidase.* Phytochemistry, 1996. **42**(5): p. 1279-1288.
18. Jurasekova, Z., A. Torreggiani, M. Tamba, S. Sanchez-Cortes, and J. Garcia-Ramos, *Raman and surface-enhanced Raman scattering (SERS) investigation of the quercetin interaction with metals: Evidence of structural changing processes in aqueous solution and on metal nanoparticles.* Journal of molecular structure, 2009. **918**(1-3): p. 129-137.
19. Rahim, M.A., H. Ejima, K.L. Cho, K. Kempe, M. Müllner, J.P. Best, and F. Caruso, *Coordination-driven multistep assembly of metal–polyphenol films and capsules.* Chemistry of Materials, 2014. **26**(4): p. 1645-1653.
20. Guo, J., Y. Ping, H. Ejima, K. Alt, M. Meissner, J.J. Richardson, Y. Yan, K. Peter, D. von Elverfeldt, and C.E. Hagemeyer, *Engineering multifunctional capsules through the assembly of metal–phenolic networks.* Angewandte Chemie, 2014. **126**(22): p. 5652-5657.
21. Ejima, H., J.J. Richardson, and F. Caruso, *Metal-phenolic networks as a versatile platform to engineer nanomaterials and biointerfaces.* Nano Today, 2017. **12**: p. 136-148.

22. Guo, J., Y. Ping, H. Ejima, K. Alt, M. Meissner, J.J. Richardson, Y. Yan, K. Peter, D. von Elverfeldt, and C.E. Hagemeyer, *Cover Picture: Engineering Multifunctional Capsules through the Assembly of Metal–Phenolic Networks (Angew. Chem. Int. Ed. 22/2014).* Angewandte Chemie International Edition, 2014. **53**(22): p. 5475-5475.
23. Liu, M., A. Kira, and H. Nakahara, *Complex formation between monolayers of a novel amphiphilic thiazolylazo dye and transition metal ions at the air/water interface.* Langmuir, 1997. **13**(4): p. 779-783.
24. Wei, J., Y. Liang, Y. Hu, B. Kong, J. Zhang, Q. Gu, Y. Tong, X. Wang, S.P. Jiang, and H. Wang, *Hydrothermal Synthesis of Metal–Polyphenol Coordination Crystals and Their Derived Metal/N-doped Carbon Composites for Oxygen Electrocatalysis.* Angewandte Chemie International Edition, 2016. **55**(40): p. 12470-12474.
25. Bertleff-Zieschang, N., M.A. Rahim, Y. Ju, J.A. Braunger, T. Suma, Y. Dai, S. Pan, F. Cavalieri, and F. Caruso, *Biofunctional metal–phenolic films from dietary flavonoids.* Chemical Communications, 2017. **53**(6): p. 1068-1071.
26. Ping, Y., J. Guo, H. Ejima, X. Chen, J.J. Richardson, H. Sun, and F. Caruso, *pH-Responsive Capsules Engineered from Metal–Phenolic Networks for Anticancer Drug Delivery.* Small, 2015. **11**(17): p. 2032-2036.
27. Abulizi, A., G.H. Yang, K. Okitsu, and J.-J. Zhu, *Synthesis of MnO2 nanoparticles from sonochemical reduction of MnO4− in water under different pH conditions.* Ultrasonics sonochemistry, 2014. **21**(5): p. 1629-1634.
28. Kroll, J., H.M. Rawel, and S. Rohn, *Reactions of plant phenolics with food proteins and enzymes under special consideration of covalent bonds.* Food science and technology research, 2003. **9**(3): p. 205-218.
29. Rawel, H.M., H. Ranters, S. Rohn, and J. Kroll, *Assessment of the reactivity of selected isoflavones against proteins in comparison to quercetin.* Journal of agricultural and food chemistry, 2004. **52**(16): p. 5263-5271.
30. Rohn, S., H.M. Rawel, and J. Kroll, *Antioxidant activity of protein-bound quercetin.* Journal of Agricultural and Food Chemistry, 2004. **52**(15): p. 4725-4729.
31. Rohn, S., K.J. Petzke, H.M. Rawel, and J. Kroll, *Reactions of chlorogenic acid and quercetin with a soy protein isolate–Influence on the in vivo food protein quality in rats.* Molecular nutrition & food research, 2006. **50**(8): p. 696-704.
32. Le Bourvellec, C. and C. Renard, *Interactions between polyphenols and macromolecules: quantification methods and mechanisms.* Critical reviews in food science and nutrition, 2012. **52**(3): p. 213-248.
33. Budryn, G. and D. Rachwal-Rosiak, *Interactions of hydroxycinnamic acids with proteins and their technological and nutritional implications.* Food reviews international, 2013. **29**(3): p. 217-230.
34. Chung, J.E., M. Kurisawa, H. Uyama, and S. Kobayashi, *Enzymatic synthesis and antioxidant property of gelatin-catechin conjugates.* Biotechnology letters, 2003. **25**(23): p. 1993-1997.
35. Curcio, M., F. Puoci, F. Iemma, O.I. Parisi, G. Cirillo, U.G. Spizzirri, and N. Picci, *Covalent insertion of antioxidant molecules on chitosan by a free radical grafting procedure.* Journal of Agricultural and Food Chemistry, 2009. **57**(13): p. 5933-5938.
36. Curcio, M., O.I. Parisi, F. Puoci, I. Altimari, U.G. Spizzirri, and N. Picci, *Antioxidant polymers by free radical grafting on natural polymers.* Antioxidant Polymers: Synthesis, Properties, and Applications, 2012: p. 153-178.
37. Spizzirri, U.G., F. Iemma, F. Puoci, G. Cirillo, M. Curcio, O.I. Parisi, and N. Picci, *Synthesis of antioxidant polymers by grafting of gallic acid and catechin on gelatin.* Biomacromolecules, 2009. **10**(7): p. 1923-1930.
38. Cho, Y.-S., S.-K. Kim, C.-B. Ahn, and J.-Y. Je, *Preparation, characterization, and antioxidant properties of gallic acid-grafted-chitosans.* Carbohydrate Polymers, 2011. **83**(4): p. 1617-1622.
39. Cho, Y.-S., S.-K. Kim, C.-B. Ahn, and J.-Y. Je, *Inhibition of acetylcholinesterase by gallic acid-grafted-chitosans.* Carbohydrate polymers, 2011. **84**(1): p. 690-693.

40. Senevirathne, M., Y.-J. Jeon, Y.-T. Kim, P.-J. Park, W.-K. Jung, C.-B. Ahn, and J.-Y. Je, *Prevention of oxidative stress in Chang liver cells by gallic acid-grafted-chitosans.* Carbohydrate polymers, 2012. **87**(1): p. 876-880.
41. Lee, D.-S. and J.-Y. Je, *Gallic acid-grafted-chitosan inhibits foodborne pathogens by a membrane damage mechanism.* Journal of agricultural and food chemistry, 2013. **61**(26): p. 6574-6579.
42. Woo, J.Y. and J.Y. Je, *Antioxidant and tyrosinase inhibitory activities of a novel chitosan–phloroglucinol conjugate.* International Journal of Food Science & Technology, 2013. **48**(6): p. 1172-1178.
43. Lee, D.-S., J.-Y. Woo, C.-B. Ahn, and J.-Y. Je, *Chitosan–hydroxycinnamic acid conjugates: Preparation, antioxidant and antimicrobial activity.* Food chemistry, 2014. **148**: p. 97-104.
44. Lei, F., F. Liu, F. Yuan, and Y. Gao, *Impact of chitosan–EGCG conjugates on physicochemical stability of β-carotene emulsion.* Food Hydrocolloids, 2014. **39**: p. 163-170.
45. Liu, F., C. Ma, Y. Gao, and D.J. McClements, *Food-Grade Covalent Complexes and Their Application as Nutraceutical Delivery Systems: A Review.* Comprehensive Reviews in Food Science and Food Safety, 2017. **16**(1): p. 76-95.
46. Lee, F., J. Lim, M.R. Reithofer, S.S. Lee, J.E. Chung, C.A. Hauser, and M. Kurisawa, *Synthesis and bioactivity of a conjugate composed of green tea catechins and hyaluronic acid.* Polymer Chemistry, 2015. **6**(24): p. 4462-4472.
47. Liang, K., K.H. Bae, F. Lee, K. Xu, J.E. Chung, S.J. Gao, and M. Kurisawa, *Self-assembled ternary complexes stabilized with hyaluronic acid-green tea catechin conjugates for targeted gene delivery.* Journal of Controlled Release, 2016. **226**: p. 205-216.
48. Liang, K., S. Ng, F. Lee, J. Lim, J.E. Chung, S.S. Lee, and M. Kurisawa, *Targeted intracellular protein delivery based on hyaluronic acid–green tea catechin nanogels.* Acta biomaterialia, 2016. **33**: p. 142-152.
49. Fang, Z. and B. Bhandari, *Encapsulation of polyphenols–a review.* Trends in Food Science & Technology, 2010. **21**(10): p. 510-523.
50. Munin, A. and F. Edwards-Lévy, *Encapsulation of natural polyphenolic compounds; a review.* Pharmaceutics, 2011. **3**(4): p. 793-829.
51. Ersus, S. and U. Yurdagel, *Microencapsulation of anthocyanin pigments of black carrot (Daucus carota L.) by spray drier.* Journal of Food Engineering, 2007. **80**(3): p. 805-812.
52. Zhang, L., D. Mou, and Y. Du, *Procyanidins: extraction and micro-encapsulation.* Journal of the Science of Food and Agriculture, 2007. **87**(12): p. 2192-2197.
53. Kosaraju, S.L., L. D'ath, and A. Lawrence, *Preparation and characterisation of chitosan microspheres for antioxidant delivery.* Carbohydrate polymers, 2006. **64**(2): p. 163-167.
54. Deladino, L., P.S. Anbinder, A.S. Navarro, and M.N. Martino, *Encapsulation of natural antioxidants extracted from Ilex paraguariensis.* Carbohydrate Polymers, 2008. **71**(1): p. 126-134.
55. Shutava, T.G., S.S. Balkundi, and Y.M. Lvov, *(−)-Epigallocatechin gallate/gelatin layer-by-layer assembled films and microcapsules.* Journal of colloid and interface science, 2009. **330**(2): p. 276-283.
56. Xiong, S., L.D. Melton, A.J. Easteal, and D. Siew, *Stability and antioxidant activity of black currant anthocyanins in solution and encapsulated in glucan gel.* Journal of agricultural and food chemistry, 2006. **54**(17): p. 6201-6208.
57. Bala, I., V. Bhardwaj, S. Hariharan, S.V. Kharade, N. Roy, and M. Ravi Kumar, *Sustained release nanoparticulate formulation containing antioxidant-ellagic acid as potential prophylaxis system for oral administration.* Journal of drug targeting, 2006. **14**(1): p. 27-34.
58. Shao, J., X. Li, X. Lu, C. Jiang, Y. Hu, Q. Li, Y. You, and Z. Fu, *Enhanced growth inhibition effect of resveratrol incorporated into biodegradable nanoparticles against glioma cells is mediated by the induction of intracellular reactive oxygen species levels.* Colloids and Surfaces B: Biointerfaces, 2009. **72**(1): p. 40-47.

59. Hu, B., C. Pan, Y. Sun, Z. Hou, H. Ye, B. Hu, and X. Zeng, *Optimization of fabrication parameters to produce chitosan− tripolyphosphate nanoparticles for delivery of tea catechins.* Journal of Agricultural and Food Chemistry, 2008. **56**(16): p. 7451-7458.
60. Shutava, T.G., S.S. Balkundi, P. Vangala, J.J. Steffan, R.L. Bigelow, J.A. Cardelli, D.P. O'Neal, and Y.M. Lvov, *Layer-by-layer-coated gelatin nanoparticles as a vehicle for delivery of natural polyphenols.* ACS nano, 2009. **3**(7): p. 1877-1885.
61. Liang, J., F. Li, Y. Fang, W. Yang, X. An, L. Zhao, Z. Xin, L. Cao, and Q. Hu, *Synthesis, characterization and cytotoxicity studies of chitosan-coated tea polyphenols nanoparticles.* Colloids and Surfaces B: Biointerfaces, 2011. **82**(2): p. 297-301.
62. Lee, J.-S., G.-H. Kim, and H.G. Lee, *Characteristics and antioxidant activity of Elsholtzia splendens extract-loaded nanoparticles.* Journal of agricultural and food chemistry, 2010. **58**(6): p. 3316-3321.
63. Dube, A., K. Ng, J.A. Nicolazzo, and I. Larson, *Effective use of reducing agents and nanoparticle encapsulation in stabilizing catechins in alkaline solution.* Food Chemistry, 2010. **122**(3): p. 662-667.
64. Takahashi, M., S. Uechi, K. Takara, Y. Asikin, and K. Wada, *Evaluation of an oral carrier system in rats: bioavailability and antioxidant properties of liposome-encapsulated curcumin.* Journal of Agricultural and Food Chemistry, 2009. **57**(19): p. 9141-9146.
65. Maheshwari, R.K., A.K. Singh, J. Gaddipati, and R.C. Srimal, *Multiple biological activities of curcumin: a short review.* Life sciences, 2006. **78**(18): p. 2081-2087.
66. Priprem, A., J. Watanatorn, S. Sutthiparinyanont, W. Phachonpai, and S. Muchimapura, *Anxiety and cognitive effects of quercetin liposomes in rats.* Nanomedicine: Nanotechnology, Biology and Medicine, 2008. **4**(1): p. 70-78.
67. Fang, J.-Y., C.-F. Hung, M.-H. Liao, and C.-C. Chien, *A study of the formulation design of acoustically active lipospheres as carriers for drug delivery.* European Journal of Pharmaceutics and Biopharmaceutics, 2007. **67**(1): p. 67-75.
68. Brune, A. and B. Schink, *Phloroglucinol pathway in the strictly anaerobic Pelobacter acidigallici: fermentation of trihydroxybenzenes to acetate via triacetic acid.* Archives of microbiology, 1992. **157**(5): p. 417-424.
69. Mingshu, L., Y. Kai, H. Qiang, and J. Dongying, *Biodegradation of gallotannins and ellagitannins.* Journal of basic microbiology, 2006. **46**(1): p. 68-84.
70. Sun, Q., J. Heilmann, and B. König, *Natural phenolic metabolites with anti-angiogenic properties–a review from the chemical point of view.* Beilstein journal of organic chemistry, 2015. **11**: p. 249.
71. Chou, L.Y., K. Ming, and W.C. Chan, *Strategies for the intracellular delivery of nanoparticles.* Chemical Society Reviews, 2011. **40**(1): p. 233-245.
72. Kamaly, N., Z. Xiao, P.M. Valencia, A.F. Radovic-Moreno, and O.C. Farokhzad, *Targeted polymeric therapeutic nanoparticles: design, development and clinical translation.* Chemical Society Reviews, 2012. **41**(7): p. 2971-3010.
73. Gazit, E., *Self-assembled peptide nanostructures: the design of molecular building blocks and their technological utilization.* Chemical Society Reviews, 2007. **36**(8): p. 1263-1269.
74. Ghadiri, M.R., J.R. Granja, R.A. Milligan, D.E. McRee, and N. Khazanovich, *Self-assembling organic nanotubes based on a cyclic peptide architecture.* Nature, 1993. **366**(6453): p. 324.
75. Ghadiri, M.R., J.R. Granja, and L.K. Buehler, *Artificial transmembrane ion channels from self-assembling peptide nanotubes.* Nature, 1994. **369**(6478): p. 301.
76. Zhang, S., T. Holmes, C. Lockshin, and A. Rich, *Spontaneous assembly of a self-complementary oligopeptide to form a stable macroscopic membrane.* Proceedings of the National Academy of Sciences, 1993. **90**(8): p. 3334-3338.
77. Reches, M. and E. Gazit, *Casting metal nanowires within discrete self-assembled peptide nanotubes.* Science, 2003. **300**(5619): p. 625-627.

78. Kol, N., L. Adler-Abramovich, D. Barlam, R.Z. Shneck, E. Gazit, and I. Rousso, *Self-assembled peptide nanotubes are uniquely rigid bioinspired supramolecular structures.* Nano letters, 2005. **5**(7): p. 1343-1346.
79. Song, Y., S.R. Challa, C.J. Medforth, Y. Qiu, R.K. Watt, D. Peña, J.E. Miller, F. van Swol, and J.A. Shelnutt, *Synthesis of peptide-nanotube platinum-nanoparticle composites.* Chemical Communications, 2004(9): p. 1044-1045.
80. Reches, M. and E. Gazit, *Formation of closed-cage nanostructures by self-assembly of aromatic dipeptides.* Nano letters, 2004. **4**(4): p. 581-585.
81. Adler-Abramovich, L., M. Reches, V.L. Sedman, S. Allen, S.J. Tendler, and E. Gazit, *Thermal and chemical stability of diphenylalanine peptide nanotubes: implications for nanotechnological applications.* Langmuir, 2006. **22**(3): p. 1313-1320.
82. Scheibel, T., R. Parthasarathy, G. Sawicki, X.-M. Lin, H. Jaeger, and S.L. Lindquist, *Conducting nanowires built by controlled self-assembly of amyloid fibers and selective metal deposition.* Proceedings of the National Academy of Sciences, 2003. **100**(8): p. 4527-4532.
83. Liu, L., K. Xu, H. Wang, P.J. Tan, W. Fan, S.S. Venkatraman, L. Li, and Y.-Y. Yang, *Self-assembled cationic peptide nanoparticles as an efficient antimicrobial agent.* Nature nanotechnology, 2009. **4**(7): p. 457.
84. Wang, H., K. Xu, L. Liu, J.P. Tan, Y. Chen, Y. Li, W. Fan, Z. Wei, J. Sheng, and Y.-Y. Yang, *The efficacy of self-assembled cationic antimicrobial peptide nanoparticles against Cryptococcus neoformans for the treatment of meningitis.* Biomaterials, 2010. **31**(10): p. 2874-2881.
85. Burkhard, P., *Self-assembling peptide nanoparticles useful as vaccines*. 2013, Google Patents.
86. Ghosh, P.S., C.-K. Kim, G. Han, N.S. Forbes, and V.M. Rotello, *Efficient gene delivery vectors by tuning the surface charge density of amino acid-functionalized gold nanoparticles.* ACS nano, 2008. **2**(11): p. 2213-2218.
87. Cheruku, P., J.-H. Huang, H.-J. Yen, R.S. Iyer, K.D. Rector, J.S. Martinez, and H.-L. Wang, *Tyrosine-derived stimuli responsive, fluorescent amino acids.* Chemical science, 2015. **6**(2): p. 1150-1158.
88. Fan, Z., L. Sun, Y. Huang, Y. Wang, and M. Zhang, *Bioinspired fluorescent dipeptide nanoparticles for targeted cancer cell imaging and real-time monitoring of drug release.* Nature nanotechnology, 2016. **11**(4): p. 388-394.
89. Sun, Y.Q., J. Liu, X. Lv, Y. Liu, Y. Zhao, and W. Guo, *Rhodamine-Inspired Far-Red to Near-Infrared Dyes and Their Application as Fluorescence Probes.* Angewandte Chemie International Edition, 2012. **51**(31): p. 7634-7636.
90. Chrysochoos, J., *Pulse radiolysis of phenylalanine and tyrosine.* Radiation research, 1968. **33**(3): p. 465-479.
91. Maskos, Z., J. Rush, and W. Koppenol, *The hydroxylation of phenylalanine and tyrosine: a comparison with salicylate and tryptophan.* Archives of biochemistry and biophysics, 1992. **296**(2): p. 521-529.
92. Galano, A. and A. Cruz-Torres, *OH radical reactions with phenylalanine in free and peptide forms.* Organic & biomolecular chemistry, 2008. **6**(4): p. 732-738.
93. Maskos, Z., J. Rush, and W. Koppenol, *The hydroxylation of tryptophan.* Archives of biochemistry and biophysics, 1992. **296**(2): p. 514-520.
94. Mujika, J.I., J. Uranga, and J.M. Matxain, *Computational study on the attack of. OH radicals on aromatic amino acids.* Chemistry-A European Journal, 2013. **19**(21): p. 6862-6873.
95. Carroll, L., D.I. Pattison, J.B. Davies, R.F. Anderson, C. Lopez-Alarcon, and M.J. Davies, *Formation and detection of oxidant-generated tryptophan dimers in peptides and proteins.* Free Radical Biology and Medicine, 2017. **113**: p. 132-142.
96. Paviani, V., G.T. Galdino, J.N.d. Prazeres, R.F. Queiroz, and O. Augusto, *Ditryptophan Cross-Links as Novel Products of Protein Oxidation.* Journal of the Brazilian Chemical Society, 2018. **29**(5): p. 925-933.

97. Shen, S., Y. Wu, Y. Liu, and D. Wu, *High drug-loading nanomedicines: progress, current status, and prospects.* International journal of nanomedicine, 2017. **12**: p. 4085.
98. L Beretta, G. and F. Cavalieri, *Engineering nanomedicines to overcome multidrug resistance in cancer therapy.* Current medicinal chemistry, 2016. **23**(1): p. 3-22.
99. Gabizon, A., A. Dagan, D. Goren, Y. Barenholz, and Z. Fuks, *Liposomes as in vivo carriers of adriamycin: reduced cardiac uptake and preserved antitumor activity in mice.* Cancer Research, 1982. **42**(11): p. 4734-4739.
100. Abraham, S.A., D.N. Waterhouse, L.D. Mayer, P.R. Cullis, T.D. Madden, and M.B. Bally, *The liposomal formulation of doxorubicin*, in *Methods in enzymology*. 2005, Elsevier. p. 71-97.
101. Waterhouse, D.N., P.G. Tardi, L.D. Mayer, and M.B. Bally, *A comparison of liposomal formulations of doxorubicin with drug administered in free form.* Drug safety, 2001. **24**(12): p. 903-920.
102. Yoo, H.S. and T.G. Park, *Biodegradable polymeric micelles composed of doxorubicin conjugated PLGA–PEG block copolymer.* Journal of controlled Release, 2001. **70**(1-2): p. 63-70.
103. Xu, Z., K. Zhang, C. Hou, D. Wang, X. Liu, X. Guan, X. Zhang, and H. Zhang, *A novel nanoassembled doxorubicin prodrug with a high drug loading for anticancer drug delivery.* Journal of Materials Chemistry B, 2014. **2**(22): p. 3433-3437.
104. Wang, H., X. Li, Z. Ma, D. Wang, L. Wang, J. Zhan, L. She, and F. Yang, *Hydrophilic mesoporous carbon nanospheres with high drug-loading efficiency for doxorubicin delivery and cancer therapy.* International journal of nanomedicine, 2016. **11**: p. 1793.
105. Hauck, T.S., T.L. Jennings, T. Yatsenko, J.C. Kumaradas, and W.C. Chan, *Enhancing the toxicity of cancer chemotherapeutics with gold nanorod hyperthermia.* Advanced Materials, 2008. **20**(20): p. 3832-3838.
106. Lee, S.-M., H.J. Kim, Y.-J. Ha, Y.N. Park, S.-K. Lee, Y.-B. Park, and K.-H. Yoo, *Targeted chemo-photothermal treatments of rheumatoid arthritis using gold half-shell multifunctional nanoparticles.* ACS nano, 2012. **7**(1): p. 50-57.
107. Vimala, K., S. Sundarraj, M. Paulpandi, S. Vengatesan, and S. Kannan, *Green synthesized doxorubicin loaded zinc oxide nanoparticles regulates the Bax and Bcl-2 expression in breast and colon carcinoma.* Process biochemistry, 2014. **49**(1): p. 160-172.
108. Ferrara, K.W., M.A. Borden, and H. Zhang, *Lipid-shelled vehicles: engineering for ultrasound molecular imaging and drug delivery.* Accounts of chemical research, 2009. **42**(7): p. 881-892.
109. Dayton, P.A. and K.W. Ferrara, *Targeted imaging using ultrasound.* Journal of Magnetic Resonance Imaging: An Official Journal of the International Society for Magnetic Resonance in Medicine, 2002. **16**(4): p. 362-377.
110. Kaufmann, B.A. and J.R. Lindner, *Molecular imaging with targeted contrast ultrasound.* Current opinion in biotechnology, 2007. **18**(1): p. 11-16.
111. Jin, Q., C.-Y. Lin, S.-T. Kang, Y.-C. Chang, H. Zheng, C.-M. Yang, and C.-K. Yeh, *Superhydrophobic silica nanoparticles as ultrasound contrast agents.* Ultrasonics sonochemistry, 2017. **36**: p. 262-269.
112. Takegami, K., Y. Kaneko, T. Watanabe, T. Maruyama, Y. Matsumoto, and H. Nagawa, *Erythrocytes, as well as microbubble contrast agents, are important factors in improving thermal and therapeutic effects of high-intensity focused ultrasound.* Ultrasound in medicine & biology, 2005. **31**(3): p. 385-390.
113. Leong, T.S., G.J. Martin, and M. Ashokkumar, *Ultrasonic encapsulation–a review.* Ultrasonics sonochemistry, 2017. **35**: p. 605-614.
114. Biggs, S. and F. Grieser, *Preparation of polystyrene latex with ultrasonic initiation.* Macromolecules, 1995. **28**(14): p. 4877-4882.
115. Cooper, G., F. Grieser, and S. Biggs, *Butyl acrylate/vinyl acetate copolymer latex synthesis using ultrasound as an initiator.* Journal of colloid and interface science, 1996. **184**(1): p. 52-63.

116. Teo, B.M., S.W. Prescott, G.J. Price, F. Grieser, and M. Ashokkumar, *Synthesis of temperature responsive poly (N-isopropylacrylamide) using ultrasound irradiation.* The Journal of Physical Chemistry B, 2010. **114**(9): p. 3178-3184.
117. Teo, B.M., S.W. Prescott, M. Ashokkumar, and F. Grieser, *Ultrasound initiated miniemulsion polymerization of methacrylate monomers.* Ultrasonics sonochemistry, 2008. **15**(1): p. 89-94.
118. Bradley, M. and F. Grieser, *Emulsion polymerization synthesis of cationic polymer latex in an ultrasonic field.* Journal of colloid and interface science, 2002. **251**(1): p. 78-84.
119. Zhu, H., F. Cavalieri, and M. Ashokkumar, *Ultrasound-Assisted Synthesis of Cross-Linked Poly (ethylene glycol) Nanostructures with Hydrophobic Core and Hydrophilic Shell.* Macromolecular Chemistry and Physics, 2018: p. 1800353.
120. McKenzie, T.G., E. Colombo, Q. Fu, M. Ashokkumar, and G.G. Qiao, *Sono-RAFT Polymerization in Aqueous Medium.* Angewandte Chemie International Edition, 2017. **56**(40): p. 12302-12306.
121. Okitsu, K. and F. Cavalieri, *Synthesis of Metal Nanomaterials with Chemical and Physical Effects of Ultrasound and Acoustic Cavitation*, in *Sonochemical Production of Nanomaterials*. 2018, Springer. p. 19-37.
122. Suslick, K.S., S.-B. Choe, A.A. Cichowlas, and M.W. Grinstaff, *Sonochemical synthesis of amorphous iron.* nature, 1991. **353**(6343): p. 414.
123. Suslick, K.S., M. Fang, and T. Hyeon, *Sonochemical synthesis of iron colloids.* Journal of the American Chemical Society, 1996. **118**(47): p. 11960-11961.
124. Comazzi, A., C. Pirola, M. Longhi, C.L. Bianchi, and K.S. Suslick, *Fe-based heterogeneous catalysts for the Fischer-Tropsch reaction: Sonochemical synthesis and bench-scale experimental tests.* Ultrasonics sonochemistry, 2017. **34**: p. 774-780.
125. Rastgoo, M., M. Montazer, R.M. Malek, T. Harifi, and M.M. Rad, *Ultrasound mediation for one-pot sonosynthesis and deposition of magnetite nanoparticles on cotton/polyester fabric as a novel magnetic, photocatalytic, sonocatalytic, antibacterial and antifungal textile.* Ultrasonics sonochemistry, 2016. **31**: p. 257-266.
126. AuáYeung, S., *Formation of gold sols using ultrasound.* Journal of the Chemical Society, Chemical Communications, 1993(4): p. 378-379.
127. Okitsu, K., I. Kurisaka, B. Nanzai, N. Takenaka, and H. Bandow, *Sonochemistry of aqueous NaAuCl4 solutions with C3–C6 alcohols under a noble gas atmosphere.* Ultrasonics sonochemistry, 2018. **41**: p. 397-403.
128. Okitsu, K., A. Yue, S. Tanabe, H. Matsumoto, Y. Yobiko, and Y. Yoo, *Sonolytic control of rate of gold (III) reduction and size of formed gold nanoparticles: relation between reduction rates and sizes of formed nanoparticles.* Bulletin of the chemical society of Japan, 2002. **75**(10): p. 2289-2296.
129. Caruso, R.A., M. Ashokkumar, and F. Grieser, *Sonochemical formation of gold sols.* Langmuir, 2002. **18**(21): p. 7831-7836.
130. Okitsu, K. and Y. Nunota, *One-pot synthesis of gold nanorods via autocatalytic growth of sonochemically formed gold seeds: The effect of irradiation time on the formation of seeds and nanorods.* Ultrasonics sonochemistry, 2014. **21**(6): p. 1928-1932.
131. Dreaden, E.C., A.M. Alkilany, X. Huang, C.J. Murphy, and M.A. El-Sayed, *The golden age: gold nanoparticles for biomedicine.* Chemical Society Reviews, 2012. **41**(7): p. 2740-2779.
132. Chen, H., L. Shao, Q. Li, and J. Wang, *Gold nanorods and their plasmonic properties.* Chemical Society Reviews, 2013. **42**(7): p. 2679-2724.
133. Nagata, Y., Y. Watananabe, S.-i. Fujita, T. Dohmaru, and S. Taniguchi, *Formation of colloidal silver in water by ultrasonic irradiation.* Journal of the Chemical Society, Chemical Communications, 1992(21): p. 1620-1622.
134. Okitsu, K., Y. Mizukoshi, H. Bandow, T.A. Yamamoto, Y. Nagata, and Y. Maeda, *Synthesis of palladium nanoparticles with interstitial carbon by sonochemical reduction of tetrachloropalladate (II) in aqueous solution.* The Journal of Physical Chemistry B, 1997. **101**(28): p. 5470-5472.

135. Mizukoshi, Y., E. Takagi, H. Okuno, R. Oshima, Y. Maeda, and Y. Nagata, *Preparation of platinum nanoparticles by sonochemical reduction of the Pt (IV) ions: role of surfactants.* Ultrasonics sonochemistry, 2001. **8**(1): p. 1-6.
136. Mizukoshi, Y., K. Okitsu, Y. Maeda, T.A. Yamamoto, R. Oshima, and Y. Nagata, *Sonochemical preparation of bimetallic nanoparticles of gold/palladium in aqueous solution.* The Journal of Physical Chemistry B, 1997. **101**(36): p. 7033-7037.
137. Pandey, S.K., S. Singh, and S. Mehta, *Ultrasonication assisted fabrication of l-lysine functionalized gadolinium oxide nanoparticles and its biological acceptability.* Ultrasonics sonochemistry, 2018. **49**: p. 53-62.
138. Mallakpour, S. and S. Mansourzadeh, *Sonochemical synthesis of PVA/PVP blend nanocomposite containing modified CuO nanoparticles with vitamin B1 and their antibacterial activity against Staphylococcus aureus and Escherichia coli.* Ultrasonics sonochemistry, 2018. **43**: p. 91-100.
139. Bai, R.G., K. Muthoosamy, F.N. Shipton, and S. Manickam, *Acoustic cavitation induced generation of stabilizer-free, extremely stable reduced graphene oxide nanodispersion for efficient delivery of paclitaxel in cancer cells.* Ultrasonics sonochemistry, 2017. **36**: p. 129-138.
140. Cavalieri, F., M. Ashokkumar, F. Grieser, and F. Caruso, *Ultrasonic synthesis of stable, functional lysozyme microbubbles.* Langmuir, 2008. **24**(18): p. 10078-10083.
141. Cavalieri, F., M. Colone, A. Stringaro, M. Tortora, A. Calcabrini, M. Zhou, and M. Ashokkumar, *Influence of the Morphology of Lysozyme-Shelled Microparticles on the Cellular Association, Uptake, and Degradation in Human Breast Adenocarcinoma Cells.* Particle & Particle Systems Characterization, 2013. **30**(8): p. 695-705.
142. Okitsu, K. and F. Cavalieri, *Synthesis of Micro-nanoparticles Using Ultrasound-Responsive Biomolecules*, in *Sonochemical Production of Nanomaterials*. 2018, Springer. p. 39-62.
143. Zhou, M., F. Cavalieri, and M. Ashokkumar, *Tailoring the properties of ultrasonically synthesised microbubbles.* Soft Matter, 2011. **7**(2): p. 623-630.
144. Mine, Y., F. Ma, and S. Lauriau, *Antimicrobial peptides released by enzymatic hydrolysis of hen egg white lysozyme.* Journal of Agricultural and Food Chemistry, 2004. **52**(5): p. 1088-1094.
145. Tran, T.D., S.D. Caruthers, M. Hughes, J.N. Marsh, T. Cyrus, P.M. Winter, A.M. Neubauer, S.A. Wickline, and G.M. Lanza, *Clinical applications of perfluorocarbon nanoparticles for molecular imaging and targeted therapeutics.* International journal of nanomedicine, 2007. **2**(4): p. 515.
146. Cosgrove, D. and C. Harvey, *Clinical uses of microbubbles in diagnosis and treatment.* Medical & biological engineering & computing, 2009. **47**(8): p. 813-826.
147. Bloch, S.H., M. Wan, P.A. Dayton, and K.W. Ferrara, *Optical observation of lipid-and polymer-shelled ultrasound microbubble contrast agents.* Applied physics letters, 2004. **84**(4): p. 631-633.
148. de Jong, N., L. Hoff, T. Skotland, and N. Bom, *Absorption and scatter of encapsulated gas filled microspheres: theoretical considerations and some measurements.* Ultrasonics, 1992. **30**(2): p. 95-103.
149. Postema, M., *Medical bubbles.* Medical Physics, 2005. **32**(5): p. 1450-1450.
150. Sirsi, S.R. and M.A. Borden, *Advances in ultrasound mediated gene therapy using microbubble contrast agents.* Theranostics, 2012. **2**(12): p. 1208.
151. Grinberg, O., M. Hayun, B. Sredni, and A. Gedanken, *Characterization and activity of sonochemically-prepared BSA microspheres containing Taxol–an anticancer drug.* Ultrasonics sonochemistry, 2007. **14**(5): p. 661-666.
152. Chen, Y.-C., L.-P. Jiang, N.-X. Liu, Z.-H. Wang, K. Hong, and Q.-P. Zhang, *P85, Optison microbubbles and ultrasound cooperate in mediating plasmid DNA transfection in mouse skeletal muscles in vivo.* Ultrasonics sonochemistry, 2011. **18**(2): p. 513-519.
153. Cavalieri, F., E. Colombo, E. Nicolai, N. Rosato, and M. Ashokkumar, *Sono-assembly of nanostructures via tyrosine–tyrosine coupling reactions at the interface of acoustic cavitation bubbles.* Materials Horizons, 2016. **3**(6): p. 563-567.

154. Wu, C., X. Liu, D. Wei, J. Fan, and L. Wang, *Photosonochemical degradation of phenol in water.* Water Research, 2001. **35**(16): p. 3927-3933.
155. Okouchi, S., O. Nojima, and T. Arai, *Cavitation-induced degradation of phenol by ultrasound.* Water Science and Technology, 1992. **26**(9-11): p. 2053-2056.
156. Petrier, C., M.-F. Lamy, A. Francony, A. Benahcene, B. David, V. Renaudin, and N. Gondrexon, *Sonochemical degradation of phenol in dilute aqueous solutions: comparison of the reaction rates at 20 and 487 kHz.* The Journal of Physical Chemistry, 1994. **98**(41): p. 10514-10520.
157. Entezari, M.H. and C. Pétrier, *A combination of ultrasound and oxidative enzyme: sono-enzyme degradation of phenols in a mixture.* Ultrasonics sonochemistry, 2005. **12**(4): p. 283-288.
158. Serpone, N., R. Terzian, P. Colarusso, C. Minero, E. Pelizzetti, and H. Hidaka, *Sonochemical oxidation of phenol and three of its intermediate products in aqueous media: catechol, hydroquinone, and benzoquinone. Kinetic and mechanistic aspects.* Research on Chemical Intermediates, 1992. **18**(2): p. 183-202.

Chapter 3

Experimental Details

This chapter provides all materials, methods and experiment details utilized throughout the PhD research work.

3.1. A Simple One-Step Ultrasonic Route to Synthesize Antioxidant Molecules and Fluorescent Nanoparticles from Phenol and Phenol-Like Molecules

3.1.1. Materials

Phenol (99.5 %), di-sodium hydrogen orthophosphate (98%) and sodium dihydrogen orthophosphate (99%) were purchased from Chem-Supply; catechol (≥ 99%), hydrogen peroxide (35 wt% of H_2O_2), 2,2'-biphenol, 1-diphenyl-2-picrylhydrazyl (DPPH), p-benzoquinone (≥ 98%), tyrosine were purchased from Sigma Aldrich; iron(II) chloride tetrahydrate was purchased from Fluka, hydroquinone was purchased from BDH AnalaR®, HPLC grade methanol (99.9%) was purchased from Fisher chemicals. All solutions were prepared in high purity water extracted from a Millipore system with resistivity of 18.2 MΩ/cm.

3.1.2. Equipment

The experimental setup used for sonication is shown in Figure 3.1. A glass vial (with reactants) was mounted over the sonication bath containing 200 ml water, which was a double walled glass cell, base of which was mounted on a stainless-steel ultrasonic plate transducer of diameter 5.4 cm. The plate transducer used was ELAC Nautik USW 51-052 transducer which was powered by a T&C Power Conversion, Inc. The unit was operated at 355 kHz and 1058 kHz frequencies and power of 60 W (which is actual power delivered calculated using calorimetry). All the reactions were performed at constant temperature of 37 ± 2 ˚C. The hydrogen peroxide and corresponding OH radical yields were determined by 'Weissler'' method discussed in *Chapter 1* under section 1.3.3. Figure 3.2 shows the hydrogen peroxide yield obtained at 60 W with ultrasonic frequency 355 kHz as a function of sonication time.

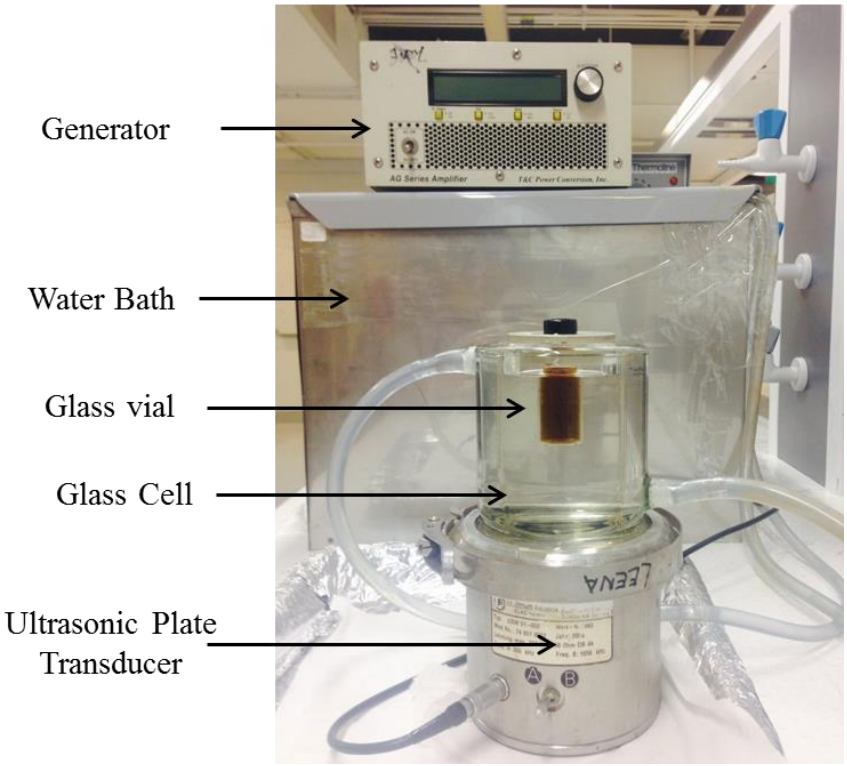

Figure 3. 1: Experimental setup of the ultrasonic system.

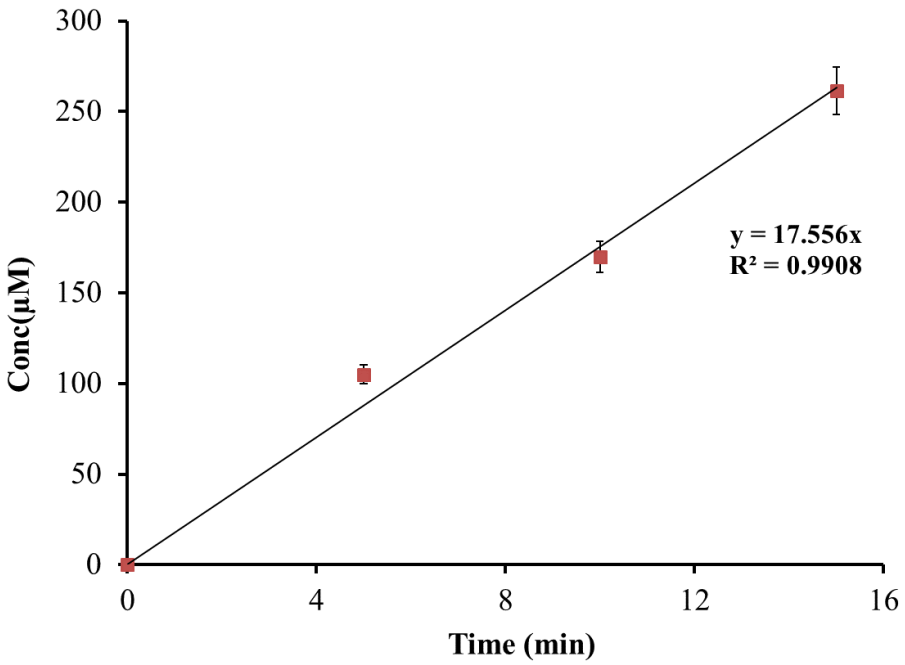

Figure 3. 2: Hydrogen peroxide yield obtained at 355 kHz and 60 W as a function of sonication time.

3.1.3. Ultrasonic treatment of phenol and phenolic molecules.

Sonication of 0.5 mM phenol (12 ml) in PBS (pH = 7) was carried out in a 15 ml sealed glass vial. The reaction was studied as a function of sonication time. To ascertain the role of ultrasound, phenol oxidation was also carried out via Fenton reaction where to the 30 ml of 0.5 mM phenol solution was added 1.5 mg of solid $FeCl_2$ to give a 0.25 mM solution followed by the addition of 10 µL of 1.02 mM H_2O_2 every 5 minutes to generate a radical concentration of 1.02 mM per hour, which was equal to the amount radicals produced by sonication in an hour.

3.1.4. Characterisation

Sonicated phenol solutions were analysed using fluorescence spectroscopy, HPLC, LC-MS and absorption spectroscopy. A Perkin Elmer AxION® 2 ToF quadrupole mass spectrometer was used for performing mass analysis. Scans were performed in both negative and positive ion modes. A gradient elution was carried with solvent A (0.1% formic acid) and solvent B (acetonitrile with 0.1% formic acid) at 30˚C. The LC gradient used was from 10% to 90% solvent B in 20 min and was held for 5 min at 90% solvent B and then from 90% solvent B to 10% solvent B in 5 min. The flow rate was 0.3 ml.min-1 and the injection volume was 50 µL. Shimadzu SCL-10AVP high-performance liquid chromatography (HPLC) equipped with a Phenomenex column model “Jupiter 5u C18 300A” and with a UV detector set at 220 nm was used to perform HPLC analysis. All chromatograms were generated by LabSolution software (Shimadzu). The injection volume was 20 µl and the flow rate used was 1 $ml.min^{-1}$ with methanol: water (35:65) mixture used as an eluent. Fluorescence spectra were obtained using a Shimadzu RF-5301PC fluorescence spectrophotometer (Shimadzu) equipped with a xenon lamp and 1.0

cm optical length quartz cell. All measurements were carried out in PBS buffer (pH 7). Samples were excited at different wavelengths and the fluorescence spectra were recorded from 340 to 600 nm using a slit width of 5 nm for excitation and 10 nm for emission spectra. UV- visible absorption spectra were recorded on a Cary Bio 50 UV-spectrophotometer. The morphology of the particles was examined by high-resolution field emission environmental Scanning Electron Microscope (Quanta 200 FEI). The particles were sputter-coated with the thin layer of gold during the sample preparation.

Antioxidant test was carried out using DPPH (1-diphenyl-2-picrylhydrazyl) method. The DPPH solution of concentration 250 μM was prepared in Ethanol:Water (50:50) mixer. 2 ml of sonicated phenol and unsonicated phenol were incubated with 3 ml of the DPPH solution for 30 min and the absorbance was noted at 520 nm. The radical scavenging activity was determined using following expression:

$$Radical\ scavenging\ activity\ (\%) = \left[\left(A_{DPPH} - A_{sample}\right)/A_{DPPH}\right]\times 100$$

Where A_{DPPH} is the absorbance of blank DPPH solution and A_{sample} is the absorbance of DPPH solution after the addition of sample.

3.2. Ultrasonic transformation of tannic acid into bio-functional ellagic acid micro/nanocrystals with distinct morphologies

3.2.1. Materials

Tannic acid (TA), gallic acid, ellagic acid (EA), phosphoric acid solution (35 wt% in H_2O), DMSO, 1-diphenyl-2-picrylhydrazyl (DPPH), hydrogen peroxide (35 wt%) and 3-(4,5-dimethylthiazol-2-yl)-2,5-diphenyltetrazolium bromide (MTT) were purchased from

Sigma Aldrich. Di-sodium hydrogen orthophosphate (98%) and sodium dihydrogen orthophosphate (99%) were purchased from Chem-Supply; iron (II) chloride tetrahydrate was purchased from Fluka, hydroquinone was purchased from BDH AnalaR®, HPLC grade methanol (99.9%) was purchased from Fisher chemicals. Sulphuric acid (95-97%) was purchased from Scharlau, hydrochloric acid (36%) and pyridines were purchased from Univar. Doxorubicin hydrochloride (~99%) was purchased from OChem Inc. (USA). All solutions were prepared in high purity water extracted from a Millipore system with resistivity of 18.2 MΩ/cm.

3.2.2. Sonication of Tannic acid

The sonication of 1 mM tannic acid solution prepared in PBS of pH 7 was carried out in a sealed glass vial. The glass vial was inserted into 200 ml water contained in a double walled glass cell, the base of which was mounted on a stainless steel ultrasonic plate transducer of diameter 5.4 cm. The plate transducer used is same as listed in section 3.2.2. The unit was operated at 355 kHz and 1058 kHz frequencies and at different ultrasonic power levels from 5.5 W/cm^3 to 20 W/cm^3). All reactions were performed at constant temperature of 37 ± 2 ˚C.

3.2.3. Fluorescence spectroscopy

Fluorescence spectra were obtained using a Shimadzu RF-5301PC fluorescence spectrophotometer equipped with a xenon lamp and 1.0 cm optical length quartz cell. All the measurements were carried out in PBS buffer (pH 7). Samples were excited at different wavelengths (from 320 nm to 460 nm) and the fluorescence spectra were recorded from 340 to 600 nm using slit widths of 5 nm for excitation and 10 nm for emission spectra. UV- visible absorption spectra were recorded on a Cary Bio 50 UV-spectrophotometer.

3.2.4. HPLC

Shimadzu SCL-10AVP high-performance liquid chromatography (HPLC) equipped with a Phenomenex column model "Jupiter 5u C18 300A" and with an UV detector set at 280 nm was used to perform HPLC analysis. All chromatograms were generated by LabSolution software (Shimadzu). The injection volume was 20 µl and the flow-rate used was 1 mL/min.

For the analysis, a gradient elution was carried out with solvent A (0.5 % phosphoric acid) and solvent B (methanol with 0.5% phosphoric acid). The gradient used was 10% solvent B from 0 -5 min, then increased to 50 % solvent B from 5-10 min and then 100 % solvent B from 10-30 min.

3.2.5. Nuclear magnetic resonance (NMR)

^{1}H and ^{13}C NMR spectra of TA and sonicated TA particles was conducted in d_6-DMSO on Varian MR400 NMR spectrometer at 400 MHz at 25 ˚C.

3.2.6. Scanning electron microscopy (SEM)

The morphology of the particles was examined by high-resolution field emission environmental Scanning Electron Microscope (Quanta 200 FEI). The particles were sputter-coated with the thin layer of gold during the sample preparation.

3.2.7. Thermogravimetric analysis (TGA)

Thermogravimetric analysis was carried out by TGA/SDTA8511e (Mettler Toledo). The analysis was conducted under the nitrogen flow at a heating rate of 10˚C/min.

3.2.8. Electrospray Mass spectrometry (ESMS)

The ESMS analyses were performed using an Agilent 6500 Q-TOF LC/MS system. Scans were performed in both negative and positive ion modes. Also, MALDI-TOF analysis was carried out. The sample (10 mg/ml) was mixed with the matrix solution (2,5-Dihydroxybenzoic acid) and cationization reagent (Sodium trifluoroacetate) in 10:1:1 ratio. The matrix and the cationization reagent used were 2, 5-dihydroxybenzoic acid and sodium trifluoroacetate, respectively.

3.2.9. Powder X-ray diffraction (PXRD)

The PXRD analysis was performed by Bruker D8 Advance X-ray diffractometer with Ni-filtered Cu kα radiation (1.54 Å). Data were collected between 5 –85° 2θ, with a step size of 0.02° and a scan rate of 1.0 s per step. An anti-scatter blade was used to reduce the diffracted background intensity at low angles. An incident beam divergence of 1.0° was used with a 2.5° soller slit in the diffracted beam. The sample was spun at 15 revolutions per minute.

3.2.10. Ellagic acid Assay

The Ellagic acid content of the sonicated tannic acid was determined using the well-established Ellagic acid assay. The method is based on the formation quinone oxime of the ellagic acid nitrosylation product. The ellagic acid standard solution in pyridine forms red colour nitrosylated product when incubated in NaNO2 solution and gives a characteristic absorbance band at around 515 nm that can be further used to quantify the concentration of ellagic acid. For hydrolysis, 10 mg of the TAS was added to 2 N H_2SO_4 solution in a test tube. The reaction mixture was frozen in liquid nitrogen and was vacuum sealed. The content was heated for 24 hr at 100 ˚C. After the hydrolysis, the content was

cooled at room temperature and filtered using vacuum filtration. The residue was then dissolved in 10 ml pyridine. 1.1 ml of pyridine and 1ml of sample solution also in pyridine were mixed and 0.100 ml concentrated HCl solution was added and the mixture was heated for 5 min at 30 ˚C. This sample was quickly mixed with 0.100 ml of 1% NaNO2 (w/v in water) solution and absorbance was immediately recorded. The absorbance was again noted after incubating the sample with NaNO2 at 30 ˚C for 36 min. Difference between the absorbance at 0 min and 36 min is proportional to the Ellagic acid concentration.

3.2.11. DPPH Assay

The antioxidant activity of TA, TAS and EA was estimated from their radical scavenging activity. The 1-diphenyl-2-picrylhydrazyl radical (DPPH) was utilised for this purpose.

To 3 ml of 250 µM solution of DPPH were added different concentrations of EA, TA and TAS solutions. The absorbance was noted at 520 nm as function of time. The radical scavenging activity was determined using following expression:

$$Radical\ scavenging\ activity\ (\%) = \left[\left(A_{DPPH} - A_{sample}\right)/A_{DPPH}\right]\times 100$$

Where A_{DPPH} is the absorbance of blank DPPH solution and A_{sample} is the absorbance of DPPH solution after the addition of sample.

3.2.12. Cell Viability Assay

The cytotoxicity of the TA and TAS was estimated using MTT (3-(4,5-dimethylthiazol-2-yl)-2,5-diphenyl tetrazolium bromide) assay. MDA-MB-231 (human breast adenocarcinoma) were plated on 96-well plates (Costar 3596, Corning, MA, USA) with seeding density of 7000 cells per well in 100 µL of DMEM medium supplemented with 10% fetal bovine serum (FBS) and 1% of Penicillin/ Streptomycin antibiotic mixture.

Cells were incubated overnight in 37°C, 5% CO_2. Particles were added to culture media at various concentrations in quadruplicates followed by incubation for 24h. Cell viability was assessed by the addition of 10 µL of 5 mg/mL MTT reagent and further incubation for 4 hours. Resulted formazan crystals were dissolved in 70 µL DMSO and absorbance was measured at 554 nm and 670 nm by Infinite M200 microplate reader (Tecan, Switzerland).

3.3. Sound-driven dissipative self-assembly of aromatic biomolecules into nanoparticles

3.3.1. Materials

Tryptophan, 1-diphenyl-2-picrylhydrazyl (DPPH), Dulbecco's phosphate-buffered saline (D-PBS), filipin from *S. filipinensis*, Hydrogen peroxide (30 %), EIPA (Ethylisopropyl amiloride) and bovine serum albumin (BSA) were purchased from Sigma Aldrich. Methanol (99.9%) HPLC grade, Formic acid was purchased from Fisher chemicals. Pitstop 2 was purchased from Abcam (Cambridge, UK). Doxorubicin hydrochloride (~99%) was purchased from Chem Inc. (USA). Triton X-100 was purchased from Chem-Supply. Phalloidin Alexa 480, rabbit anti-EEA-1 monoclonal antibody and rabbit anti-Rab7 monoclonal antibodies were purchased from Cell Signalling Technology. Alamar blue assay kit, Rabbit LAMP-1 and goat anti-rabbit IgG secondary antibody Alexa Fluor 647 were supplied by Invitrogen. Fetal bovine serum (FBS) was purchased from Bovogen. *Dulbecco's Modified Eagle's medium* (DMEM) was purchased from Lonza. All the solutions were prepared in high purity water.

3.3.2. Sonication of Tryptophan

The sonication of 10 ml of 1 mg/ml Tryptophan was carried out at ultrasonic frequency and power of 355 kHz and 6 W/cm^3 respectively. The sonication was performed in the

Milli-Q water for 5 hours. The nanoparticles were then separated by centrifugation at 6000 rpm for 10 min and washed several times before the characterisation.

3.3.3. HPLC and Mass spectrometry

Shimadzu SCL-10AVP HPLC equipped with UV detector set at 205 nm was utilised to carry out the further analysis of sonicated product. The Phenomenex "Jupiter 5u C18 300A" column was used. The injection volume was 20 μL and flow rate was 1 ml/min with methanol: water: formic acid (70:30:0.5) used as an eluent. Electrospray ionisation mass spectrometry was performed by Agilent Accurate-Mass QToF LC/MS in positive ion mode to estimate molecular weight of the sonicated product.

3.3.4. Scanning electron microscopy (SEM)

The morphology and size of the particles was observed by field emission scanning electron microscope (Quanta 200 FEI) at 10 kV. The drop of nanoparticle suspension was placed on the metallic support with carbon tape and was sputter coated with gold prior to imaging.

3.3.5. Molecular Dynamics Simulations

The Molecular Dynamics (MD) simulations were carried out with the GROMACS 4.6.5 software package [1]. Six replicas of the compound 4 in the Figure 1a (hereafter dTrp) were randomly inserted in a cubic box of 64 nm^3 and hydrated with 2058 pre equilibrated SPC water molecules [2]. The W2-OH parameters were obtained by starting from those provided by the Prodrg server [3] with slight modifications introduced by analogy with the standard gromos 43a1 parameters. In particular, the tryptophan parameters were used as model, except for the hydroxyl group, for which the corresponding tyrosine parameters were used. The torsional dihedral angle connecting the two aromatic rings was described

according to previous report [4]. The charges were assigned by analogy with the gromos 43a1 force field [5] considering a neutral pH, as a consequence both the amino and the carboxyl groups were considered charged. The simulation was carried out according to a protocol previously used, with slight changes [6-8]. Briefly, the system was energy-minimized and then equilibrated using a 100 ps MD, where the positions of the dTrp atoms were harmonically restrained. Production simulations were performed for 1 μs, at a temperature of 300 K, controlled by means of the V-rescale scheme [9]. Pressure coupling was applied using the Berendsen algorithm, with a time constant of 1.0 ps and a reference pressure of 1 bar [10]. Bond lengths were constrained with the LINCS algorithm [11]. Short-range electrostatic interactions were cut-off at 0.9 nm and long range electrostatic interactions were calculated using the particle mesh Ewald (PME) algorithm [12]. Simulations were run with a 2 fs time step. To evaluate the Solvent Accessible Surface Area (SAS) and the number of hydrogen bonds, the g_sas and g_hbond tools in GROMACS was used with the default settings. The structural figures were produced by using VMD [13] or Chimera [14]. At each time, a single dTrp molecule was considered part of an aggregate if the minimum distance with any other molecules in the aggregate falls below 0.35 nm. The minimum distances were evaluated with the g_mindist tool in GROMACS between all the pairs of molecules; starting from these distances, a homemade program was used to obtain the number of molecules in the aggregates.

3.3.6. Surface tension measurements

The surface tension of dissolved dimer solutions at different concentration was measured in water/air system using pendant drop method on OCA 15 EC**.** The slope of the graph of

surface tension vs lnC was used to calculate the surface excess of dimers using Gibbs adsorption isotherm equation given as follows.

$$\Gamma = \frac{-1}{RT}\frac{\partial\gamma}{\partial lnC}$$

Where R is Gas constant (8.314 J/ mol K), T is the temperature in K, γ is the surface tension, C is the concentration of the solute, Γ is the surface excess. Then the area occupied by each molecule was calculated using the expression 1/ $N_A\Gamma$ where N_A is Avogadro's number.

3.3.7. Fluorescence spectroscopy

To study the optical properties of the sonicated product Shimadzu RF-5301PC fluorescence spectrophotometer (Shimadzu) equipped with a xenon lamp and 1.0 cm optical length quartz cell was utilized to obtain the fluorescence excitation and emission spectra. The fluorescence spectra were obtained at different wavelength in PBS (pH=7.4).

3.3.8. Dynamic Light Scattering (DLS), ζ-potential

The zeta potential and hydrodynamic diameter of the particles was determine using ZEN0040, Malvern Instruments. The 100 µL particles (2 mg/ml) were suspended 1 ml in Milli-Q and zeta potential and hydrodynamic diameter of particles was determined.

3.3.9. Protein Adsorption

The dTrpNPs were incubated with 100 % Fetal bovine serum and the adsorption of protein was determined from the increase in size of particle measured by Malvern Analytical NanoSight NS300. Nanosight combines the principle of light scattering and Brownian motion of particles in liquid suspension and use the Stokes Einstein equation to obtain the hydrodynamic diameter of the particles.

3.3.10. Quantum yield

The Quantum yield of the sonicated product having emission maxima at 690 nm was determined by using Rhodamine B as a reference standard in water. Following equation used to estimate the quantum yield

$$\frac{\phi_{f1}}{\phi_{f2}} = \frac{(1-10^{-A2})n_1^2\alpha_1}{(1-10^{-A1})n_2^2\alpha_2}$$

Where ϕ is the quantum yield, A is the Absorbance, n is the refractive index and α is the area under the fluorescence emission spectrum and subscript 1 and 2 illustrated the reference sample and sample respectively.

3.3.11. Antioxidant activity

The antioxidant activity was monitored using 2,2-diphenyl-1-picrylhydrazyl (DPPH) assay. To the 3 ml DPPH solution (250 µM in 50:50 ethanol: water) was added tryptophan with and without the treatment with ultrasound and absorption of DPPH was noted at 520 nm. Percentage of radicals scavenged can be determined by using following equation:

% Radical scavenging activity = [(A_{DPPH} - A_{sample})/A_{DPPH}] X 100

Where A_{DPPH} and A_{sample} are the absorption values for blank DPPH solution and after the addition of sample respectively.

3.3.12. Loading of DOX to dTrpNPs

The 0.5 mg/ml dTrpNPs were incubated with 20 µl Dox (Doxorubicin) solution giving final Dox concentration of 280 µg/ml. The particles were incubated overnight with Dox. They were well washed five times with water to remove excess Dox and were refrigerated

at 4˚C.The amount of Dox loaded was quantified using fluorescence intensity at λ_{ex} = 480 nm.

3.3.13. Release of DOX from dTrpNP

dTrpNPs loaded with the Dox were incubated with 0.01 M PBS buffer (pH= 7.4) at 37 ˚C. The release of Dox was studied as a function of time. The mixture was centrifuged, and supernatant was collected and analysed by fluorescence spectroscopy at an excitation wavelength of 480 nm.

3.3.14. Flow cytometry

The association and uptake of the dTrpNPs with human breast adenocarcinoma MDA-MB-231 breast cancer cell line was evaluated using Flow cytometry. Since the particles were fluorescent no further functionalization of particles was required. The cells after incubation with the particles at different times (2 h, 4.5 h, 6.5 h, 12 h and 24 h) were detached using trypsin, then washed twice using 1% BSA/PBS and centrifuged at 400 rpm for 5 mins at 4 °C. After this, cells were analysed using BD Accuri™ C6 flow cytometer under different fluorescence channels and FlowJo was used for data analysis.

3.3.15. Cell Viability

The human breast adenocarcinoma MDA-MB-231 cells were plated in 96 well plate with seeding density of 40,000 cells per well in 100 µL DMEM media with 10 % FBS. The cells were incubated for 24 hours in 37°C 5 % CO_2. The particles (5 µg/ml) were added into the cells at different concentrations for 24 and 48 h in triplicates and cell viability of the sonicated tryptophan was assessed by addition of alamar blue assay. Similarly, DOX loaded dTrpNPs and free doxorubicin were at different DOX concentration were added to the MDA-MB-231 cells to compare the cell viability after 24 h and 48 h.

3.3.16. Mechanism of internalization of dTrpNP

For mechanism of internalization MDA-MB-231 cells were seeded with seeding density of 50,000 cells per well in 24 well plate and incubated overnight at 37 °C. The cells were incubated with different endocytosis inhibitors namely filipin (5 µg/ml), pitstop-2 (12 µg/ml), and Ethylisopropyl amiloride (EIPA) (15 µg/ml) to inhibit caveoloe-dependent endocytosis, clathrin-dependent endocytosis and micropinocytosis for 30 min and then incubated with dTrpNP (final concentration 10 µg/ml) for 2 h. The cells were washed twice with PBS and detached with trypsin. Then cells were washed twice using 1% BSA/PBS and centrifuged at 400 rpm for 5 min at 4 °C. The cells were analysed using Apogee A50-Micro Flow Cytometer and FlowJo was used for data analysis.

3.3.17. Laser Scanning Confocal Microscope Imaging

All samples with cells were imaged using Nikon A1R confocal microscope with a 60× 1.4NA oil immersion objective. For the live cell imaging the MDA-MB-231 cells were seeded with seeding density of 40,000 cells per well in DMEM media with 10 % FBS were incubated with the dTrpNPs at 37 °C for 24 h and Dox loaded dTrpNPs for 2-24 hrs and after refreshing the culture media, the cells were observed under the confocal microscope.

For intracellular trafficking, the particles were removed after 2.5 h and were kept at 37 °C for 2.5 h, 5 h and 21.5 h in fresh media corresponding to observation times of 2.5 h, 5 h, 8.5 h and 24 h. Then for each sample the media was removed after the desired time, cells were washed 3 times with PBS and fixed with 4% paraformaldehyde for 10 min. After washing 3 times again the cells were permeabilized with 0.1 % TritonX-100 (in PBS) for 5 min and washed again with PBS and Blocked for 1 hour with 1 % BSA solution in PBS. After this, cells were incubated with rabbit anti-EEA1 monoclonal antibody (2

μg/ml), rabbit anti-Rab7 monoclonal antibody (2 μg/ml) and rabbit LAMP-1 (1 μg/ml) for 1.5 h followed by 3 time washing with PBS and further incubation for 1 h with goat anti-rabbit Alexa Fluor 647 conjugate secondary antibody (2 μg/ml). The samples were then imaged using confocal microscope. The 647 laser was set at the power where no signal from the dTrpNPs was observed. The Pearson's correlation function was determined with ImageJ software.

3.4. Synthesis of bio-functional nanoparticles from sono-responsive amino acids using high frequency ultrasound

3.4.1. Materials

Tryptophan, phenylalanine, 1-diphenyl-2-picrylhydrazyl (DPPH) were purchased from Sigma Aldrich. Methanol (99.9%) HPLC grade and formic acid were purchased from Fisher chemicals. All solutions were prepared with high purity water.

3.4.2. Synthesis of phenylalanine nanoparticles

1 mg/ml solution of phenylalanine or a 1:1 mixture containing 1 mg/ml phenylalanine and 1 mg/ml tryptophan was irradiated with ultrasonic frequency of 490 kHz at different ultrasonic powers of 5 W /cm^3, 10 W/cm^3 and 15 W/cm^3. The piezo-electric ceramic plate transducer with operating frequency 490 kHz from Honda Electric was used, however cavitation efficiency of the unit was similar to the previous equipment mentioned in section 3.1.2. The sonication was performed for up to 5 hours. The dark brown suspension obtained was then centrifuged at 6000 rpm for 5 min and washed 3 times prior to further analysis.

3.4.3. HPLC and Mass spectrometry

HPLC analysis was performed using Shimadzu SCL-10AVP HPLC implemented with UV detector set at 205 nm and Phenomenex “Jupiter 5u C18 300A” column. The flow rate was 1 ml/min and a mixture of methanol: water: formic acid (70:30:0.5) was used as an eluent. The injection volume used was 20 µL.

Agilent Accurate-Mass QToF LC/MS in positive ion mode was used to carry out the Electrospray ionisation mass spectrometry to estimate molecular weight of the sonicated product.

3.4.4. Scanning electron microscopy (SEM)

The morphology of the nanoparticles was studied by field emission scanning electron microscope (Quanta 200 FEI) at 10 kV. On to the metallic support with the carbon tape on it, a drop of nanoparticle suspension was added which after air drying was sputter coated with the gold and imaging experiments were conducted.

3.4.5. Fluorescence spectroscopy

The emission and absorption spectra of the sonicated products at different sonication times was recorded in different wavelength ranges (refer to section 3.3.7.). The sonicated products were diluted in PBS pH=7.4 prior recording the spectra.

3.4.6. Dynamic Light Scattering (DLS), ζ-potential

ZEN0040, Malvern Instruments was utilized to determine the zeta potential and hydrodynamic diameter of the nanoparticles. The 80 µL nanoparticle suspension (2 mg/ml) was diluted in Milli-Q and zeta potential and hydrodynamic diameter of particles was determined.

3.4.7. Antioxidant activity

The DPPH assay was conducted to measure the antioxidant activity of the phenylalanine and other sonicated mixtures. 250 µM DPPH solution was prepared in ethanol: water (50:50) mixture. Then to 3 ml DPPH solution 100 µL phenylalanine and its mixture with tryptophan with and without sonication was added (30 µg/ml final concentration). The percentage radical scavenging activity was measured using absorption at 520 nm and the following equation:

$$\% \text{ Radical scavenging activity} = [(A_{DPPH} - A_{sample})/A_{DPPH}] \times 100$$

Where A_{DPPH} and A_{sample} are the absorption values for blank DPPH solution and after the addition of sample, respectively.

3.5. Ultrasonic synthesis of Nano-formulation of chemotherapy drug-Doxorubicin

3.5.1. Materials

Doxorubicin hydrochloride was purchased from OChem Incorporation., Dulbecco's phosphate-buffered saline (D-PBS) filipin from S. filipinensis, Horseradish peroxidase, Hydrogen peroxide (30 %), EIPA (Ethylisopropyl amiloride) and bovine serum albumin (BSA) were purchased from Sigma Aldrich. Pitstop 2 was purchased from Abcam (Cambridge, UK). Methanol (99.9%) HPLC grade, Formic acid was purchased from Fisher chemicals. Triton X-100 was purchased from Chem-Supply. Phalloidin Alexa 480, rabbit anti-EEA-1 monoclonal antibody and rabbit anti-Rab7 monoclonal antibodies were purchased from Cell Signalling Technology. Alamar blue assay kit, Rabbit LAMP-1 and goat anti-rabbit IgG secondary antibody Alexa Fluor 647 were supplied by Invitrogen. The A2780 ovarian carcinoma cell line, the LoVo colorectal carcinoma cell

line and doxorubicin-resistant sublines (A2780/Dx, LoVo/Dx) were maintained at 37 °C in RPMI-1640 (ThermoFisher Scientific) supplemented with 10% foetal bovine serum (ThermoFisher Scientific). The MDA-MB-231 breast carcinoma cell line was cultured in DMEMF-12 medium (ThermoFisher Scientific) plus 5% foetal bovine serum. All the solutions were prepared in high purity water.

3.5.2. Synthesis of Doxorubicin nanoparticles

The sonication of 10 ml of 0.5 mg/ml Doxorubicin.HCl was carried out at ultrasonic frequency and power of 490 kHz and 6 W/cm^3 respectively. The sonication was performed in the Milli-Q water for 4 hours. The nanoparticles were then separated by centrifugation at 7000 rpm for 10 min and washed three times with MilliQ water before the characterisation

3.5.3. Mass spectroscopy & NMR

The electrospray ionisation (ESI) mass spectrometry, using a Thermo Scientific Exactive Plus Orbitrap mass spectrometer. ^1H spectra were recorded on a Varian INOVA 400 instrument, operating at 400 MHz for DOX and DOXNP after dissolution DMSO.

3.5.4. Size exclusion chromatography (SEC)

Size exclusion chromatography was carried out using Shimadzu SCL-10AVP HPLC equipped with UV detector set at 280 nm. The TSK gel G3000 SW_{XL} column (7.8 mm I.D. X 30 cm with pore size 5 μm) was used. The injection volume was 20 μL and flow rate was 1 ml/min with 0.1 mol/L Na_2SO_4, 0.05 % NaN_3 and 0.1 mol/L sodium phosphate buffer (pH=6.7).

3.5.5. Fluorescence spectroscopy

To study the optical properties of the sonicated doxorubicin the fluorescence excitation and emission spectra were acquired (refer to section 3.3.7). The fluorescence spectra were obtained at different wavelength in PBS (pH=7.4).

3.5.6. Dynamic Light Scattering (DLS), ζ-potential

The zeta potential and hydrodynamic diameter of the particles were determined using ZEN0040, Malvern Instruments. The 100 μL particles (2 mg/ml) were suspended in Milli-Q and zeta potential and hydrodynamic diameter of particles was determined.

3.5.7. Protein Adsorption

The particles were incubated with 100 % Fetal bovine serum and the adsorption of protein was determined from the increase in size of particle measured by Malvern Analytical NanoSight NS300. Nanosight combines the principle of light scattering and Brownian motion of particles in liquid suspension and use the Stokes Einstein equation to obtain the hydrodynamic diameter of the particles.

The sodium dodecyl sulphate poly-acrylamide gel electrophoresis (SDS-PAGE) analysis was performed to confirm the adsorption protein using Bio- Rad (Bio-Rad Technologies Gladesville, NSW, Australia) and Pre-cast 12.5 % criterion gels (Bio-Rad Technologies Gladesville, NSW, Australia). The Tris glycine SDS (Bio-Rad) was used as a running buffer. The DOXNP were incubated with 100 % FBS at 37 °C. The nanoparticles were then centrifuged, the access protein was removed and washed 3 times using MilliQ water. The samples - FBS, supernatant removed after incubating with DOXNP, washed DOXNP were then diluted with Laemmli buffer in 1:1 and heated at 90 °C for 10 min. The 20 μl sample along with protein standard was then loaded into the gel lanes and gels were run

for 45 min at 200 V. The gel was then removed and stained with Coomassie G250 dye for 1h and detained using MilliQ water (shaking in water overnight). The stained gel was them imaged.

3.5.8. Release Kinetics of DOXNP

DOXNPs (100 µg/ml) were incubated with 0.01 M PBS buffer (pH= 7.4 and pH 5) at 37 ˚C. The release of particles was studied as a function of time. The mixture was centrifuged, and supernatant was collected and analysed by fluorescence spectroscopy at an excitation wavelength of 520 nm.

3.5.9. Flow cytometry

The association and uptake of the DOXNPs with human breast adenocarcinoma MDA-MB-231 breast cancer cell line were evaluated using Flow cytometry. The cells after incubation with the DOXNP (5 µg/ml) at different times (2 h, 4.5 h, 9 h and 24 h) were detached using trypsin, then washed twice using 1% BSA/PBS and centrifugation at 400 rpm for 5 mins at 4 °C. After this, cells were analysed using BD Accuri™ C6 flow cytometer under different fluorescence channels and FlowJo was used for data analysis.

3.5.10. Cell Viability

Exponentially growing cells were harvested and seeded in 12-well plate. Twenty-four hours later, cells were exposed to different DOX and DOXNP concentrations for 2, 72 and 144 h. Aliquots of freshly dissolved compounds from stock solution or from serial dilutions performed in water were added to culture medium. After drug exposure, cells were harvested for counting with a cell counter. IC_{50} is defined as the drug concentration producing 50% decrease of cell growth. Three independent experiments were performed for each type of treatment.

Also, the human breast adenocarcinoma MDA-MB-231 cells, HCC-1143 HCC- 1937 and 3T3 fibroblast cells were plated in 96 well plate with seeding density of 7000 cells per well in 100 µL DMEM (MDA-MB-231 cells and 3T3 cells) and RPMI (HCC-1143, HCC-1937 cells) media with 10 % FBS. DOXNP and free DOX were added into the cells at different concentrations for 24 h, 48 h, 72 h, 96 h in triplicates and cell viability of the DOXNP and DOX was assessed by alamar blue assay.

3.5.11. Mechanism of Internalization of DOXNP

For mechanism of internalization MDA-MB-231 cells were seeded with seeding density of 50,000 cells per well in 24 well plate and incubated overnight at 37 °C. The cells were incubated with different endocytosis inhibitors namely filipin (5 µg/ml), pitstop-2 (12 µg/ml), and Ethylisopropyl amiloride (EIPA) (15 µg/ml) to inhibit caveolae-dependent endocytosis, clathrin-dependent endocytosis and micropinocytosis for 30 min and then incubated with DOXNP (final concentration 3 µg/ml) for 2 h. The cells were washed twice with PBS and detached with trypsin. Then cells were washed twice using 1% BSA/PBS and centrifuged at 400 rpm for 5 min at 4 °C. The cells were analysed using Apogee A50-Micro Flow Cytometer and FlowJo was used for data analysis.

3.5.12. Western Immunoblotting Assay

Cells were exposed to DOX or DOXNP for 24 h and harvested 24 h later. Cell lysates were fractionated by SDS–polyacrylamide gel electrophoresis and blotted onto nitrocellulose sheets. Blots were pre-blocked in phosphate-buffered saline containing 5% (w/v) dried nonfat milk and incubated overnight at 4 °C with antibodies γ-H2AX (Millipore) and β-actin (AbCam).

3.5.13. Laser Scanning Confocal Microscope Imaging

The Cells incubated with DOX and DOXNP were imaged using Nikon A1R confocal microscope with a 60× 1.4NA oil immersion objective. For the cellular imaging MDA-MB-231 cells were seeded with seeding density of 20,000 cells per well in DMEM media with 10 % FBS were incubated with the DOXNP and DOX for different incubation times. Then for each sample the media was removed after the desired time, cells were washed 3 times with PBS and fixed with 4 % paraformaldehyde for 10 min. After washing 3 times again the cells were permeabilized with 0.1 % TritonX-100 (in PBS) for 5 min and washed again with PBS and Blocked for 1 hour with 1 % BSA solution in PBS. The samples were then incubated with primary antibody namely rabbit anti-Tom20 for Mitochondria staining, rabbit anti-ERp72 for Endoplasmic Reticulum staining, rabbit anti-GM130 for Golgi staining, rabbit anti-α/β Tubulin staining followed by AF 647 goat anti-rabbit conjugate secondary antibody. For F-Actin staining AF488 conjugate of Phalloidin was used.

3.5.14. Stochastic Optical Reconstruction microscopy

The DOXNP were dual labelled using NHS Alexa 488 and NHS Alexa 647. Both the dyes were incubated with DOXNP solution (1mg /ml of sodium bicarbonate buffer pH=9) and solution was stirring for 2 h. After 2 h incubation the mixture was centrifuged, and particles were washed 3 times before STORM imaging.

The MDA-MB-231 cells with seeding density 20,000 per well in 8-well Lab-Tek chamber slide were seeded at 37 °C in DMEM media with 10 % FBS. The cells were transfected with DOXNP (3 µg/ml) for 2-24 hrs. For intracellular trafficking the particles were removed after 2 h and were kept at 37 °C for 5 h, 8 h and 24 h in fresh media. At different times cells were fixed, permeabilized and blocked. After this cell were incubated with

rabbit anti-EEA1 monoclonal antibody (2 µg/ml), rabbit anti-Rab7 monoclonal antibody (2µg/ml), rabbit LAMP-1 (1 µg/ml) for 1.5 h followed by 3 time washing with PBS and further incubation for 1 h with dual labelled Alexa Fluoro 555/647 goat anti-rabbit conjugate secondary antibody (2 µg/ml). The mitochondria staining was carried out using Rabbit Tom20 primary antibody followed by Alexa Fluoro 555/647 goat anti-rabbit conjugate secondary antibody.

STORM images were aquired using Nikon N-STORM system equipped with Nikon 100X 1.4 NA oil immersion objective. The focus and TIRF (total internal reflection fluorescence imaging) angle were adjusted to obtain high signal to noise ratio. The 488, 561 and 647 lasers were for used for excitation of the fluorophores. All time lapses were recorded onto a 256 pixel × 256-pixel region using an EMCCD camera. For each channel, 3000–5000 frames were sequentially acquired.

3.5.15. DNA interaction study

To favor DOXNP dissolution in dimers, DOXNP were diluted in water at concentration of 2-200 ng/µL and left at room temperature for 24 h in the dark. pBleuscript DNA plasmid (11.65 ng/µL, e.g. 233 ng/sample) was incubated with dissolved DOXNP or DOX at different concentrations (0.05, 2.5, 5, 25 ng/µL; ratio DNA/compound: 233; 4.6; 2.33; 0.46) in PBS 0.5X at 37°C for 2h. Ethidium bromide (a potent DNA intercalator) at concentration of 25 ng/µL was used as positive control. Samples were run on 1% agarose gel in absence of ethidium bromide. Image was acquired following ethidium bromide staining

3.5.16. Reactive oxygen species detection

Intracellular ROS production was determined in MDA-MB 231 cells using Cellular Reactive Oxygen Species Detection Assay Kit (Deep Red Fluorescence) (AbCam)

according to manufactured protocol. Briefly, cells (8×10^5) were plated into T-25 flasks and 24 h later incubated for 24 h with 0.2 µg/ml DOXNP in presence or absence of 100 µM N-acetyl cysteine or vitamin C. Under low light conditions, ROS-specific detection probe was added and incubated for 60 min at 37°C. Cells were harvested, transferred to foil-wrapped tubes and immediately analyzed by flow cytometry.

3.6. References

1. Hess, B., C. Kutzner, D. Van Der Spoel, and E. Lindahl, *GROMACS 4: algorithms for highly efficient, load-balanced, and scalable molecular simulation.* Journal of chemical theory and computation, 2008. **4**(3): p. 435-447.
2. Berendsen, H.J., J.P. Postma, W.F. van Gunsteren, and J. Hermans, *Interaction models for water in relation to protein hydration*, in *Intermolecular forces*. 1981, Springer. p. 331-342.
3. Schüttelkopf, A.W. and D.M. Van Aalten, *PRODRG: a tool for high-throughput crystallography of protein–ligand complexes.* Acta Crystallographica Section D: Biological Crystallography, 2004. **60**(8): p. 1355-1363.
4. Oostenbrink, C. and W.F. van Gunsteren, *Free energies of binding of polychlorinated biphenyls to the estrogen receptor from a single simulation.* Proteins: Structure, Function, and Bioinformatics, 2004. **54**(2): p. 237-246.
5. van Gunsteren, W.F., S.R. Billeter, A.A. Eising, P.H. Hünenberger, P. Krüger, A.E. Mark, W.R. Scott, and I.G. Tironi, *Biomolecular simulation: the {GROMOS96} manual and user guide.* 1996.
6. Konai, M.M., S. Samaddar, G. Bocchinfuso, V. Santucci, L. Stella, and J. Haldar, *Selectively targeting bacteria by tuning the molecular design of membrane-active peptidomimetic amphiphiles.* Chemical Communications, 2018. **54**(39): p. 4943-4946.
7. Farrotti, A., P. Conflitti, S. Srivastava, J.K. Ghosh, A. Palleschi, L. Stella, and G. Bocchinfuso, *Molecular Dynamics Simulations of the Host Defense Peptide Temporin L and Its Q3K Derivative: An Atomic Level View from Aggregation in Water to Bilayer Perturbation.* Molecules, 2017. **22**(7): p. 1235.
8. Bocchinfuso, G., P. Conflitti, S. Raniolo, M. Caruso, C. Mazzuca, E. Gatto, E. Placidi, F. Formaggio, C. Toniolo, and M. Venanzi, *Aggregation propensity of Aib homo-peptides of different length: an insight from molecular dynamics simulations.* Journal of Peptide Science, 2014. **20**(7): p. 494-507.
9. Bussi, G., D. Donadio, and M. Parrinello, *Canonical sampling through velocity rescaling.* The Journal of chemical physics, 2007. **126**(1): p. 014101.
10. Berendsen, H.J., J.v. Postma, W.F. van Gunsteren, A. DiNola, and J. Haak, *Molecular dynamics with coupling to an external bath.* The Journal of chemical physics, 1984. **81**(8): p. 3684-3690.
11. Hess, B., H. Bekker, H.J. Berendsen, and J.G. Fraaije, *LINCS: a linear constraint solver for molecular simulations.* Journal of computational chemistry, 1997. **18**(12): p. 1463-1472.

12. Essmann, U., L. Perera, M.L. Berkowitz, T. Darden, H. Lee, and L.G. Pedersen, *A smooth particle mesh Ewald method.* The Journal of chemical physics, 1995. **103**(19): p. 8577-8593.
13. Humphrey, W., A. Dalke, and K. Schulten, *VMD: visual molecular dynamics.* Journal of molecular graphics, 1996. **14**(1): p. 33-38.
14. Pettersen, E.F., T.D. Goddard, C.C. Huang, G.S. Couch, D.M. Greenblatt, E.C. Meng, and T.E. Ferrin, *UCSF Chimera—a visualization system for exploratory research and analysis.* Journal of computational chemistry, 2004. **25**(13): p. 1605-1612.

Chapter 4

A Simple One-step Ultrasonic Route to Synthesize Antioxidant molecules and Fluorescent Nanoparticles from Phenol and Phenol-like Molecules

ACS *Sustainable Chemistry and engineering* 2017, 5,6081-6089

This chapter reports that acoustic cavitation could promote polymerization of simple phenolic molecules to generate bioactive oligomers and nanostructures with varying functional properties without the use of enzymes, metal catalysts or other toxic reagents. It was demonstrated that the cavitation bubble surface acted as a catalytic binding site for oxidative coupling reactions among phenolic molecules and the ultrasonic frequency, concentration, and other physicochemical properties of phenolic building blocks can affect the formation of oligomers.

ACS Sustainable Chemistry & Engineering

Research Article

pubs.acs.org/journal/ascecg

A Simple One-Step Ultrasonic Route To Synthesize Antioxidant Molecules and Fluorescent Nanoparticles from Phenol and Phenol-Like Molecules

Sukhvir Kaur Bhangu,[†] Muthupandian Ashokkumar,*[,†] and Francesca Cavalieri*[,‡,§]

[†]School of Chemistry, University of Melbourne, Parkville, VIC 3010, Australia

[‡]Department of Chemical and Biomolecular Engineering, University of Melbourne, Parkville, VIC 3010, Australia

[§]Dipartimento di Scienze e Tecnologie Chimiche, Universita' degli Studi di Roma "Tor Vergata", via della Ricerca Scientifica 1, 00173 Roma, Italy

Supporting Information

ABSTRACT: Fluorescent oligomeric structures were synthesized from the phenolic moieties by a simple one-step sonochemical approach without the use of enzymes, metal catalyst, or other toxic reagents. The formation of phenol dimers, trimers, and oligomers was confirmed by absorption spectroscopy, fluorescence spectroscopy, HPLC, and mass spectroscopy. We have demonstrated that the cavitation bubble surface acted as a catalytic binding site to generate such oligomers, and the ultrasonic frequency, concentration, and other physicochemical properties (surface activity) of phenolic building blocks can affect the formation of these oligomers. The sonochemically produced phenolic oligomers showed antioxidant activity which was determined by DPPH assay. The study suggests that acoustic cavitation could promote polymerization of simple phenolic molecules to generate bioactive oligomers and nanostructures with varying functional properties.

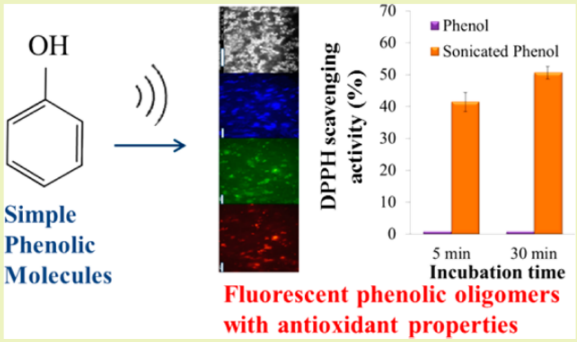

KEYWORDS: *Acoustic cavitation, Phenol oligomers, Antioxidant, Fluorescent nanostructures*

INTRODUCTION

The polymerization of phenolic moieties to generate polyphenolic structures has received much attention recently due to their applications in biomedicine, food industry, dyes, formation of plastics, etc.[1−5] Different catalytic methods including enzymatic reactions have been used for the polymerization of these moieties. For example, horseradish peroxidase (HRP) has been used to polymerize 3-methylcatechol, which has applications in germanium recovery.[2] The proposed mechanism involved the generation of radicals by HRP and H_2O_2, transfer of radicals to the monomer, polymerization of the monomer, and ultimately precipitation of the polyphenols. Heat-induced oxidative coupling was carried out to assemble green tea polyphenol using copper(II) as catalysts.[3] In addition, an oxidative coupling reaction using $AgNO_3$ under microwave irradiation was used to synthesize metal−tea polyphenol nanoparticles.[4]

The oxidation of phenol has gained attention due to the use of its oxidative products (catechol, hydroquinone) in various applications such as in dyes, perfumes, rubber, medicine, etc.[5] Polymerization of phenol by using peroxidase catalysis has been carried out with different techniques; for example, soybean peroxidase along with H_2O_2 was used to carry out the oxidative polymerization of phenol.[6,7] Use of copper ions and copper complexes as catalysts has also been employed in the polymerization of phenol.[7,8] Enzymatic polymerization of phenol using templates like poly(ethylene glycol) and poly(ethylene glycol) monododecyl ether has been carried out to synthesize a soluble polyphenol-poly(ethylene glycol) complex.[9−11]

Previously, a significant amount of work has been reported on the sonochemical degradation of phenol.[12−15] None of these studies reported the formation of dimers, trimers, or oligomers of phenol as the focus of these studies was the degradation of phenol and they just monitored the reduction in the concentration of phenol. Also, these previous studies have reported on the degradation of phenol and formation of a few intermediate species such as catechol, hydroquinone, 1,4-benzoquinone, and 1,2-benzoquinone which also ultimately degraded on continuous sonication.[16] These studies have not focused on the coupling reaction of phenol mediated by ultrasound irradiation to synthesize new building blocks and nanostructures.

Received: March 30, 2017
Revised: May 26, 2017
Published: June 8, 2017

DOI: 10.1021/acssuschemeng.7b00966
ACS Sustainable Chem. Eng. 2017, 5, 6081−6089

A recent study has reported that ultrasound can be utilized for oxidative coupling reactions of complex molecules.[17] It has been shown that the sonication of BTEE (N-Benzoyl-L-Tyrosine Ethyl Ester) led to the formation of nanoparticles and polymerized products.[17] We have demonstrated that the reactive and oscillating surface of acoustic cavitation microbubbles acts as a catalytic binding site for the coupling of surface active biomolecules bearing tyrosine moieties at the gas−liquid interface. We first observed that only complex molecules such as hydrophobically modified tyrosine can be used for this process, whereas no oxidative coupling was observed with hydrophilic tyrosine. However, this study shows that under certain experimental conditions even simpler and less hydrophobic molecules can form oligomers using high frequency ultrasound.

The aim of the current study is to develop a fundamental knowledge on the ultrasonic coupling of phenolic moieties starting with a simple system, phenol, to identify the critical reaction parameters to obtain nanoparticles. The main scientific questions we aim to answer are whether oligomeric structures could be generated with simple molecules containing a phenolic moiety. Should the precursor molecules possess specific properties to form oligomers and subsequent assembly into nanoparticles? In order to answer these questions, we have studied the effect of high frequency ultrasound (355 kHz and 1058 kHz) on the simple molecule phenol under different experimental conditions. A comprehensive characterization of the sonicated products was performed to monitor the formation of higher molecular weight species. We identified the experimental conditions that lead to the formation of phenolic oligomeric structures when a simple molecule such as phenol is sonicated. We have also noticed that these oligomeric structures self-assemble to form antioxidant nanoparticles. Thus, high frequency ultrasound can be used to polymerize different phenolic moieties leading to the formation of complex structures with new functional properties.

EXPERIMENTAL SECTION

Materials. Phenol (99.5%), disodium hydrogen orthophosphate (98%), and sodium dihydrogen orthophosphate (99%) were purchased from Chem-Supply. Catechol (≥99%), hydrogen peroxide (35 wt % of H_2O_2), 2,2′-biphenol, 1-diphenyl-2-picrylhydrazyl (DPPH), p-benzoquinone (≥98%), and tyrosine were purchased from Sigma-Aldrich. Iron(II) chloride tetrahydrate was purchased from Fluka. Hydroquinone was purchased from BDH AnalaR. HPLC grade methanol (99.9%) was purchased from Fisher chemicals. All solutions were prepared in high purity water extracted from a Millipore system with resistivity of 18.2 MΩ/cm.

Ultrasonic Treatment of Phenol and Phenolic Molecules. Sonication of 0.5 mM phenol (12 mL) in PBS (pH 7) was carried out in a 15 mL sealed glass vial. This glass vial was mounted over the sonication bath containing 200 mL of water. This water bath was a double-walled glass cell, the base of which was mounted on a stainless steel ultrasonic plate transducer of with a diameter of 5.4 cm. The plate transducer used was an ELAC Nautik USW 51-052 transducer which was powered by T&C Power Conversion, Inc. The unit was operated at 355 and 1058 kHz frequencies and 60 W acoustic power. All the reactions were performed at a constant temperature of 37 ± 2 °C. The reaction was studied as a function of sonication time. The hydrogen peroxide and correlated OH radicals yield were determined by the previously reported Weissler method.[17] To ascertain the role of ultrasound, phenol oxidation was also carried out via a Fenton reaction where to 30 mL of a 0.5 mM phenol solution was added 1.5 mg of solid $FeCl_2$ to give a 0.25 mM solution followed by the addition of 10 μL of 1.02 mM H_2O_2 every 5 min to generate a radical concentration of 1.02 mM per hour, which was equal to the amount of radicals produced by sonication in an hour.

An antioxidant test was carried out using the DPPH (1-diphenyl-2-picrylhydrazyl) method. A DPPH solution of concentration 250 μM was prepared in an ethanol:water (50:50 v/v) mixture. Here, 2 mL of sonicated phenol and unsonicated phenol were incubated with 3 mL of the DPPH solution for 30 min, and the absorbance was noted at 520 nm. The radical scavenging activity was determined using following expression:

$$\text{Radical scavenging activity (\%)} = [(A_{\text{DPPH}} - A_{\text{sample}})/A_{\text{DPPH}}] \times 100$$

where A_{DPPH} is the absorbance of the blank DPPH solution and A_{sample} is the absorbance of the DPPH solution after addition of the sample.

Characterization. Sonicated phenol solutions were analyzed using fluorescence spectroscopy, HPLC, LC-MS, and absorption spectroscopy. A PerkinElmer AxION 2 ToF quadrupole mass spectrometer was used for performing mass analysis. Scans were performed in both negative and positive ion modes. A gradient elution was carried with solvent A (0.1% formic acid) and solvent B (acetonitrile with 0.1% formic acid) at 30 °C. The LC gradient used was from 10% to 90% solvent B in 20 min and was held for 5 min at 90% solvent B and then from 90% solvent B to 10% solvent B in 5 min. The flow rate was 0.3 mL min^{-1}, and the injection volume was 50 μL. Shimadzu SCL-10AVP high-performance liquid chromatography (HPLC) equipped with a Phenomenex column model Jupiter 5u C18 300A and with a UV detector set at 220 nm was used to perform HPLC analysis. All chromatograms were generated by LabSolution software (Shimadzu). The injection volume was 20 μL, and the flow rate used was 1 mL min^{-1} with a methanol:water (35:65) mixture used as an eluent. Fluorescence spectra were obtained using a Shimadzu RF-5301PC fluorescence spectrophotometer (Shimadzu) equipped with a xenon lamp and 1.0 cm optical length quartz cell. All measurements were carried out in PBS buffer (pH 7). Samples were excited at different wavelengths, and the fluorescence spectra were recorded from 340 to 600 nm using a slit width of 5 nm for excitation and 10 nm for emission spectra. UV−visible absorption spectra were recorded on a Cary Bio 50 UV-spectrophotometer. The morphology of the particles was examined by a high-resolution field emission environmental scanning electron microscope (Quanta 200 FEI). The particles were sputter-coated with a thin layer of gold during the sample preparation.

RESULTS AND DISCUSSION

Spectroscopic Properties of Sonicated Phenol. Sonication of an aqueous solution under certain experimental conditions leads to the generation of hydroxyl radicals, with localized high temperatures and pressures by means of acoustic cavitation.[17−20] As mentioned in the Introduction, the current investigation is focused on expanding the fundamental knowledge on ultrasonic generation of oligomers and nanostructures from simple phenols. High frequency (355 and 1058 kHz) sonication of 0.5 mM phenol was performed in a phosphate-buffered saline solution at pH 7 up to 6 h. The absorption spectra (Figure S1, Supporting Information) of a 0.5 mM phenol solution acquired as a function of sonication time shows an absorption band in the range of 250−300 nm, with characteristics of $\pi-\pi^*$ electronic transitions in phenolic compounds.[21,22] With an increase in sonication time, a new band centered around 330 nm which increases in intensity was also observed. An increase in the absorption intensity, in particular, beyond the UV region, may be associated with the formation of conjugated aromatic structures as a result of sonochemical polymerization. It was also reported previously that an increase in absorption intensity in the wavelength range of 300−800 nm may indicate the extended degree of

DOI: 10.1021/acssuschemeng.7b00966
ACS Sustainable Chem. Eng. 2017, 5, 6081−6089

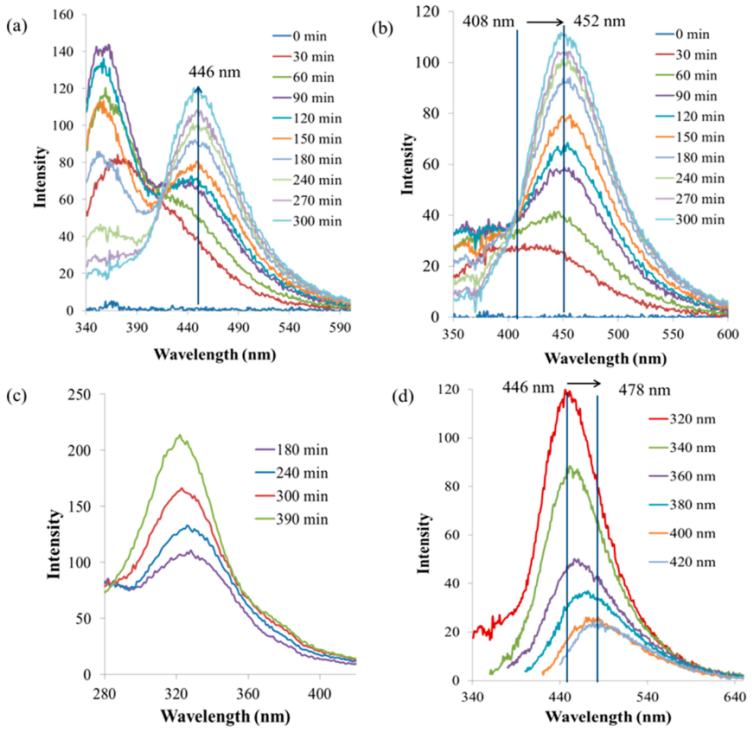

Figure 1. Fluorescence emission spectra of sonicated 0.5 mM phenol solution at 355 kHz 60 W in PBS pH 7. (a) Emission spectra of the polymerized phenol at λ_{ex} = 320 nm. (b) Emission spectra of the polymerized phenol at λ_{ex} = 330 nm. (c) Excitation spectra of 0.5 mM phenol solution as a function of sonication time at λ_{em} = 450 nm. (d) Dependence of emission spectra of final products on the excitation wavelength.

polymerization of phenol when chemically oxidized by horseradish peroxidase and by oxygen at elevated pH.[22,23]

Additionally, to gain further insight into the formation of oligomers during sonication, fluorescence spectroscopic analysis was carried out. It is known that phenol has no fluorescence in the wavelength range of 340−600 nm,[24] whereas dityrosine and phenolic dimers exhibit fluorescence in this range due to the conjugated system and the phenolate form of the excited singlet state.[17,25,26] Figure 1 shows the fluorescence spectra of sonicated phenol solutions as a function of sonication time, measured at pH 7 in a PBS buffer solution. It is shown from the spectra (Figure 1) that (i) a fluorescent species exhibiting an emission peak at 360−370 nm is formed after 30 min of sonication (Figure 1a), (ii) upon sonication the peak at 360 nm decreases with the concomitant increase of a second peak at 446 nm indicating the conversion of one species to another (Figure 1a), (iii) conversion of one species to another can also be observed from the Figure 1b when fluorescent emission spectra of products were obtained at λ_{ex} = 330 nm, (iv) the excitation spectra of the sonicated phenol at emission wavelength of 450 nm shows accordingly a peak at approximately 330 nm and an increase in the intensity with increasing sonication time (Figure 1c) which is consistent with the absorption spectra (Figure S1, Supporting Information), (v) the dependence of the emission peak (red-shift) of the final products at around 446−478 nm on the excitation wavelength (Figure 1d) suggests that multiple species are responsible for the overall fluorescence.

These results are consistent with the previous report on BTEE sonication where shift in the wavelength was observed with increasing sonication time indicating the formation of different oligomeric species. However, in this case, the spectroscopic properties of phenol allow us to clearly identify a peak at 360−370 nm that can be attributed to the dimer which can also be correlated to 2,2′-biphenol (Figure S2, Supporting Information) and which on further sonication gives rise to the formation of oligomers. While these results may indicate the formation of fluorescent dimers and oligomeric phenols, other possible reactions should not be ruled out. As mentioned earlier, sonication of phenol leads to the formation of different aromatic products such as hydroquinone, catechol, p-benzoquinone, pyrogallol, and resorcinol.[16,27] To confirm that the observed fluorescence was not due to catechol, hydroquinone, and benzoquinone, fluorescence spectra of these compounds were recorded. It was observed that these compounds do not have any fluorescence in the spectral range 350−600 nm. Therefore, it is speculated that the fluorescence observed from sonicated phenol solution at 446 nm is due to dimeric and oligomeric products formed during sonication.

We have also investigated the effect of pH on the ultrasonic oligomerization of phenol at pH ranging from 3 to 7 to prevent the possible oxidation of catechol and quinone by air (oxygen). It is known that catechol and the other oxidation products can spontaneously polymerize at basic pH in the presence of oxygen, without the assistance of ultrasound.[22] We observed a higher oligomerization yield using a phosphate buffer solution at neutral pH (Figure S3).

HPLC and Mass Spectrometry Analysis of Sonication Phenol. In order to get further support for the formation of oligomeric structures, chromatographic analysis of the sonicated solutions was carried out. Figure 2 shows the HPLC data of the sonication phenol, which indicates the formation of various products. By comparing the elution peaks

DOI: 10.1021/acssuschemeng.7b00966
ACS Sustainable Chem. Eng. 2017, 5, 6081−6089

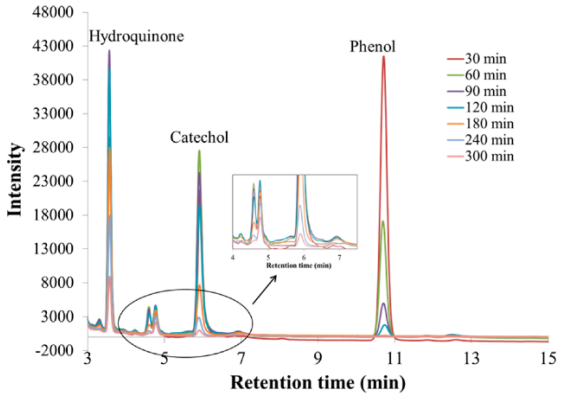

Figure 2. HPLC data of 0.5 mM phenol solution with increasing sonication time.

with reference standards, the peaks at retention times 3.5, 4.8, 5.8, and 10.7 min are ascribed to hydroquinone, p-benzoquinone, catechol, and phenol, respectively. The amount of phenol continuously decreased during the sonication. On the other hand, the amount of catechol and hydroquinone increased within 90−120 min of sonication and then started to decline. This may be due to the conversion of these species to various degraded products and to the higher molecular weight species. Some less intense peaks at retention times 4.5 and 7 min were observed, possibly due to the dimeric species as they follow the same trend observed in Figure 1a.

The presence of the more hydrophobic oligomers was verified on the 5 mM phenol solution sonicated for 5 h. The HPLC chromatogram (Figure S4, Supporting Information) shows peaks between 12 and 30 min retention times which were attributed to the oligomeric species. These results confirm that the all the intermediate products formed from the phenol could led to the formation of dimers, trimers, and oligomers.

To substantiate the claim that oligomers of phenol were produced due to sonication, mass spectrometric analysis was performed. Figure 3 shows the mass spectrum of the sonication of phenol after 3 h. It is shown that a number of dimers, trimers, and oligomers of phenol were obtained. Table 1 summarizes the different products obtained which include catechol, hydroquinone, and their dimers and trimers. Therefore, it is evident from the mass spectrometric analysis as well

Table 1. Different Possible High Molecular Weight Products Deduced from MS

m/z	possible dimer, trimer, or oligomer formed
109	catechol and hydroquinone
217	dimers of catechol/hydroquinone
337	trimer of 2 benzoquinone and catechol/hydroquinone + OH
359	trimer of catechol/hydroquinone + 2 OH
417	tetramer of phenol + 3 catechol/hydroquinone
457	tetramer of catechol/hydroquinone + Na
599	hexamer of 3 phenol + 2 catechol + p-benzoquinone
621	hexamer of 3 phenol + 2 catechol + p-benzoquinone + Na

that sonication of simple phenolic moieties can also give rise to the formation of different high molecular weight species.

Overall the analytical data presented in Figures 1−3, Figures S1−S4 (Supporting Information), and Table 1 strongly suggest the formation of hydroxylated phenolic dimer and oligomers. Previous studies on ultrasonic degradation of phenols have only suggested the formation of hydroxylated phenols as reaction intermediate species leading to degradation and formation of small molecular weight products, i.e., maleic acid, oxalic acid, formic acid, succinic acid, etc.[12−15,28] However, the formation of higher molecular weight oligomeric species has not been given much attention. From the above results, it is clear that apart from degradation of phenol, sonication leads to the formation of fluorescent dimeric and oligomeric species with new optical and functional properties.

Possible Mechanism for Formation of Dimers and Oligomers. Prior to providing further discussion, first, let us consider a possible mechanism for the sonochemical formation of dimeric and oligomeric structures. Ultrasound under specific experimental conditions, such as used in the current study, generates acoustic cavitation, which is the growth of bubble nuclei and violent collapse of bubbles after reaching a specific size range. The collapse of a cavitation bubble leads to the generation of very high temperatures (>5000 K) and pressures (>1000 atm) within the bubble. As a consequence of these extreme conditions, a variety of reactive radicals and molecular products such as H, OH, OOH radicals, H_2O_2, etc. are generated in air-saturated aqueous solutions. Scheme 1 shows schematics of a possible mechanism for the formation of dimeric species from phenol by sonication. OH/H radicals, generated as a result of sonication, would abstract hydrogen from the phenol to give phenoxy radical at ortho, meta, or para

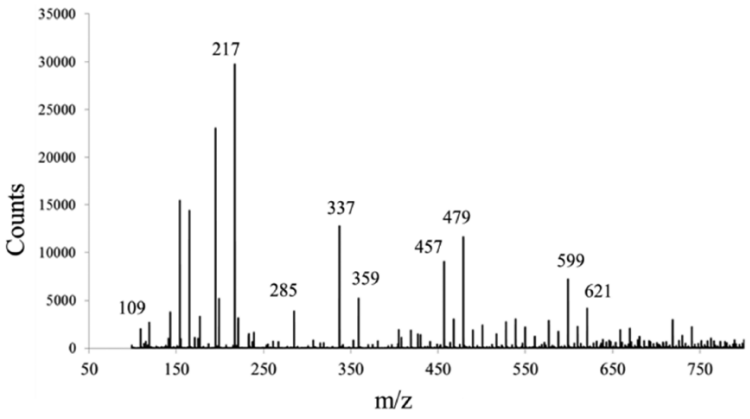

Figure 3. Mass spectrum of 0.5 mM phenol solution after 3 h of sonication at 355 kHz.

DOI: 10.1021/acssuschemeng.7b00966
ACS Sustainable Chem. Eng. 2017, 5, 6081−6089

Scheme 1. Possible Reaction Mechanism for Formation of Oligomeric Products

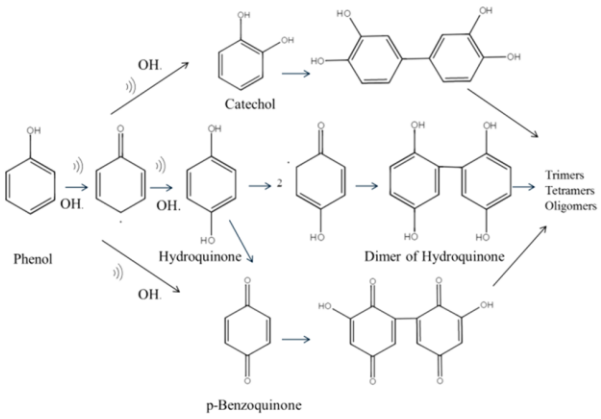

positions. Then, the OH radical will combine with the phenoxy radical to form catechol, hydroquinone, and p-benzoquinone. In addition, it is possible that two phenoxy radicals combine to form a dimeric species (hydroxylated biphenyls). The continuation of H-abstraction followed by radical formation leads to the formation of different dimeric and oligomeric products.

Considering the proposed mechanism above, OH radicals seem to be primarily responsible for the formation of oligomeric products. If that was true, oligomeric structures should be formed when OH radicals are generated by other means, such as Fenton's reaction. In order to see if oligomeric structures could be formed by Fenton's reaction, further experiments were carried out. During Fenton's reaction, Fe(II) is oxidized to Fe(III) by H_2O_2 with simultaneous formation of hydroxyl radicals and hydroxide ions.[29] Figure S5 in the Supporting Information shows the fluorescence emission spectra of a sonicated phenol solution and the product obtained as a result of Fenton's reaction of phenol (in the absence of sonication) after 2 h. Results show that the generation of a similar quantity of OH radicals (1.02 mM/h as generated during sonication) by Fenton's reagent (0.25 mM $FeSO_4$) did not produce fluorescent species similar to those generated by sonication. This suggests that OH radicals alone are not responsible for the formation of phenolic oligomeric species, and additional factors are involved in this process.

It was suggested in our previous report that the formation of oligomeric species occurs at the "hot" cavitation bubble surface which acts as a catalytic binding site.[17] The catalytic coupling of a phenoxy radical at the bubbles−solution interface implies that the aromatic molecules approach each other prior to their oxidation and coupling. Phenol is a surface-active molecule[30] due to the phenyl ring, and hence, it adsorbs at the cavitation bubble surface. When cavitation bubbles collapse, the bubble surface reaches a higher temperature (of the order of a few hundred degrees).[20] When OH radicals attack phenol at the bubble solution interface, as shown in the proposed mechanism, the higher temperature and shear forces may promote coupling reactions leading to the formation of oligomeric species. The coupling among phenol and catechol rings can take place through C−C or C−O−C links.

To gain further insight into the involvement of the cavitation bubble surface as a catalytic binding site, further experiments were carried out by varying the acoustic frequency (20 kHz and 1 MHz) and power. It is known that the amount of OH radicals and bubble temperature generated are influenced by ultrasonic frequency and power. With an increase in the ultrasonic frequency, the number of antinodes and hence the number of cavitation bubbles increase and their size decreases.[20] It was reported that the radical yield increases with an increase in ultrasonic frequency, reaching a maximum around 300−500 kHz and then decreases with a further increase in the frequency.[20,31] A study dealing with the OH radical yield at different frequencies (20, 358, and 1062 kHz) demonstrated that the OH radical yield was highest at 358 kHz. This is due to the fact that the bubble temperature generated at higher frequencies is relatively low and the amount of water vapor that can evaporate into the bubble during the expansion phase[20,31] of the acoustic cycle is also relatively low, and hence, the OH radical yield is relatively lower at 1 MHz despite an increase in the number of bubbles.

When the reaction was carried out at 20 kHz, no fluorescent dimers and oligomers were formed as the OH radical yield was very low. Interestingly, when the reaction was carried out at 1 MHz, where the OH radical yield is less than that observed at 355 kHz, only the fluorescent dimer emitting at ~390 nm was obtained (Figure 4). If the formation of oligomeric phenolic

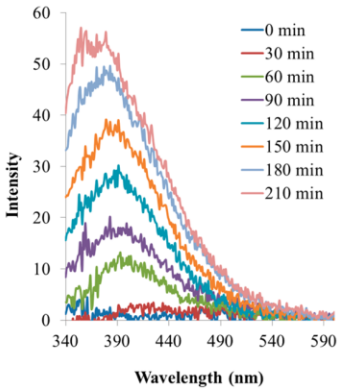

Figure 4. Fluorescence emission spectra of 0.5 mM phenol sonicated at 1 MHz at 60 W as a function of sonication time.

species just depends on the hydroxyl radical yield, we should be able to observe a similar spectral pattern for both 355 kHz and 1 MHz with just a decrease in the intensity of the fluorescence signal. However, the acoustic cavitation of the bubble oscillating at 1 MHz generates only phenolic dimers. This result confirms our previous finding that faster oscillation of cavitation bubbles produced at 1 MHz before collapse is less effective in collecting phenolic molecules at an air−liquid interface depending on their diffusion coefficient.[17]

It is reported that chemically active stable cavitation bubbles within the ultrasonic frequency range from 200 kHz to 1 MHz exist for about 0.3−0.1 ms,[32] and the cavitation bubbles oscillate at a faster speed at 1 MHz than 355 kHz. As phenol is a small molecule, it has sufficient time to diffuse, absorb, and react at the interface of a 1 MHz oscillating bubble to form dimers. However, dimeric species cannot reach the interface before the bubbles collapse. Consequently, the formation of other oligomeric species was not observed.

Finally, the effect of ionic strength on the ultrasonic coupling reaction of phenolic was explained. It is worth noting that all the reactions reported in the current study were carried out in

DOI: 10.1021/acssuschemeng.7b00966
ACS Sustainable Chem. Eng. 2017, 5, 6081−6089

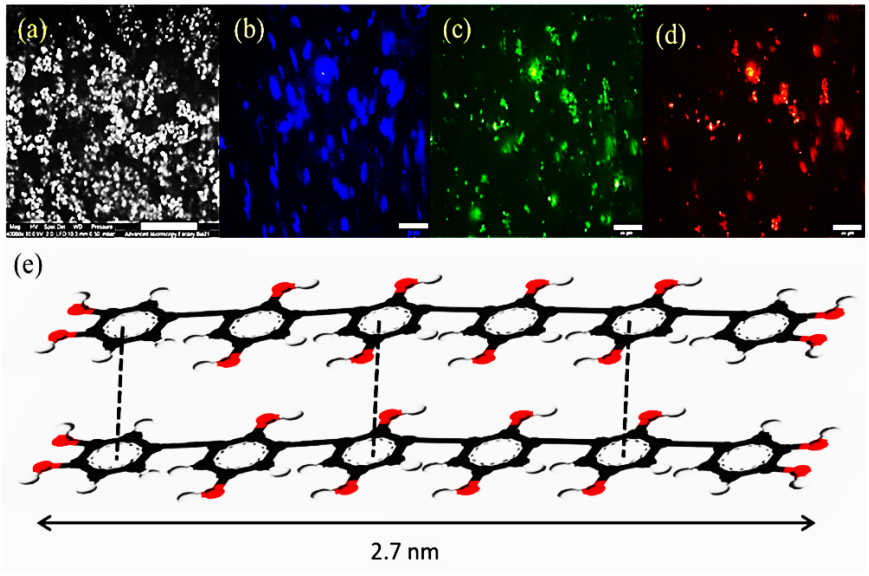

Figure 5. (a) SEM image of the phenol (10 mM) sonicated with 355 kHz at 60 W for 5 h (scale bar = 2 μm). (b–d) Fluorescence microscopy image of the sonicated phenol particles (10 mM) showing blue, green, and red emission, respectively (scale bar = 20 μm). (e) Structure of phenolic oligomers stacked together by $\pi-\pi$ interactions.

PBS, whereas in the previous study BTTE sonication was carried out in water. As mentioned earlier, surface activity of the phenolic molecule is an important factor for the molecules to be adsorbed and react on the air–liquid interface of the cavitation bubble. The efficiency of phenol dimerization and the oligomerization reaction was reduced to a large extent (83% less) when sonication was performed in water instead of a PBS buffer. This can be correlated to the surface tension of the solution. It is well known that the surface tension of aqueous phenol solution decreases in the presence of salts due to increased surface activity of phenol.[30] The presence of salt lowers the surface tension, and more phenol molecules adsorb on the surface enhancing the yield of dimeric and oligomeric species. In conclusion, to answer the first question, simple phenolic molecules such as phenol can generate phenolic oligomers by sonication provided that the molecules have certain surface activity which can be improved by ionic strength. However, in contrast to the previous study on more hydrophobic BTEE oligomers,[17] we were unable to obtain nanoparticles at a low concentration (0.5 mM) of phenol. A higher concentration of sonicated phenol (10 mM) was required to produce higher molecular weight oligomers that can aggregate by $\pi-\pi$ stacking, leading to the formation of nanoparticles having sizes between 90 and 150 nm. Nanoparticles were found to be soluble in methanol and alkaline solution (pH 10) which means that the $\pi-\pi$ stacking interactions are the driving force for the formation of oligomeric nanoparticles. The electrostatic repulsion between different phenolate aromatic moieties and the interaction between organic solvent and solute molecules can lead to the dissolution of aggregated oligomeric particles to the soluble phenolic oligomers. Hence, self-assembly of phenolic oligomers into nanoparticles upon sonication is highly dependent on the solubility and molecular weight of the amphiphilic species formed during sonication. Figure 5a shows the SEM image of obtained nanoparticles. Fluorescence microscopic images (Figure 5b–d) show that particles have blue, green, and red emissions which were also confirmed by fluorescence spectroscopy and are discussed in the following section. The composition of the nanoparticles after dissolution was tested using the mass spectroscopy, and the number of high molecular weight oligomers ranging from m/z = 200 to 1200 were observed corresponding approximately to 12 phenolic units (Figure S6). Short and partially charged oligomers (oligomers have a phenolic pK_a near 7) can organize themselves in elongated conformations (Scheme 1 and Figure 5e). An end-to-end estimated distance for the elongated oligomers can be approximately 3 nm for 6-phenol units. These units can stack together to form nanostructures with $\pi-\pi$ interactions (Figure 5e). The distance between the different stacked units could be speculated to be around 3.5–3.7 Å depending on the type of interaction.

Optical and Fluorescence Properties of Oligomeric Phenol Nanoparticles. Optical properties of the phenolic nanoparticles were further studied and compared with the fluorescence properties of the soluble phenolic oligomers. Figure 6a shows the fluorescence emission spectra of the phenol oligomeric nanoparticles, and it is observed that besides emission in the spectral range of 340–500 nm additional bands centered at 588 and 668 nm were observed when excited at 540 and 600 nm, respectively. The excitation spectrum shows peaks at 553 nm (Figure 6b) and 590 nm (Figure 6c) corresponding to emission bands observed at 588 and 668 nm, respectively.

Red emission of the nanoparticles was also confirmed by fluorescence microscope image of the particles (Figure 5c). However, emission bands between the spectral range of 550–700 nm completely disappeared when particles were dissolved in the alkaline solution, whereas fluorescence from the soluble oligomers was observed (Figure 6d).

This again provides evidence for $\pi-\pi$ stacking interactions between the aromatic phenolate moieties of oligomers, which can reduce the ground and excited state energy leading to new red-shifted emissive bands.[17,33] It has been reported that green emission in green fluorescent proteins (GFP) was red-shifted

DOI: 10.1021/acssuschemeng.7b00966
ACS Sustainable Chem. Eng. 2017, 5, 6081–6089

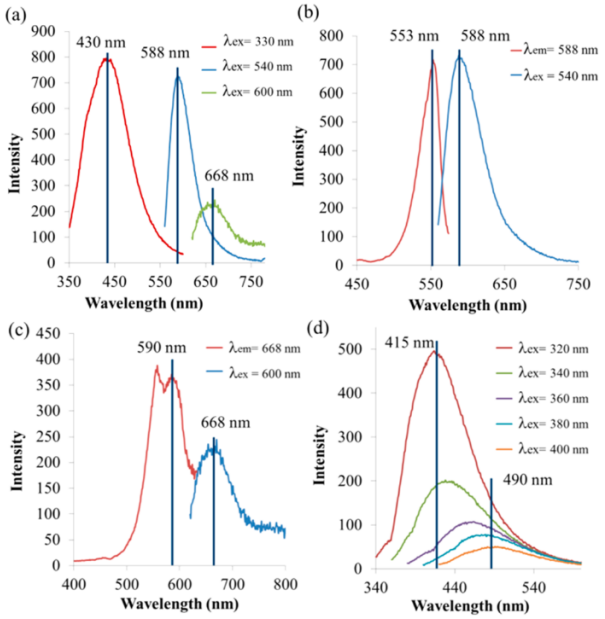

Figure 6. (a) Fluorescence emission spectra of phenol oligomeric particles at excitation wavelength 320 nm (red line), 540 nm (blue line), 600 nm (green line). (b, c) Excitation (red line) and emission spectra (blue line) of oligomeric particles. (d) Fluorescence emission of spectra phenol oligomeric particles after dissolution in the alkaline solution.

due to the $\pi-\pi$ stacking interaction between a phenolate anion and different moieties with aromatic rings.[33]

This study was also extended to other phenolic molecules (catechol, hydroquinone, tyrosine, benzoquinone) which are summarized in Table S1 and Figure S7 of the Supporting Information.

Overall, we have shown that ultrasonic oxidation and polymerization of phenol offers a simple one-step approach for making phenolic oligomers and nanoparticles without the use of any external biocatalysts, inorganic catalysts, and any other toxic agents.

Antioxidant Activity of Phenol and Sonicated Phenol. Most polyphenolic compounds can be effective as antioxidants, as antibacterial/anticancer agents.[17] Phenol itself is not an antioxidant; however, during the polymerization process, the number of phenolic rings as well as the OH groups increases. The antioxidant activity is governed by the reactivity of a substance as a hydrogen- or electron-donating agent.[34] Therefore, we sought to investigate whether sonicated phenol can also be used as an antioxidant. In order to check if the sonochemically generated oligomeric species possess any antioxidant activity, a DPPH radical scavenging assay was used. The DPPH radical has UV absorption at 520 nm, and the antioxidant activity can be determined from the decrease in absorption intensity.[35] Radical scavenging activity can be observed from the change in color of the DPPH solution (Figure 7a). Figure 7b shows that sonicated phenol exhibits greater than 50% radical scavenging activity or antioxidant activity when incubated for 30 min relative to the phenol which shows no radical scavenging activity. The IC_{50} value for the sonicated phenol was found to be 120 μM. The IC_{50} value is the concentration of the compound which can cause 50% inhibition of activity of DPPH.[36] Figure 7c shows the proposed mechanism for the oxidation of dimeric species formed as a result of sonication of phenol.

CONCLUSION

This study has established a general ultrasonic concept for the formation fluorescent oligomeric species from simple phenolic compounds with new functional properties. We have shown that the gas−liquid interface of the cavitation bubble can act as a catalytic binding site even for simple phenolic moieties leading to formation oligomers provided that experimental conditions are finely controlled. The oligomers formed by 2−6 units of phenol can aggregate together with a $\pi-\pi$ interaction to form phenolic nanostructures. Ultrasonic frequency, surface activity, and concentration of the solute are the crucial parameters needed to be controlled in order to form oligomers and nanostructures. High frequency sonication therefore is a very promising technique for carrying out oxidative coupling reactions of phenolic moieties without the use of any external agents such as enzymes, metal cross-linkers, and other toxic agents to convert simple molecules to value-added antioxidant compounds.

ASSOCIATED CONTENT

Supporting Information

The Supporting Information is available free of charge on the ACS Publications website at DOI: 10.1021/acssuschemeng.7b00966.

Absorption spectroscopy of sonicated 0.5 mM phenol; fluorescence emission spectroscopy at different frequencies, different pH, Fenton's reaction; HPLC of sonicated

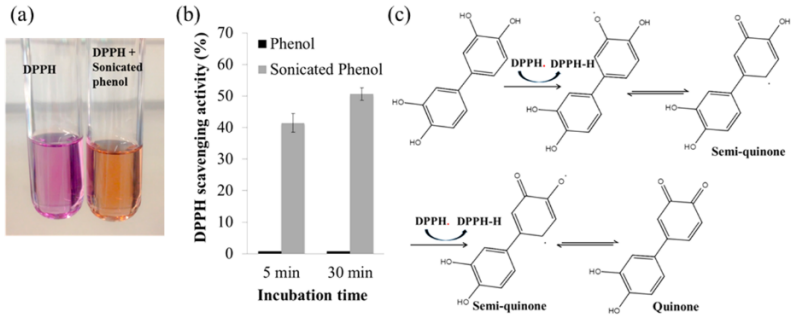

Figure 7. Radical scavenging activity shown by the color of DPPH after addition of sonicated phenol. (b) DPPH scavenging activity of phenol and sonicated phenol as a function of incubation time. (c) Proposed mechanism for oxidation of sonicated phenol.

DOI: 10.1021/acssuschemeng.7b00966
ACS Sustainable Chem. Eng. 2017, 5, 6081−6089

5 mM phenol solution; fluorescence emission spectroscopy of different phenolic moieties; mass spectra of 10 mM sonicated phenol. (PDF)

AUTHOR INFORMATION

Corresponding Authors

*E-mail: masho@unimelb.edu.au (M. Ashokkumar).
*E-mail: francesca.cavalieri@unimelb.edu.au (F. Cavalieri).

ORCID

Francesca Cavalieri: 0000-0001-5391-5069

Author Contributions

The manuscript was written through contributions of all authors. All authors have given approval to the final version of the manuscript.

Notes

The authors declare no competing financial interest.

ACKNOWLEDGMENTS

This research was funded by the ARC Future Fellowship 2014 (project number FT140100873, to FC). S.K.B. acknowledges the University of Melbourne for the scholarships (MRS). The authors also acknowledge Enrico Colombo for his help during initial stages of this work.

REFERENCES

(1) Pilato, L. *Phenolic Resins: A Century of Progress*; Springer, 2010.
(2) Nozoe, A.; Abe, M.; Ohto, K.; Kawakita, H. Germanium recovery using polyphenol microspheres prepared by horseradish peroxidase reaction. *J. Chem. Technol. Biotechnol.* **2011**, *86*, 1374−1378.
(3) Chen, Z.; Wang, C.; Chen, J.; Li, X. Biocompatible, functional spheres based on oxidative coupling assembly of green tea polyphenols. *J. Am. Chem. Soc.* **2013**, *135*, 4179−4182.
(4) Fei, J.; Zhao, J.; Du, C.; Wang, A.; Zhang, H.; Dai, L.; Li, J. One-Pot Ultrafast Self-Assembly of Autofluorescent Polyphenol-Based Core@ Shell Nanostructures and Their Selective Antibacterial Applications. *ACS Nano* **2014**, *8*, 8529−8536.
(5) Qiao, J.-Q.; Yuan, N.; Tang, C.-J.; Yang, J.; Zhou, J.; Lian, H.-Z.; Dong, L. Determination of catalytic oxidation products of phenol by RP-HPLC. *Res. Chem. Intermed.* **2012**, *38*, 549−558.
(6) Dubey, S.; Singh, D.; Misra, R. Enzymatic synthesis and various properties of poly (catechol). *Enzyme Microb. Technol.* **1998**, *23*, 432−437.
(7) Eker, B.; Zagorevski, D.; Zhu, G.; Linhardt, R. J.; Dordick, J. S. Enzymatic polymerization of phenols in room-temperature ionic liquids. *J. Mol. Catal. B: Enzym.* **2009**, *59*, 177−184.
(8) Kobayashi, S.; Higashimura, H. Oxidative polymerization of phenols revisited. *Prog. Polym. Sci.* **2003**, *28*, 1015−1048.
(9) Bruno, F. F.; Nagarajan, R.; Kumar, J.; Samuelson, L. A. Novel enzymatic polyethylene oxide-polyphenol system for ionic conductivity. *J. Macromol. Sci., Part A: Pure Appl.Chem.* **2002**, *39*, 1061−1068.
(10) Kim, Y.-J.; Uyama, H.; Kobayashi, S. Regioselective synthesis of poly (phenylene) as a complex with poly (ethylene glycol) by template polymerization of phenol in water. *Macromolecules* **2003**, *36*, 5058−5060.
(11) Kim, Y. J.; Uyama, H.; Kobayashi, S. Peroxidase-catalyzed oxidative polymerization of phenol with a nonionic polymer surfactant template in water. *Macromol. Biosci.* **2004**, *4*, 497−502.
(12) Wu, C.; Liu, X.; Wei, D.; Fan, J.; Wang, L. Photosonochemical degradation of phenol in water. *Water Res.* **2001**, *35*, 3927−3933.
(13) Okouchi, S.; Nojima, O.; Arai, T. Cavitation-induced degradation of phenol by ultrasound. *Wat. Sci. Technol.* **1992**, *26*, 2053−2056.
(14) Petrier, C.; Lamy, M.-F.; Francony, A.; Benahcene, A.; David, B.; Renaudin, V.; Gondrexon, N. Sonochemical degradation of phenol in dilute aqueous solutions: comparison of the reaction rates at 20 and 487 kHz. *J. Phys. Chem.* **1994**, *98*, 10514−10520.
(15) Entezari, M. H.; Pétrier, C. A combination of ultrasound and oxidative enzyme: sono-enzyme degradation of phenols in a mixture. *Ultrason. Sonochem.* **2005**, *12*, 283−288.
(16) Serpone, N.; Terzian, R.; Colarusso, P.; Minero, C.; Pelizzetti, E.; Hidaka, H. Sonochemical oxidation of phenol and three of its intermediate products in aqueous media: catechol, hydroquinone, and benzoquinone. Kinetic and mechanistic aspects. *Res. Chem. Intermed.* **1993**, *18*, 183−202.
(17) Cavalieri, F.; Colombo, E.; Nicolai, E.; Rosato, N.; Ashokkumar, M. Sono-assembly of nanostructures via tyrosine−tyrosine coupling reactions at the interface of acoustic cavitation bubbles. *Mater. Horiz.* **2016**, *3*, 563−567.
(18) Ashokkumar, M.; Mason, T. J. Sonochemistry. In *Kirk-Othmer Encyclopedia of Chemical Technology*; Wiley: New York, 2007. DOI 10.1002/0471238961.1915141519211912.a01.pub2.
(19) Berthelot, J.; Benammar, Y.; Lange, C. A mild and efficient sonochemical bromination of alkenes using tetrabutylammonium tribromide. *Tetrahedron Lett.* **1991**, *32*, 4135−4136.
(20) Bhangu, S. K.; Ashokkumar, M. Theory of Sonochemistry. *Top. Curr. Chem.* **2016**, *374*, 56.
(21) Duarte, R. M.; Santos, E. B.; Duarte, A. C. Spectroscopic characteristics of ultrafiltration fractions of fulvic and humic acids isolated from an eucalyptus bleached Kraft pulp mill effluent. *Water Res.* **2003**, *37*, 4073−4080.
(22) Jha, P. K.; Halada, G. P. The catalytic role of uranyl in formation of polycatechol complexes. *Chem. Cent. J.* **2011**, *5*, 12.
(23) Bruno, F. F.; Nagarajan, R.; Stenhouse, P.; Yang, K.; Kumar, J.; Tripathy, S. K.; Samuelson, L. A. Polymerization of water-soluble conductive polyphenol using horseradish peroxidase. *J. Macromol. Sci., Part A: Pure Appl.Chem.* **2001**, *38*, 1417−1426.
(24) Pistonesi, M. F.; Di Nezio, M. S.; Centurión, M. E.; Palomeque, M. E.; Lista, A. G.; Band, B. S. F. Determination of phenol, resorcinol and hydroquinone in air samples by synchronous fluorescence using partial least-squares (PLS). *Talanta* **2006**, *69*, 1265−1268.
(25) Smith, G. J.; Haskell, T. G. The fluorescent oxidation products of dihydroxyphenylalanine and its esters. *J. Photochem. Photobiol., B* **2000**, *55*, 103−108.
(26) Malencik, D. A.; Sprouse, J. F.; Swanson, C. A.; Anderson, S. R. Dityrosine: preparation, isolation, and analysis. *Anal. Biochem.* **1996**, *242*, 202−213.
(27) Chen, J. W.; Smith, G. V. *Feasibility Studies of Applications of Catalytic Oxidation in Wastewater*; Carbondale, Southern Illinois University; U.S. Environmental Protection Agency, 1971.
(28) Berlan, J.; Trabelsi, F.; Delmas, H.; Wilhelm, A.; Petrignani, J. Oxidative degradation of phenol in aqueous media using ultrasound. *Ultrason. Sonochem.* **1994**, *1*, S97−S102.
(29) Barbusiński, K.; Filipek, K. Use of Fenton's reagent for removal of pesticides from industrial wastewater. *Polym. J. Environ.* **2001**, *10*, 207−212.
(30) Goard, A. K.; Rideal, E. K. CCXXI.—The surface tensions of aqueous phenol solutions. Part II. Activity and surface tension. *J. Chem. Soc., Trans.* **1925**, *127*, 1668−1676.
(31) Chandrapala, J.; Zisu, B.; Palmer, M.; Kentish, S.; Ashokkumar, M. Effects of ultrasound on the thermal and structural characteristics of proteins in reconstituted whey protein concentrate. *Ultrason. Sonochem.* **2011**, *18*, 951−957.
(32) Dharmarathne, L.; Ashokkumar, M.; Grieser, F. Reaction of ferricyanide and methyl viologen with free radicals produced by ultrasound in aqueous solutions. *J. Phys. Chem. A* **2012**, *116*, 7775−7782.
(33) Tsien, R. Y. The green fluorescent protein. *Annu. Rev. Biochem.* **1998**, *67*, 509−544.
(34) Rice-Evans, C.; Miller, N.; Paganga, G. Antioxidant properties of phenolic compounds. *Trends Plant Sci.* **1997**, *2*, 152−159.
(35) Antolovich, M.; Prenzler, P. D.; Patsalides, E.; McDonald, S.; Robards, K. Methods for testing antioxidant activity. *Analyst* **2002**, *127*, 183−198.

DOI: 10.1021/acssuschemeng.7b00966
ACS Sustainable Chem. Eng. 2017, 5, 6081−6089

(36) Burits, M.; Bucar, F. Antioxidant activity of Nigella sativa essential oil. *Phytother. Res.* **2000**, *14*, 323−328.

DOI: 10.1021/acssuschemeng.7b00966
ACS Sustainable Chem. Eng. 2017, 5, 6081−6089

Supporting Information

A simple one-step ultrasonic route to synthesize antioxidant molecules and fluorescent nanoparticles from phenol and phenol-like molecules

Sukhvir Kaur Bhangu[a], *Muthupandian Ashokkumar*[a*], *and Francesca Cavalieri*,[b,c*]

[a] *School of Chemistry, University of Melbourne, Parkville, VIC 3010, Australia*

[b] *Department of Chemical and Biomolecular Engineering, University of Melbourne, Parkville, VIC 3010, Australia*

[c] *Dipartimento di Scienze e Tecnologie Chimiche, Universita' degli Studi di Roma ''Tor Vergata'', via della Ricerca Scientifica 1, 00173, Roma, Italy*

AUTHOR INFORMATION

francesca.cavalieri@unimelb.edu.au

Contents

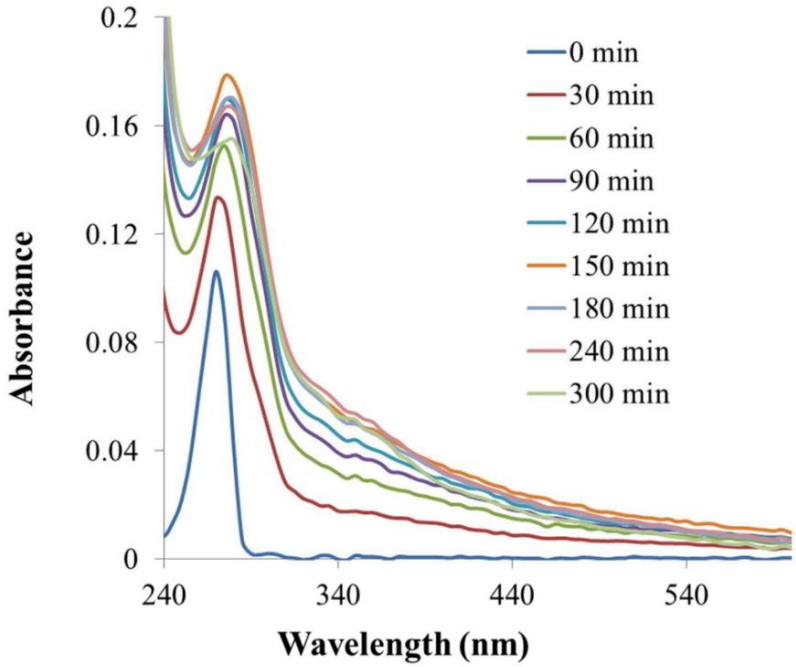

Figure S2: The absorbance spectra of 0.5 mM phenol solution as a function of sonication time

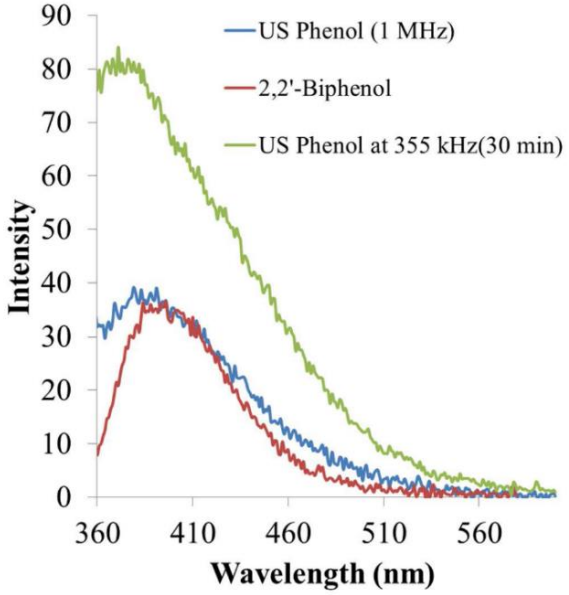

Figure S2: Comparison of fluorescence emission spectra of sonicated phenol at 355 kHz after 30 min, 1 MHz after 150 min and reference standard of dimer of phenol (2,2'-biphenol).

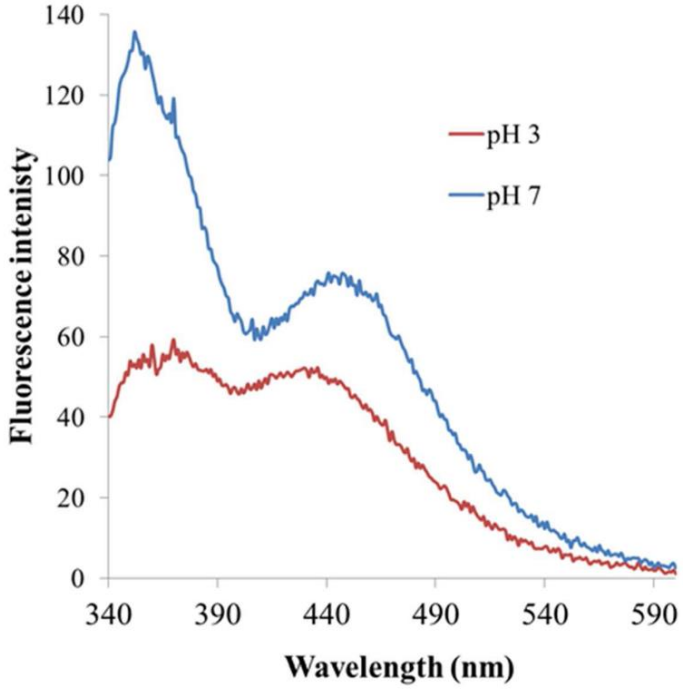

Figure S3: Comparison of fluorescence spectra (λ_{ex} = 320 nm) of sonicated phenol at pH 3 and pH 7

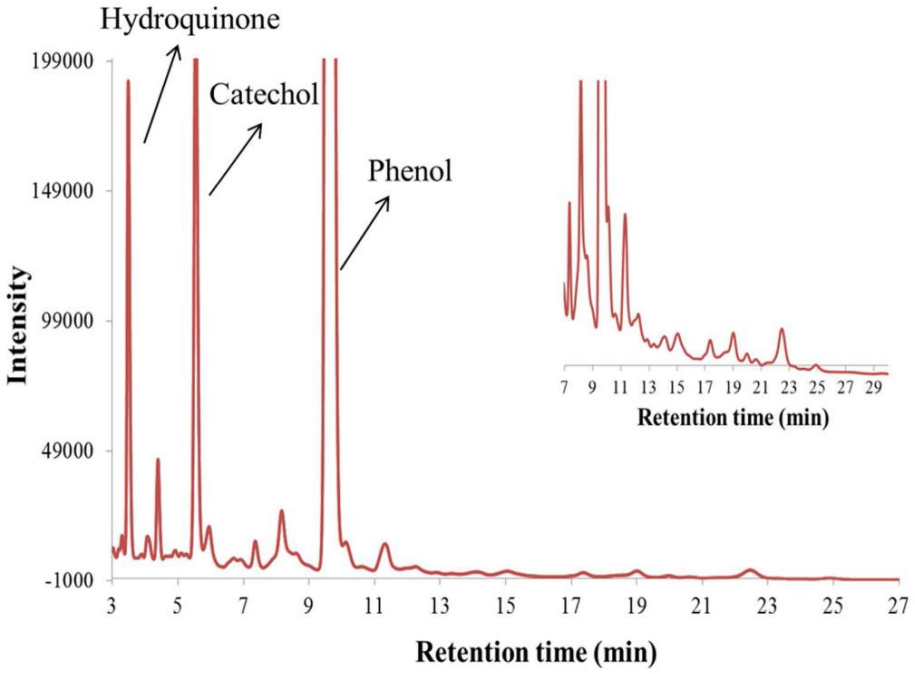

Figure S4: HPLC chromatogram of 5 mM sonicated phenol at 355 kHz 60 W after 5 h.

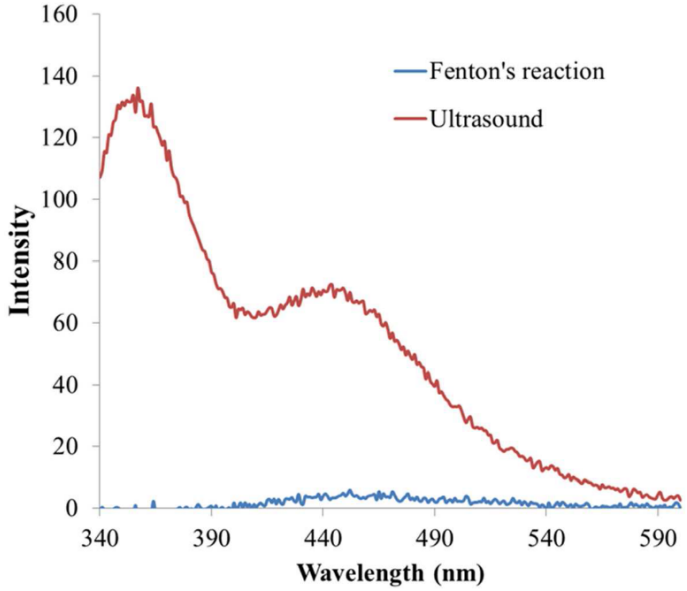

Figure S5: Comparison of fluorescence spectra (λ_{ex} = 320 nm) of 0.5 mM phenol with ultrasound and Fenton's reaction after 2 hours.

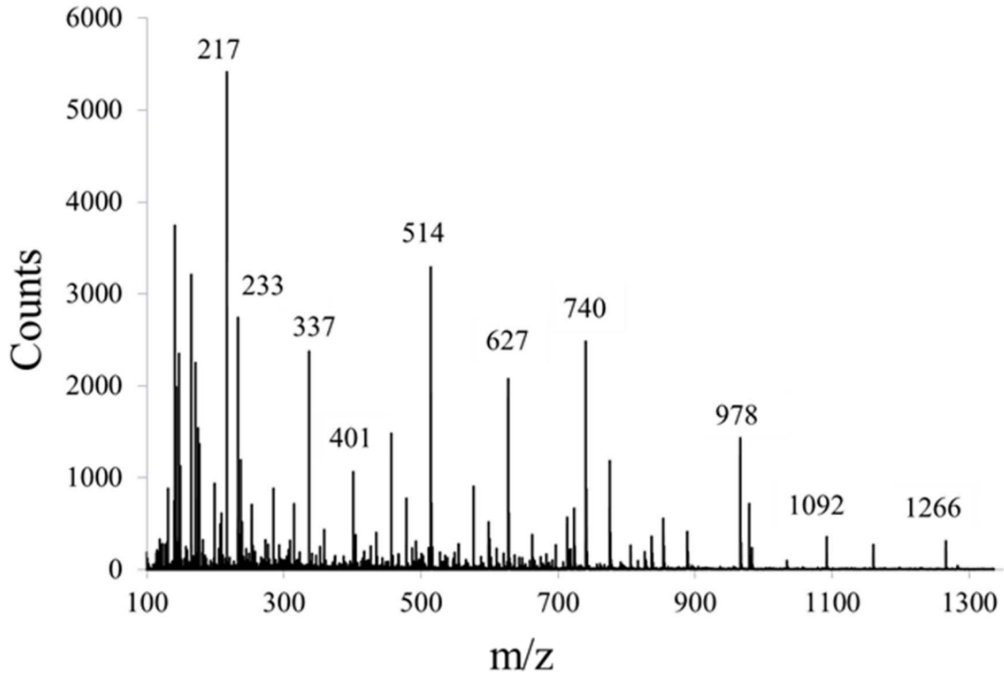

Figure S6: Mass spectra of 10 mM sonicated phenol (at 355 kHz 60 W) after 5 hours.

This study has also been extended to the other phenolic molecules. Table S1 summarizes the other compounds studied and their λmax values which were obtained from the fluorescence emission spectra when excited at 320 nm. Sonication of all these species under similar experimental conditions (355 kHz, 60W, pH =7) has also produced the similar results i:e the formation dimers and oligomers (Figure S6).

Table S1: List of compounds investigated at 355 kHz, 60 W

Compound studied	**Concentration**	**λ_{max} in Fluorescence emission spectra (Figure S6)**
Catechol	0.5 mM	455 nm
Hydroquinone	0.5 mM	447 nm
p-Benzoquinone	0.5 mM	447 nm
3,4-Dihydroxybenzoic acid	1 mM	434 nm
Tyrosine	1 mM	410 nm

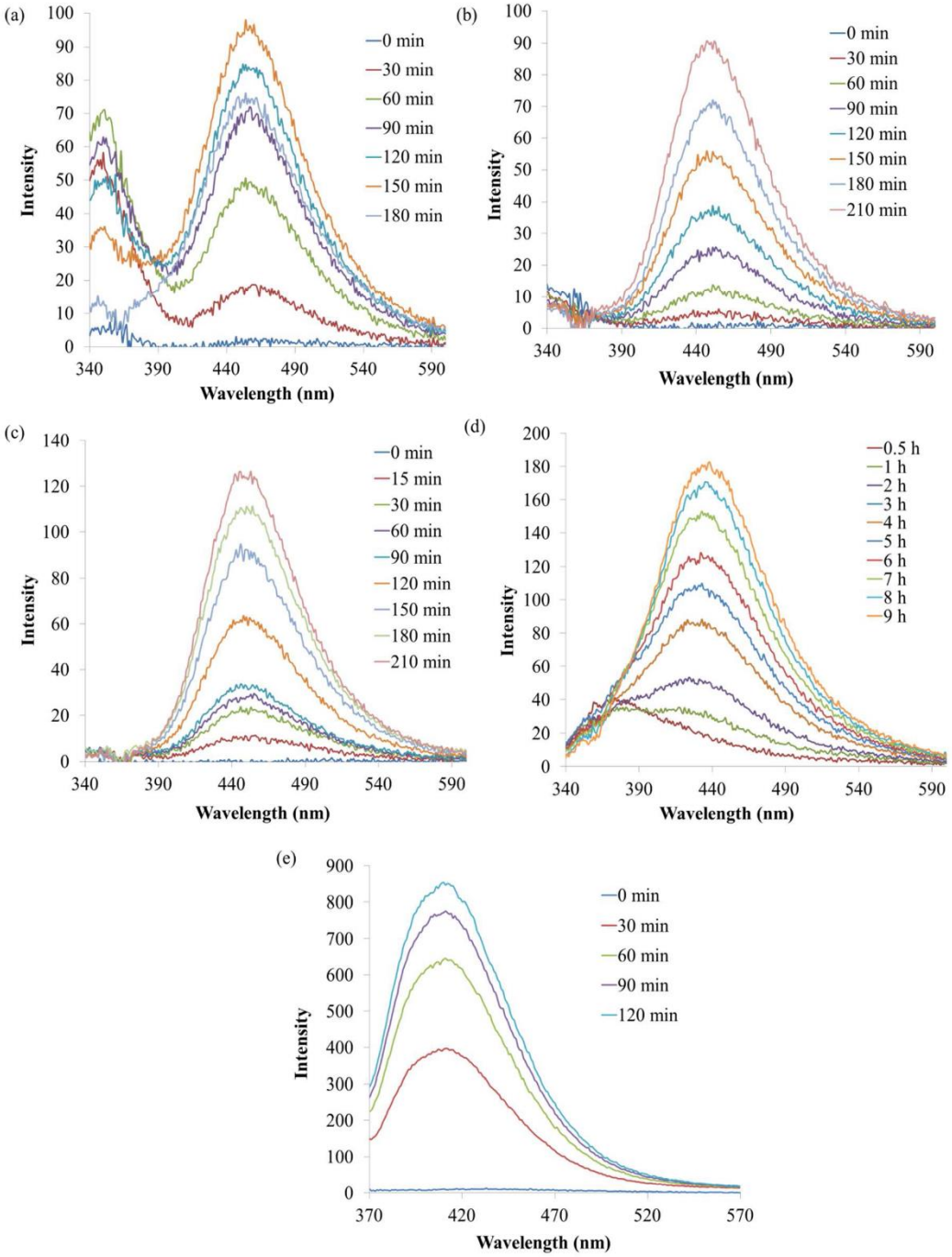

Figure S7: Fluorescence emission spectra at λ_{ex} = 320 nm of different sonicated compounds with 355 kHz 60 W at different sonication times (a) 0.5 mM Catechol, (b) 0.5 mM Hydroquinone, (c) 0.5 mM p- Benzoquinone, (d) 1 mM 3,4-Dihydroxybenzoic acid and (e) 1 mM Tyrosine

Chapter 5

Sono-transformation of tannic acid into biofunctional ellagic acid micro/nanocrystals with distinct morphologies

Green Chemistry 2018, 20, 4, 816-821

This Chapter demonstrates that cavitation bubbles are simple micro- reactors with reactive surfaces to perform multiple reactions on tannic acid namely (i) hydrolysis of an ester linkage, (ii) C–C coupling reactions, (iii) condensation reactions to generate ellagic acid and (iv) crystallization of the ellagic acid into regularly shaped particles

Green Chemistry

COMMUNICATION

View Article Online
View Journal

Cite this: DOI: 10.1039/c7gc03163g

Received 20th October 2017,
Accepted 9th January 2018

DOI: 10.1039/c7gc03163g

rsc.li/greenchem

Sono-transformation of tannic acid into biofunctional ellagic acid micro/nanocrystals with distinct morphologies†

Sukhvir Kaur Bhangu, [a] Ritu Singla,[a] Enrico Colombo,[a] Muthupandian Ashokkumar *[a] and Francesca Cavalieri *[b,c]

A sustainable, reagent-less and one-pot ultrasonic methodology has been developed to transform amorphous tannic acid into regularly shaped crystalline ellagic acid particles. Multiple and consecutive reactions have been performed on tannic acid, in aqueous solution without the addition of any external reagent. The size, morphology and bio-activity of ellagic acid micro-nanocrystals can be finely tuned by choosing appropriate ultrasonic parameters.

Acoustic cavitation in aqueous solutions results in the generation of a reactive green processing environment enabling a number of reactions without the addition of any external reagents. Extremely high local temperatures and pressures, oxidizing and reducing agents and physical effects (microjets, turbulence, shear forces, *etc.*) are generated by acoustic cavitation, which may exert synergistic effects. High and low frequency ultrasound has been employed in materials synthesis, polymerization, degradation of organic and inorganic pollutants, wastewater treatment, crystallisation, and microcapsule synthesis encapsulating food and cosmetic ingredients.[1–4]

Recently, we have demonstrated a new concept that cavitation bubbles generated by high frequency ultrasound in the range of 0.35–1 MHz can act as catalytic binding sites for the radical mediated C–C coupling of phenolic moieties.[5,6] Simple phenolic molecules such as tyrosine and phenol were coupled by a C–C linkage to form oligomeric bio-functional phenolic systems, which are not obtained with other radical sources (such as Fenton's reaction).

Herein, we show that cavitation bubbles are simple microreactors with reactive surfaces to perform one-pot multiple reactions on complex organic molecules, namely (i) hydrolysis of an ester linkage, (ii) C–C coupling reactions, (iii) condensation reactions and (iv) crystallisation of the product into regularly shaped particles. To our knowledge, multiple and consecutive reactions induced by acoustic cavitation have never been reported before.

As a proof of concept, we have developed a sustainable, reagent-less and cost effective synthetic methodology to transform amorphous tannic acid into regularly shaped crystalline ellagic acid particles, with tunable morphologies and functionality. The size and shape of ellagic acid micro-nanocrystals can be finely tuned by choosing appropriate ultrasonic parameters such as sonication time, power and frequency. Ellagic acid powder is conventionally obtained either through the enzymatic hydrolysis oxidation of ellagitannins with tannase and decarboxylase[7,8] or multistep organic synthesis[9] without any control over size and shape.

Conversely, in this work we demonstrate a remarkably simple and unique green synthetic route to generate ellagic acid micro-nanocrystals. In addition, our approach should be readily extendable to other sono-responsive biomolecules.

The chemical functionalization and assembly of phenolic biomolecules such as gallotannins, ellagitannins, catechins and flavonoids have recently attracted much attention due to their potential application in different fields including sensing, imaging, drug delivery, live-cell protection, and catalysis.[10–13] The current approaches for the manipulation of phenol moieties into the desired nanoarchitectures require the formation of catechol–metal coordination complexes or oxidative coupling reactions catalyzed by metals or enzymes.[14] The biomolecule obtained in this study, ellagic acid (EA), is of particular interest in the biomaterials area because *in vitro* and *in vivo* studies have shown that EA can significantly inhibit cancer formation in the colon, oesophagus, liver, lung, tongue and skin and the infection of human T-cell lymphotropic virus type-1-carrying MT-4 cells by human immunodeficiency virus (HIV).[7,15]

The direct sono-transformation of tannic acid into ellagic acid micro-nanoparticles is a versatile method for the engineering of ellagic acid-based biomaterials with tailored structural and functional properties.

[a]*School of Chemistry, The University of Melbourne, VIC 3010, Australia. E-mail: masho@unimelb.edu.au*
[b]*Department of Chemical and Biomolecular Engineering, The University of Melbourne, VIC 3010, Australia. E-mail: francesca.cavalieri@unimelb.edu.au*
[c]*Dipartimento di Scienze e Tecnologie Chimiche, Universita' di Roma "TorVergata", via della ricerca scientifica 1, 00133 Rome, Italy*

†Electronic supplementary information (ESI) available. See DOI: 10.1039/c7gc03163g

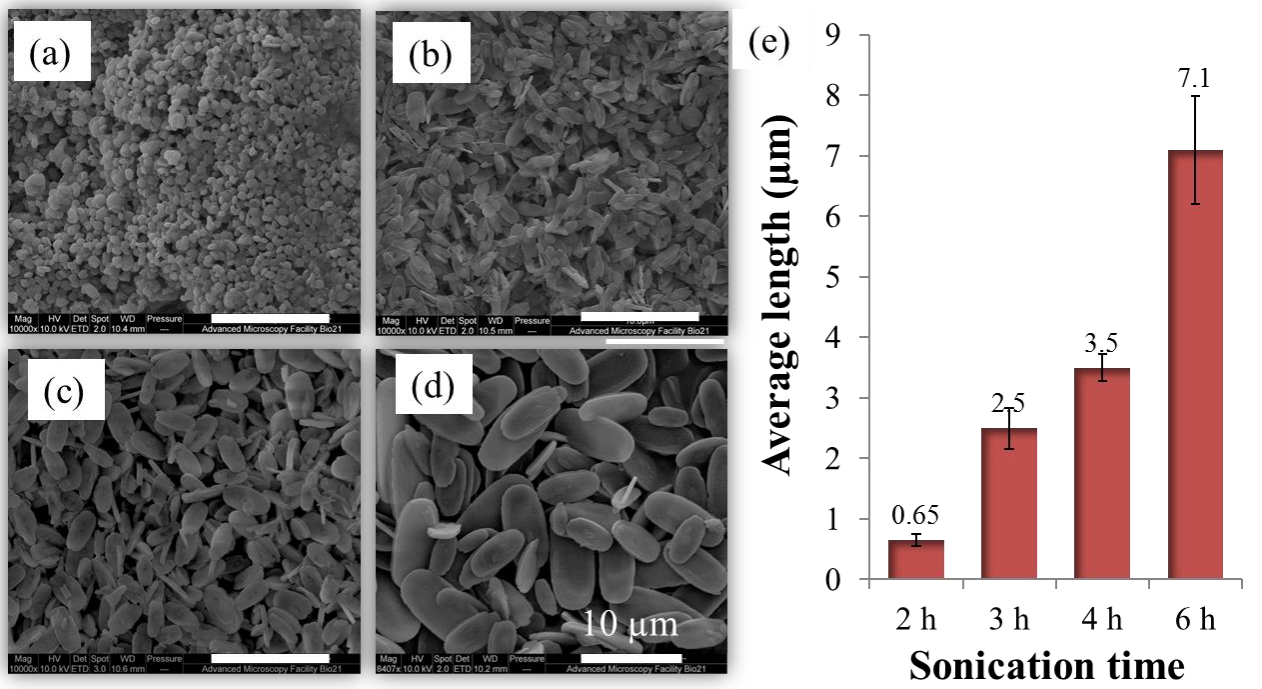

Fig. 1 The effect of sonication time on the TAS particles obtained. (a) 2 h, (b) 3 h, (c) 4 h., and (d) 6 h; (e) average length of the particles as a function of sonication time (scale bar = 10 μm). Samples were sonicated at 355 kHz and 5.5 W cm^{-3}.

Tannic acid is a biomass belonging to the category of hydrolysable tannins with a multiple number of gallic acid and galloyl units attached to the central sugar core which is mostly D-glucopyranose.[16,17] The aim of the study was to explore the chemical transformation of tannic acid induced by ultrasound. The sonication of an aqueous solution of tannic acid at 355 kHz and 5.5 W cm^{-3} was carried out at pH 7 for up to six hours. Surprisingly, we discovered that the sonicated tannic acid undertook a more complex modification pathway. We observed the formation of nano-micrometer sized crystalline particles hereafter referred to as TAS particles. The SEM images of the TAS particles obtained after different sonication times are shown in Fig. 1a–d. It can be seen that the size, shape and morphology of the crystals depends on the sonication time. Nanoparticles with a discoidal shape turned into a flat ellipsoidal shape growing in size. The graph shown in Fig. 1e illustrates that the average length of particles increased from 650 nm to 7 μm when the sonication time was increased from 2 h to 6 h.

We sought to investigate the chemical composition and the mechanism of the formation of the obtained particles. In order to gain insight into the composition of TAS particles mass spectrometry, spectroscopy, chromatography and NMR analysis were conducted. The electrospray mass spectrometry (ESMS) and MALDI-TOF data (Fig. S1a, ESI†) acquired after the dissolution of the TAS particles in Milli-Q water have shown the presence of a major peak at *m/z* 301 that could be assigned to ellagic acid (see Fig. 2 for the structure),

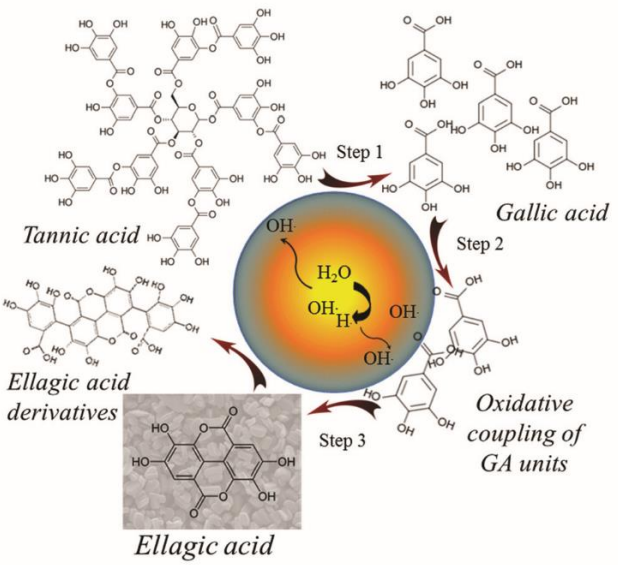

Fig. 2 Schematic of the proposed mechanism for the ultrasonic transformation of TA to ellagic acid. The core of cavitation bubbles generating high temperatures leading to the homolysis of the water molecule to H˙ and OH˙, step 1 showing the hydrolysis of tannic acid to gallic acid, step 2 the oxidative coupling of gallic acid units at the bubble surface to form a dimer and step 3 where the dimer spontaneously lactonized to form EA and its derivatives.

accompanied by some small peaks ascribed to higher molecular weight species (Fig. S1a and b, ESI†). The sono-transformation of tannic into ellagic acid was further confirmed by HPLC (Fig. S1, ESI†), absorption spectroscopy, ^{1}H and ^{13}C NMR spectroscopy (Fig. S2–S5, ESI† respectively) and PXRD analyses.

In particular the X-ray diffraction patterns indicate that commercial tannic acid is amorphous, which is consistent with the literature,[18] whereas the TAS particles are crystalline (Fig. S6, ESI†). The X-ray diffraction pattern of the TAS particles was identical to the commercial ellagic acid,[19] for example, peaks at 2θ values of 17.9°, 21.4°, 24.8°, 26.7° and 28.5°, indicating the crystalline nature of the particles.[20] However, some additional peaks were also observed. Overall our data suggest that high frequency sonication provides a simple one-step approach for the synthesis of crystalline ellagic acid particles from tannic acid with different shapes and sizes. Fig. 2 shows the possible mechanism involved in the formation of ellagic acid from TA. It is well known that cavitation bubbles driven by high frequency ultrasound can give rise to physical effects such as shear forces, turbulence, microjets, *etc.* and chemical effects such as the generation of radicals due to the homolysis of water to $H^{\bullet}$ to $OH^{\bullet}$ (Fig. 2). The recombination of 2 $OH^{\bullet}$ would lead to the formation of H_2O_2.[1,3] The combination of all these effects can play a significant role in inducing different chemical reactions. TA is composed of a multiple number of galloyl units and shear stress and radicals generated by cavitation induces the hydrolysis of galloyl moieties (step 1) without the use of any acid or base catalyst. Subsequently, two gallic acid units undergo catalytic oxidative coupling through a C–C linkage to form a dimer at the bubble–solution interface (step 2) as observed in our previous studies.[5,6] The spontaneous lactonization likely occurs in the bulk phase to form EA (step 3).

Ellagic acid can further react with gallic acid molecules on the surface of cavitation bubbles to form derivatives by C–C oxidative coupling mediated by $OH^{\bullet}$ radicals. Finally, the ultrasound assisted assembly and crystallisation of ellagic acid completes the series of reactions triggered by ultrasound.

Ultrasound assisted crystallisation has been reported in the literature and it was suggested that the ultrasonic parameters can be used to control size distribution, average crystal size and type of polymorph obtained.[21–23] Particularly, crystal size can be controlled by two cavitation effects, the generation of shock waves by acoustic cavitation which increases the nucleation rate and microturbulence that can direct the subsequent growth of the crystals.[22] Interestingly, different crystal morphology was observed at different sonication times. After two hours of sonication, the EA concentration reaches the supersaturation condition, forming submicron particles (Fig. 1a). Subsequently the ultrasonically generated EA, with increasing sonication time, contributes to the particle growth up to 7 micrometers (Fig. 1d). It is worth noting that the use of $OH^{\bullet}$ radicals generated from hydrogen peroxide sources, such as Fenton's reagents, didn't result in the formation of fluorescent and regularly shaped particles. This suggests that the simultaneous presence of OH radicals and a reactive cavitation bubble interface are necessary for the coupling of gallic acid molecules.

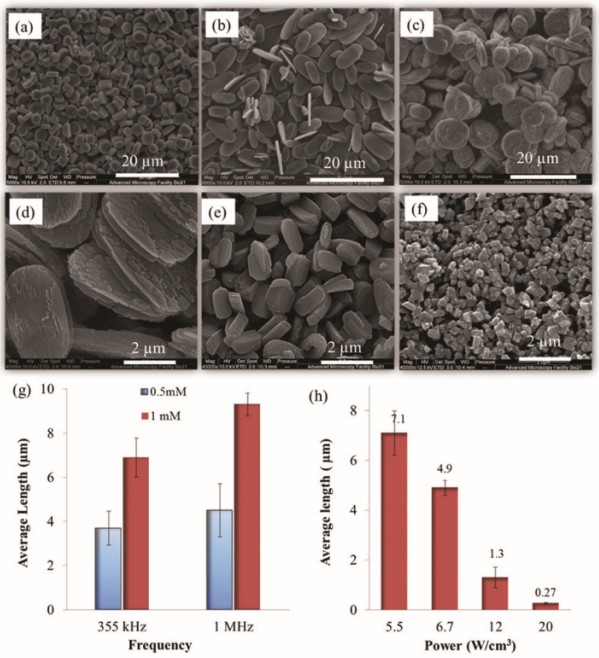

Fig. 3 SEM images of the TAS particles obtained using different TA concentrations and ultrasonic parameters: (a) TA 0.5 mM at 355 kHz and 5.5 W cm^{-3}, (b) TA 1 mM at 355 kHz and 5.5 W cm^{-3}; (c) TA 1 mM at 1 MHz and 5.5 W cm^{-3}; (d) SEM image of the TAS particles at 355 kHz and 6.7 W cm^{-3}, (e) SEM image of the TAS particles at 355 kHz and 12 W cm^{-3}, (f) SEM image of the TAS particles at 355 kHz and 20 W cm^{-3}; (g) the graph provides the average length of the TAS particles at different concentrations of TA as a function of ultrasonic frequency and (h) average length of the TAS particles as a function of ultrasonic power.

In order to gain further insight into the effect of ultrasonic parameters on EA particle morphologies, further experiments were carried out. Fig. 3 shows the SEM images of the TAS particles obtained as a function of different ultrasonic frequencies (355 kHz and 1 MHz), initial concentrations of TA (0.5 mM and 1 mM) and ultrasonic powers (5.5, 6.7, 12, and 20 W cm^{-3}). Micro-nanoparticles with different morphologies were obtained including small and large discoidal shape particles, flat ellipsoidal particles and brick-like particles. These images suggest that the morphology of the TAS particles is affected significantly by the experimental parameters. When the initial concentration of TA was increased from 0.5 mM (Fig. 3a) to 1 mM (Fig. 3b), the size of the particles increased from 3.7 to 7 μm at 355 kHz. Also, when the ultrasonic frequency was switched from 355 kHz (Fig. 3b) to 1 MHz (Fig. 3c) at 1 mM concentration of TA, changes in the morphology, *viz.*, size (from 7 to 9.5 microns) as well as the aspect ratio, *i.e.*, the length to width ratio (from 1.8 to 1.1) of the crystals, were observed.

Similarly, the effect of ultrasonic power was studied on the morphology and the size of the TAS crystals. Fig. 3d, e and f represent the SEM images of the particles obtained when TA

solution was sonicated for 5 hours at 6.7 W cm^{-3}, 12 W cm^{-3} and 20 W cm^{-3}, respectively. The results showed that when the power was increased from 5 W cm^{-3} to 20 W cm^{-3}, the crystal size reduced from 7 microns to 200–350 nm (Fig. 3h). Fig. 3g summarises how the average length of the TAS crystals changed with changes in the frequency and TA concentration. Also, the yield of EA produced varied from 40 to 70% when the power was increased from 5.5 W cm^{-3} to 20 W cm^{-3}.

Fig. 4 shows a schematic to explain how the morphology, size and aspect ratio of the TAS particles are affected by various parameters such as sonication time, concentration of TA, ultrasonic power and frequency. As crystal size and size distribution are influenced by the population and growth rate of the nuclei, a rise in the number of nuclei formed (nucleation rate) would lead to a reduction in the amount of the solute available for the growth of individual crystals leading to small sized crystals.[22,23]

With an increase in the ultrasonic frequency from 355 kHz to 1 MHz, a decrease in the number of $OH^{\bullet}$ radicals produced and shear forces has been reported.[1,3] $OH^{\bullet}$ radicals are required for the oxidative coupling reaction; therefore, at a higher frequency the amount of EA generated would decrease resulting in the decrease in the local supersaturation and nucleation rate; thus an increase in the crystal size and aspect ratio is observed (Fig. 3b and c).

Similarly, ultrasonic power can be also used to tune the size of the particles (Fig. 3d–f). The crystal size decreases with increasing power due to the enhanced physical effects and chemical effects. Peculiarly, increased shear forces, turbulence and shock waves as well as the number of radicals (required for the oxidative coupling reaction) can significantly improve the local supersaturation resulting in higher nucleation rates and smaller crystal sizes.[21–23] Hence, the decrease in the crystal size is observed with the upsurge of ultrasonic power.

The aspect ratio of microparticles is dictated by the concentration of ultrasonically produced EA. EA assembles into discoidal shaped particles at a higher frequency (Fig. 3c) when the rate of generation of $OH^{\bullet}$ radicals is low and also at low concentrations of TA (Fig. 3a), consequently, decreasing the concentration of EA. However, at a higher concentration of EA, microparticles preferentially form ellipsoidal crystals.

The optical properties of the TAS particles were investigated by fluorescence spectroscopy and microscopy. Fig. 5a represents the fluorescence emission spectra of the TAS particles at different excitation wavelengths. It can be observed that λ_{max} is around 440 nm when excited at 360 nm. The observed spectroscopic properties were similar to those of pure EA (Fig. S7, ESI†). The dependence of the emission wavelength on the excitation wavelength indicates the presence of multiple other oli-

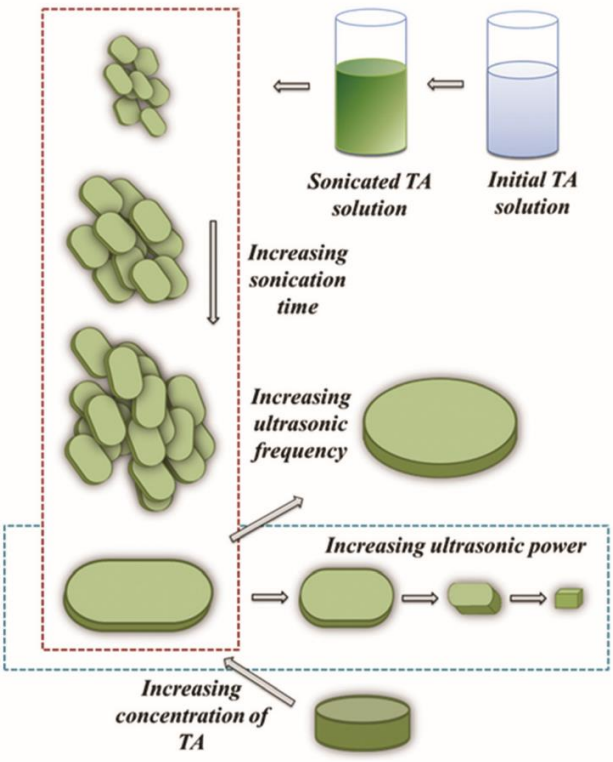

Fig. 4 Schematic illustration of the effect of sonication time, frequency, power and concentration of TA on the morphology and size of the TAS particles.

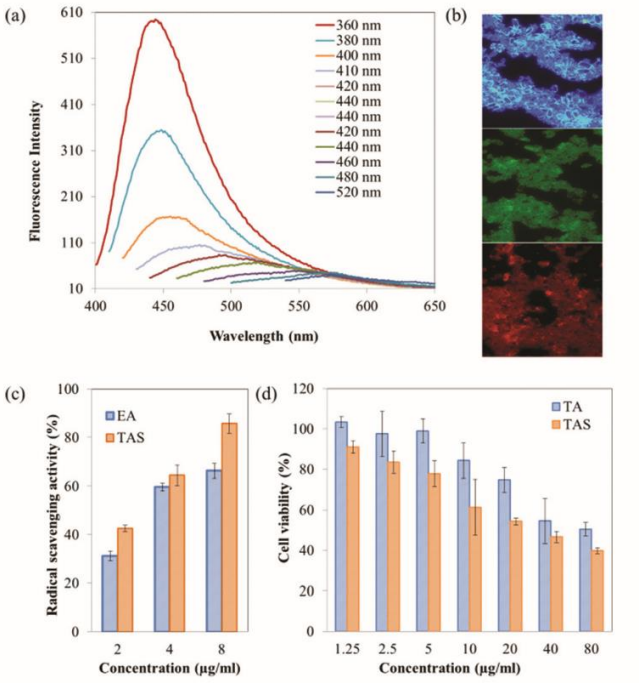

Fig. 5 (a) Fluorescence emission spectra of 1 mM TA solution sonicated at 355 kHz and 5.5 W cm^{-3} recorded at different excitation wavelengths, (b) fluorescence microscopy images of the TAS particles showing blue, green and red emission. (c) DPPH radical scavenging activity of TA and EA particles as a function of concentrations after 3 min incubation time, (d) cytotoxicity of TA and TAS as a function of the concentration after 24 h incubation at 37 °C with MDA-MB-231 cells.

gomeric species along with the formation of EA, in agreement with previous results. The fluorescence of the TAS particles was confirmed by fluorescence microscopy where blue, green and red emissions (Fig. 5b) were observed.

To demonstrate the functional properties of the TA and TAS particles, further studies were performed. The thermal stability study of the TA and TAS particles was performed by thermogravimetric analysis. Fig. S8, ESI† shows that the TAS particles are also more thermostable compared to tannic acid. The ζ-potentials of the TAS particles were measured to be around −56 mV ± 11 mV in deionized water. This indicates that the surface of the particles is negatively charged most likely due to the presence of acidic phenoxy groups and the ζ-potential of the TAS particles is in the range for the colloidal stability of the particles. Hence, the TAS particles did not aggregate in aqueous solution.

The antioxidant properties of TAS and EA were studied and compared using a DPPH assay. Fig. 5c shows the percentage radical scavenging activity of the TAS and EA particles as a function of concentration after 3 min incubation. Firstly, it was observed that the activity increased as a function of TAS and EA concentrations. Secondly, it was also observed that TAS nanoparticles had a better radical scavenging activity than EA at all the concentrations. Polyphenolic molecules have the capacity to prevent DNA and protein damage as they can scavenge the OH radicals, peroxyl radicals and nitrogen reactive species[24] due to the high degree of hydroxylation. These results confirm that the antioxidant properties of TA are improved when converted to TAS particles. The antioxidant properties can be exploited in various biomedical applications to protect the cells and biomolecules against free radicals.

Finally, the cytotoxicity and anticarcinogenic activity of the TA and TAS nanoparticles were assessed by an MTT viability assay. MDA-MB-231 breast cancer cells were incubated with TA and EA at different concentrations. Fig. 5d shows that the TAS nanoparticles have higher anticancer activity as compared to TA at all concentrations. The IC_{50} value of the TAS particles was between 20 and 10 μg mL^{-1}, whereas TA has a value >80 μg mL^{-1}. The chemo-preventive properties of different polyphenols have been determined both *in vivo* and *in vitro* in the past. They exert such effects as they have the tendency to reduce proliferation by inducing apoptosis.[24] Ellagic acid moieties in solution are proven to have anticarcinogenic activity towards breast cancer cells.[24,25] They can inhibit cell proliferation as well as they help in the migration of cells through VEGF-induced angiogenesis, VEGF-2 tyrosine kinase activity (as it can interact through hydrogen bonding and aromatic interactions within the ATP-binding region of VEGFR kinase) and its downstream MAPK and PI3K/Akt pathways.[25,26] Our results indicate that the newly synthesized TAS particles can be utilized as nanoformulations for the treatment of breast cancer cells. In addition, the TA nanoparticles can also be loaded with other antineoplastic hydrophobic drugs to enhance their therapeutic activity.

Conclusions

We have demonstrated the unexpected ability of ultrasound to perform multiple and consecutive reactions on tannin molecules. The product, *i.e.*, ellagic acid assembles and crystallizes into regularly shaped particles. The particle sizes and morphologies can be tuned by changing the ultrasonic parameters and concentration of tannic acid. We have demonstrated that the radical yield and shear forces can alter the size and morphology of the particles. TAS particles possess optical properties in a wide range of wavelengths as well as anticancer and antioxidant properties. In particular, TAS nanoparticles showed significantly higher cytotoxicity and higher radical scavenging activity as compared to that of soluble TA and EA. In conclusion, this study highlights the importance of using a powerful and green ultrasonic methodology to synthesize EA particles starting from a biomass such as TA. The synthesis was performed without using any reagents or organic solvents with a fine control over particle size and morphology. We are currently investigating the potential use of TA nanoparticles as drug delivery carriers. In addition, future efforts will be directed towards the utilization of this strategy to modify other sono-reactive molecules to obtain biofunctional molecules.

Conflicts of interest

There are no conflicts to declare.

Acknowledgements

This research was funded by the ARC Future Fellowship 2014 (project number FT140100873, to FC). S. K. B. acknowledges the University of Melbourne for the scholarships (MRS). We thank Prof. Frank Caruso for helpful discussion.

Notes and references

1 M. Ashokumar, *Handbook of Ultrasonics and Sonochemistry*, Springer, 2016.
2 M. Ashokkumar, D. Sunartio, S. Kentish, R. Mawson, L. Simons, K. Vilkhu, *et al.*, *Innov Food Sci Emerg Technol.*, 2008, **9**, 155–160.
3 S. K. Bhangu and M. Ashokkumar, *Top. Curr. Chem.*, 2016, **374**, 56.
4 R. Bund and A. Pandit, *Ultrason. Sonochem.*, 2007, **14**, 143–152.
5 F. Cavalieri, E. Colombo, E. Nicolai, N. Rosato and M. Ashokkumar, *Mater. Horiz.*, 2016, **3**, 563–567.
6 S. K. Bhangu, M. Ashokkumar and F. Cavalieri, *ACS Sustainable Chem. Eng.*, 2017, **5**, 6081–6089.
7 L. Mingshu, Y. Kai, H. Qiang and J. Dongying, *J. Basic Microbiol.*, 2006, **46**, 68–84.
8 A. Brune and B. Schink, *Arch. Microbiol.*, 1992, **157**, 417–424.

9 Q. Sun, J. Heilmann and B. König, *Beilstein J. Org. Chem.*, 2015, **11**, 249.
10 S. Quideau, D. Deffieux, C. Douat-Casassus and L. Pouysegu, *Angew. Chem., Int. Ed.*, 2011, **50**, 586–621.
11 H. Ejima, J. J. Richardson and F. Caruso, *Nano Today*, 2017, **12**, 13.
12 N. Bertleff-Zieschang, M. A. Rahim, Y. Ju, J. A. Braunger, T. Suma, Y. Dai, S. Pan, F. Cavalieri and F. Caruso, *Chem. Commun.*, 2017, **53**, 1068.
13 E. D. Bartzoka, H. Lange, K. Thiel and C. Crestini, *ACS Sustainable Chem. Eng.*, 2016, **4**, 5194–5203.
14 Z. Chen, C. Wang, J. Chen and X. Li, *J. Am. Chem. Soc.*, 2013, **135**, 4179–4182.
15 T. Mizuno, K. Uchino, T. Toukairin, A. Tanabe, H. Nakashima, N. Yamamoto, *et al.*, *Planta Med.*, 1992, **58**, 535–539.
16 I. Mueller-HarveY, *Anim. Feed Sci. Technol.*, 2001, **91**, 3–20.
17 L. Pouységu, D. Deffieux, G. Malik, A. Natangelo and S. Quideau, *Nat. Prod. Rep.*, 2011, **28**, 853–874.
18 S.-J. Wu, Y.-C. Ho, S.-Z. Jiang and F.-L. Mi, *Food Funct.*, 2015, **6**, 2283–2292.
19 M. Z. Hussein, S. H. Al Ali, Z. Zainal and M. N. Hakim, *Int. J. Nanomed.*, 2011, **6**, 1373–1383.
20 S. Goriparti, M. Harish and S. Sampath, *Chem. Commun.*, 2013, **49**, 7234–7236.
21 M. W. Park and S. D. Yeo, *Sep. Sci. Technol.*, 2010, **45**, 1402–1410.
22 V. S. Nalajala and V. S. Moholkar, *Ultrason. Sonochem.*, 2011, **18**, 345–355.
23 S. Kaur Bhangu, M. Ashokkumar and J. Lee, *Cryst. Growth Des.*, 2016, **16**, 1934–1941.
24 H. M. Zhang, L. Zhao, H. Li, H. Xu, W. W. Chen and L. Tao, *Cancer Biol. Med.*, 2014, **11**, 92.
25 N. Wang, Z. Y. Wang, S. L. Mo, T. Y. Loo, D. M. Wang, H. B. Luo, *et al.*, *Breast Cancer Res. Treat.*, 2012, **134**, 943–955.
26 L. Tang, X. Ma, Q. Tian, Y. Cheng, H. Yao, Z. Liu, *et al.*, *Food Chem. Toxicol.*, 2013, **56**, 204–213.

Sono-transformation of tannic acid into biofunctional ellagic acid micro/nanocrystals with distinct morphologies

Sukhvir Kaur Bhangu[a], Ritu Singla[a], Enrico Colombo[a], Muthupandian Ashokkumar[a*], and Francesca Cavalieri[b,c*]

[a]School of Chemistry, University of Melbourne, VIC 3010, Australia

[b]Department of Chemical and Biomolecular Engineering, University of Melbourne, VIC 3010, Australia

[c]Dipartimento di Scienze e Tecnologie Chimiche, Universita' degli Studi di Roma "Tor Vergata", via della ricerca scientifica 1, 0017, Rome, Italy

Contents:

1. Experimental Procedures

Materials

Tannic acid (TA), gallic acid, ellagic acid (EA), phosphoric acid solution (35 wt% in H_2O), DMSO, 1-diphenyl-2-picrylhydrazyl (DPPH), hydrogen peroxide (35 wt%) and3-(4,5-dimethylthiazol-2-yl)-2,5-diphenyltetrazolium bromide (MTT) were purchased from Sigma Aldrich. Di-sodium hydrogen orthophosphate (98%) and sodium dihydrogen orthophosphate (99%) were purchased from Chem-Supply; iron (II) chloride tetrahydrate was purchased from Fluka, hydroquinone was purchased from BDH AnalaR®, HPLC grade methanol (99.9%) was purchased from Fisher chemicals. Sulphuric acid (95-97%) was purchased from Scharlau, hydrochloric acid (36%) and pyridines were purchased from Univar. Doxorubicin hydrochloride (~99%) was purchased from OChem Inc. (USA). All solutions were prepared in high purity water extracted from a Millipore system with resistivity of 18.2 MΩ/cm

Sonication of TA: The sonication of 1 mM tannic acid solution prepared in PBS of pH 7 was carried out in a sealed glass vial. The glass vial was inserted into 200 ml water contained in a double walled glass cell, the base of which was mounted on a stainless steel ultrasonic plate transducer of diameter 5.4 cm. The plate transducer used was ELAC Nautik USW 51-052 transducer which was powered by a T&C Power Conversion, Inc. The unit was operated at 355 kHz and 1058 kHz frequencies and at different ultrasonic power levels from 5.5 W/cm^3 to 20 W/cm^3). All reactions were performed at constant temperature of 37 ± 2 ˚C.

Characterisation

Fluorescence spectroscopy: Fluorescence spectra were obtained using a Shimadzu RF-5301PC fluorescence spectrophotometer equipped with a xenon lamp and 1.0 cm optical length quartz cell. All the measurements were carried out in PBS buffer (pH 7). Samples were excited at different wavelengths (from 320 nm to 460 nm) and the fluorescence spectra were recorded from 340 to 600 nm using slit widths of 5 nm for excitation and 10 nm for emission spectra. UV- visible absorption spectra were recorded on a Cary Bio 50 UV-spectrophotometer

HPLC: Shimadzu SCL-10AVP high-performance liquid chromatography (HPLC) equipped with a Phenomenex column model "Jupiter 5u C18 300A" and with an UV detector set at 280 nm was used to perform HPLC analysis. All chromatograms were generated by LabSolution software (Shimadzu). The injection volume was 20 µl and the flow-rate used was 1 mL/min.

For the analysis, a gradient elution was carried out with solvent A (0.5 % phosphoric acid) and solvent B (methanol with 0.5% phosphoric acid). The gradient used was 10% solvent B from 0 - 5 min, then increased to 50 % solvent B from 5-10 min and then 100 % solvent B from 10-30 min.

NMR: ^{1}H and ^{13}C NMR spectra of TA and sonicated TA particles was conducted in d_6-DMSO on Varian MR400 NMR spectrometer at 400 MHz at 25 ˚C.

SEM: The morphology of the particles was examined by high-resolution field emission environmental Scanning Electron Microscope (Quanta 200 FEI). The particles were sputter-coated with the thin layer of gold during the sample preparation.

TGA: Thermogravimetric analysis was carried out by TGA/SDTA8511e (Mettler Toledo). The analysis was conducted under the nitrogen flow at a heating rate of 10˚C/min.

Electrospray Mass spectrometry (ESMS): The ESMS analyses were performed using an Agilent 6500 Q-TOF LC/MS system. Scans were performed in both negative and positive ion modes. Also, MALDI-TOF analysis was carried out. The sample (10 mg/ml) was mixed with the matrix solution and cationization reagent in 10:1:1 ratio. The matrix and the cationization reagent used were 2, 5-dihydroxybenzoic acid and sodium trifluoroacetate, respectively.

Powder X-ray diffraction (PXRD): The PXRD analysis was performed by Bruker D8 Advance X-ray diffractometer with Ni-filtered Cu kα radiation (1.54 Å). Data were collected between 5 – 85° 2θ, with a step size of 0.02° and a scan rate of 1.0 s per step. An anti-scatter blade was used to reduce the diffracted background intensity at low angles. An incident beam divergence of 1.0° was used with a 2.5° soller slit in the diffracted beam. The sample was spun at 15 revolutions per minute.

DPPH Assay: The antioxidant activity of TA, TAS and EA was estimated from their radical scavenging activity. The 1-diphenyl-2-picrylhydrazyl radical (DPPH) was utilised for this purpose.

To 3 ml of 250 µM solution of DPPH were added different concentrations of EA, TA and TAS solutions. The absorbance was noted at 520 nm as function of time. The radical scavenging activity was determined using following expression:

$$Radical\ scavenging\ activity\ (\%) = \left[\left(A_{DPPH} - A_{sample}\right)/A_{DPPH}\right]\times 100$$

Where A_{DPPH} is the absorbance of blank DPPH solution and A_{sample} is the absorbance of DPPH solution after the addition of sample.

Cell Viability Assay: The cytotoxicity of the TA and TAS was estimated using MTT (3-(4,5-dimethylthiazol-2-yl)-2,5-diphenyl tetrazolium bromide) assay.MDA-MB-231 (human breast adenocarcinoma) were plated on 96-well plates (Costar 3596, Corning, MA, USA) with seeding density of 7000 cells per well in 100 µL of DMEM medium supplemented with 10% fetal bovine serum (FBS) and 1% of Penicillin/ Streptomycin antibiotic mixture. Cells were incubated overnight in 37°C, 5% CO_2. Particles were added to culture media at various concentrations in quadruplicates followed by incubation for 24h. Cell viability was assessed by the addition of 10 µL of 5 mg/mL MTT reagent and further incubation for 4 hours. Resulted formazan crystals were dissolved in 70 µL DMSO and absorbance was measured at 554 nm and 670 nm by Infinite M200 microplate reader (Tecan, Switzerland).

2. HPLC and Mass spectrometry of TA sonicated solution

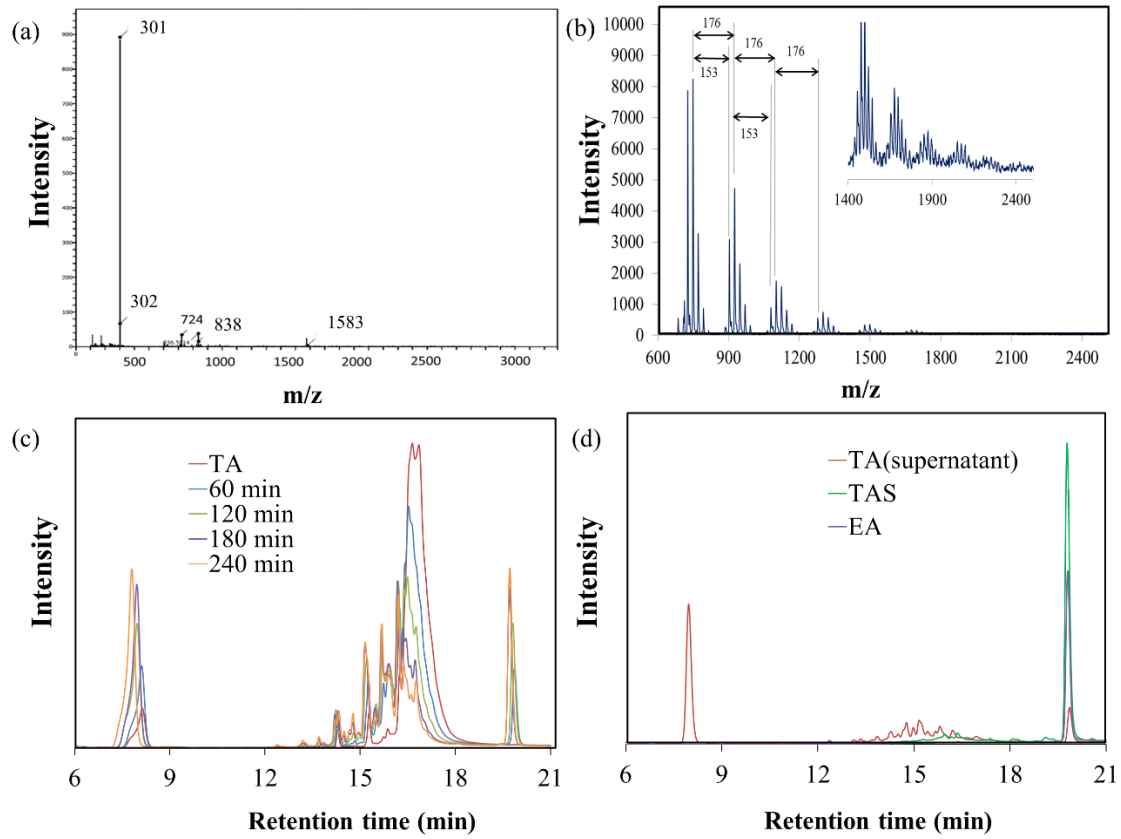

Figure S1. Analysis of sonicated TA solution and TAS particles using Mass spectroscopy and HPLC (a) ESMS analysis of TAS particles (b) MALDI-ToF spectra of TAS particles: to identify the minor high molecular weight component of microparticles, MALDI-ToF analysis was performed, which revealed the formation of some high molecular weight products with repeating unit of m/z 153 and 176 corresponding to galloyl moiety and galloyl + Na (Supplementary Fig 1b), respectively. (c) HPLC analysis of sonicated TA solution after different sonication times at 355 kHz and 5.5 W/cm^3 and (d) HPLC profile of standard EA, TAS particles and supernatant.

HPLC chromatograms indicate:

(i) The disappearance of the peak assigned to TA at 17. 5 min as a function of sonication time and the appearance of gallic acid peak at retention time 8 min which increases with an increase in sonication time (Figure S1c). This indicates the ultrasonic conversion of TA into gallic acid by hydrolysis of the ester linkages,

(ii) The appearance of a peak at 20 min which increases with an increase in sonication time. This peak could be attributed to EA as the standard EA also has a similar HPLC profile as shown in Figure 1c. This clearly suggests that major component of the particles generated by sonication was ellagic acid.

(iii) The presence of some other species in the supernatant, eluted between 12-18 min was also observed (Figure S1d), could be attributed to soluble ellagic acid derivatives.

3. UV-vis spectra of sonicated TA solution at different sonication times and of TA, TAS and EA

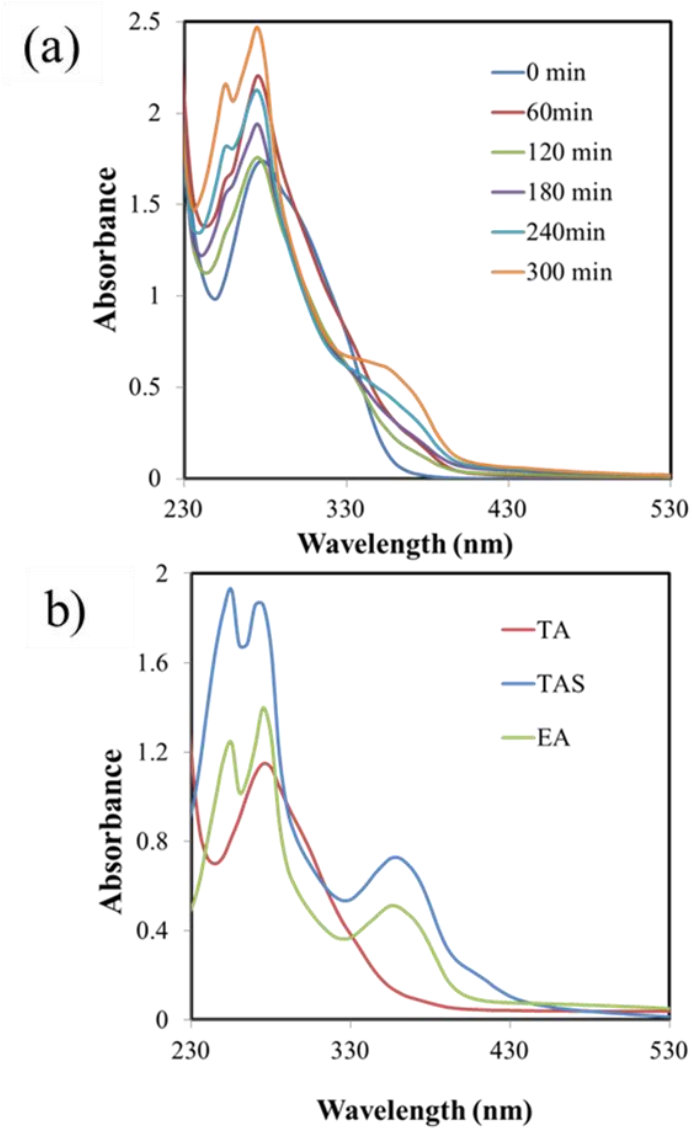

Figure S2. (a) Absorption spectra of sonicated TA solution (355 kHz and 5.5 W/cm3 after different sonication times, (b) Absorption spectra of TA, EA and TAS after dissolution in water. The absorption spectra of sonicated TA solution as a function of sonication time and TAS particles dissolved in water revealed a spectral profile similar to that of a standard EA solution with a new peak appearing at 370 nm.

4. Experimental procedure for determination of ellagic acid content

The Ellagic acid content of the sonicated tannic acid was determined using the well-established Ellagic acid assay [1].

The method is based on the formation quinone oxime of the ellagic acid nitrosylation product [1]. The ellagic acid standard solution in pyridine forms red colour nitrosylated product when incubated in $NaNO_2$ solution and gives a characteristic absorbance band at around 515 nm that can be further used to quantify the concentration of ellagic acid

For hydrolysis, 10 mg of the TAS was added to 2 N H_2SO_4 solution in a test tube. The reaction mixture was frozen in liquid nitrogen and was vacuum sealed. The content was heated for 24 hr at 100 ˚C. After the hydrolysis, the content was cooled at room temperature and filtered using vacuum filtration. The residue was then dissolved in 10 ml pyridine. 1.1 ml of pyridine and 1ml of sample solution also in pyridine were mixed and 0.100 ml concentrated HCl solution was added and the mixture was heated for 5 min at 30 ˚C. This sample was quickly mixed with 0.100 ml of 1% $NaNO_2$ (w/v in water) solution and absorbance was immediately recorded. The absorbance was again noted after incubating the sample with $NaNO_2$ at 30 ˚C for 36 min. Difference between the absorbance at 0 min and 36 min is proportional to the Ellagic acid concentration.

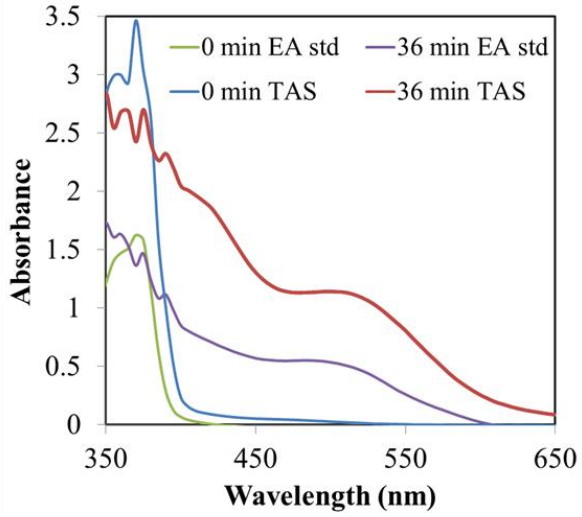

Figure S3. The absorbance spectra of nitrosylated product of EA and TAS in pyridine and after 36 min of incubation with $NaNO_2$. The appearance of the band at 515 nm indicate the presence of ellagic acid.

5. ^{1}H NMR of TAS particles

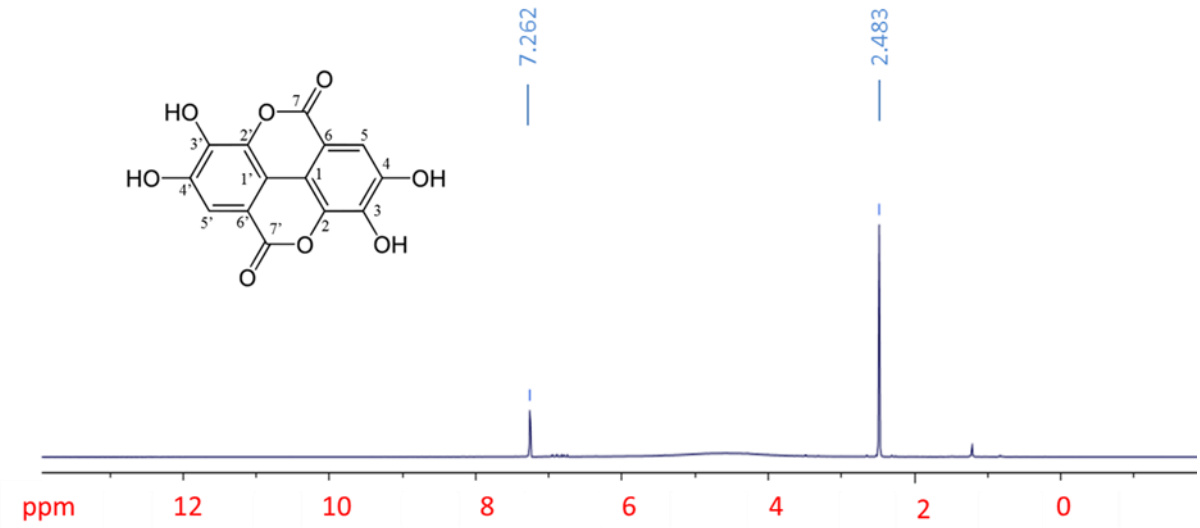

Figure S4. ^{1}H NMR spectrum of the TAS particles dissolved in DMSO represents peak at δ 7.262 due to 5, 5’ proton

6. ^{13}C NMR of TAS particles

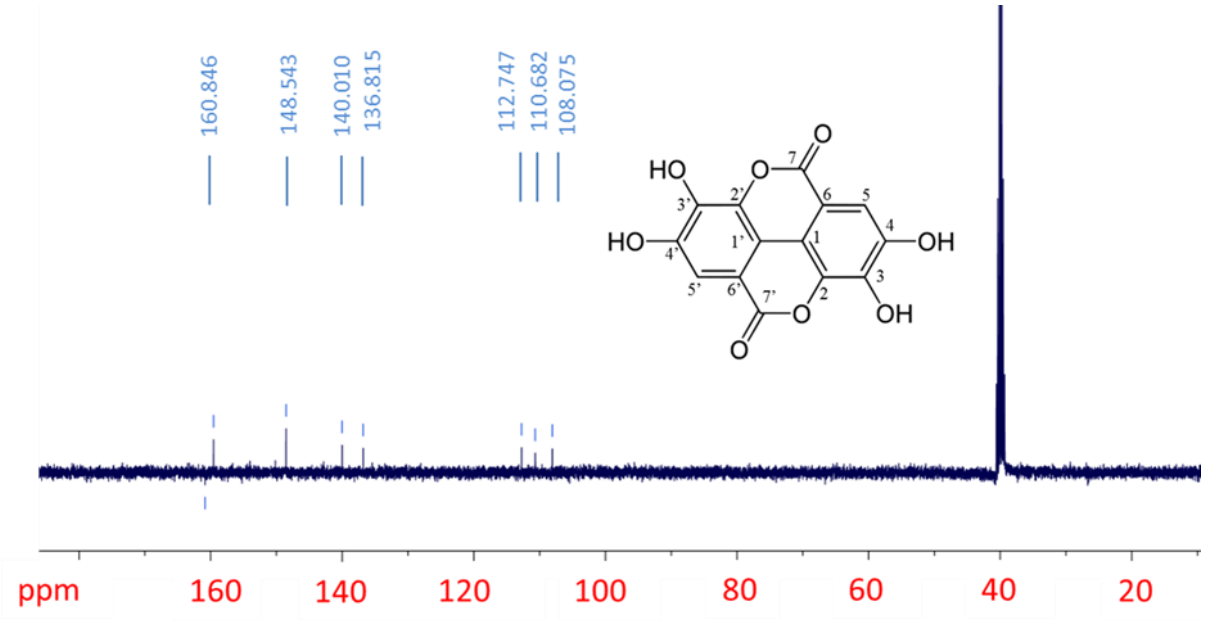

Figure S5: Figure S5: ^{13}C NMR spectrum of the TAS particles dissolved in DMSO. The peaks are assigned as follows δ 160.846 ppm- C7, 148.08 ppm- C4, 140.010 ppm - C3, and 136.35 ppm - C2. 112.747 ppm -C1, 110.682 ppm -C5, 108.075 ppm - C6

7. PXRD diffraction pattern of TA and TAS particles

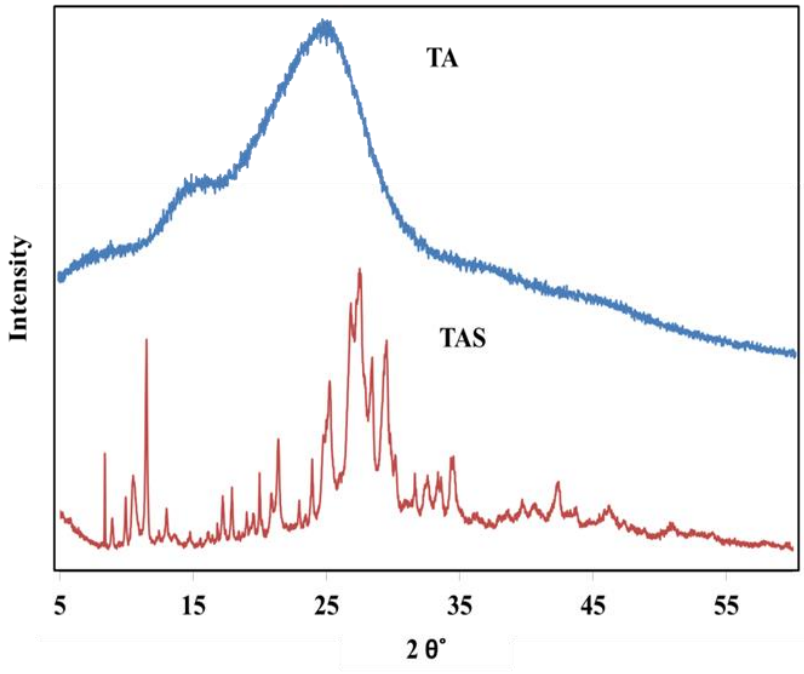

Figure S6. X-ray diffraction patterns of TA and TAS particle

8. Fluorescence spectroscopy of TA solution

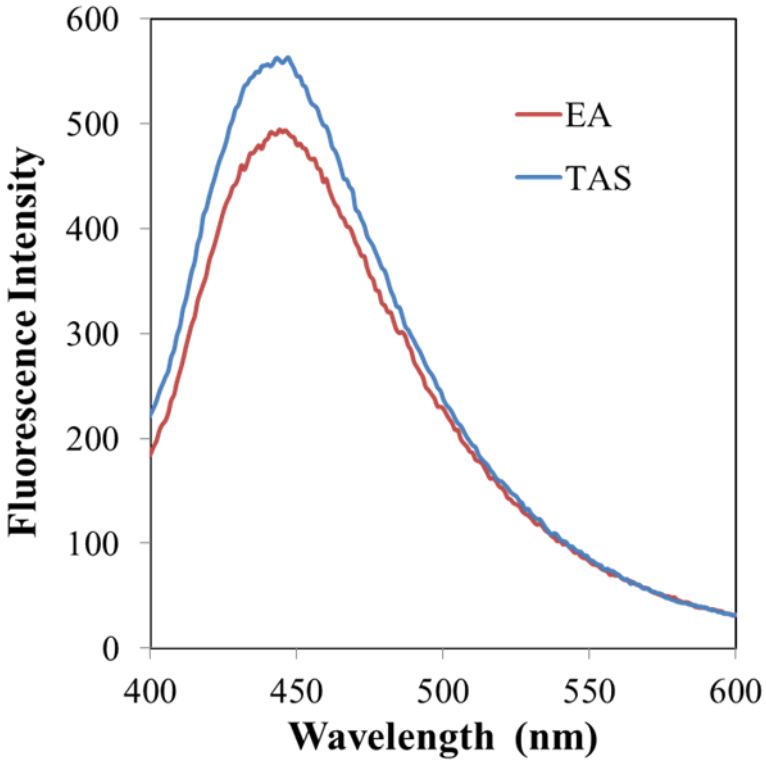

Figure S7. Fluorescence emission spectra of TAS and EA particles after dissolution in 0.1 N NaOH obtained at excitation wavelength of 360 nm

9. Thermogravimetric analysis of TA and TAS particles

Figure S8 illustrates thermal degradation curves of TA and TAS particles formed by using ultrasound. The weight loss of TA molecules started at about 80 ℃ and continued up to 200 ℃ by slight degradation with 2% weight loss. This could be due to the loss of moisture in the sample. The decomposition temperature of the tannic acid was around 230 ˚C. However, TAS particles prepared by ultrasound have different degradation temperatures. The initial weight loss was measured between 80 and 171 ℃; again, this could be due to the loss of adsorbed water, and the onset for the decomposition of TAS particles was estimated around 430 ˚C. Therefore, the tannic acid nanoparticles obtained after sonication are also more thermostable compared to tannic acid.

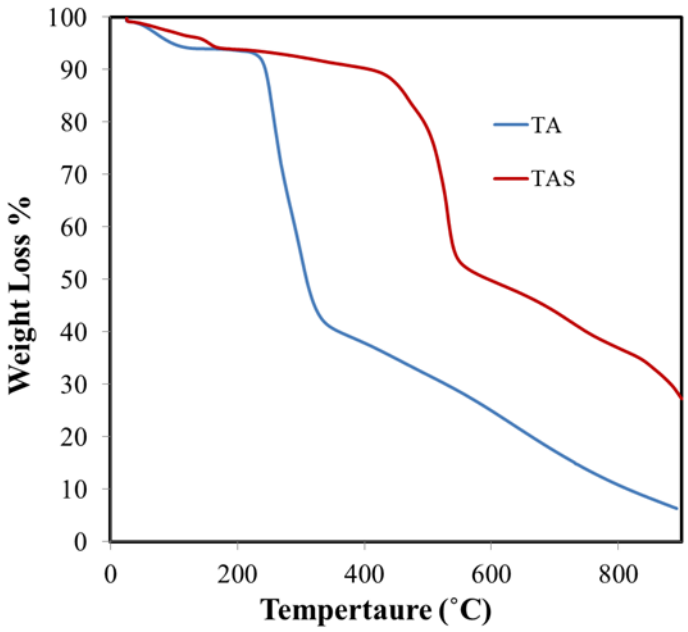

Figure S8. TGA profile of TA and TAS particles as a function of increasing temperature showing the decomposition of TA at around 200 °C and of TAS at 430 °C

10. References

[1] TC. Wilson, AE. Hagerman. *J. Agric. Food Chem.*, 1990, **38**, 1678-1683.

Chapter 6

Sound-driven dissipative self-assembly of aromatic biomolecules into nanoparticles

This chapter demonstrates the use of sound-driven dissipative self-assembly processes to assemble tryptophan dimers into supramolecular structures. Herein, experimental and computational approaches were used to unveil the role of acoustic cavitation in the formation of supramolecular nanoaggregates by dissipative self-assembly. The acoustic cavitation bubbles were employed as an energy source and transient interface to fuel and refuel the dissipative self-assembly of simple aromatic biomolecules into uniform nanoparticles. Molecular Dynamics simulations were applied to predict the formation of metastable aggregates and the dynamic exchange of the interacting molecules in the nanoaggregates. The intracellular trafficking and dissipative dissolution of the nanoparticles were tracked by microscopy imaging

6.1. Introduction

The dissipative self-assembly processes are out-of-equilibrium ubiquitous phenomena observed in biological systems. For instance, the reversible formation of actin filaments is a case of dissipative self-assembly [1]. The products of these out-of-equilibrium biochemical reactions require a continuous supply of energy to persist, and their integrity is controlled by the relative rates of formation and disassembly driven by the energy dissipation processes [2, 3]. Although common in biology, the dissipative self-assembly is only recently emerging as strategy for designing new functional materials with programmable lifetimes [2-5]. Man-made precursor systems are turned into self-assembling building blocks by an activation reaction, triggered by a source of energy, typically provided by light or a fuel molecule [2-8]. The assemblies can only be maintained in their out-of-equilibrium state by a continuous input of energy or fuels that is subsequently converted to thermal energy and waste products. Chemical fuel- and light driven DSA of organic and synthetic building blocks have been investigated, such as the self-assembly of vesicular nanoreactors [9], the gelation of dibenzoyl-L-cysteine [10], the light-driven azobenzene self-assembly into rod-like aggregates [3] and the synthetic nucleic acid strands to design synthetic DNA-based receptors [11]. Strikingly, the acoustic energy has not yet been considered as fuel in dissipative self-assembly processes. However, it was reported that low frequency sonication (29 and 80 kHz) can exert thermal and kinetic effects to promote the nucleation and the supramolecular reorganization of thermodynamically stable amyloid-like fibrils [12, 13]. To the best of our knowledge, the ultrasound-driven dissipative self-assembly has never been reported. Here, we provide an additional conceptual framework to obtain dissipative self-assembly of natural aromatic biomolecules. We combine experimental and computational approaches to unveil the role of the acoustic field in the formation of out-of-equilibrium nanoaggregates using, as a

proof of concept, a simple amino acid, L-tryptophan. We anticipate that this approach can be used for the dissipative self-assembly of many other aromatic biomolecules, including phenylalanine, peptides, aromatic drugs and natural compounds. We demonstrate that the acoustic bubbles driven at high frequency standing waves, provides a reactive surface for the dimerization of aromatic amino acids into amphiphilic molecules and an energy source to fuel and refuel their dissipative self-assembly into uniform nanoaggregates. The computational study predicts that the aggregation of tryptophan dimers occurs in less than 20 ns when a high local concentration is experienced at the cavitation bubble-solution interface. The lifetime of the nanoaggregates can be tuned by changing the pH of the media when the supply of acoustic energy is discontinued. The unique optical and bio-functional properties of nanoparticles have been employed for probing their intracellular dissipative dissolution by imaging.

6.2. Results and Discussion

6.2.1. The oscillation and collapse of transient cavitation bubbles induce DSA of tryptophan dimers.

To investigate the ability of ultrasound as a source of energy to induce DSA processes, an aqueous solution of tryptophan (1 mg/mL, 4.9 mM) was sonicated up to 5 h at pH 5 using ultrasonic frequency and power of 355 kHz and 6 W/cm^3, respectively. The phenomenon occurring during sonication is depicted in Figure 1a. We recently reported that the oscillating surface of acoustic cavitation microbubbles acts as a reactive and catalytic site for the C-C coupling of amphiphilic moieties [14]. In this study, hydroxylated tryptophan species and hydroxylated tryptophan dimers, hereafter referred to as dTrp, were formed on the bubbles surface (Step 1 - Figure 1a step 1 and Figure 1c). The dTrp ultimately self-assembled into uniformly shaped spherical nanoparticles during bubbles collapse (Step 2 - Figure 1b) with ~ 40 % yield. To gain insight into molecular

composition of the nanoparticles and on the reaction mechanism, HPLC (Supplementary Figure S1), mass spectroscopy (Supplementary Figure S2), and EDS (energy dispersive X-ray spectroscopy, Supplementary Figure S3) analyses were performed. The analytical characterization of the sonicated solutions indicated the formation of different hydroxylated and dimeric species upon ultrasonic treatment of tryptophan. Figure 1c shows a schematic of ultrasonic modification of tryptophan describing the process of formation of hydroxylated products and the further coupling of these species into dimers. It is well known that sonication of an aqueous solution results in the formation of H and OH radicals due to acoustic cavitation [15]. Previous computational and experimental studies have shown that tryptophan bears multiple sites for the OH radical attack and hydrogen can be abstracted from the indole rings [16]. In our system, OH radicals generated during the high frequency ultrasonic treatment can abstract protons from the pyrrole or benzene moiety which then undergo OH radical addition to form hydroxylated products (structure 2, 3 and 4 in Figure 1c). In addition, two Trp radicals can combine through C-C or C-N coupling to form dimers or hydroxylated dTrp (structure 5, 6 and 7 in Figure 1c).

The dynamic behaviour of cavitation bubbles and the resulting physical and chemical effects are intertwined with the dissipative self-assembly of dTrp molecules as depicted in Figure 1a. The change in bubble radius as a function of time (Figure S4a) was calculated using Rayleigh-Plesset equation for the given frequency (355 kHz) and power (6 W/cm^3) [15, 17-19]. From these data the maximum radius of gas bubbles driven by the acoustic field was estimated as ~14 μm. Figure S4a shows that a single acoustic cycle lasts for approximately 2 μs at given conditions, during which the bubble size increases until the R_{max} is reached and bubble collapses. Based on the diffusion coefficient of the amino acids (700-1000 μm^2/s) and dTrp (870±78 μm^2/s) which was measured by

fluorescence correlation spectroscopy (see Supplementary Figure S5), this is likely a sufficient time for both Trp and dTrp molecules to diffuse, adsorb, dimerize and further aggregate on the bubble surface [14, 17]. First, the tryptophan molecules will be adsorbed at the bubble surface (Step 1-Figure 1a) to form hydroxylated and dimeric species mediated by bubbles collapse and generated OH radicals. Although there are several reports suggesting the dimerization of Trp moieties by Fenton's reactions and photolysis oxidation, none of these studies have ever reported the formation of nanoparticles [20, 21]. Next, after 3 h sonication uniform spherical nanoparticles (dTrpNPs) were formed by the self-assembly of the dTrp species (Figure 1a). In Figure 1b, a representative SEM image of the uniform dTrpNP is shown. The average diameter of tryptophan nanoparticles obtained from the SEM analysis was 230 nm±50 nm. The ζ -potential of dTrpNP measured at pH 7 was found to be -26 ± 7 mV. dTrpNP were negatively charged because of the deprotonation of the carboxyl and aromatic hydroxyl groups in water at pH 7. This is supported by the potentiometric titration of dTrp (Supplementary Figure S6) indicating three pK_a values at approximately 2, 6 and 10 ascribed to carboxylic acid, hydroxyl and ammonium groups deprotonation respectively [22]. The chemical composition of dTrpNP after dissolution in alkaline conditions was determined by mass spectrometry (Supplementary Figure S2b). The mass spectrometry analysis confirmed that dTrpNP were mostly composed of hydroxylated Trp dimer (m/z 445- dTrp). It is also worth mentioning that nanoparticles obtained in this study (through oxidative coupling) are different to dipeptide particles, as no evidence for the formation peptide bond was observed.

We noticed that at these experimental conditions, the dTrp have a strong tendency to aggregate into nanoparticles only when ultrasound is applied. Conversely, after the dissolution of dTrpNP in alkaline conditions at the same concentration they were formed

during sonication (50 μg/mL), they were unable to self-aggregate, once the pH was brought back to neutral or acidic conditions. This indicates that the self-assembly of dTrp is thermodynamically disfavoured in bulk at that concentration and it is likely to be energetically fuelled by the high frequency ultrasound. To confirm this, the surface and aggregation properties of dTrp were evaluated. The surface tension of aqueous solution of dTrp dissolved at the same concentration (1.6 mM) was 67.3 mN/m indicating surface activity and therefore ability to adsorb on the cavitation bubbles. The critical aggregation concentration, cac, and the surface excess concentration (determined using Gibbs adsorption equation) of the dTrp were 100 μg/mL and $1.1x10^{-6}$ mol/m^2, respectively. These results further confirm that the ultrasound assisted self-assembly of dTrp occurred well below the cac (50 μg/mL). Hence, the association of dTrp building blocks to give aggregates is not thermodynamically favoured because the molecules reside in a global minimum in the energy landscape as depicted in Figure 2a. However, a transient energy input provided by ultrasound (cavitation) can push the building blocks into a high-energy state where the self-assembly can take place (Figure 2a). The thermodynamically favoured dTrp nanoaggregates can be formed only at concentrations higher than cac and showed a different morphology with micrometer sized clusters which lack structural organization (Supplementary Figure S4b). The lifetimes of out of equilibrium dTrpNPs can be tuned by altering the kinetics of the dissipative step, i.e., by changing the pH (Figure 2b). dTrpNPs were stable at pH 5 over weeks, dissolve within 48 hours at pH 7 whereas they promptly dissolve by increasing pH above the pK_a of the aromatic hydroxyl and amine groups (> pH 10) (Figure 2b). This indicates that the repulsive electrostatic interactions between negatively charged molecules at alkaline pH, perturb the stability of the nanoaggregates, inducing their dissolution into water soluble building blocks. We hence, speculate on the possible role of cavitation bubbles in driving DSA processes. The

oscillating bubbles, driven by the high frequency acoustic field, provide an interface for the formation of dTrp aggregates far below the cac by pre-organizing the molecules on the transient liquid-air interface (step 2 in Figure 2c). The experimental value of area

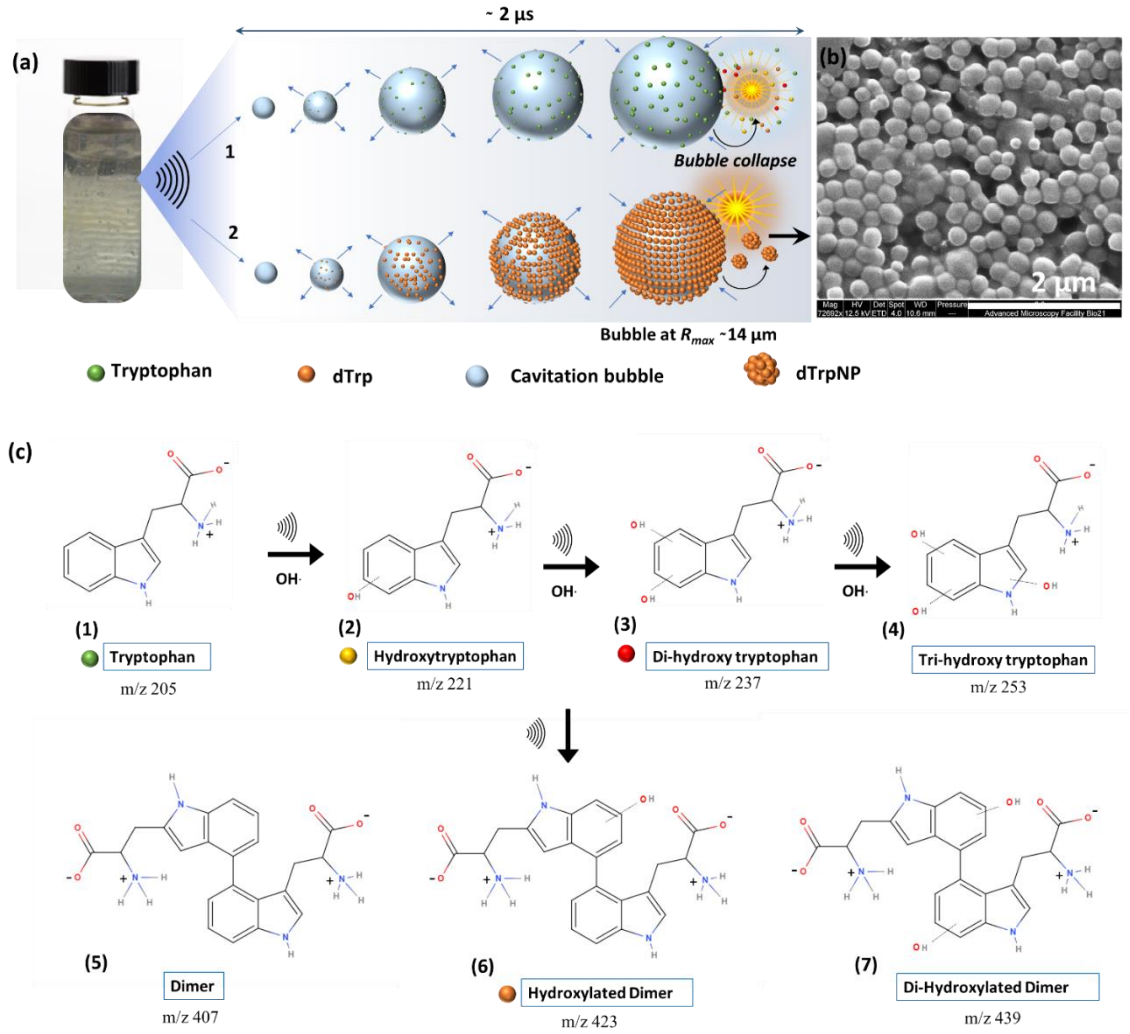

Figure 1: Reaction scheme and proposed mechanism for the formation dTrpNPs by dissipative self-assembly (a) Schematic showing the formation of standing waves in the glass vial on sonication, increase in bubble size and gathering of Trp (step 1) and dTrp molecules (step 2) on bubble-solution interface during one oscillation cycle where collapse of the bubble generates hydroxylated products and dTrp (step 1) and dTrpNPs (step 2). (b) SEM images of the dTrpNPs generated after 3 h sonication of tryptophan below the cac (c) A reaction scheme showing the formation of the hydroxylated products due to attack of hydroxyl radicals on indole ring of tryptophan followed by dimerization reaction to form dTrp species which ultimately self-assemble into nanoparticles.

occupied by each molecule on the gas-liquid interface was calculated using the surface excess measurements and it was found to be approximately 1.52 nm^2. Assuming the molecules as spherical, the number of dTrp covering the surface of oscillating bubbles at the maximum expansion (Step 2 -Figure 1c) can be approximately estimated as 2.4 $x10^8$.

In these transient conditions, the dTrp molecules experience an activated state where the surface tension and the high local concentration results in a transient thermodynamically favoured aggregation process and formation of uniform spherical nanoparticles (Step 3-Figure 2c). This is also energetically allowed because a higher local concentration and strong intermolecular interactions are simultaneously experienced by the building blocks. Overall the dissipative self-assembly of dTrp is coupled to a chemical reactions network that includes (i) the irreversible chemical conversion of precursors (Trp) into building block (dTrp) (Step 1-Figure 2c), (ii) the reversible activation of building blocks on the surface of cavitation bubbles which results in high local concentration of dTrp (Step 2 -Figure 2c) and (iii) a reversible reaction where the activated building blocks self-assemble to form nanoaggregates (Step 3 -Figure 2c). The nanoaggregates dissipate the free energy acquired during the steps (ii) and (iii) to recover the original non-activated building block state over prolonged time, depending upon the pH conditions (Step 4-Figure 2c). The overall process has been described schematically in Figure 2c. The nanoaggregates can dissipate the energy and relax to the thermodynamic state in the presence of an external agent such as OH-. Of note, if the acoustic energy supply stops, the nanoaggregates relax spontaneously to the thermodynamically stable state over prolonged times (24-48 h) (Step 4 -Figure 2c). Two assembly-disassembly cycles were performed to demonstrate that the system can be re-fuelled by the acoustic energy. In the second cycle the protonation of carboxyl groups was required to assist the self-assembly of dTrp (Step 5- Figure 2c). Figure S7a&b shows the size distribution and SEM image of the nanoparticle obtained in second cycle. The Z-average size of nanoparticles was ~ 188 ± 50 nm. This may indicate that the amphiphilic properties of the building block changed upon sonication by further hydroxylation of dTrp molecules and the surface properties must be tuned by the protonation of carboxyl groups to maximize the surface activity and diffusion

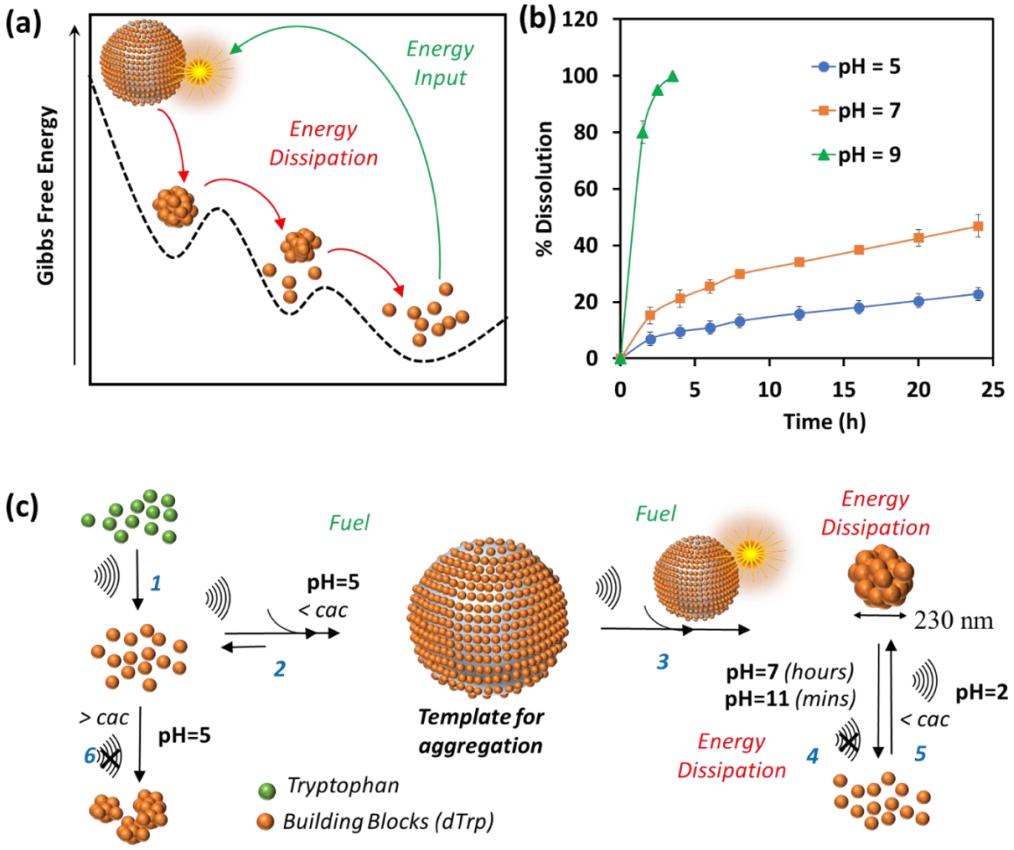

Figure 2: (a) The Gibbs free energy landscape of dissipative self-assembly of dTrp to form dTrpNPs where dTrp building blocks are residing in global minimum and transient energy input due to acoustic cavitation lead to out of equilibrium self-assembly of dTrp into dTrpNP. Furthermore, dTrpNPs undergo subsequent energy dissipation to recover to the original non-activated building block state over prolonged period of time; (b) Dissolution kinetics of dTrpNPs at 37 °C at different pH as a function time suggesting slow dissolution of dTrpNP at pH 5, pH 7 and prompt dissolution at higher pH (pH 9) around the pK_a of the aromatic hydroxyl and amine groups; (c) General scheme for the ultrasound driven dissipative self-assembly of dTrp to dTrpNPs. Step1 shows the ultrasonic conversion of Trp to building blocks dTrp, step 2 and 3 shows how the cavitation bubble act as fuel providing a template for adsorption of dTrp and high concentration conditions to facilitate the aggregation upon collapse leading to the formation dTrpNPs. Step 4 shows the energy dissipation step upon increasing pH to form the pristine building blocks, step 5 shows how the acoustic energy can refuel the dissipative self-assembly of dTrp below the cac at pH 2

at the gas-liquid interface of dTrp. To support this hypothesis, the surface activity of dTrp in aqueous solution was determined using surface tension measurements at different pH values. The surface tensions at pH 2, pH 7 and pH 11 were 58.9 mN/m, 70.5 mN/m and 80.7 mN/m, respectively, suggesting higher surface activity of dTrp molecules at low pH. However, The fluorescence emission spectra of dissolved particles obtained during recycle of dissipative self-assembly process showed λ_{em} ~474 nm (λ_{ex} = 400)which

was similar to what was obtained with dTrpNP obtained intially (Figure S8a), suggesting no significant chemical changes in the composition.

6.2.2. Molecular Dynamics (MD) simulations predict the formation of metastable aggregates at high local concentration

To gain insight into the driving forces behind the formation of dTrpNPs and further confirm the vital role of acoustic cavitation bubbles, Molecular Dynamics (MD) simulations of tryptophan dimers were performed. To this end, six replicas of dTrp were randomly inserted in a 64 nm^3 cubic box in the presence of water Figure 3a. This condition can mimic the high local concentration experienced by the amphiphilic dTrp molecules adsorbed on the surface of cavitation bubbles as depicted in Figure 1a. MD simulations are usually unable to reproduce the spatial and the temporal scales required for analysis of larger aggregates, however, the early stages of aggregation can be simulated, and the data can be used to characterize the structural features of the final aggregates [23]. Representative snapshots from MD simulations up to 865 ns are shown in Figure 3a. In Figure 3b1, the Solvent Accessible Surface Area (SAS) of the six dTrp molecules during the first 50 ns of simulation is reported. The global SAS value of the solutes typically decreases when aggregation takes place, and this parameter is sensitive to both the number of the aggregates present in the simulation box and their compactness [23, 24]. At the simulation start point, dTrp molecules are far from each other and the global SAS value is slightly below 33 nm^2. Figure 3b1 shows that during the first 20 ns the SAS value of the six dTrp molecules decreases from 33 to roughly 20 nm^2. This observed decrease in the global SAS is likely due to the occurrence of contacts between molecules upon aggregation. To confirm this, the SAS of each single dTrp molecule, during the whole simulation was evaluated (Figure 3b2). In this case, the surface of each single dTrp molecule is considered as totally exposed to the solvent and its value could change only

because of intra-molecular conformational transition. Figure 3b2 shows that the starting SAS value of each single dTrp molecule is retained during the whole simulation, irrespective of presence or absence of aggregates. A value of 5.5 ± 0.2 nm^2 was measured for all the molecules, which is exactly a sixth of the starting value of the global SAS. This suggests that the intramolecular conformational changes only slightly affect the SAS of the single dTrp molecule, and the global SAS variation is effectively probing the aggregation process. In addition, data reported in Figure 3b1 indicate that, in the

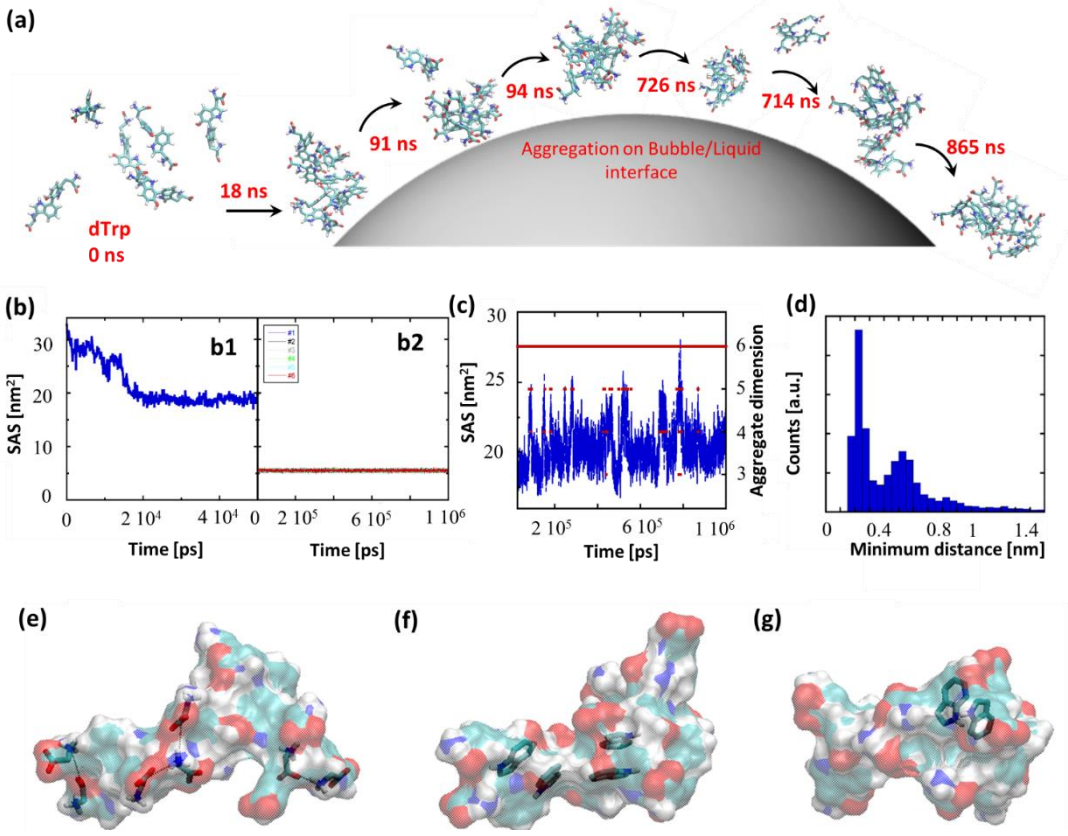

Figure 3: (a) Molecular dynamics simulation of six replicas of dTrp molecules, snapshots at 0 ns, 18 ns, 91 ns, 94 ns, 714 ns, 726 ns, and 868 ns and their schematic adsorption at bubble-liquid interface. The first aggregate was formed just after 18 μs, (b1) Global SAS of the six dTrp molecules during the first 50 ns of the simulation, (b2) SAS calculated for all the six dTrp molecules singularly considered during the whole trajectory (1 μs) (c) SAS value calculated on all the six dTrp molecules (blue line, y axis on the left) and number of monomers in the aggregates (red points, y axis on the right) during the simulation time, (d) Distribution of the minimum distance of a pair of dTrp during the simulation. The distance has been calculated between 25 ns and 1 μs (e), (f) and (g) Snapshot from MD simulations. The dTrp molecule are shown as semitransparent surfaces. Models of (e) ionic, (f) π-π interactions and (g) H-bond involving aromatic rings as acceptors. The involved atoms are represented as solid sticks. The C, H, N and O atoms are colored in cyan, white, blue and red, respectively

simulated conditions, stable aggregates form in less than 25 ns. This lag time has been excluded from the further simulation analysis run up to 1 μs. Figure 3c shows the behaviour of the global SAS from 25 ns to the end of the simulation (1 μs). From the minimum distances between all the possible pairs of monomers, we have evaluated at each time, the number of units present in the aggregates, i.e. aggregation number. Figure 3c shows that a single aggregate involving all the six molecules is present in almost all the simulation time (continuous red line). More in detail, aggregates of 6, 5, 4 and 3 dTrp molecules are present for the 87.6, 8.1, 4.2 and 0.1 % of the simulation time (dashed red lines) respectively. Figure 3c shows that when only an aggregate of six dTrp is present, the global SAS remains below roughly 22 nm^2; on the other hand, when single monomers or dimers come off from the aggregate the SAS suddenly increases to higher value.

To discriminate the different contributions to the stabilization of the formed aggregates, the different interactions observed during the simulation were screened. The average number of hydrogen bonds detected during the simulations were 5±2, however other interactions can play a role in the aggregate stabilization. Figure 3e-g depicts the different interactions observed during the simulation. Ionic interactions between the charged carboxyl and amine groups have been first identified (Figure 3e). The presence of aromatic moieties in aqueous environment favours the stabilization of π-π interactions (Figure 3f) between the indole moieties present in the dTrp molecules, which may result in peculiar optical features later investigated. Finally, in Figure 3g an example of unusual hydrogen bonds in which the aromatic ring act as acceptor is also reported. This kind of interaction, which is about half as strong as a normal hydrogen bond, is known to play a significant role in molecular associations [25]. All these types of interactions have been systematically observed during the all simulation process and we can assume they all contribute to the formation and stabilization of the nanoaggregate.

To investigate the persistence of the interactions between couples of molecules in the aggregate, we have calculated the distribution of the minimum distances for all the possible 15 pairs of dTrp molecules during the simulations. All distributions are similar, Figure 3d reports an example of this distribution profiles. The distribution shows that the pairs populate both low and high minimum distances values during the simulation. This suggests that, although the aggregation of six molecules persists for almost all the simulation, the molecules assembled into the aggregate are dynamically interacting with each other. Overall the computational results are consistent with the rapid formation and stability of dTrp nanoparticles via salts bridges, π-π and H-bonding interactions. In addition, the dynamic exchange of the interacting molecules in the aggregates may contribute to the dissipation of energy process resulting in the dissolution of the nanoaggregates.

Finally, from the MD data we have evaluated the number of dTrp molecules present in a single 230 nm sized nanoparticle. From the six dTrp molecules aggregates SAS value (20±1 nm^2) and assuming a spherical shape for the formed aggregates, we can estimate a volume of 8.4 nm^3. As a result, the estimated number of dTrp molecules present in a single 230 nm sized nanoparticle are approximately $5x10^6$. From the SAS data of isolated dTrp molecules (surface and planar area of to 5.5±2 nm^2 of 1.5 nm^2 respectively), we can also estimate the maximum number of dTrp molecules that can be placed into a monolayer covering the whole surface of a microbubble which is approximately $245x10^6$. This is in good agreement with the experimentally measured surface excess concentration ($2.4\ x10^8$). These results suggest that the collapse of a single bubble can in principle produces a single or more NPs. As the number of dTrp molecules covering the bubble surface exceeds the estimated number of molecules present in a single dTrpNP we can speculate that each collapsing bubble can give rise to the formation of a few nanoparticles

as show in Figure 1a. In conclusion, the experimental and computational results are consistent with the hypothesis that the dTrpNPs arise from the rapid collapse of the microbubble and that they are formed by DSA of the molecules adsorbed at the surface of the same microbubble during the acoustic cavitation.

6.2.3. Probing the intracellular dissipative processes of dTrpNPs in different cellular compartments by imaging.

A key challenge is however, understanding the interactions of dTrpNPs with biological systems at the cellular and subcellular levels. The kinetics of cellular uptake, intracellular trafficking, dissolution and ultimately bioactivity of dTrpNPs strongly depend on whether the dissipative processes investigated in test tube can take place in the crowded and complex intracellular milieu. We found that the optical properties of dTrpNPs offer a tool to gain insight into the intracellular behaviour of dTrpNPs. For this purpose, first, the optical properties of obtained dTrpNPs in the visible range were studied using fluorescence spectroscopy (Figure S8a). The fluorescence emission spectra of dTrpNPs acquired at different excitation wavelengths show different emission bands at 465 nm, 690 nm and 750 nm when excited at 400 nm, 575nm and 640 nm, respectively (Figure S8a). A very weak emission was observed when dTrpNPs were excited at 488 nm (Supplementary Figure S9c). As tryptophan and hydroxylated tryptophan are not fluorescent in the visible and near- red regions, the emission peaks can be ascribed to dTrp and its nanoaggregates. The extended degree of conjugation in the dTrp dimers lead to the emission peak at 465 nm [22]. Intense emission bands in the far-red and near IR region (650-860 nm) were observed when the dTrpNPs suspension was excited at 575 nm and 640 nm (Figure S8b). These emissive states can arise from the aggregates as a result of the π-π stacking interactions between aromatic moieties which was also predicted by MD study [26]. In fact, when the fluorescence spectrum of dissolved dTrpNPs was

acquired, the peaks in the red region were absent, whereas the emission of the soluble dTrp at 470 nm was preserved (Figure S8a), confirming that the red-shifted peaks at higher wavelengths > 600 nm are due to intermolecular interactions stabilizing the dTrpNPs. The quantum yield of tryptophan self-assembled particles was measured at excitation wavelength 575 nm was found to be around 0.39. This was measured using rhodamine B as a reference. The good photostability of dTrpNPs is shown in Supplementary Figure S9a where insignificant decrease in the fluorescence intensity was noted, when dTrpNPs were irradiated under the microscope by 401 nm and 488 nm laser for over 5 min. In addition, the fluorescence intensity (at 465 nm and 690 nm) did not decrease even after months of storage at room temperature confirming the stability of the dTrpNPs (Supplementary Figure S9b). On the other hand, fluorescence probes like Rhodamine 6G, FITC, Cy3, etc. undergo bleaching in few seconds and require storage at -20 ˚C [27-29]. Overall, the spectral features, the good quantum yield, the high photostability of dTrpNPs can be advantageous to track their intracellular trafficking and disassembling. There are different factors that can affect the optical properties and stability of dTrpNPs in the extra and intracellular environment. Important factors are the pH changes and protein interactions. The stability, and integrity and interactions of dTrpNPs with serum protein was investigated. The possible association or disassembly of dTrpNPs with Fetal Bovine Serum (FBS) was studied using Nanoparticle Tracking Analysis in PBS and 100 % FBS. A slight increase in particle size from 230 ± 50 nm to 280 nm ± 65 nm was noticed. This increase can be attributed to the adsorption of protein corona onto the surface of nanoparticles due to the hydrophobic or electrostatic interactions. These results also indicate that there was no aggregation or disassembly of dTrpNPs even in 100% FBS solution revealing that NP have a good colloidal and structural stability in the extracellular milieu. Interestingly, the adsorption of protein

corona on dTrpNPs surface produce a 3-fold increase in green emission (Supplementary Figure S9c) compared to untreated dTrpNPs. This increase in quantum yield was also observed when dTrpNPs were suspended in alkaline conditions (Supplementary Figure S9d), therefore it is ascribed to either the deprotonation or protein induced coordination of the aromatic hydroxyl groups in dTrpNPs. However, interaction of particles with serum proteins can alter slightly circulation lifetime, uptake efficiency, immune response and intracellular trafficking of the particles. Next, we verified possible cellular cytotoxicity effects exerted by dTrpNPs. The MDA-MB-231 cells were incubated with dTrpNPs at different concentrations from 3 to 100 µg/ml for 24 h and 48 h. Figure S10a shows that the particles exhibit negligible cytotoxicity even after 24 h and 48 h at all the tested concentrations. We evaluated the association of dTrpNPs with MDA-MB 231 cells as a function of time using flow cytometry under different fluorescent channels (Figure S10b).

The association of dTrpNPs with cells relies on both membrane binding and intracellular uptake processes. We observed rapid and complete association of dTrpNPs with cells in the first 6.5 h of incubation (Figure S10b). To gain insight into cell internalization mechanism the cells were incubated with filipin, pitstop-2, and ethylisopropyl amiloride (EIPA) to inhibit caveoloe-dependent endocytosis, clathrin-dependent endocytosis and macropinocytosis and then incubated with dTrpNP (10 µg/ml). Figure 4a and 4b suggests that almost no uptake inhibition was observed with filipin and pitstop-2, however,EIPA on the other hand led to 50 % inhibition of uptake of dTrpNP. Therefore, the uptake of dTrpNP can be through macropinocytosis. Furthermore, for the intracellular trafficking of dTrpNPs, cells were incubated with 10 µg/mL nanoparticle suspension for 5 h and media was replaced followed by further incubation for up to 8 h, 24 h and 48 h at 37 °C in fresh media. The imaging of live cells incubated with dTrpNPs was carried out using

confocal microscopy to investigate the kinetic of disassembly of dTrpNPs inside the cells and blue, green, red fluorescence was observed under different fluorescence channels (Figure 5a). After 8 h and 24 h incubation, cells show mainly the punctuate fluorescence pattern with limited fluorescence diffusely spread throughout the cytosol in the blue, green and red channel. After 48 h incubation, the cells exhibited blue and green fluorescence signal which spread in the cytosol whereas the red fluorescence disappeared. The punctuate pattern indicates the partial confinement of dTrpNPs into acidic endo-lysosomes (pH 5-6). As the red emission is indicative of the dTrpNPs aggregate state, these results suggest that a time dependent dissolution of dTrpNPs occurs in the cytosol (pH 7) after escaping from endo-lysosomes.

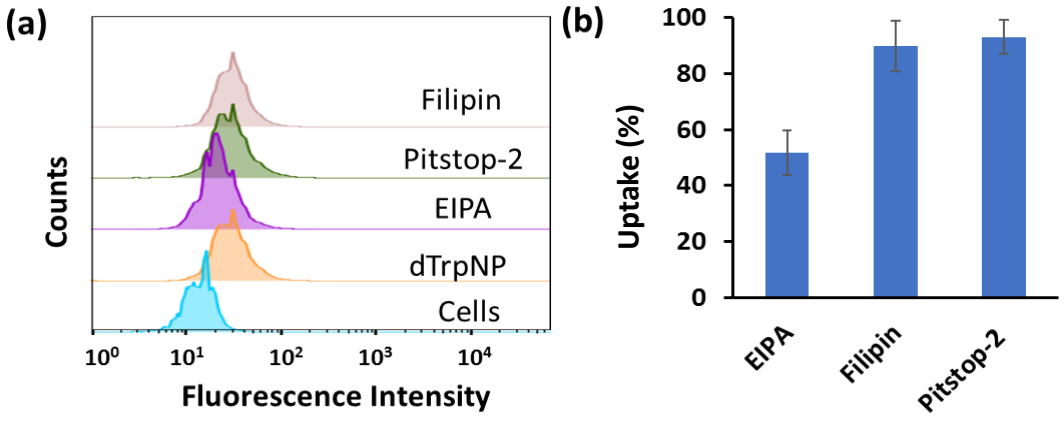

Figure 4: (a) Fluorescnce intensity histogram of MDA-MB-231 cells before and after treatment with endocytic inhibitors and dTrpNPs measured using flow cytometry, (b) The effect of different endocytic inhibitors on the uptake of dTrpNP.

To advance the understanding of the intracellular route of dTrpNPs, we examined their endocytic trafficking as a function of time in fixed cells by using the immunostaining of organelles. The MDA-MB-231 cells were incubated with dTrpNPs for 2.5 h, washed with fresh medium to remove the extracellular dTrpNPs, and cultured for further 2.5 h, 5 h and 21.5 h at 37 ˚C corresponding to observation after 2.5 h, 5 h, 8.5 h and 24 h.

Immunostaining of early endosome, late endosome and lysosome was performed using EEA1 antibody, Rab7 antibody, LAMP 1 markers and AF 647 secondary antibody. Figure 5b shows the representative confocal microscopy images of cells vesicles (red signal) and dTrpNPs (green signal) acquired using 640 nm and 560 nm lasers respectively, after 2.5 h, 5 h, 8.5 h and 24 h observation times. Confocal parameters were adjusted to minimize the intrinsic fluorescence of dTrpNPs under 640 laser scanning. It was observed that for all three organelles i.e., late endosome, early endosome, and lysosome; the colocalization (yellow signal) was maximum until first 5 h and almost negligible after that. The PCC (Pearson correlation coefficient) values were used to analyse the images and quantify the extent of colocalization (yellow signal) of organelles with dTrpNPs (Supplementary Table S1).

The PCC values estimated at different incubation times indicates the amount of colocalization. Figures 5b 1-2 and 5b 5-6 and corresponding PCC values (0.5-0.6) suggest that dTrpNPs partially colocalize with both early and late endosome compartments after 2.5 h and 5 h observation time. Conversely after 8 h and 24 h, the confocal microscopic images (Figure 5b 3-4 and Figure 5b 7-8) and the corresponding PCC values (0.2-0.3) indicate a weak colocalization of dTrpNPs with both early and late endosome. In addition, negligible colocalization with lysosome at all times was found (Figure 5b 9-12) indicating that endosome and lysosome were not fusing, and lysosomes were not involved in the dTrpNPs trafficking. Taken together, these results clearly suggest that the endosomal escape of dTrpNPs toward the cytosol progressively occurs after 2.5 h incubation. Subsequently, the shift in pH from 5.5 to 7 can trigger the dissipative dissolution of dTrpNPs in the cytosol. This agrees with our study in test tube that show that dTrpNPs are dissolving very slowly at the endosomal acid pH 5-6.

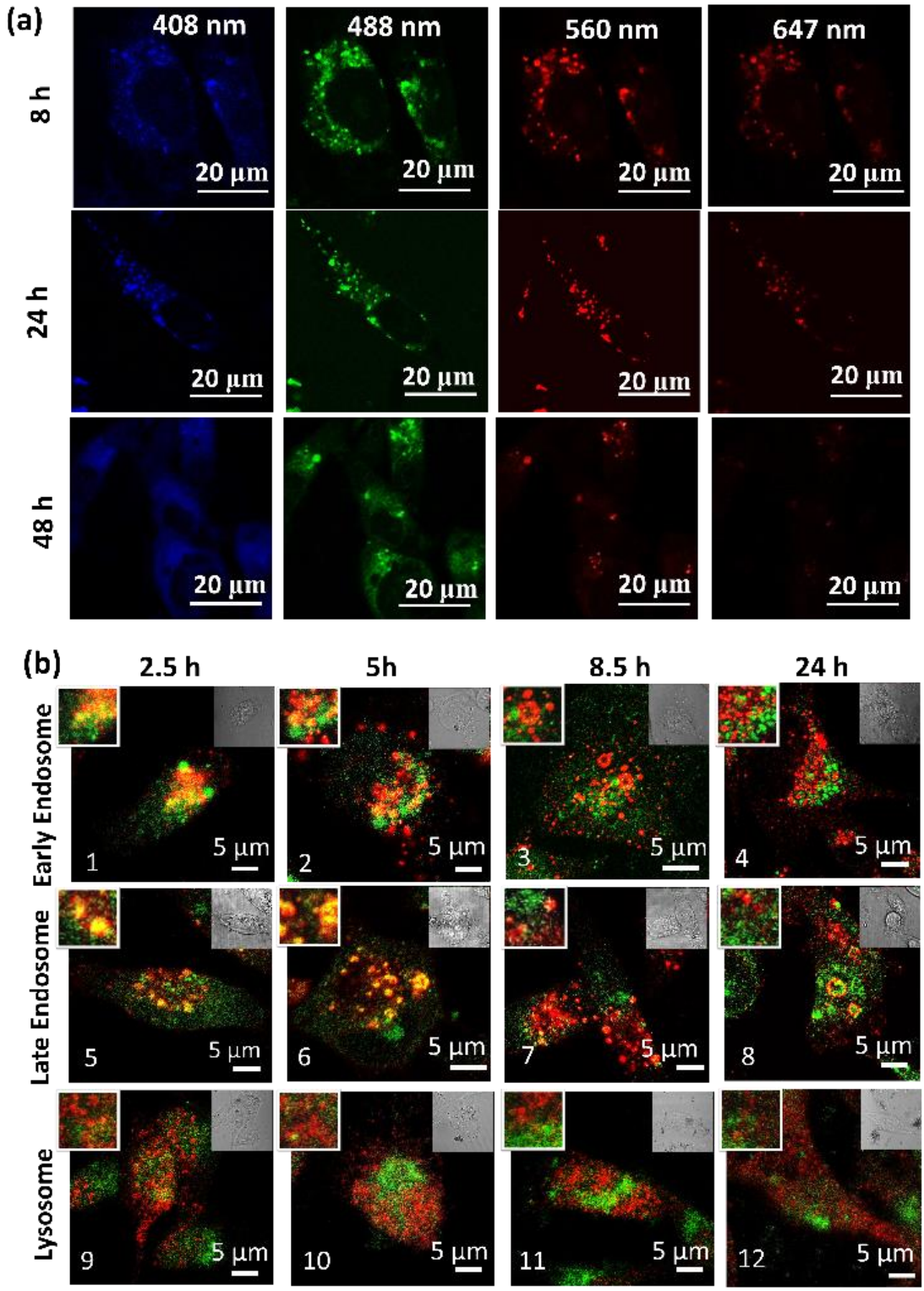

Figure 5: (a) Confocal microscopic images of the MDA-MB-231 cells incubated with the dTrpNPs at 37 °C for 8 h, 24 h and 48 h; (b) Colocalization studies of dTrpNPs (green) with different constructs(red) after 2.5 h washout and further 5 h, 8 h and 24 h incubation with confocal microscopy. The early endosome, late endosome and lysosome were stained with rabbit anti-EEA1 monoclonal antibody, rabbit anti-Rab7 monoclonal antibody and rabbit LAMP-1 respectively followed by staining with the anti-rabbit secondary Alexa Fluor-647 conjugated antibody. Insert left zoomed image and insert bright field image of the principal image.

A possible mechanism for dTrpNPs endosomal escape could be the “proton sponge effect” depicted in Supplementary Figure S11. This is typically mediated by species with high buffering capacity in the endosomal “pH change window”, such as amine-rich molecules with pK_a around 6, which can produce osmotic imbalance inside the endosome and ultimately lead to disruption of endosomal membrane [30, 31]. Indeed, the potentiometric titration curve of dTrp (Supplementary Figure S6), shows its buffering capacity in the biological relevant region, between pH 5 and 7 because of protonation/deprotonation of aromatic hydroxyl groups. Hence, the endosomal escape of the dTrpNPs could potentially be mediated by “proton sponge effect”, triggered by dTrpNPs.

In conclusion, our results show that the dTrpNPs provide a multispectral bioimaging tool suitable to track their intracellular fate. dTrpNPs are promptly internalized in MDA-MB-231 cells, trafficked from early to late endosome, released into the cytosol by escaping the endosomes and dissolved in the neutral cytosolic environment. It is worth noting that apart from pH, in the intracellular milieu dTrpNPs may also experience alternative dissipation condition which may induce the disassembling of the aggregates. Competitive interaction with lipids or associating protein with dTrp could potentially also fuel the dissolution of dTrpNPs in the cytosol. We finally sought to investigate possible applications of dTrpNPs in the biomedical field. For instance, Figure S12 show that dTrpNPs possess high antioxidant and radical scavenging properties. Therefore, dTrpNPs can be potentially used to protect cells against any oxidative damage.

Furthermore, the applicability of dTrpNP as a platform for sustained anticancer drug delivery was also considered. The sustained release of drug from nanoparticles fuelled by the cytosolic pH can be advantageous to attain intracellular

therapeutic concentrations with higher selectivity and specificity. In fact, the burst release of doxorubicin from the nanocarriers into the cytosol typically results in high concentration of drug, randomly interacting with undesignated molecular

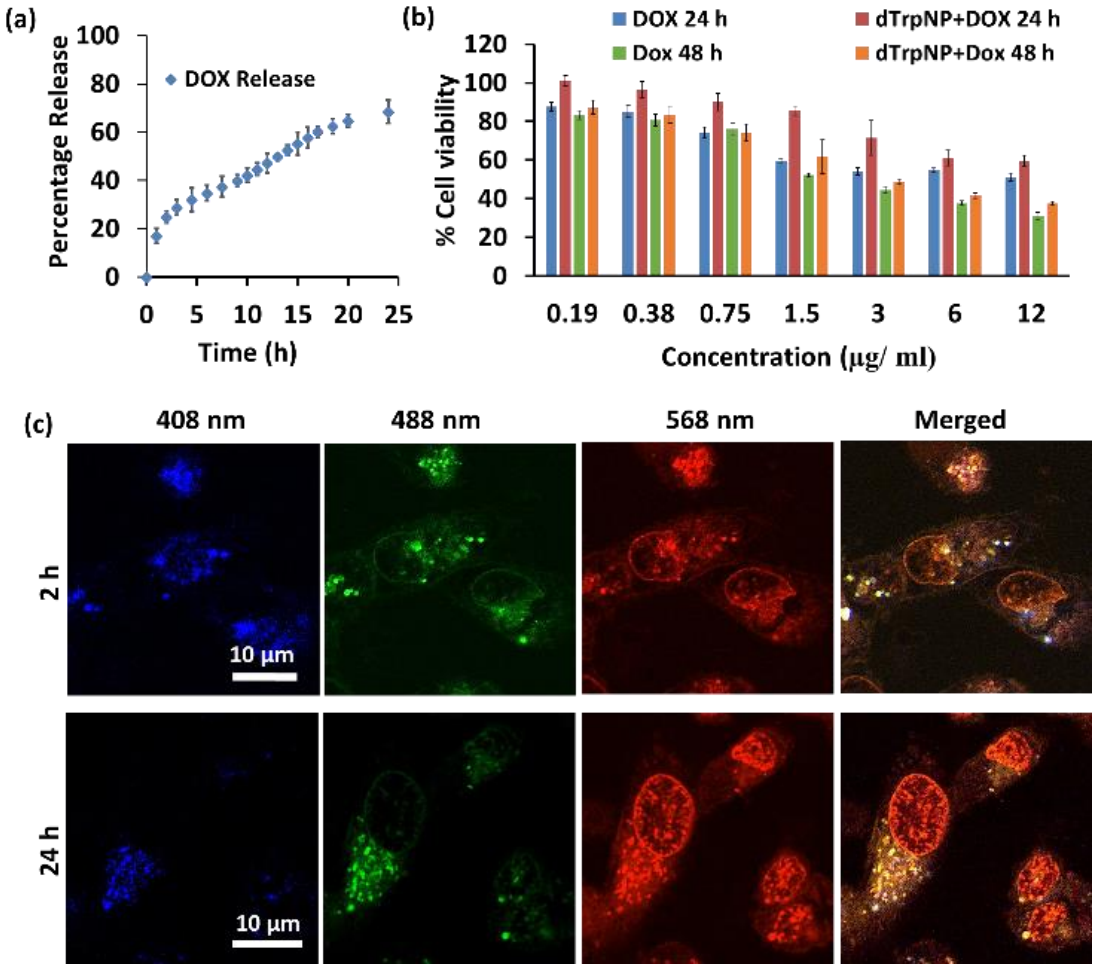

Figure 6: Drug delivery by tryptophan particles (a) The percentage release of DOX from the dTrpNP +DOX (Blue) dissolution in PBS (pH=7.4) at 37 °C as a function of time. (b) Cell viability evaluation of DOX and dTrpNP +DOX at different concentrations of DOX after 24 and 48 hours towards MDA-MB 231 cells. (c) Confocal microscopic images of the MDA-MB-231 cells incubated with dTrpNP +DOX for 2 and 24 h showing the release of DOX from nanoparticles into nucleus.

target [32, 33]. Doxorubicin was incubated with dTrpNPs at pH 5-6 and a high loading efficiency (70 % with 0.38 mg DOX/1 mg of dTrp)) was observed. The high loading capacity can be attributed to the electrostatic and hydrophobic

interaction between dTrpNPs and doxorubicin. The release of doxorubicin was studied in PBS (pH 7.4) at 37 °C by monitoring the intensity of fluorescence emission spectra at λex = 480 nm. Figure 6a shows the percentage release of the doxorubicin as a function of time. The nanoparticles show a slow and bimodal release profile of the drug however, initial release could be due to some adsorbed drug on to the surface of dTrpNP. The surge in the release of the drug after 10 h could be due to the erosion or dissolution of dTrpNP .

Figure 6b illustrates the MDA-MB 231 viability when treated with DOX and DOX loaded dTrpNP (dTrpNP + DOX) as a function of different concentration of doxorubicin ranging from 0.19 to 12 µg/ml after 24 h and 48 h. These data show that the cell viability decreases with an increase in the concentration of DOX. The toxicity of dTrpNP +DOX was less than that of free DOX after 24 hours due to the slower release of DOX from the nanoparticles, however cytotoxicity of the doxorubicin released from dTrpNP was comparable with that of free DOX after 48 hrs. Figure 6c shows the confocal microscopy images of the cells incubated with dTrpNP +DOX particles at different incubation times 2 h and 24 h. The green fluorescence signal arising from dTrpNP remain confined in the cytosol whereas an increase in red fluorescence as a function of time is observed in the nucleus. This clearly indicate the slow accumulation of doxorubicin into the nucleus upon release from dTrpNP. On the other hand, free DOX at the same concentration can completely accumulate into the nucleus just after 1-2 hour of incubation as shown in the Figure S13. Hence, this study suggests that the dTrpNP can be successfully used to attain the controlled release of the drug so that the required concentration of the drug can be maintained within therapeutic levels over extended period of time.

6.3. Conclusion

In conclusion we have presented computational and experimental approaches to demonstrate the role of the acoustic field in the formation of out-of-equilibrium nanoaggregates using a simple amino acid, L-tryptophan, as a building block. The collapse of acoustic cavitation bubble first triggered the formation of tryptophan dimers and then ultimately acted as a fuel for dissipative self-assembly of tryptophan dimers to form uniform nanostructures with multifarious properties. The characteristic optical and bio-functional properties of synthesized nanoparticles made them a powerful tool for probing the intracellular trafficking of an anti-cancer drug. In addition, the insight provided in this work paved the way for the ultrasound driven dissipative self-assembly applicable on set of biomolecules which are currently under investigation. An alternative strategy to pursue is the rational design of ad-hoc building blocks combining experiments, simulation and acoustic theory to predict the ultrasonic driven self-assembly.

6.4. References

1. E. Reisler and E. H. Egelman, J. Biol. Chem, 2007, 282, 36133-36137.
2. S. A. van Rossum, M. Tena-Solsona, J. H. van Esch, R. Eelkema and J. Boekhoven, Chem. Soc. Rev., 2017, 46, 5519-5535.
3. S. De and R. Klajn, Adv. Mater., 2018, 30, 1706750.
4. E. Mattia, Elio, and S Otto, Nat. nanotech. (2015), 2 111.
5. A. Sorrenti, J. Leira-Iglesias, A. J. Markvoort, T. F. de Greef and T. M. Hermans, Chem. Soc. Rev., 2017, 46, 5476-5490.
6. G. Ragazzon, M. Baroncini, S. Silvi, M. Venturi and A. Credi, Nat. nanotechnol, 2015, 10, 70.
7. C. G. Pappas, T. Mutasa, P. W. Frederix, S. Fleming, S. Bia, S. Debnath, S. M. Kelly, A. Gachagan and R. V. Ulijn, Mater. Horiz., 2015, 2, 198-202.
8. F. Rakotondradany, M. Whitehead, A. M. Lebuis and H. F. Sleiman, Chem. Eur. J. 2003, 9, 4771-4780.
9. J. Boekhoven, A. M. Brizard, K. N. Kowlgi, G. J. Koper, R. Eelkema and J. H. van Esch, Angew Chem, 2010, 122, 4935-4938.
10. J. Boekhoven, A. M. Brizard, K. N. Kowlgi, G. J. Koper, R. Eelkema and J. H. van Esch, Angew Chem Int Ed, 2010, 49, 4825-4828.
11. E. Del Grosso, A. Amodio, G. Ragazzon, L. J. Prins and F. Ricci, Angew Chem Int Ed, 2018, 57, 10489-10493.

12. K. Nakajima, H. Ogi, K. Adachi, K. Noi, M. Hirao, H. Yagi and Y. Goto, Scientific reports, 2016, 6, 22015.
13. W. Pim, Mater. Horiz., 2015, 2, 198-202.
14. F. Cavalieri, E. Colombo, E. Nicolai, N. Rosato and M. Ashokkumar, Mater. Horiz., 2016, 3, 563-567.
15. S. K. Bhangu and M. Ashokkumar, in Sonochemistry, Springer, 2017, pp. 1-28.
16. J. I. Mujika, J. Uranga and J. M. Matxain, Chem. Eur. J. 2013, 19, 6862-6873.
17. D. Sunartio, M. Ashokkumar and F. Grieser, J. Am. Chem. Soc., 2007, 129, 6031-6036.
18. K. Yasui, in Acoustic Cavitation and Bubble Dynamics, Springer, 2018, pp. 37-97.
19. Y. Shen, K. Yasui, T. Zhu and M. Ashokkumar, Phys. Chem. Chem. Phys, 2017, 19, 20635-20640.
20. L. Carroll, D. I. Pattison, J. B. Davies, R. F. Anderson, C. Lopez-Alarcon and M. J. Davies, Free Radic. Biol. Med, 2017, 113, 132-142.
21. V. Paviani, G. T. Galdino, J. N. d. Prazeres, R. F. Queiroz and O. Augusto, J. Braz. Chem. Soc., 2018, 29, 925-933.
22. P. Cheruku, J.-H. Huang, H.-J. Yen, R. S. Iyer, K. D. Rector, J. S. Martinez and H.-L. Wang, Chem. Sci, 2015, 6, 1150-1158.
23. A. Farrotti, P. Conflitti, S. Srivastava, J. K. Ghosh, A. Palleschi, L. Stella and G. Bocchinfuso, Molecules, 2017, 22, 1235.
24. G. Bocchinfuso, C. Mazzuca, P. Conflitti, D. Cori, T. Coviello and A. Palleschi, Z. Phys. Chem., 2016, 230, 1395-1410.
25. M. Levitt and M. F. Perutz, J. Mol. Biol., 1988, 201, 751-754.
26. Tsien, Roger Y, Annual reviews, 1998, 509-544.
27. C. Eggeling, J. Widengren, R. Rigler and C. Seidel, Anal. Chem., 1998, 70, 2651-2659.
28. H. NamáChan, Chem Comm, 2014, 50, 13578-13580.
29. Y. Q. Sun, J. Liu, X. Lv, Y. Liu, Y. Zhao and W. Guo, Angew. Chem. Int. Ed., 2012, 51, 7634-7636.
30. D. W. Pack, D. Putnam and R. Langer, Biotechnol. Bioeng, 2000, 67, 217-223.
31. C. Lin and J. F. Engbersen, J.Control. Release, 2008, 132, 267-272.
32. E. Lounkine, M. J. Keiser, S. Whitebread, D. Mikhailov, J. Hamon, J. L. Jenkins, P. Lavan, E. Weber, A. K. Doak and S. Côté, *Nature*, 2012, 486, 361.
33. Q. Zhu, H. Qi, Z. Long, S. Liu, Z. Huang, J. Zhang, C. Wang and L. Dong, *Scientific Reports*, 2016, 6, 28596.

Appendix 6

6.5. Supporting Information

6.5.1. Characterisation of dTrpNP

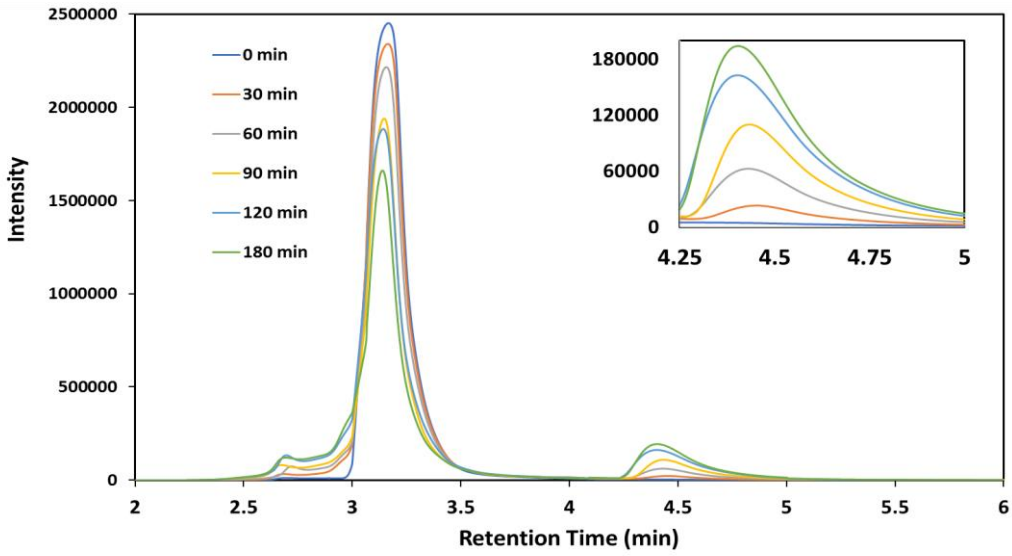

Figure S1*: HPLC of the sonicated tryptophan at different sonication time. The HPLC analysis shows the degradation of tryptophan (retention time 3.2 min) along with the formation of hydroxylated products eluting before the tryptophan peak. The peak at 4.4 min is attributed to the dimers and hydroxylated dimers of tryptophan, which increases with an increase in sonication time.*

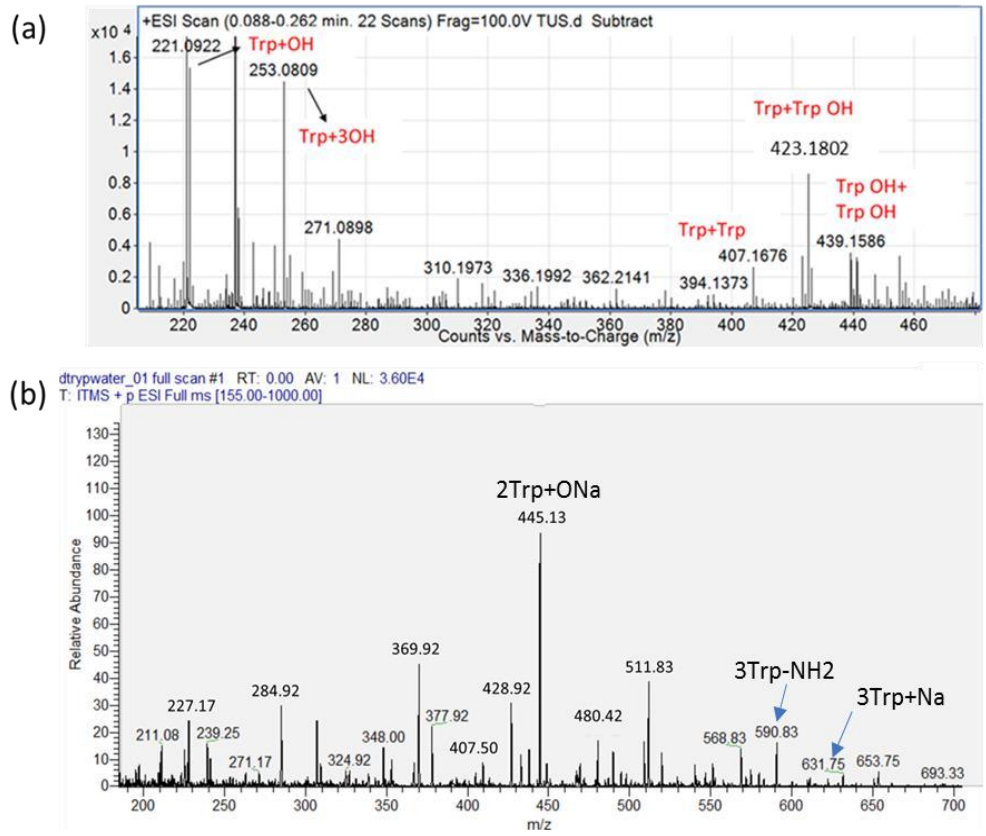

Figure S2*: ESI/MS of sonicated tryptophan showing the formation of dimer and hydroxylated dimers. The HPLC data was further supported by the ESI-MS, which was performed in positive ion mode. (a) mass spectroscopy of sonicated tryptophan confirms the formation of hydroxylated products such as Trp+OH, Trp+2OH and Trp+3OH at m/z of 221, 237 and 253, respectively. In addition to these, different dimeric species with different degree of hydroxylation were also obtained (e.g. the peaks at m/z 407, 423, 439), (b) The mass spectroscopy of dTrpNps after dissolution. The peak at m/z 407.50, 429 and 445 correspond to Trp-Trp, Trp-Trp+Na, and sodium adduct of dTrp-OH(Trp-Trp+ONa) respectively. Apart from dimer, trimer at m/z 631 was also observed.*

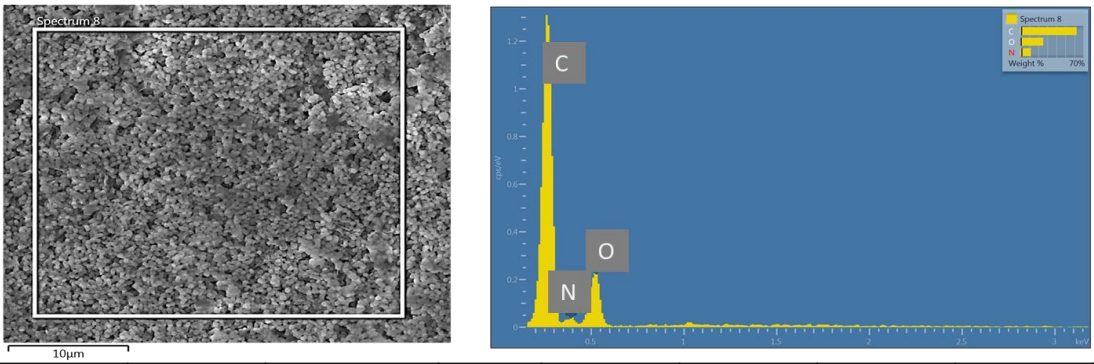

Element	Line Type	Apparent Concentration	k Ratio	Wt%	Wt% Sigma	Atomic %	Standard Label
C	K series	1.75	0.01748	62.64	1.63	68.12	C Vit
N	K series	0.45	0.00081	11.82	1.91	11.02	BN
O	K series	0.80	0.00269	25.55	1.12	20.86	SiO2
Total:				100.00		100.00	

***Figure S3**: EDS analysis of the dTrpNP confirming the presence of carbon, oxygen and nitrogen and increase in oxygen percentage. The energy dispersive X-ray spectroscopy of the dTrpNP also confirmed the presence of carbon, nitrogen and oxygen with atomic percentages of 68 %, 11 % and 21 % respectively. The atomic percentage of C, N, and O in tryptophan itself is 68.7 %, 14.6 %, 16.7 % respectively. Therefore, there is an increase in the percentage of oxygen with could be attributed to the presence of multiple hydroxyl groups.*

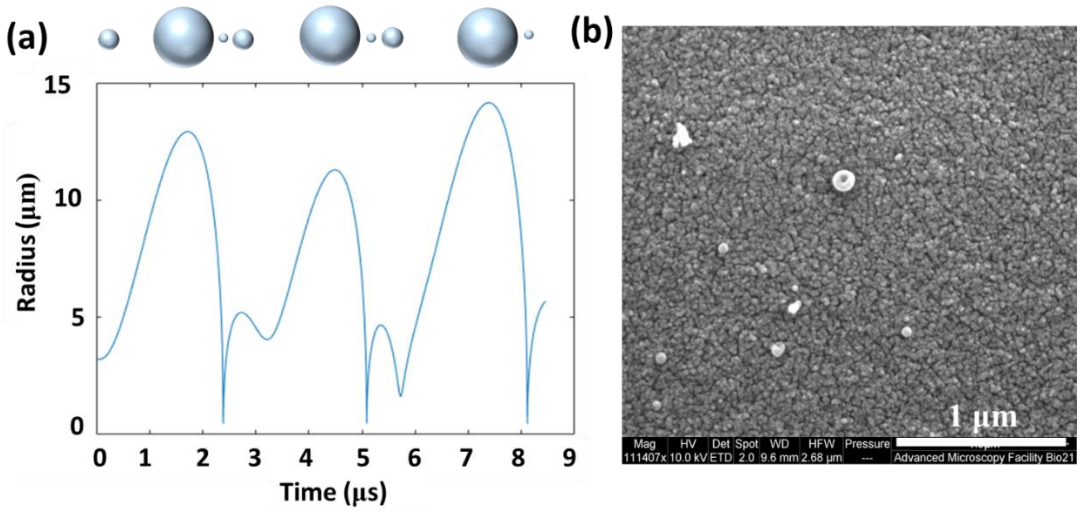

***Figure S4**: (a) The numerical simulation of the change in bubble radius as a function of oscillation time at 355 kHz and 6 W/cm^3 calculated using bubble dynamic equations and scheme illustrating the changes in the bubble size (at the top) and (b) SEM of dTrp nanoaggregates formed above cac in acidic environment.*

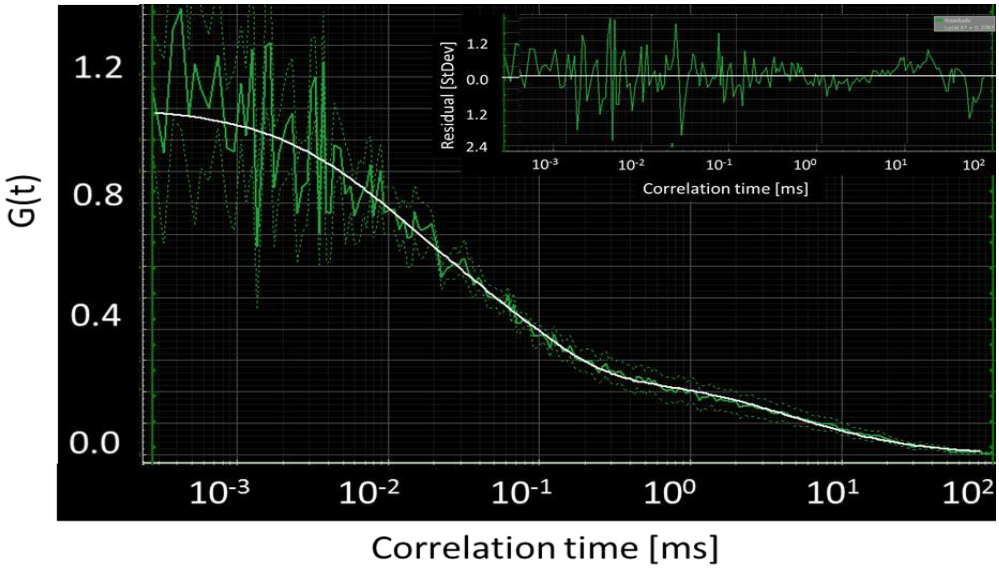

***Figure S5**: Normalised FCS function G(t) for 568 nm in tryptophan sonicated suspension. The fit residual has been shown in the inset. The fast and slow components at correlation times 0.02349±0.0072 ms and 6.50±0.49 ms respectively were obtained, attributed to free dTrp dimers (fast component) and nanoparticles (slow component). The diffusion coefficient of free tryptophan dimers and nanoparticles was found to be 870±78 µm2/s and 4.3±0.33 µm2/s.*

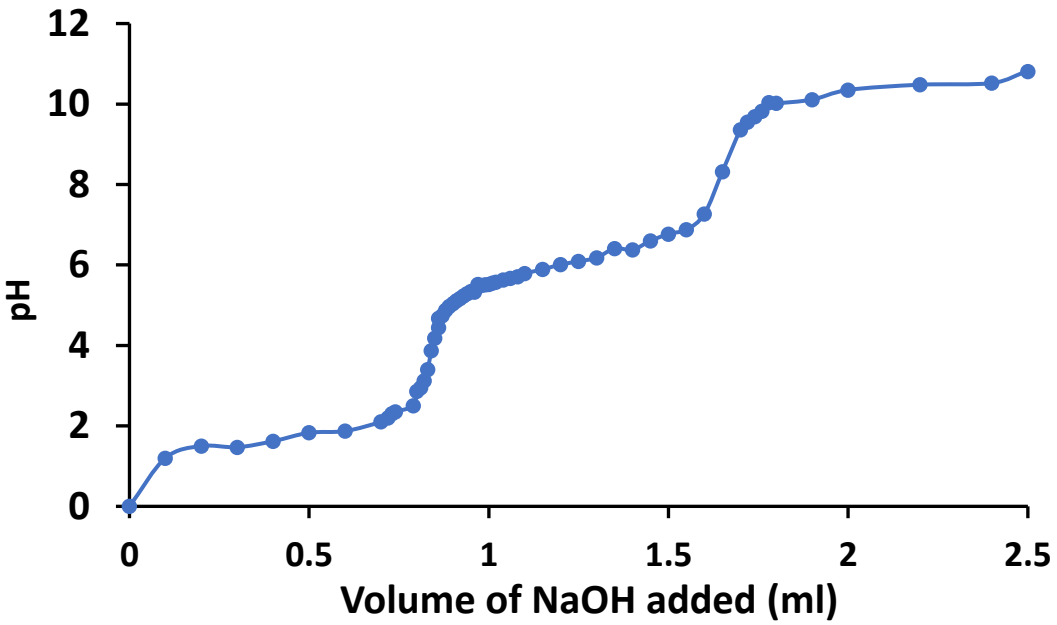

***Figure S6**: Titration curve of the dTrpNPs after dissolution showing changes in pH against volume of NaOH (ml) added.*

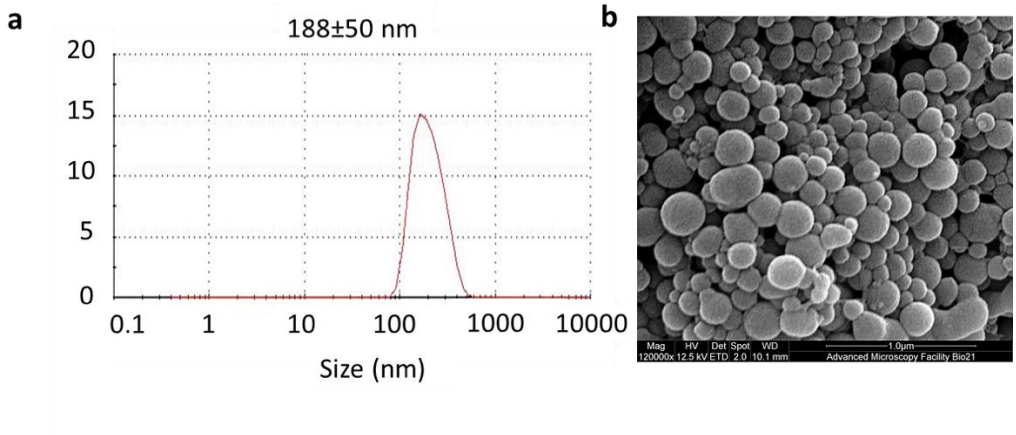

***Figure S7**: (a) Particle size distribution and (b) SEM image of dTrpNP obtained during cycle 2 where the NP obtained during cycle one were dissolved in alkaline conditions and then ultrasound was applied after bringing back to acidic pH.*

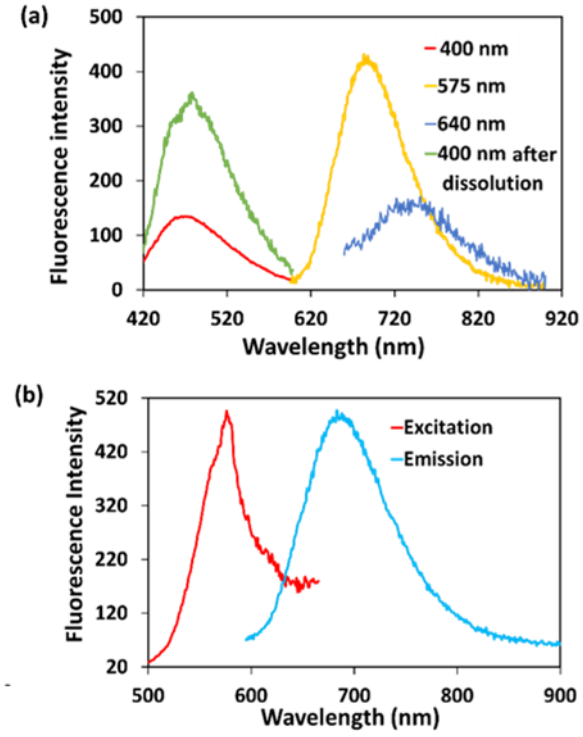

***Figure S8**: (a) Fluorescence emission spectra of dTrpNPs at different excitation wavelengths before dissolution, and after dissolution at λex = 400 nm (green) (b) Fluorescence excitation spectra at emission wavelength 680 nm and fluorescence emission spectra at excitation wavelength 575 nm of dTrpNPs before dissolution*

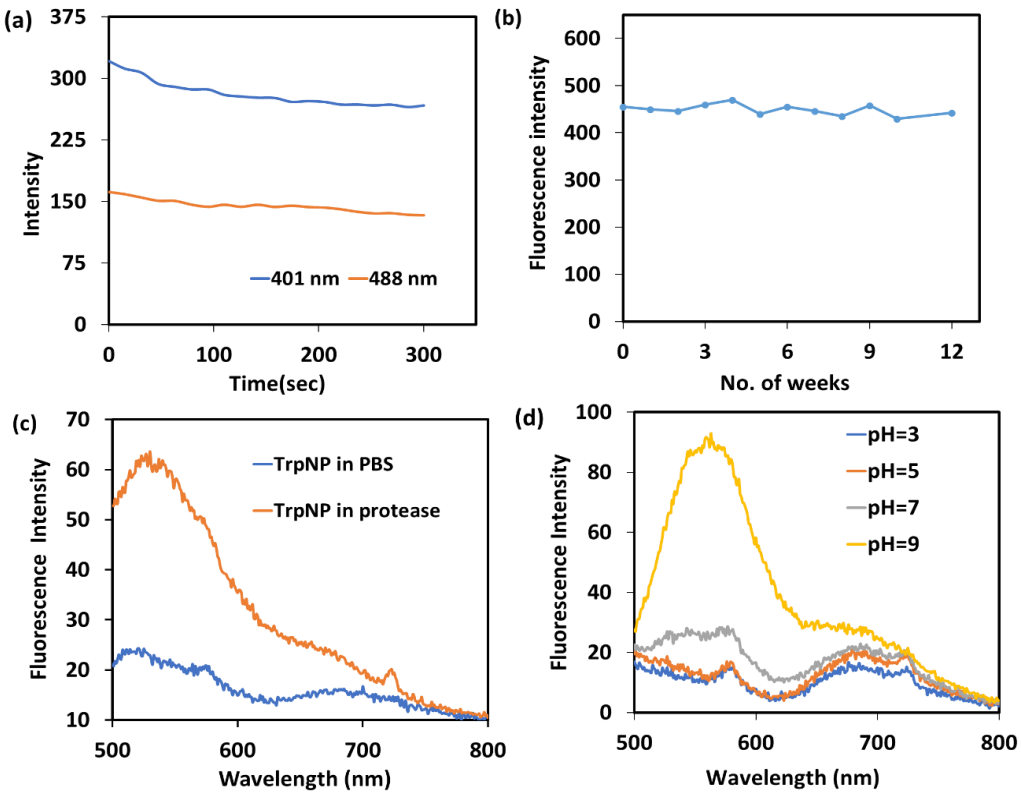

***Figure S9**: (a) Photostability study of sonicated tryptophan suspension showing fluorescence intensity as a function of time when irradiated at 401 and 488 nm. (b) Fluorescence intensity of nanoparticles when irradiated at 488 nm as a function of number of storage weeks at pH 5 showing that the intensity didn't decrease, showing the stability of nanoparticles, (c) fluorescence emission spectra of dTrpNP in PBS and protease when irradiated at 488 nm, (d) pH dependence of fluorescence intensity of dTrpNPs at excitation wavelength of 480 nm. The green emission of dTrpNPs at 555 nm increased 3 folds in alkaline environment This may be ascribed to the deprotonation of the aromatic hydroxyl groups at pH 9 and to the higher quantum yield of the deprotonated species as indicated by the potentiometric titration curve (Figure S6).*

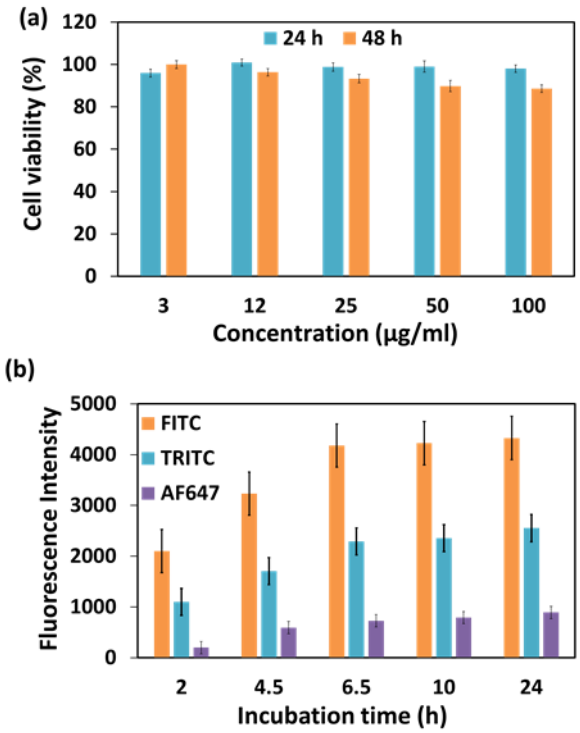

Figure S10: *(a) Cell viability percentage of dTrpNPs against MDA-MB-231 cells after 24 h and 48 h showing the biocompatibility of nanoparticles, and (b) Flow cytometry of the dTrpNPs under different fluorescence channels such as FITC, TRITC, AF 647 illustrating association of particles to cells.*

Table S1: *Table summarizing the PCC values depicting colocalization of dTrpNP with Early endosome, Late endosome and Lysosome at different incubation times*

	2.5 h	5h	8.5 h	24 h
Early endosome	0.563	0.502	0.23	0.23
Late endosome	0.529	0.6385	0.312	0.3
Lysosome	0.323	0.373	0.255	0.21

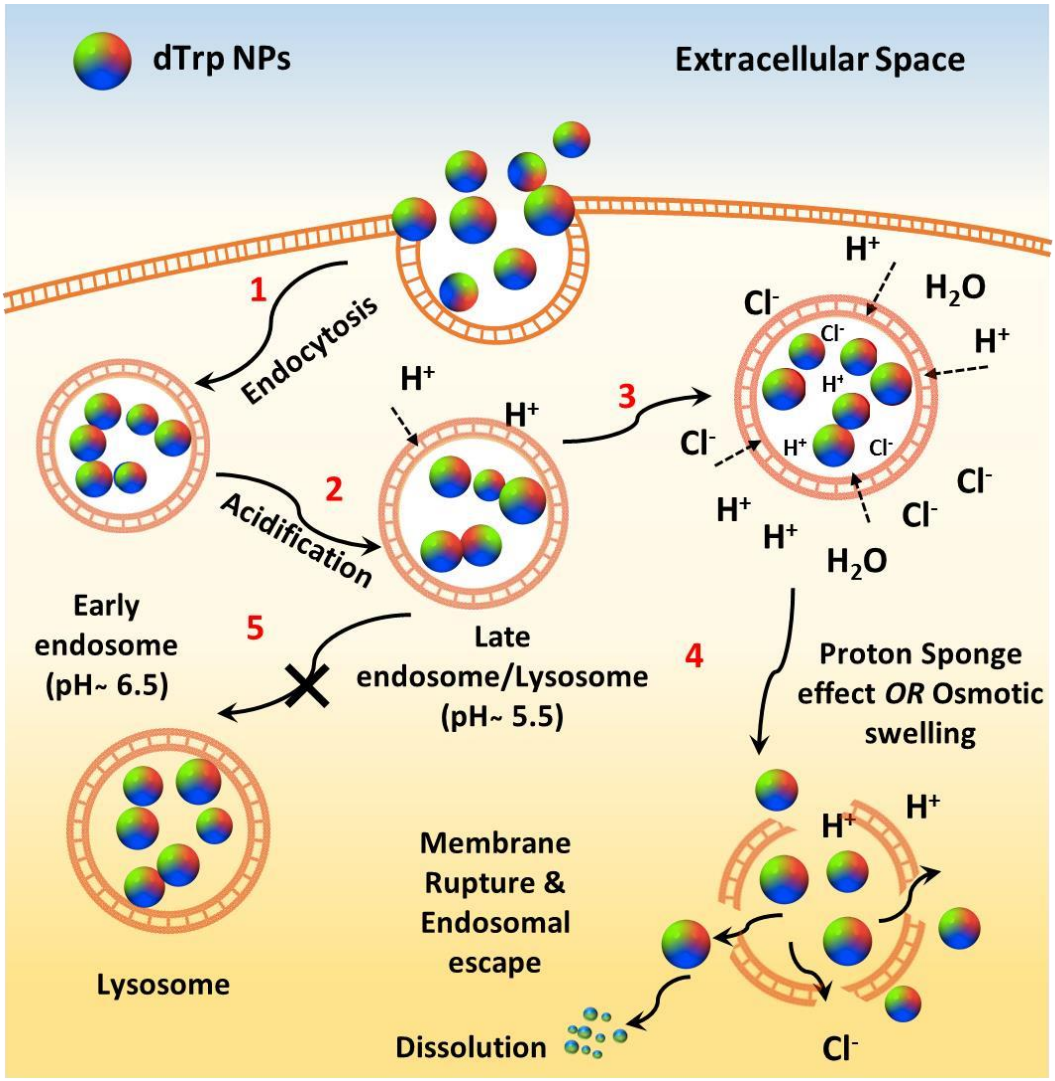

Figure S11: *Schematic showing proposed mechanism for the intracellular trafficking, cellular uptake and endosomal escape of dTrpNPs. The particles are uptaken by endocytosis leading to the formation of early endosome (pH~6.5) (step 1) due to the acidification (activity of ATP dependent proton pump), then can enter late endosome/lysosome (pH 5.5) (step 2). The protonation can mediate the flow of ions and water into the endosome/lysosome compartments and counter ions (Cl-) to maintain electrical neutrality (step 3). The process would lead to the high osmotic pressure (step 4) and ultimately escape of dTrpNPs. Later the particles can undergo dissolution in the cytosol.*

6.5.2. Antioxidant properties of dTrpNPs

The antioxidant and radical scavenging properties of dTrpNP nanoparticles were evaluated using the assay based on DPPH radical reduction. Tryptophan itself can act as an antioxidant, since the indole group is a hydrogen donor and it can quench oxygen radicals.

However, the higher degree of hydroxylation significantly enhances the antioxidant properties of dTrpNP compared to Tryptophan, as shown in Figure S12. We have also considered the applicability of dTrpNP as a platform for sustained anticancer drug delivery

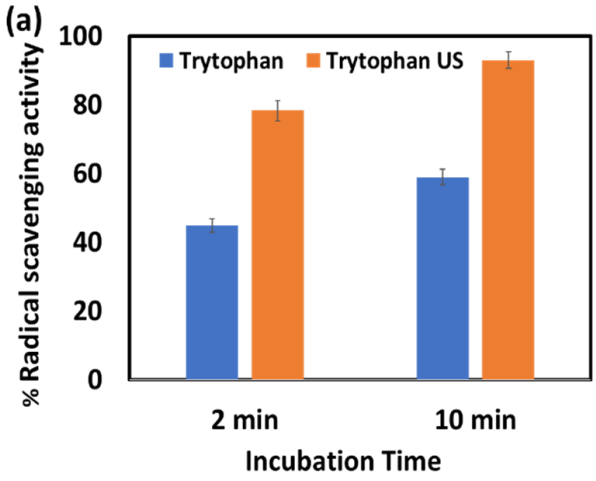

***Figure S12**: DPPH radical scavenging activity of tryptophan with and without ultrasound (US-ultrasound) after 2 and 10 min of incubation with of DPPH solution*

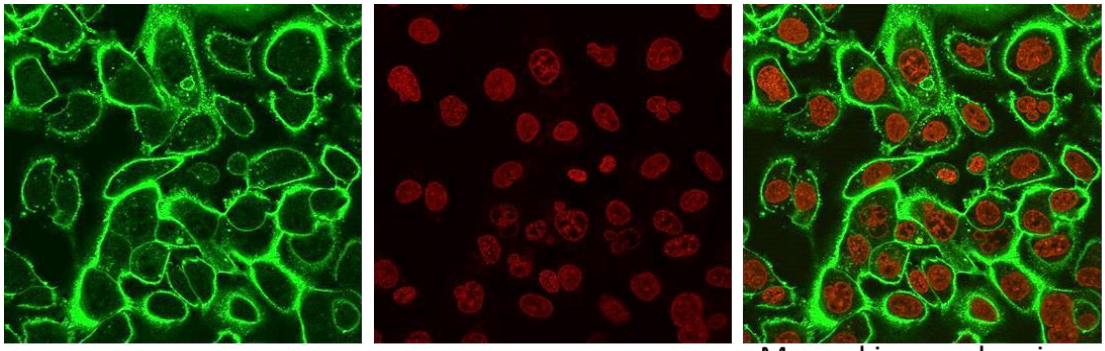

Figure S13: *Confocal microscopy images of the MDA-MB-231 human breast cancer cells when treated with doxorubicin after 2 h incubation.*

Chapter 7

Synthesis of bio-functional nanoparticles from sono-responsive amino acids using high frequency ultrasound

This chapter provides a one-pot high frequency ultrasonication (490 kHz) methodology to convert hydrophobic and amphipathic amino acids into nanostructures. The approach involved the oxidative coupling of aromatic amino acids (phenylalanine and tryptophan) to form high molecular weight oligomers, which could then self-assemble to generate spherical and uniform nanostructures. The synthesized particles exhibited fluorescence in a blue, green and red emission region. The particles showed a strong antioxidant activity

7.1. Introduction

Ultrasound has been utilized for a vast number of biomedical applications. These include alteration of gene and protein expression[1], diagnosis and molecular imaging [2-4] , targeted drug and gene delivery [1], tissue ablation [5] and many other therapeutic effects. It is well known that all the effects of ultrasound are due to the generation of chemical and physical effects when it is passed through a liquid medium. The physical effects (shear, microjetting, shock waves) of sonication are applicable for various reactions requiring mass transfer whereas chemical effects (formation of $H^{\cdot}$, $OH^{\cdot}$, H_2O_2 etc.) have been utilized for the reduction of gold, silver, iron and platinum ions to generate nanoparticles [6-8]. The physical and chemical effects of ultrasound can be controlled by various experimental parameters.

On the other hand, different kinds of nanostructures originating from amino acids, peptides or proteins are of great interest for biologists. Such nanostructures have attracted much attention due to their biodegradability, biocompatibility and applications in drug delivery, drug targeting, optical sensing and bioimaging [9-11]. Fan et al. have exploited different peptide systems to obtain nanostructures [11]. They obtained peptide-based nanoparticles formed from tryptophan-phenylalanine linkages through Zn (II) coordination. The products formed through such linkages can shift the intrinsic fluorescence of the peptide from ultraviolet to visible region. It was also reported that diphenylalanine can self-assemble by aromatic stacking interactions to form nanotubes which bear high rigidity and chemical stability [12]. Despite these studies, very limited research has been carried out for the synthesis of nanostructures just from the single amino acids.

Ultrasound in aqueous solutions can form OH radicals due to the homolysis of water molecules but none of the studies [12-15] have utilized the hot cavitation bubble surface and radicals generated by ultrasound for the oxidative coupling of the phenylalanine and tryptophan. Oxidation of amino acids by OH radicals has been demonstrated using Fenton reaction, pulse radiolysis and γ-radiolysis [13-15]. It was shown that with Fenton reaction and γ-radiolysis of phenylalanine; o-, m-, & p- hydroxyphenylalanine together with 2,4-dihydroxyphenylalanine, 2,3 dihydroxyphenylalanine were obtained [14]. Correspondingly, tryptophan's Fenton reaction and γ- radiolysis also led to the formation of different hydroxytryptophans, N-formylkynurenine, oxindole3-alanine, [16]. However, none of these studies have shown the formation of any amino acid-based nanostructures.

Recently, Cavalieri et al. have demonstrated the role of cavitation bubble surface on the polymerization of the N-Benzoyl-L-Tyrosine Ethyl Ester to obtain nanostructures [17]. It was manifested that the oscillating cavitation bubble surface can act as a catalytic binding site for the oxidative coupling reactions among phenol-type molecules which can later self-assemble to form nanoparticles without employing to any metal catalysts or enzymes [17, 18]. Similarly, our recent findings with tryptophan (Chapter 6) have suggested that ultrasound (collapse of cavitation bubble) triggers out of equilibrium dissipative self-assembly of tryptophan dimers into nanostructures below the critical aggregation concentration. Owing to such benefits, high frequency ultrasound can offer straightforward synthetic route for the generation of different amino acid - based nanostructures which are of substantial interest.

The current study aims to expand the knowledge base on how the cavitation bubble surface can be utilized for the oxidative coupling reaction among different hydrophobic and amphipathic biomolecules. The work intends to study the impact of high frequency

ultrasound on the dimerization and oligomerization of the phenylalanine and its mixture with tryptophan to fabricate nanostructures which has never been studied before. This unique methodology purveys a simple and green methodology to synthesize nanostructures from different biomolecules without the use any toxic external agents. The effect of sonication power on the size of nanoparticle was also explored. The synthesized nanoparticles can act as a single platform for multi-disperse biological applications such as drug delivery and cellular imaging. The antioxidant properties of the particles have also been demonstrated.

7.2. Results and Discussion

7.2.1. Synthesis and characterisation of phenylalanine nanoparticles.

An aqueous solution of phenylalanine (1mg/ml) was sonicated for 5 h at 490 kHz ultrasonic frequency and at different ultrasonic power levels of 5 W/cm^3, 10 W/cm^3, 15 W/cm^3. During sonication, the color of the mixture changed from colorless to dark brown along with the formation of nanostructured products.

The composition of the nanoparticles and mechanism involved in the phenylalainine derived nanoformulation were also investigated. Figure 1a shows the HPLC chromatograms of sonicated phenylalanine solution at different sonication times at 5 W/cm^3 . A decrease in the peak area at retention time 3.5 min (corresponding to phenylalanine) along with appearance of new peaks at early retention times are observed in Figure 1a, which can be attributed to the (hydrophilic) hydroxylated phenylalanine species. It can also be noticed that the peak at retention time 4.4 min increases with an increase in sonication time. This peak can be attributed to the high molecular weight species formed by sonication which could be more hydrophobic since they were eluted after phenylalanine.

The HPLC results are also supported by mass spectrometry analysis which confirmed the formation of dimers and trimers of phenylalanine. Figure 1b shows the mass spectrum of sonicated phenylalanine suggesting the formation of hydroxylated phenylalanine at m/z 182 (Phe+OH), 198 (Phe+2OH), dimer of phenylalanine at m/z 329 (Phe-Phe), hydroxylated dimers at m/z 345(2Phe+OH), 361 (2Phe+2OH) and trimer of phenylalanine at m/z 492 (3Phe).

Figure 1c shows the proposed mechanism along with possible structures of species obtained after the sonication of phenylalanine with respect to their mass to charge ratio. In brief, both OH radicals and adsorption of biomolecules on to the cavitation bubble surface are pivotal for the reaction to occur. The active cavitation bubbles within the ultrasonic frequency range of 200- 1000 kHz have a life time of about 0.3 - 1 ms [24]. This could provide sufficient time for the hydrophobic amino acid molecules, depending upon their diffusion kinetics, to diffuse, adsorb and react at the bubble-solution interface. In accordance with previous studies (Chapter 4,5 and 6), OH radicals generated by ultrasound can abstract a proton from the aromatic ring of phenylalanine adsorbed at solution- bubble interface leading to the formation of phenyl radicals (Figure 1c).

Furthermore, the reaction between $OH^{\cdot}$ and phenyl radicals could result in the formation of hydroxylated phenylalanine or two phenyl radicals can combine to form dimer of phenylalanine. Continuation of these reaction results in the formation of higher molecular weight species, which can self-assemble through different molecular interactions (H-bonding, π-π stacking) to form nanoparticles.

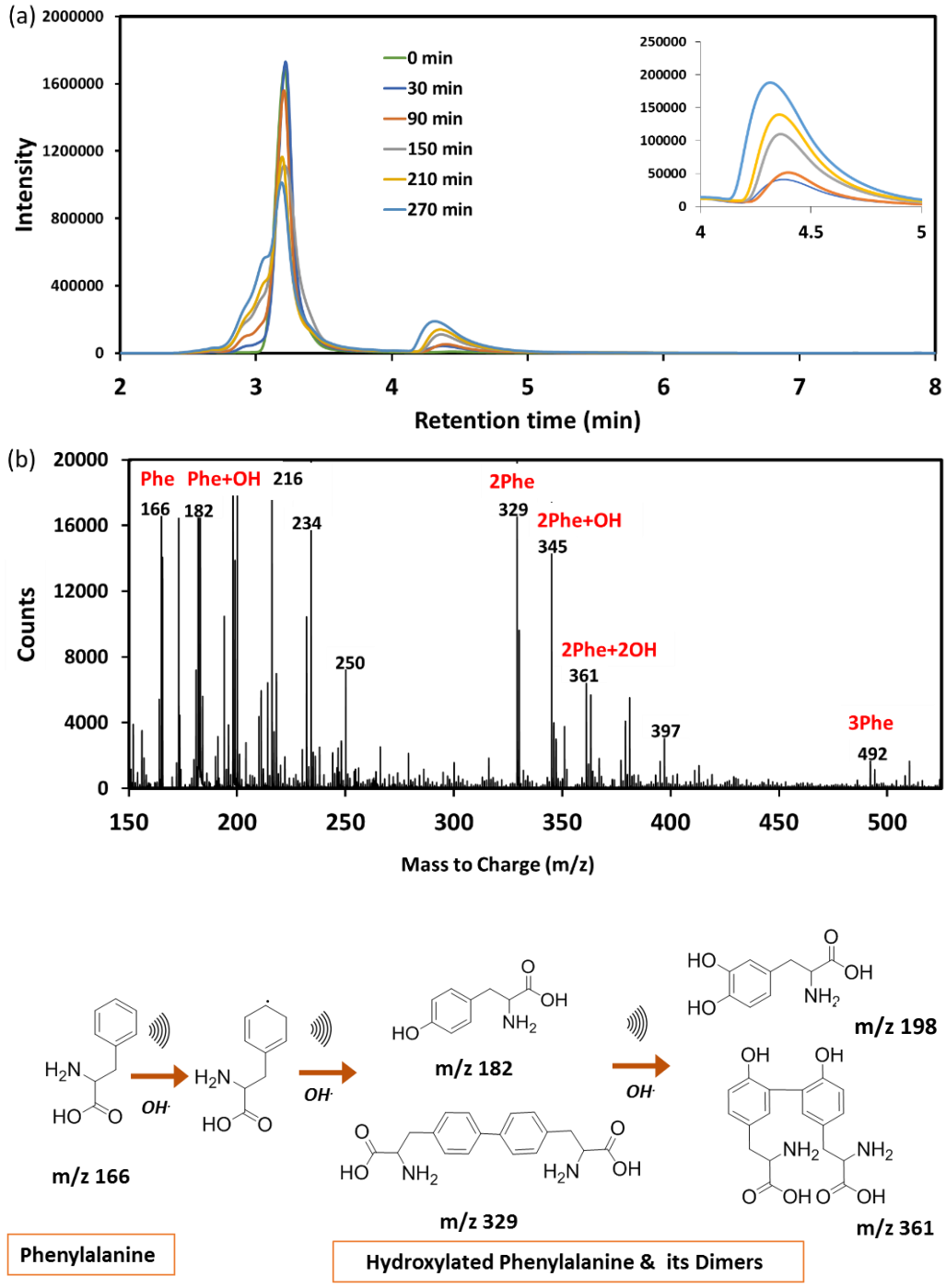

Figure 1: (a) HPLC chromatograms of sonicated phenylalanine at 490 kHz and 5 W/cm^3 as a function of sonication time, (b) The mass spectrum of the sonicated phenylalanine at 490 kHz and 5 W/cm^3 after 5 h. and (c) A schematic of proposed mechanism for the ultrasonic driven hydroxylation and dimerization of the phenylalanine.

The morphology of these nanostructures was analysed by SEM. Figures 2a, b and c show SEM images of the particles obtained by sonication of phenylalanine at different acoustic power levels- 5 W /cm^3, 10 W/cm^3 and 15 W/cm^3 respectively. It can be observed that

the particles have spherical morphology and their size was decreasing with an increase in power. The hydrodynamic radius of the particles and particle size distribution were determined by dynamic light scattering. The Z-average size of the particles decreased from 607 ± 88 nm to 190 ± 50 nm when the power density was switched from 5 to 15 W/cm^3 (Figures 2 a, b, c). The effect of ultrasonic power on the size has been demonstrated several times [20]. With increasing power, the acoustic cavitation activity is known to be enhanced. There occurs two types of cavitation bubbles; stable (oscillate for hundreds of acoustic cycles) and transient bubbles (live for few acoustic cycles) [21, 22]. A higher amplitude (higher power) would increase the number of transient and active bubbles. All these factors can then generate high amount of shear, shock waves and OH radicals which can enhance the supersaturation and possibility of collisions between the solute molecules leading to an increase in the nucleation rate. A higher nucleation rate would lead to a reduction in the size of nanoparticles as the rate of nucleation and radius of crystal are inversely related to each other [23, 24]. Based on this hypothesis, a reduction in nanoparticle size could be expected at high power levels. The zeta potential of the nanoparticles was around -30 ± 6 mV providing colloidal stability to the particles.

The cac (critical aggregation concentration) of nanoparticles as determined from surface tension measurements was ~80 µg/ml. However the concentration at which aggregates were formed during sonication was ~50 µg/ml. The nanoparticles were rapidly dissolved at this concentration at pH 11 and were unable to re-assemble when pH was brought back to acidic. On the other hand, when ultrasound was applied to this solution of nanoparticles in acidic environment, it successfully led to the formation of nanoaggregates. Therefore, in accordance to previous findings, the self-assembly of phenylalanine-based nanoparticles was also found to be out of equilibrium and was taking place below cac

where ultrasound apart from formation of dimer and trimer of phenylalanine can trigger the formation of nanoaggregate through dissipative self-assembly.

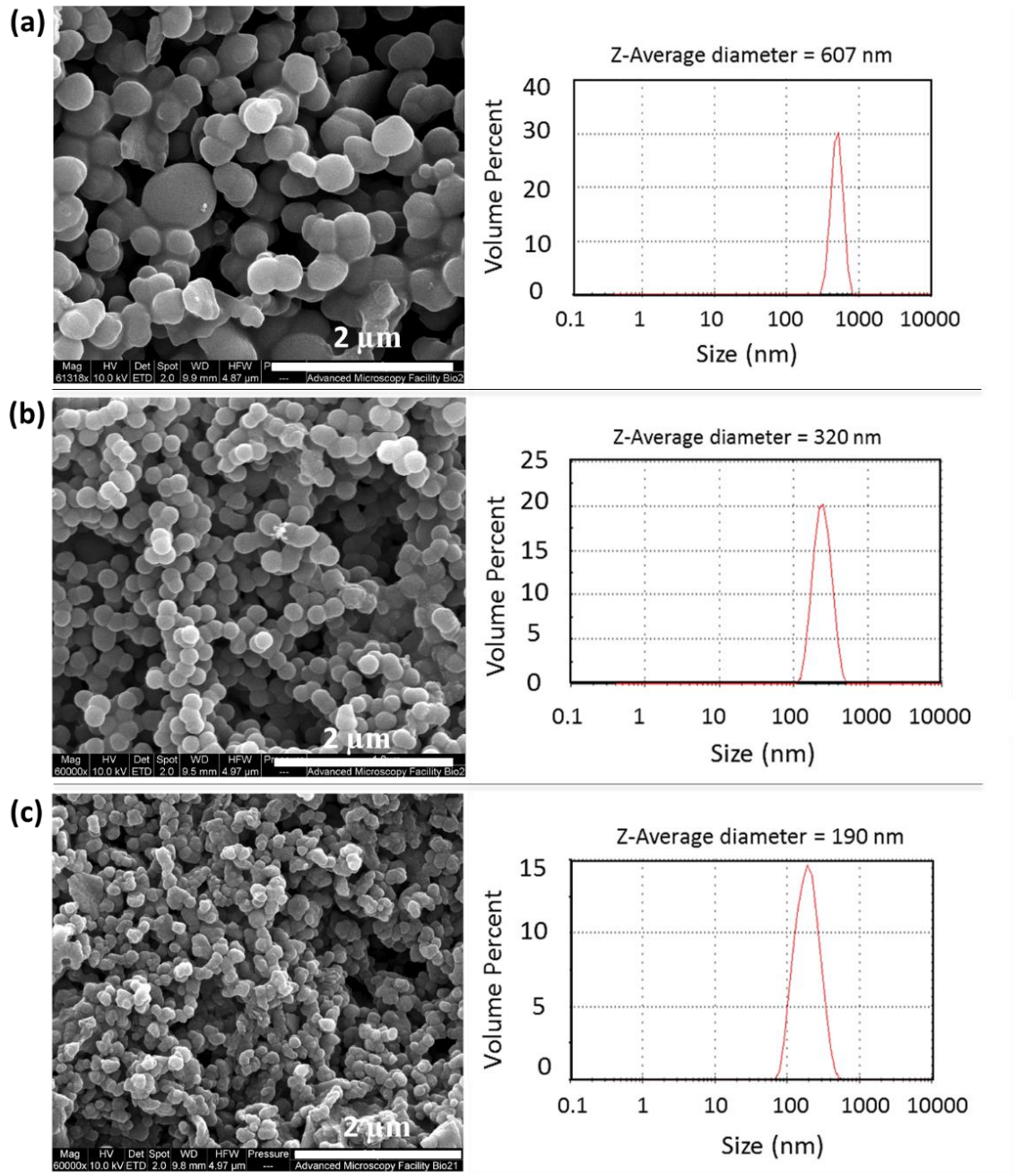

Figure 2: SEM images and size distribution of nanoparticles obtained by sonication of phenylalanine at 490 kHz at ultrasonic powers (a): 5 W /cm^3, (b) 10 W/cm^3 and (c) 15 W/cm^3

7.2.2. Optical properties of phenylalanine nanoparticles

The self -assembly of dimers and trimers to form nanostructures is further discussed based on absorption, fluorescence and solubility studies of the nanoparticles. Figure 3a shows

the absorption spectra of sonicated phenylalanine at different sonication times. Absorption spectra show new bands around 310 nm and 350 nm with increase in sonication time together with an overall increase in absorption. The trend observed is similar to that observed during the polymerization of aromatic phenolic molecules, where enhanced conjugation led to new absorption bands at higher wavelengths with an increase in absorption suggesting an increase in conjugation with an increase in sonication time [18, 25]. Figure 3b shows the fluorescence emission spectra of sonicated phenylalanine at different sonication times at an excitation wavelength of 320 nm. A new emission band centered at 430 nm can be observed which was increasing with the time of sonication. It is known that the monomeric form of phenylalanine doesn't exhibit any fluorescence in the wavelength range of 400-600 nm, thus this new emission could be due to the conjugated system i.e.; dihydroxyphenylalanine and dimers of phenylalanine [26, 27]. Figure 3c illustrates the fluorescence excitation spectra of phenylalanine after 3 h ultrasonic irradiation at different excitation wavelengths. The shift in fluorescence emission maximum from 430 nm to 460 nm was observed when excitation wavelength was changed from 320 nm to 380 nm.

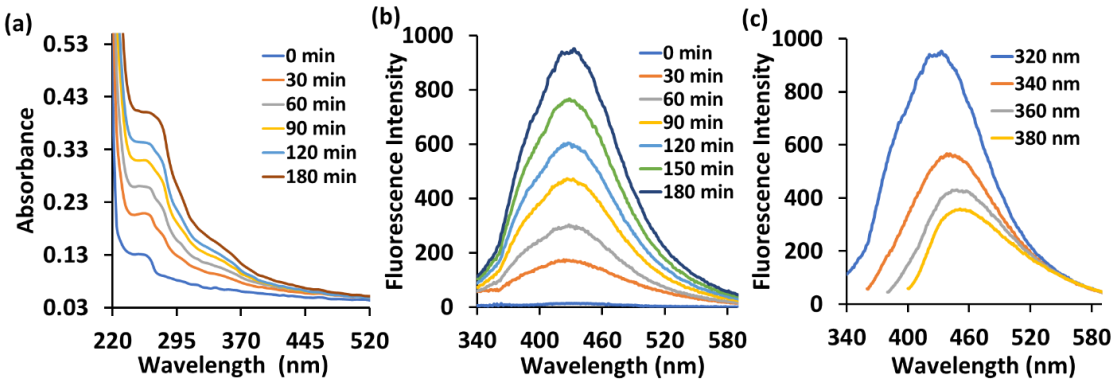

Figure 3: (a) The absorption spectra and (b) The fluorescence emission spectra at λ_{ex}= 320 nm of the sonicated phenylalanine at different sonication times, (c) The fluorescence emission spectra of sonicated phenylalanine after 180 min at different excitation wavelengths.

These results suggest the presence of multiple species which is in accordance with the mass spectrometry analysis. The red shift and broadening of absorption and fluorescence spectra also indicate π-π interactions between aromatic moieties.

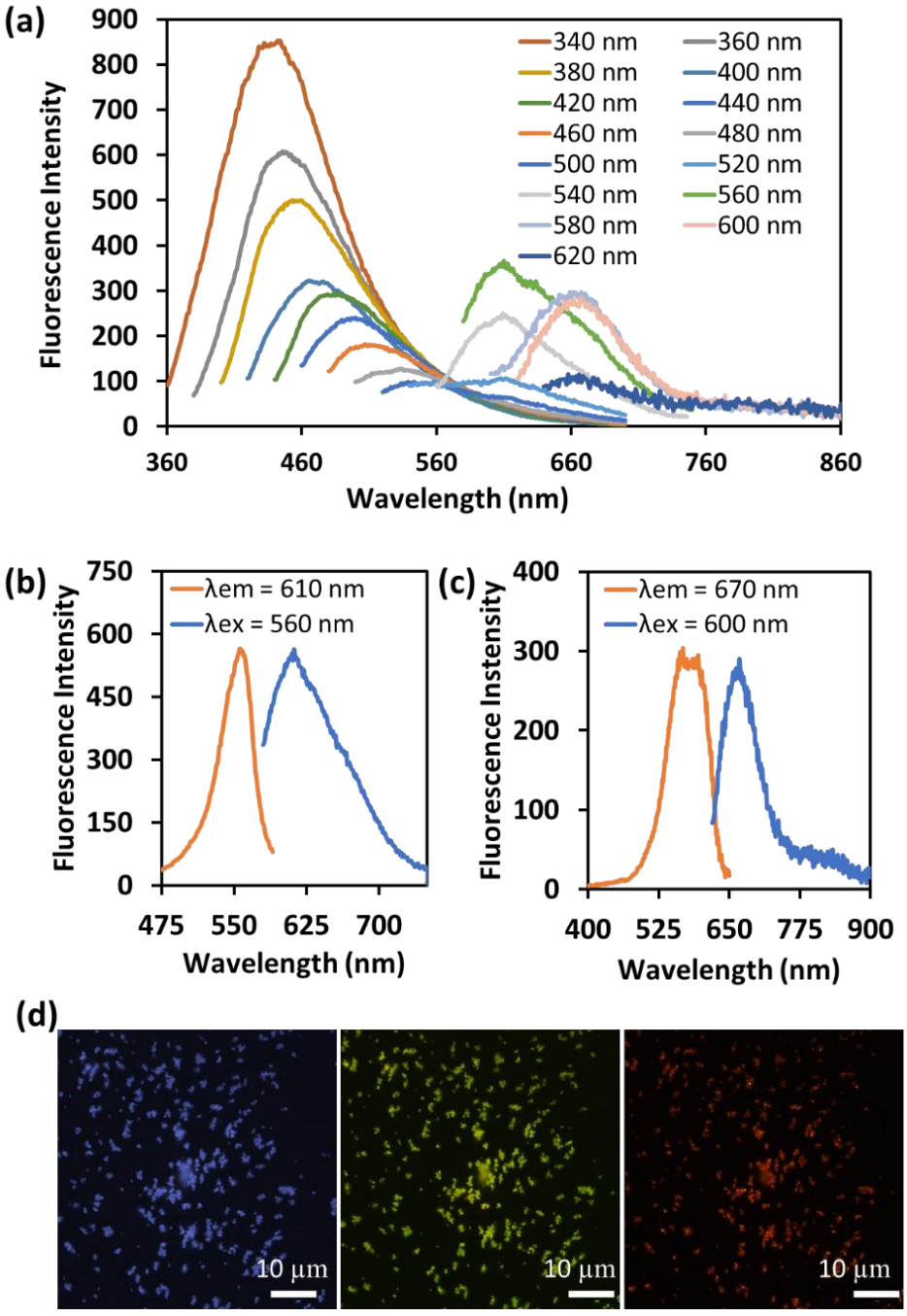

Figure 4: (a) The dependence of fluorescence of emission spectra on the excitation wavelength of the phenylalanine nanoparticles, (b) The fluorescence emission and excitation spectra of the phenylalanine nanoparticles at λ_{ex}=560 nm and λ_{em} =610 nm, respectively. (c) The fluorescence emission and excitation spectra of the phenylalanine nanoparticles at λ_{ex}= 600 nm and λ_{em} = 670 nm, respectively, and (d) The fluorescence microscopic images of phenylalanine nanoparticles showing the blue, green and red fluorescence.

Next, the optical properties of the phenylalanine-derived particles obtained by high frequency sonication were investigated. Figure 4a shows the dependence of emission spectra on excitation wavelength where a shift in emission maximum from 430 nm to 475 nm can be observed with a change in excitation wavelength from 310 nm to 529 nm. This shift could be attributed to the presence of different hydroxylated, dimeric and trimeric species. On the other hand, new bands with maxima at 610 nm and 670 nm were also observed at higher excitation wavelengths of 560 and 600 nm, respectively. The respective excitation spectra of emission spectra are provided in Figure 4 b and 4 c. The red shift and bands at higher wavelengths might suggest electron delocalization which again indicates strong π-π interactions between the high molecular weight species obtained by sonication. The fluorescence of the nanoparticles in blue, green and red region was also confirmed by fluorescence microscopy as shown in Figure 4d.

7.2.3. Sonication of phenylalanine and tryptophan in mixture

Next, a mixture of phenylalanine and tryptophan at the same concentration (1 mg/mL) was sonicated using the same experimental condition to obtain nanoparticles. Figure 5a shows the nanoparticles obtained after the sonication of Phe:Trp (1:1) mixture. These particles also exhibit spherical morphology with Z- average size of the nanoparticles about 385 nm ± 65 nm. Figure 5b shows the fluorescence emission spectra of Phe:Trp nanoparticles at different excitation wavelengths. The emission peaks in the wavelength range of 400-480 nm were observed. As mentioned before, phenylalanine and tryptophan do not exhibit emission in the range of 400-480 nm. Therefore, these emissions peaks can be attributed to the increased conjugation due to the formation high molecular weight products. Moreover, higher shift in emission and excitation wavelengths to 690 nm and 580 nm respectively yet again suggest intermolecular interaction (H bonding and π-π

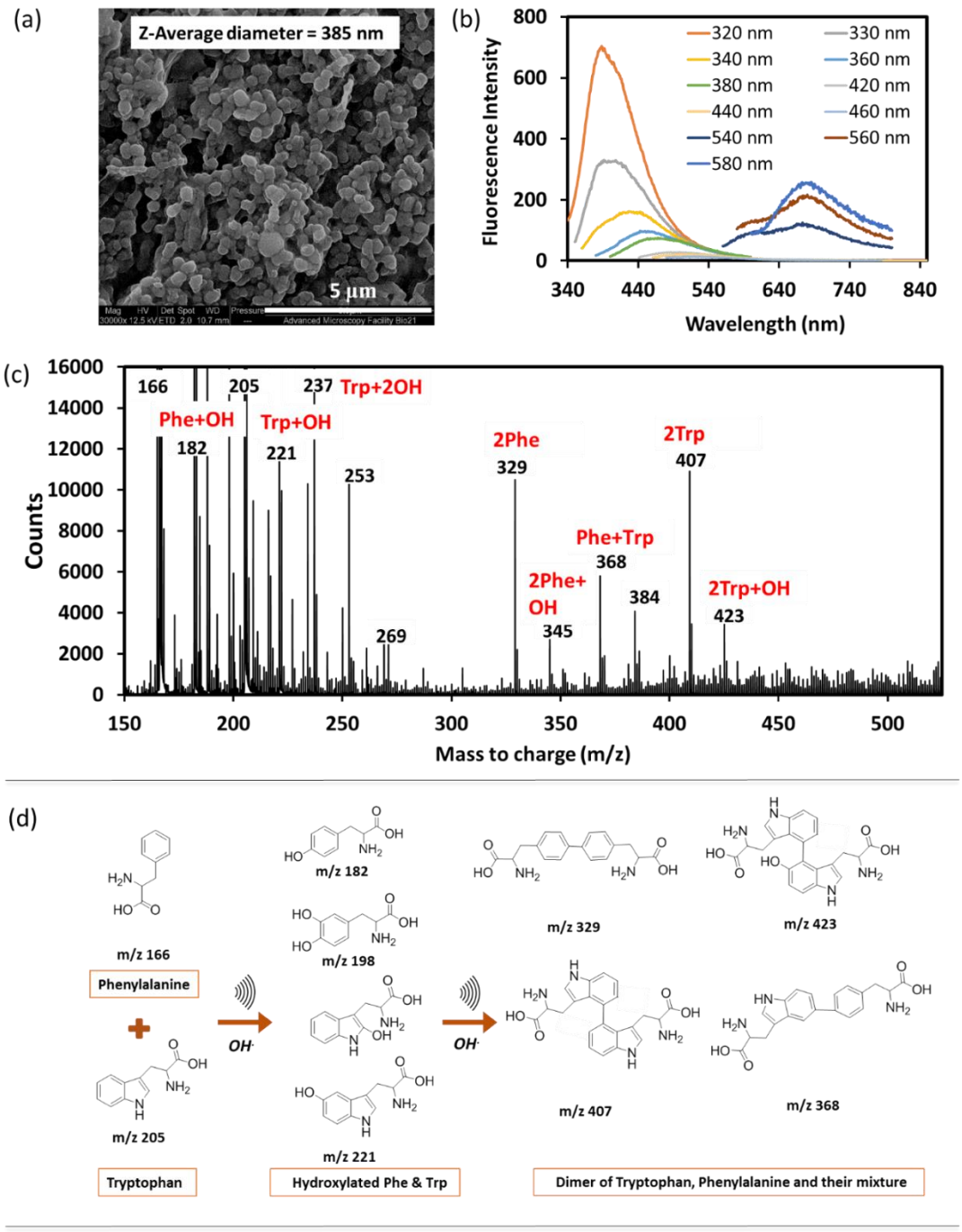

Figure 5: Sonication of Phe:Trp (1:1) at 490 kHz and 5 W/cm^3 (a) SEM image of the nanoparticles obtained after 5 h sonication, (b)The dependence of fluorescence emission spectra on excitation wavelength of Phe:Trp nanoparticles, (c) Mass spectra of the sonicated mixture of phenylalanine and tryptophan and (d)) The schematic and proposed mechanism for the ultrasonic driven hydroxylation and dimerization of the phenylalanine and tryptophan.

interactions) among different molecules to self-assembly into nanoparticles. Figure 5b shows the mass spectrum of the mixture of tryptophan and phenylalanine. It shows the formation of hydroxylated and high molecular weight species of phenylalanine (similar to observed in Figure 2b during phenylalanine sonication) along with variety of other

products. For instance, hydroxylated tryptophan at m/z 221, dimer of tryptophan at m/z 407 and phenylalanine and tryptophan linkage suggested by peak at m/z 368, hydroxylated tryptophan dimer at m/z 423. Figure 5d illustrates the proposed mechanism and structures of the products formed by sonication of Trp:Phe mixture. Tryptophan bears different sites for OH radical attack which are discussed in the previous chapter. OH radicals can attack either the phenyl or pyrrole moiety of the tryptophan to abstract a proton and to form hydroxytryptophan at different positions. The Trp and Phe radicals can also react with each other to form Trp-Phe or they can combine with their own radical to form dimers and trimers.

Overall these results show a new approach to synthesize phenylalanine and tryptophan-phenylalanine based nanoparticles using merely aqueous solutions of aromatic amino acids and high frequency sonication, without the use of any external agents. These amino acid-based nanostructures owing to their fluorescent properties can be ideally used for live cell bioimaging, or as a platform for the loading of any hydrophobic drugs.

In order to evaluate the functional properties of the synthesized nanoparticles, the antioxidant activity of the particles was studied. Most antioxidant molecules bear high degree of hydroxylation. As mentioned, sonication results in the addition of OH groups and the oligomerization of biomolecules also tend to enhance the degree of hydroxylation. The DPPH radical scavenging assay was carried out to quantify the antioxidant activity. Figure 6 shows the radical scavenging activity of phenylalanine in comparison with its sonicated analogues at the same concentration. It can be noted that the phenylalanine itself has a very limited radical scavenging activity of 10 %. Conversely, sonicated phenylalanine and phenylalanine/tryptophan particles after dissolution exhibited 80% radical scavenging activity within 2 min of incubation with DPPH radical. Therefore, these results show that the ultrasonic treatment of aromatic amino acids and assembly

into nanoparticles can significantly enhance the antioxidant activity of the native biomolecules. Therefore, nanoparticles synthesised from tryptophan (chapter 6) and phenylalanine and their mixture apart from being fluorescent and to be used in bioimaging, drug delivery, can also protect the cells against any oxidative damage due to free radicals. Moreover, they can find potential applications as preservatives in food (meat, dairy, oils etc) as they can inhibit the oxidative rancidity.

The current ultrasonic approach has a versatile applicability as it can be utilized to generate nanoformulation from different types of aromatic biomolecules. Depending on the types of biomolecules and ultrasonic parameters the properties of the nanostructures can be tuned.

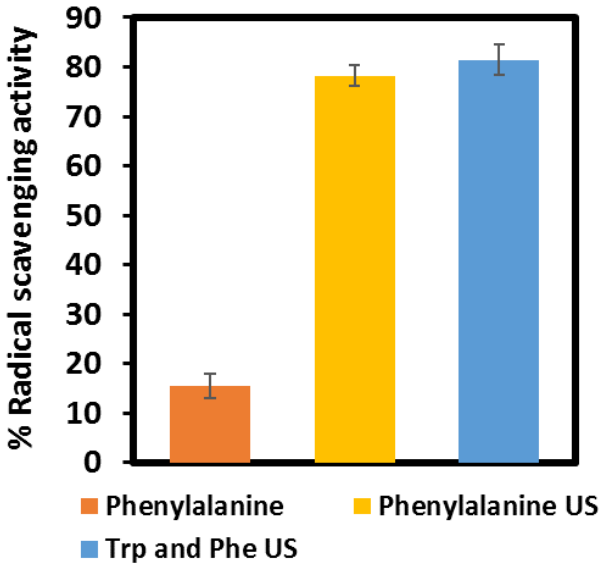

Figure 6: The percentage DPPH radical scavenging of phenylalanine in comparison with sonicated phenylalanine and its mixture with Tryptophan after 2 min incubation with DPPH solution and final concentration of 30 µg/ml.

7.3. Conclusions

The study has explored the use of high frequency ultrasound as a new approach for the synthesis of nanostructures from single aromatic amino acids. The size of the

nanostructures can be controlled using different ultrasonic parameters. The new strategy applied in this study illustrated the role of cavitation bubble surface and OH radicals to carry out hydroxylation, oligomerization and out of equilibrium self-assembly of phenylalanine and tryptophan to form spherical nanostructures. The nanostructures formed, together with significant antioxidant properties, have fluorescence in blue, green and red region and hence, can be utilized as bioimaging probes for live cell imaging. The current ultrasonic approach can be extended to other aromatic biomolecules for the construction of different nanostructures for multifarious biological and other applications.

7.4. References

1. Ferrara, K.W., M.A. Borden, and H. Zhang, *Lipid-shelled vehicles: engineering for ultrasound molecular imaging and drug delivery.* Accounts of chemical research, 2009. 42(7): p. 881-892.
2. Dayton, P.A. and K.W. Ferrara, *Targeted imaging using ultrasound.* Journal of Magnetic Resonance Imaging: An Official Journal of the International Society for Magnetic Resonance in Medicine, 2002. 16(4): p. 362-377.
3. Kaufmann, B.A. and J.R. Lindner, *Molecular imaging with targeted contrast ultrasound.* Current opinion in biotechnology, 2007. 18(1): p. 11-16.
4. Jin, Q., C.-Y. Lin, S.-T. Kang, Y.-C. Chang, H. Zheng, C.-M. Yang, and C.-K. Yeh, *Superhydrophobic silica nanoparticles as ultrasound contrast agents.* Ultrasonics sonochemistry, 2017. 36: p. 262-269.
5. Takegami, K., Y. Kaneko, T. Watanabe, T. Maruyama, Y. Matsumoto, and H. Nagawa, *Erythrocytes, as well as microbubble contrast agents, are important factors in improving thermal and therapeutic effects of high-intensity focused ultrasound.* Ultrasound in medicine & biology, 2005. 31(3): p. 385-390.
6. Caruso, R.A., M. Ashokkumar, and F. Grieser, *Sonochemical formation of gold sols.* Langmuir, 2002. 18(21): p. 7831-7836.
7. Salkar, R., P. Jeevanandam, S. Aruna, Y. Koltypin, and A. Gedanken, *The sonochemical preparation of amorphous silver nanoparticles.* Journal of materials chemistry, 1999. 9(6): p. 1333-1335.
8. Mizukoshi, Y., R. Oshima, Y. Maeda, and Y. Nagata, *Preparation of platinum nanoparticles by sonochemical reduction of the Pt (II) ion.* Langmuir, 1999. 15(8): p. 2733-2737.
9. Ayoub, M. and D. Scheidegger, *Peptide drugs, overcoming the challenges, a growing business.* Chimica oggi, 2006. 24(4): p. 46.
10. Cheruku, P., J.-H. Huang, H.-J. Yen, R.S. Iyer, K.D. Rector, J.S. Martinez, and H.-L. Wang, *Tyrosine-derived stimuli responsive, fluorescent amino acids.* Chemical science, 2015. 6(2): p. 1150-1158.
11. Fan, Z., L. Sun, Y. Huang, Y. Wang, and M. Zhang, *Bioinspired fluorescent dipeptide nanoparticles for targeted cancer cell imaging and real-time monitoring of drug release.* Nature nanotechnology, 2016. 11(4): p. 388-394.
12. Reches, M. and E. Gazit, *Molecular self-assembly of peptide nanostructures: mechanism of association and potential uses.* Current Nanoscience, 2006. 2(2): p. 105-111.

13. Chrysochoos, J., *Pulse radiolysis of phenylalanine and tyrosine.* Radiation research, 1968. 33(3): p. 465-479.
14. Maskos, Z., J. Rush, and W. Koppenol, *The hydroxylation of phenylalanine and tyrosine: a comparison with salicylate and tryptophan.* Archives of biochemistry and biophysics, 1992. 296(2): p. 521-529.
15. Galano, A. and A. Cruz-Torres, *OH radical reactions with phenylalanine in free and peptide forms.* Organic & biomolecular chemistry, 2008. 6(4): p. 732-738.
16. Maskos, Z., J. Rush, and W. Koppenol, *The hydroxylation of tryptophan.* Archives of biochemistry and biophysics, 1992. 296(2): p. 514-520.
17. Cavalieri, F., E. Colombo, E. Nicolai, N. Rosato, and M. Ashokkumar, *Sono-assembly of nanostructures via tyrosine–tyrosine coupling reactions at the interface of acoustic cavitation bubbles.* Materials Horizons, 2016. 3(6): p. 563-567.
18. Bhangu, S.K., M. Ashokkumar, and F. Cavalieri, *A simple one-step ultrasonic route to synthesize antioxidant molecules and fluorescent nanoparticles from phenol and phenol-like molecules.* ACS Sustainable Chemistry & Engineering, 2017.
19. Dharmarathne, L., M. Ashokkumar, and F. Grieser, *Reaction of ferricyanide and methyl viologen with free radicals produced by ultrasound in aqueous solutions.* The Journal of Physical Chemistry A, 2012. 116(30): p. 7775-7782.
20. Gao, D., Z. Li, Q. Han, and Q. Zhai, *Effect of ultrasonic power on microstructure and mechanical properties of AZ91 alloy.* Materials Science and Engineering: A, 2009. 502(1-2): p. 2-5.
21. Ashokkumar, M. and F. Grieser, *A comparison between multibubble sonoluminescence intensity and the temperature within cavitation bubbles.* Journal of the American Chemical Society, 2005. 127(15): p. 5326-5327.
22. Ashokkumar, M., M. Hodnett, B. Zeqiri, F. Grieser, and G.J. Price, *Acoustic emission spectra from 515 kHz cavitation in aqueous solutions containing surface-active solutes.* Journal of the American Chemical Society, 2007. 129(8): p. 2250-2258.
23. Kaur Bhangu, S., M. Ashokkumar, and J. Lee, *Ultrasound assisted crystallization of paracetamol: crystal size distribution and polymorph control.* Crystal Growth & Design, 2016. 16(4): p. 1934-1941.
24. Lee, J. and S. Yang, *Antisolvent Sonocrystallisation of Sodium Chloride and the Evaluation of the Ultrasound Energy Using Modified Classical Nucleation Theory.* Crystals, 2018. 8(8): p. 320.
25. Jha, P.K. and G.P. Halada, *The catalytic role of uranyl in formation of polycatechol complexes.* Chemistry Central Journal, 2011. 5(1): p. 12.
26. Smith, G.J. and T.G. Haskell, *The fluorescent oxidation products of dihydroxyphenylalanine and its esters.* Journal of Photochemistry and Photobiology B: Biology, 2000. 55(2-3): p. 103-108.
27. Malencik, D.A., J.F. Sprouse, C.A. Swanson, and S.R. Anderson, *Dityrosine: preparation, isolation, and analysis.* Analytical biochemistry, 1996. 242(2): p. 202-213.

Chapter 8

A Sono-drug to Combat Drug Resistance in Cancer Therapy

High frequency ultrasound (490 kHz, 6 W/cm^3) was used to convert a chemotherapy drug, i.e doxorubicin, into nanoparticles. Ultrasound led to the formation of dimers and hydroxylated products of doxorubicin and then triggered their self-assembly into nanoparticles. The newly developed nanoformulation of modified doxorubicin was tested against different cancer cell lines. It was found to be effective in overcoming the doxorubicin resistance in A2780 dx MDR cell line. The intracellular trafficking and mechanism of action of the DOXNP was identified using super resolution microscopy. The mechanism of DOXNP induced cellular damage was found to be Radical Oxygen Species (ROS) dependent.

8.1. Introduction

Doxorubicin (DOX) is a chemotherapy drug used to treat different types of cancers such as bladder cancer, breast cancer, leukemia, ovarian carcinoma, etc [1]. A variety of nanomedicine platforms have been developed for the delivery of doxorubicin to the site of action. These include dendrimers, protein nano/microcapsules, immuno-toxin/drug fusion proteins, carbon-based nanoparticles, polymer-drug conjugates, liposomes, micelles, inorganic nanoparticles (Au, Ag, Fe_3O_4, Pt, Si, ZnO), and nucleic acid nanostructures based on DNA and RNA [2-4]. Potential benefits offered by these nanoparticles include: (1) the ability to carry drugs and improving their pharmacological properties without doing any alteration of the drug itself, (2) delivery of drugs and active ingredients to targeted sites using both active and passive (enhanced permeability and retention effect (EPR)) ligand-based targeting techniques thus enhancing the therapeutic efficacy manner, (3) sustained delivery of pay load across a range of biological barriers (epithelial and endothelial) specifically to the desired intracellular sites of action, and (4) preventing the premature degradation of drugs [2-6].

Herein, a nano-formulation made solely of modified doxorubicin without resorting to any other nanocarriers was synthesized. The doxorubicin nano-formulation can offer sustained release of the drug within therapeutic limits which in turn can minimise the side effects of the drug (which occur due to high concentration of drug in body at once). The ultrasonic methodology used in this case was previously demonstrated for different aromatic biomolecules to generate dimer, trimers through oxidative coupling reactions which then self-assemble to form nanostructures. The delivery of drugs in a nanoparticle formulation consisting of dimers and aggregates of the drug molecules, may potentially have several advantages over conventional formulations. In this work, the role of high

frequency ultrasound to manipulate the chemical structure of the anticancer drug at molecular level and simultaneously induce its self-assembly into nanoparticles (DOXNPs) was investigated. We employed a combination of biochemical and microscopy techniques including single molecule Stochastic Optical Reconstruction Microscopy (STORM), to elucidate the endosomal escape and the mechanism of action of DOXNPs. We probed the different intracellular trafficking processes, with 20 nm lateral resolution, and visualised the localization of DOXNPs in mitochondria This allowed us to speculate on the mechanism of action of DOXNPs. We can anticipate the use of this synthesis approach to transform many other sono-reactive drugs into nano-formulations which would eliminate the requirement of any nanocarrier.

8.2. Results and discussion

8.2.1. Synthesis and Characterisation of DOXNP

A solution of doxorubicin in water (0.5 mg/ml) was sonicated at high frequency (490 kHz) and 6 W/cm^3 for 3 h and the formation of nanoaggregates was observed during sonication. The size distribution of the doxorubicin nanoparticles, hereafter referred to as DOXNP, in aqueous solution was determined using Stochastic Optical Reconstruction Microscopy (STORM) after labelling the surface of the nanoparticles with the photoswitchable dye Alexa 647, The images were acquired in Tris Buffer, pH 8, in the presence of 50 mM 2- mercaptoethanol (MEA) and oxygen scavenging system. The size of the DOXNP was ~193 ± 56 nm as determined from STORM images (Figure 1b) and~ 250 nm ± 99 nm from DLS measurements. The particles were found to be uniform, monodisperse and spherical in morphology. Figure 1c and 1d illustrates the absorption and fluorescence spectra of DOX and DOXNP respectively. A slight shift in both absorption and fluorescence peaks was observed. The λ_{max} for DOXNP was obtained at

the excitation wavelength of 540 nm (Figure S1). Slight changes in fluorescence and absorption spectra can be attributed to the chemical modifications of the structure of doxorubicin after the sonication,

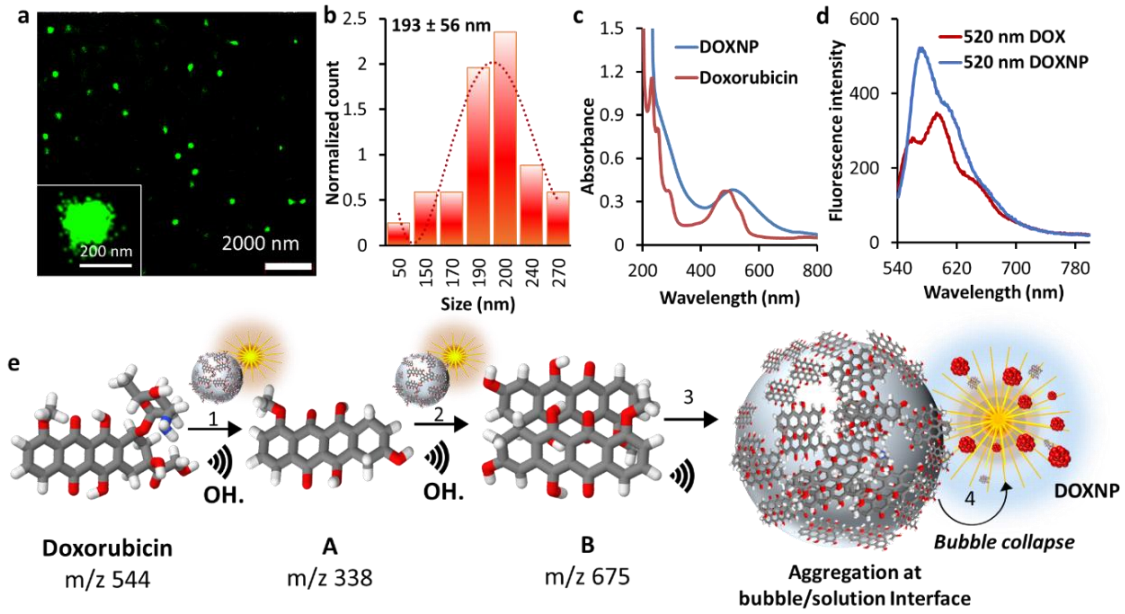

Figure 1: (a) STORM image of the DOXNP synthesized using high frequency ultrasound at 490 kHz and 6 W/cm^3 labelled with photoswitchable dye AF, (Insert show the magnified image of single nanoparticle),(b) Size distribution of DOXNP (c) Absorption spectra of free DOX and DOXNP after dissolution, (d) Fluorescence emission spectra of free DOX and DOXNP at excitation wavelength of 520 nm and (e) Schematic and mechanism involved in the formation of DOXNP, step 1 – The formation of molecules with m/z 338 and step 2- the formation of dimer of molecules with m/z 338, step 3-Adsortion of dimer onto the cavitation bubble interface where bubble collapse can lead to formation of DOXNP.

DOXNP were structurally characterised using NMR, size exclusion chromatography, mass spectroscopy, EDX elemental mapping. Our recent findings have demonstrated that the cavitation bubble has the tendency not only to generate H, OH radicals and H_2O_2 but can also act as a catalytic binding site to form high molecular weight species from amphiphilic molecules [7, 8]. In addition, it can act as a template and collapse of the bubble can trigger the self-assembly of these high molecular weight molecules into uniform nanoparticles. Similarly, in this case mass spectrometry analysis suggested the formation of high molecular weight species at m/z 675, 881, minor traces of m/z 1222, 1428 etc along with lower molecular weight fragments at m/z 338 and different

hydroxylated products as shown in Figure S2. The possible structure of molecules at m/z 338 is provided in Figure 1e and S2b. Figure S2c provides the list of different m/z observed and their proposed molecules. Majority of DOXNP were composed of m/z 675 which is dimer of respective m/z 338 (Step1-2 in Figure 1e). To summarise, different types of dimers with different degree of hydroxylation were obtained which then were adsorbed at cavitation bubble/solution interface where collapse of bubble can trigger the self-assembly to form nanoparticles (DOXNP) (Step -3 Figure 1e). The process is schematically depicted in Figure 1e. The size exclusion chromatography of DOX in comparison with dissolved DOXNP illustrated in Figure S2d confirmed the presence of high molecular weight species in DOXNP. Figure S3 represent the ^{1}H NMR spectra of DOX and DOXNP in DMSO. The NMR spectra showed differences in aromatic region due to formation of dimers and additional peaks due to hydroxylation of aromatic rings. Figure S4a represent the TEM- Energy Dispersive X-Ray Spectroscopy (EDX) elemental mapping of DOXNP which was performed to detect the presence of nitrogen. These data showed the presence of amino sugar moiety indicating that traces of DOX molecules might also be embedded into DOXNP.

Next, the stability of the nanoparticles in fetal bovine serum (FBS) was examined using Nanosight particle tracking analysis. Most of the nanoparticles tend to aggregate due to the adsorption of proteins and then interactions among these proteins. The proton corona effect on DOXNP was studied and is schematically depicted in Figure S5a. Figure S5b provides the size of nanoparticles before incubation (252±99 nm) and after incubation with 10% FBS (280 nm ± 99 nm), 50 % FBS (315±104 nm) and 100 % FBS (332 ± 107 nm). The nanosight analysis did not provide any evidence of aggregation of DOXNP, however an increment in size of nanoparticles was observed due to the adsorption of proteins on to the nanoparticles surface, driven by electrostatic or hydrophobic

interactions. The formation of protein corona was further confirmed using fluorescence spectroscopy and SDS-PAGE analysis Figure S5c shows a 26% decrease in fluorescence of 10% FBS (λ_{ex} = 280 nm) supernatant after incubating with DOXNP for 30 min at 37 °C, confirming the interaction of serum proteins with DOXNP. The SDS gel electrophoresis analysis was performed with 10% FBS, nanoparticles after incubation with FBS, and supernatant after removal of nanoparticles. These data also provide an evidence for the formation protein corona (Figure S5d). Apart from increase in size the zeta potential of DOXNP was decreased from -25 ±8 nm to -15.8 nm ±4.9 nm (Figure S6). Taken together, these results indicate that despite the expected interaction with serum proteins which can alter slightly the circulation lifetime, uptake and immune response, DOXNP would exhibit good stability in cell culture media.

To gain insight into the dissolution behaviour, DOXNP were incubated at pH 5 or 7.4 at 37°C and dissolution was evaluated as a function of time. As shown in Figure S7, higher dissolution of DOXNP at pH 7.4 (100 % after 18 h) compared to pH 5 (~ 40% after 20 h) was found. This result likely depends on the favourable deprotonation of OH groups of DOXNP at pH 7.4, which makes dissolution faster.

8.2.2. Cytotoxicity and DNA damage induced by DOXNP towards different cancer cell lines

To study whether DOXNP maintain anticancer properties, cytotoxicity experiments were performed using human tumor cell lines of different origin, including DOX-resistant variants selected *in vitro* by culturing the parental sensitive cell lines in presence of increased concentrations of DOX. Specifically, three human breast cancer cell lines (MDA-MB-231, HCC-1143 and HCC-1937), one colorectal carcinoma cell line and the corresponding resistant variant (LoVo and LoVo/DX), one ovarian carcinoma cell line and its DOX-resistant variant (A2780 and A2780/DX) were considered. The two resistant

variants express high levels of P-glycoprotein (P-gp), a membrane ABC transporter implicated in the efflux of different drugs, including DOX, and responsible for drug resistance. MDA-MB-231, A2780, A780/DX, LoVo and LoVo/DX cells were exposed for 2, 72, and 144 h to DOX and DOXNP and IC_{50} (concentration inhibiting cell growth by 50 %) values were determined (Figure 2a). Additionally, HCC-1143 and HCC-1937 cells were exposed to DOX and DOXNP for 48, 72, 96 and 126 h (Figure S8). The results reported in Figure 2a1-3, and S8 indicate that, although less potent than DOX, DOXNP maintain cytotoxic activity on all the tumor cell lines considered. This finding indicates that DOXNP antiproliferative potency is improved by prolonging the exposure time (Figure 2a2). The observed behaviour likely depends on the different mechanism of cellular uptake of DOXNP compared with DOX, and on the extra time required before DOXNP are dissolved to release the drug. As far as resistant index (R) is concerned, compared to DOX, DOXNP showed lower R in both the pairs of sensitive and resistant cell lines considered (Figure 2a4). Specifically, R of DOXNP was ~2.5-times lower after 2, 72 and 144 h exposure in A2780 and A2780/DX pairs of cell lines (Figure 2a4). Although with less magnitude, this finding was observed also in LoVo-LoVo/DX pairs after short-term exposure (19-times and 1.2-times lower at 2 and 72 h exposure, respectively) but not for long term exposure (Figure 2a4). The lower R observed for both the pairs of cell lines indicated that DOXNP partially overcome the mechanism of cellular resistance activated by cell lines resistant to DOX. It is well known that the anthracycline structures can led to the cell death through difference mechanistic ways. Particularly DOX is known to (i) intercalate into the DNA double strands to inhibit protein synthesis and many transcription processes [9, 10], (ii) produce reactive oxygen species (ROS) causing cellular damage (cytotoxicity secondary to lipid peroxidation) ultimately cell death by apoptosis or necrosis [11, 12] , (iii) inhibit topoisomerase II (nuclear DNA transcription

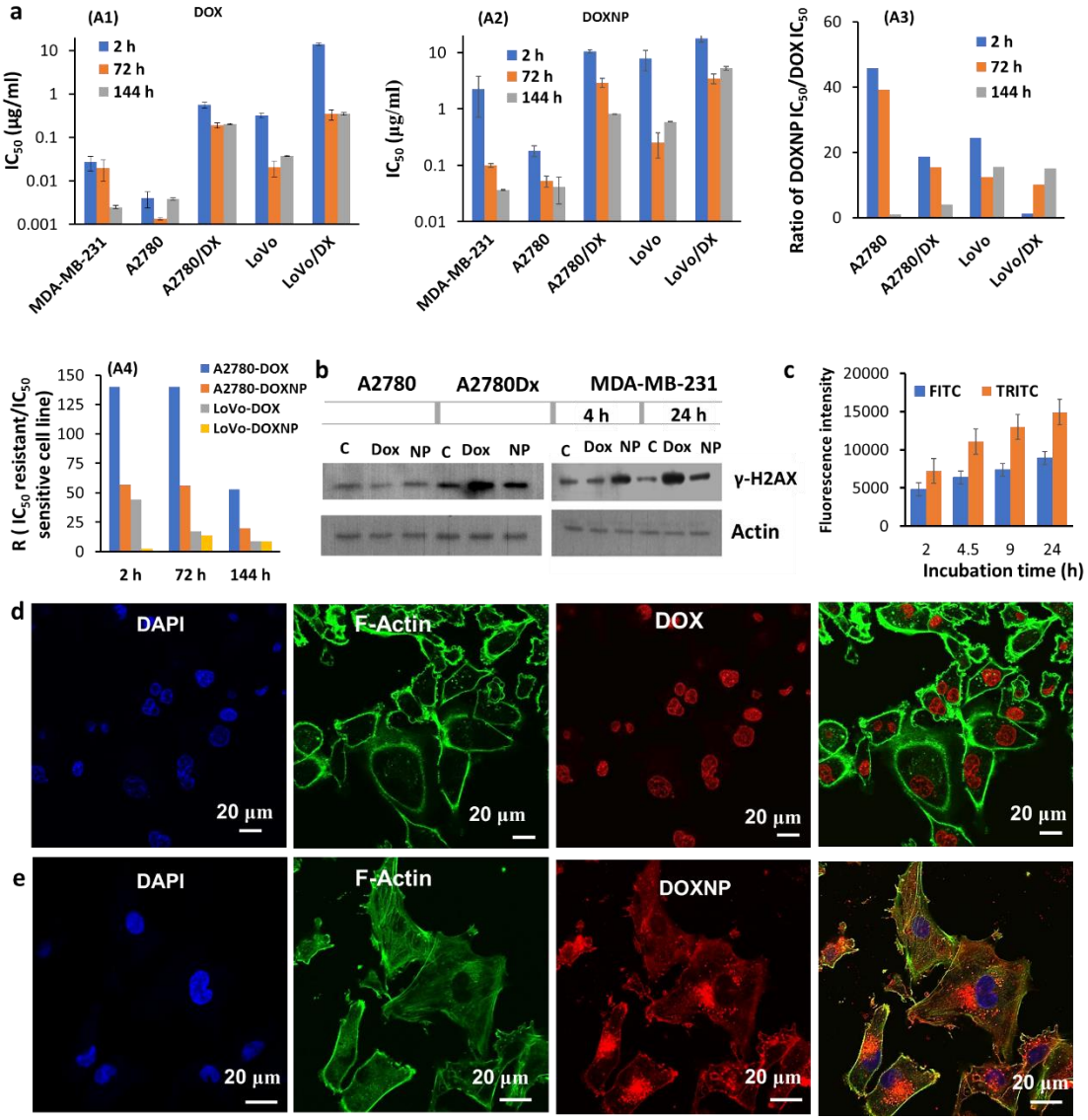

Figure 2: (a) DOX(A1) and DOXNP (A2) cytotoxicity in pairs of doxorubicin-sensitive and –resistant cell lines (MDA-MB-231, A2780, A2780/DX, LoVo, LoVo/DX) at various exposure times, (A3) Ratio of IC_{50} of DOXNP to the IC_{50} of DOX when different lines were exposed to DOXNP and DOX for different times, (A4) The resistance index (R, resistance index, ratio between IC_{50} (expressed in µg/ml) of resistant and sensitive cells) of DOX and DOXNP in pairs of doxorubicin-sensitive and –resistant cell lines namely A2780, A2780/DX, LoVo, LoVo/DX (b) DOXNP-mediated DNA damage in human tumor cell lines of different origin. A2780, A2780/DX, and MDA-MB-231 cells were exposed for 24 h to DOX or DOXNP at concentrations corresponding to 2xIC_{50} at 72 h. Cells were harvested for protein extraction, and cell lysates were fractionated on SDS-PAGE. Nitrocellulose films were incubated with antibody against γ-H2AX and β-actin, which was used as control for equal loadingc); (c) Flow cytometry – association studies time vs. fluorescence intensity of DOXNP at different channels; (d) and (e) Confocal microscopy images of the MDA-MB- 231 cells. Images were taken after incubation of DOXNP (3 µg/ml) and free DOX with the MDA-MB-231 cells. Red fluorescence is due to DOXNP and DOX and Green-Cells stained with phalloidin for F-Actin.

enzymes-important for tertiary structure of DNA) which can increase the cleavable enzyme-DNA linked complex and block the DNA separation and replication [13], (iv) exert intrinsic mitochondrial apoptotic signalling [14]. Therefore, we used western blot assay to test whether DOXNP produce DNA damage. To this purpose, cell lines were treated for 24 h with DOX or DOXNP at concentration corresponding to 2xIC_{50} for 72 h. Treatment-induced DNA damage was monitored using the specific γ-H2AX marker. DNA damage induces serine 139 phosphorylation of the H2AX histone protein which recognizes the double strand DNA breaks. A comparison between DOX-sensitive and -resistant cell lines revealed that, in the conditions considered, DNA damage was observed only in DOX-resistant cell line variants exposed to DOX and DOXNP (Figure 2b). The DNA damage induced by DOXNP in all cell lines after 24 h was less than dox, however when exposed to higher concentration of drug (10 μg/mL of DOX and DOXNP) for 4 h, DOXNP exhibit enhanced DNA damage due to the fact that cells do not have time to counteract DNA damage at higher concentration and shorter incubation time. In addition, for long time exposure at low concentration, DNA repair mechanisms, as well as scavenger molecules, have the time to work and repair DNA damages as observed from Figure 2b. After internalization and during incubation DOXNP likely release dimers molecules inside the cells. The dimers molecules lack the glucose moiety necessary to bind topoisomerase II and are too large to intercalate into the DNA double strand. Therefore, a possible interaction of the dimers with DNA and topoisomerase II to inhibit the enzyme can in principle be ruled out.

To evaluate whether dimers interact with DNA, plasmid DNA gel-retardation assay in agarose gel electrophoresis was used. DOXNP were diluted in water (2-200 ng/μL) and left in the dark for 24 h at room temperature. This time period of incubation was required for DOXNP dissolution. pBluescript DNA plasmid was incubated with different

concentrations of dimers (dissolved DOXNP) or DOX for 2 h at 37 °C and samples were run on 1% agarose gel. The migration of DNA exposed to DOXNP or DOX was compared with that of control DNA. The potent DNA intercalator, ethidium bromide, was used as positive control (Figure S9). The migration of plasmid DNA exposed to dimers was very similar to that of the control DNA. A very weak DNA gel shift was observed only for high concentration (25 ng/µL) of dimers. Conversely, DOX (for concentrations > 0.05 ng/µL) and ethidium bromide importantly impact on DNA plasmid migration.

To further gain insight into mode of action DOXNP, flow cytometry and confocal microscopy imaging were carried out. First, the association of DOXNP with MDA-MB-231 cells using flow cytometry at different times was investigted. The particles showed an efficient association with cells after approximately 4 h (Figure 2c). Figure 2d and 2e represent confocal microscopy images of the MDA-MB -231 cells when incubated with DOXNP and DOX at 37 °C for 5 h. Figure 2d shows that free DOX was accumulating in the nucleus where it intercalates with DNA and inhibit topoisomerase II enzymes. Conversely, Figure 2e shows that DOXNP accumulated in others cellular compartments, as well as around the peri-nuclear region. This finding, together with the poor/no interaction with DNA observed for DOXNP, suggests that topoisomerase II-mediated DNA damages are not involved in DOXNP mode of action.

8.2.3. Mechanism of action and intracellular trafficking of DOXNP using super resolution microscopy

To clarify the mechanism of DOXNP uptake, studies on endosomal trafficking were performed using super resolution microscopy (STORM). Confocal microscopy has a resolution of ~ 250 nm whereas STORM provides up to 20 nm lateral resolution by reconstructing images on the basis of the accurate localization of single, stochastically blinking fluorescent molecules [15]. Recently, super-resolution microscopy was

exploited to image different cellular structures and nanomaterials [15]. Figure 3a and 3b provides a comparison between the confocal microscopy and STORM images of MDA-MB-231 cell transfected with DOXNP. Figure 3a2 represent the confocal microscopy (Figure 3a4 & 3a5 magnified images of S8a2) showing poor resolution as compared to STORM images (Figure 3b1-4). During STORM analysis it was observed that DOXNP form highly organised pattern near the cellular membrane (Figure 3b 2-3). This feature is likely dependent on the interaction of DOXNP with F-actin associated with the cellular membrane, as observed in confocal microscopy image of MDA-MB-231 cells stained with Phalloidin (Figure 2e and Figure 3a3 & colocalization of DOXNP and F-Actin is marked with arrow and magnified image is shown in Figure 3a6). The interaction of DOXNP with α/β tubulin, another component of cytoskeleton, was also studied using confocal microscopy. Negligible colocalization between tubulin and DOXNP was observed (Figure S10).

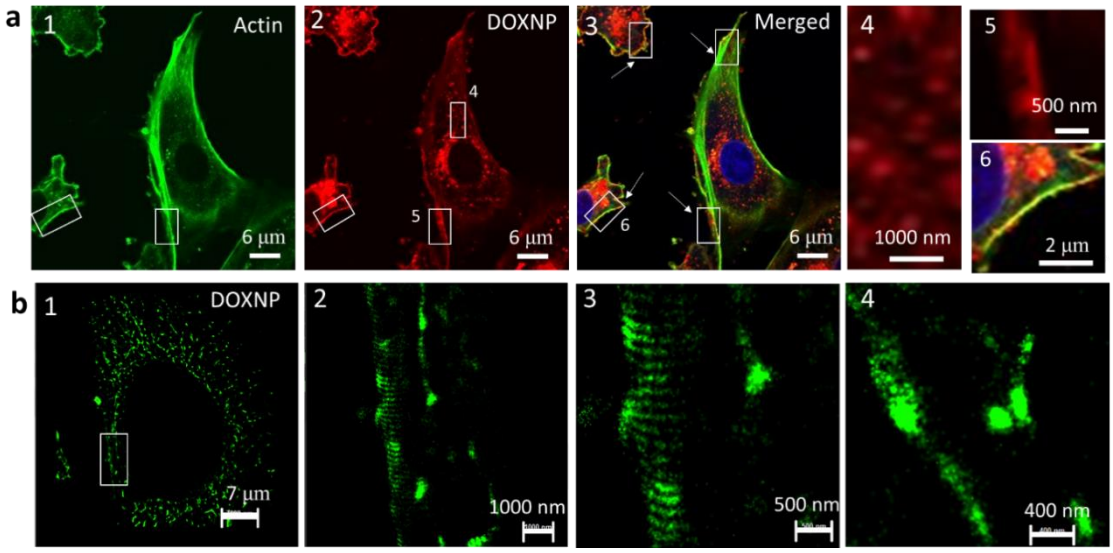

Figure 3: (a) Confocal microscopy images of the MDA-MB-231 cells incubated with DOXNP (3 µg/ml) for 5 h. Red fluorescence is due to DOXNP. Green due to F-actin stained with Phalloidin. (b) STORM image of MDA-MB-231 cells incubated with AF 488/ AF 647 dual labelled DOXNP (green) for 5 h, (b2-4) magnified images of the b1.

Next, to study the intracellular trafficking of DOXNP using STORM microscopy, MDA-MB-231 cells were transfected with dual labelled DOXNP (activator reporter pair of AF 488/ AF 647) for 2 h. The media was replaced and further incubation for 3 h, 6 h and 22 h corresponding to total incubation time of 5 h, 8 h and 24 h was performed. The cells were fixed after 2 h, 5 h, 8 h and 24 h incubation time. The early endosome, late endosome and lysosome vesicles were labelled with marker-specific antibodies - Early Endosome Antigen 1 (EEA1), Rab 7 and LAMP 1 respectively, and subsequently with the dual labelled secondary antibody (AF 555/AF 647) [16]. Figure 4 a, b, and c represent the STORM images of the MDA-MB-231 specimens after 2 h, 5 h, 8 h and 24 h incubation with DOXNP with early endosome staining, late endosome staining and lysosome staining respectively.

Constructs shown in Figure 4a 1-2 (2h), a1 (8h), b1 (2h) and c1(2h) were considered colocalized (where nanoparticles are trapped in the endosome and lysosome compartments), whereas constructs shown in Figures 4 a3(2h), a7(2h), a7(8h), S12 a5 (24 h), S12 b2-7(24 h), c 1-2(8 h), S12 c1-2 (24 h) were considered non-colocalised (particles escaping from the endosome or escaped to the cytosol). Figure 4d summarises the statistical analysis of co-localized and non-colocalized nanoobjects imaged at different incubation times. Figure 4d shows that after 2 h more than 60 % of DOXNP were colocalized with the early, late endosome and 80 % with lysosome. However, slight decrement in colocalization was observed after 5 h and significant decrease was observed between 5 h (50-40 %) and 8 h and 24 h (5-20 %). This indicates that nanoparticles endosomal/lysosomal escape to the cytosol occurred between 5 h and 8 h. The endo-lysosomal escape of DOXNP or dissolved DOX dimers can occur via different mechanisms. The DOXNP can disassemble inside the vesicles, the DOX dimers can

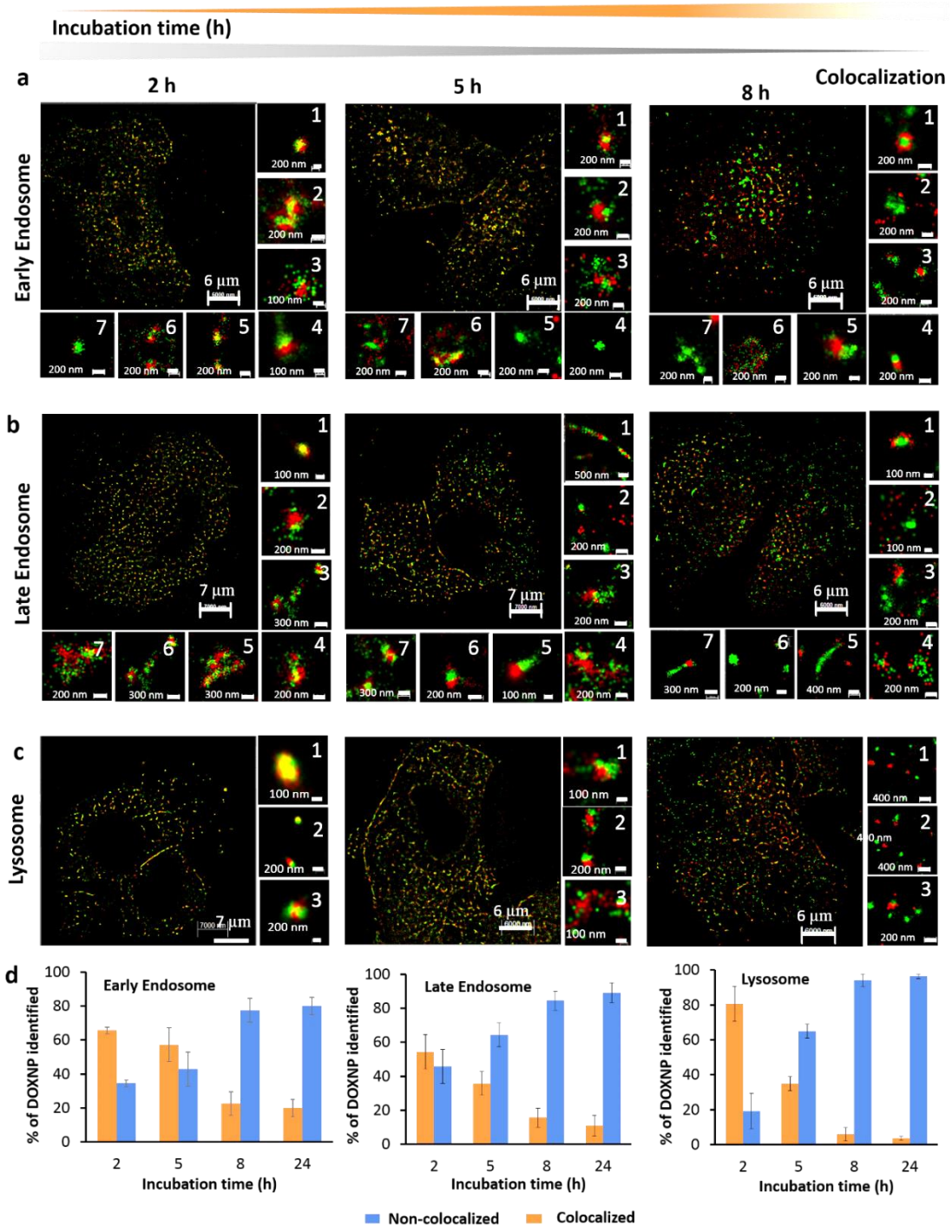

Figure 4: Multicolour STORM images of the MDA-MB-231 cells representing DOXNP and (a) Early endosome, (b) Late endosome, (c) Lysosome. The intracellular trafficking of DOXNP and Early endosome, Late endosome, lysosome after 2 h, 5 h, and 8 h incubation with MDA-MB-231 cells. Figures a1-7, b1-7 and c1-3 are magnified images of the intracellular nano-objects. The red colour illustrates the anti- EEA1, anti-Rab 7 and LAMP1 dual labelled AF 555/AF 647 used for staining early endosome, late endosome and lysosome respectively; and green colour is due to the AF 488/ AF 647 dual labelled DOXNP (d) Percentage fraction of DOXNPs colocalized with Early endosome, Late endosome and Lysosome as a function of incubation time.

rupture the cellular membrane through fusion of hydrophobic moieties into the lipid bilayer, causing membrane disruption and escape of the entrapped species. Furthermore, the dissolution of DOXNP could burst the endo/lysosome compartments due to osmotic swelling and osmotic pressure gradient. From the STORM images it can also be observed the some DOXNP dissemble due to dissolution of nanoparticles and some escape the cytosol intact form the endo-lysosome compartments (Figure 4 a7(2h), 4 a4-5 (5 h), 4 b6 (8h), 4 c3(8h)). Moreover, to understand the mechanism of endocytosis through which particles were uptaken, cells were incubated with filipin, pitstop-2, and ethylisopropyl amiloride (EIPA) to inhibit caveoloe-dependent endocytosis, clathrin-dependent endocytosis and macropinocytosis and then incubated with DOXNP (3 µg/ml). Figure 5a and 5b suggests that almost 20-30 % inhibition was observed with all the endocytic inhibitors suggesting the uptake of DOXNP through caveoloe and clathrin-dependent endocytosis and macropinocytosis.

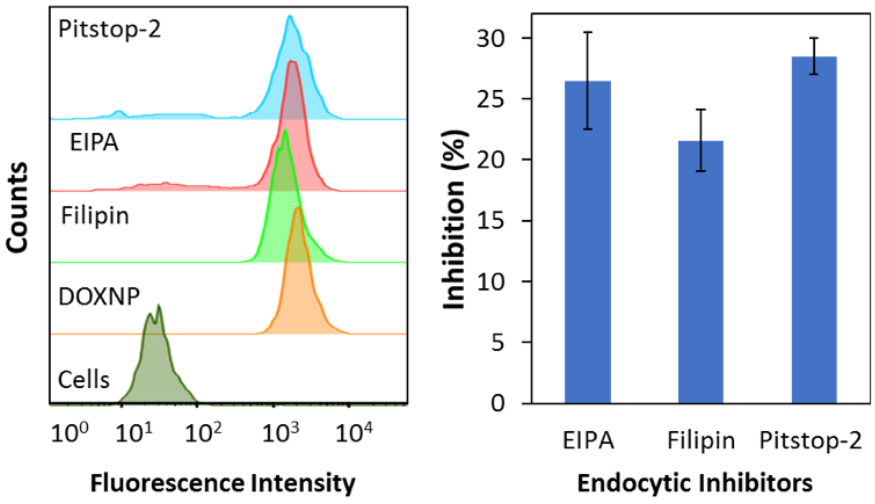

Figure 5: (a) Fluorescnce intensity histogram of MDA-MB-231 cells before and after treatment with endocytic inhibitors and DOXNP measured using flow cytometry, (b) The percentage inhibition by different endocytic inhibitors on the uptake of DOXNP

As the confocal microscopy images indicated, the DOXNP localized in the perinuclear region (Figure 2e) the immunostaining of different intracellular compartments namely,

endoplasmic reticulum (FigureS11a), golgi (Figure S11b)), mitochondria was performed. The DOXNP were found to be colocalized with golgi and mitochondria. Figure 6a and 6b show the confocal microscopy and STORM images of MDA-MB-231 cells after 24 h incubation with DOXNP. The DOXNP were labelled with activator reporter pair of AF 488/ AF 647 (green) and mitochondria were stained with TOM20 (primary antibody) and secondary antibody with AF 555/ AF 647 activator reporter pair for STORM imaging. The interaction of mitochondria and DOXNP was evident from Figure 6a and 6b where colocalization of green and red signals was observed (yellow). In addition, DOXNP produced a peculiar cellular distribution of the organelles in the perinuclear region (Figure S13a and S13b). This behaviour was previously reported to play a role in enhancing ROS concentration in the nucleus and, in turn, leading to increased nuclear DNA damage [17]. Since DOX formulations that specifically targeting mitochondria were reported to overcome drug resistance and limit normal cell toxicity [18, 19], we tested whether DOXNP impact on 3T3 fibroblast viability and compared to DOX, DOXNP exhibited almost no toxicity toward fibroblasts (Figure S14).

To evaluate whether DOXNP are responsible for ROS production, MDA-MB-231 cells were further analyzed. Cells were treated for 24 h with DOXNP and DOX at the concentrations corresponding to $2xIC_{50}$ at 72 h in presence or absence of 100 µM NAC or 100 µM vitamin C. Figure 6c shows that NAC counteracts both doxorubicin and DOXNP mediated DNA damage, as demonstrated by reduced levels of γ-H2AX observed after combined exposure to compounds and antioxidants. This finding was confirmed in FACS assay using a specific probe recognizing ROS (Figure 6d). When exposed for 24 h to DOXNP, ROS level in MDA-MB-231 cells was increased in comparison to the control untreated cells (Figure 6d). Conversely, in the presence of 100 µM vitamin C or NAC (radical scavenging agents), a strongly reduction in ROS generation was observed.

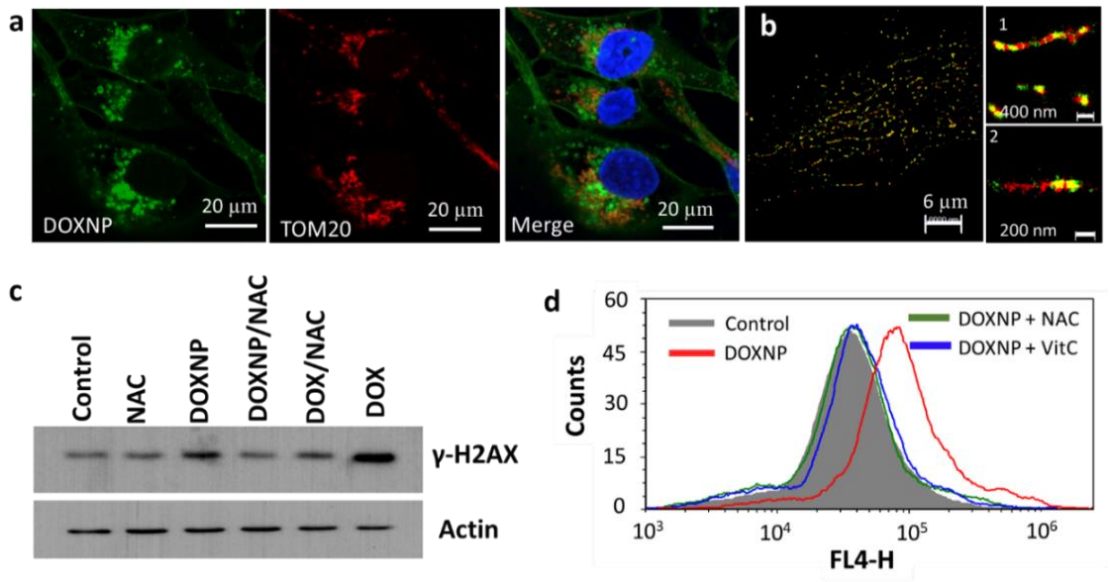

Figure 6: (a) Confocal microscopy of the MDA-MB -231 cells incubated with DOXNP (green) and stained with Mitochondria using TOM20 (Red), Blue DAPI nuclear stain, (b) Multicolour STORM image of MDAMB 231 cell stained with AF 555/ AF 647 labelled mitochondria maker (TOM20- red) and AF 488/ AF 647 dual labelled DOXNP (green), (b1-2) magnified images of the c1 showing colocalization of the DOXNP with mitochondria. (c) Effect of antioxidants vitamin C and NAC on DOXNP-induced DNA damage and ROS generation in MDA-MB-231 cells. Cells were treated for 24 h with DOX or DOXNP at concentrations corresponding to 2xIC50 at 72 h in presence or absence of 100 µM vitamin C or NAC. After drug exposure, cells were harvested for protein extraction, and cell lysates were fractionated on SDS-PAGE. Nitrocellulose films were incubated with antibody against γ-H2Ax and β-actin, which was used as control for equal loading. (d) The same conditions were used to measure ROS induction by FACS assay using a specific probe that recognizes ROS. After drug exposure, ROS-specific detection probe was added for 60 min at 37°C. Under low light conditions, cells were harvested, transferred to foil-wrapped tubes and immediately analyzed by flow cytometry.

Taken together, these results confirm that the mode of action of DOXNP was ROS dependent, where the redox cycling of anthracycline drug can enhance the cellular oxidative stress and deplete ATP production. The anthracycline type structures are known to interact with DNA and cause mitochondrial dysfunctions [14]. Mitochondrial functioning depends on mitochondrial (mtDNA) and nuclear DNA, ATP levels, reactive oxygen species (ROS) levels etc [20, 21]. The DOXNP have high affinity for inner membrane of mitochondria where they can be reduced to unstable semiquinone The semiquinone is then oxidised by transfer of an electron to oxygen to generate superoxide anion O_2^- and other excess mtROS such as H_2O_2 [22, 23]. H_2O_2 can then react with iron

(iron is mostly translocated from lysosome to mitochondria) and undergo Fenton type reactions to generate OH radical and OH ions leading to lipid oxidation, protein modification, DNA damage and mitochondrial dysfunction. A schematic illustrating the possible mechanism of ROS generation is shown in Figure S15.

Hence, the tendency of DOXNP to overcome the drug resistance can also be due to their binding with mitochondria, that would allow them to inhibit the production of ATP (which is indispensable for the efflux pumps and transporters to function) by consuming NAPH and oxidising it to NAD+ for the ROS production.

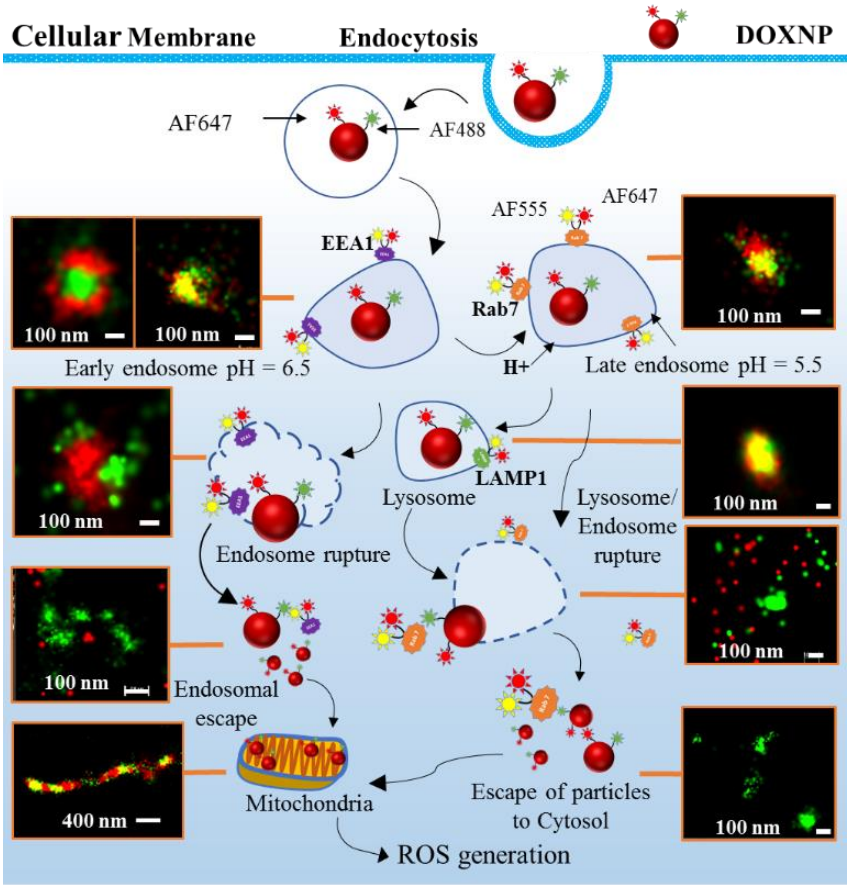

Figure 7: Schematic representing intracellular trafficking of DOXNP and different cellular organelles and vesicles such as early endosome, late endosome, lysosome and mitochondria illustrating the mechanism of uptake, escape and cell death.

Overall, the intracellular trafficking of DOXNP has been summarised in Figure 7. The particles were taken up by endocytosis and trafficked through the early endosomes (pH~

6.5) The ATP mediated proton pump can induce the acidification of the early endosomes which subsequently mature to late endosomes (pH~5.5) and can also merge with lysosome compartments. Then rupture of the endo-lysosomal membranes leads to the release the dimers or intact DOXNP in the cytosol. Both released DOXNP and dimers can interact with other cellular organelles and mitochondria, where the high levels of mtROS production can occur according to the mechanism summarised in Figure S15. The production of ROS causes mitochondrial dysfunction, nuclear damage, various other cellular damages and ultimately cell death.

8.3. Conclusions

In this chapter, the synthesis of nanoparticles solely made of modified doxorubicin is demonstrated using high frequency ultrasound. The chemically modified DOXNPs were found to be still active in different types of cancer cell lines and were surpassing drug resistance better than that of doxorubicin. STORM and confocal microscopy techniques were used to investigate the intracellular trafficking pathway and mechanism of action of DOXNP. The DOXNP, rather than intercalating with nuclear DNA, interact with mitochondria where they generate high levels of ROS species as measured using FACS, leading to nuclear DNA damage and cell death.

8.4. References

1. Kaushik, D. and G. Bansal, *Four new degradation products of doxorubicin: An application of forced degradation study and hyphenated chromatographic techniques.* Journal of pharmaceutical analysis, 2015. **5**(5): p. 285-295.
2. Sun, T., Y.S. Zhang, B. Pang, D.C. Hyun, M. Yang, and Y. Xia, *Engineered nanoparticles for drug delivery in cancer therapy.* Angewandte Chemie International Edition, 2014. **53**(46): p. 12320-12364..
3. Burgess, P., P.B. Hutt, O.C. Farokhzad, R. Langer, S. Minick, and S. Zale, *On firm ground: IP protection of therapeutic nanoparticles.* Nature biotechnology, 2010. **28**(12): p. 1267.
4. Misra, R., S. Acharya, and S.K. Sahoo, *Cancer nanotechnology: application of nanotechnology in cancer therapy.* Drug discovery today, 2010. **15**(19-20): p. 842-850.

5. Kamaly, N., Z. Xiao, P.M. Valencia, A.F. Radovic-Moreno, and O.C. Farokhzad, *Targeted polymeric therapeutic nanoparticles: design, development and clinical translation.* Chemical Society Reviews, 2012. **41**(7): p. 2971-3010.
6. Hu, C.-M.J., S. Aryal, and L. Zhang, *Nanoparticle-assisted combination therapies for effective cancer treatment.* Therapeutic delivery, 2010. **1**(2): p. 323-334.
7. Bhangu, S.K., M. Ashokkumar, and F. Cavalieri, *A simple one-step ultrasonic route to synthesize antioxidant molecules and fluorescent nanoparticles from phenol and phenol-like molecules.* ACS Sustainable Chemistry & Engineering, 2017. **5**(7): p. 6081-6089.
8. Cavalieri, F., E. Colombo, E. Nicolai, N. Rosato, and M. Ashokkumar, *Sono-assembly of nanostructures via tyrosine–tyrosine coupling reactions at the interface of acoustic cavitation bubbles.* Materials Horizons, 2016. **3**(6): p. 563-567.
9. Agudelo, D., P. Bourassa, G. Bérubé, and H.-A. Tajmir-Riahi, *Intercalation of antitumor drug doxorubicin and its analogue by DNA duplex: structural features and biological implications.* International journal of biological macromolecules, 2014. **66**: p. 144-150.
10. Quach, B., A. Birk, and H. Szeto, *Mechanism of preventing doxorubicin-induced mitochondrial toxicity with cardiolipin-targeted peptide, SS-31 (966.1).* The FASEB Journal, 2014. **28**(1_supplement): p. 966.1.
11. Cheregi, B., C. Timpani, K. Nurgali, A. Hayes, and E. Rybalka, *Chemotherapy-induced mitochondrial respiratory dysfunction, oxidant production and death in healthy skeletal muscle C2C12 myoblast and myotube models.* Neuromuscular Disorders, 2015. **25**: p. S202.
12. Deavall, D.G., E.A. Martin, J.M. Horner, and R. Roberts, *Drug-induced oxidative stress and toxicity.* Journal of toxicology, 2012. **2012**.
13. Sawyer, D.B., X. Peng, B. Chen, L. Pentassuglia, and C.C. Lim, *Mechanisms of anthracycline cardiac injury: can we identify strategies for cardioprotection?* Progress in cardiovascular diseases, 2010. **53**(2): p. 105-113.
14. Sarosiek, K.A., T.N. Chonghaile, and A. Letai, *Mitochondria: gatekeepers of response to chemotherapy.* Trends in cell biology, 2013. **23**(12): p. 612-619.
15. Wojnilowicz, M., A. Glab, A. Bertucci, F. Caruso, and F. Cavalieri, *Super-resolution Imaging of Proton Sponge-Triggered Rupture of Endosomes and Cytosolic Release of Small Interfering RNA.* ACS nano, 2018. **13**(1): p. 187-202.
16. Feng, Y., B. Press, and A. Wandinger-Ness, *Rab 7: an important regulator of late endocytic membrane traffic.* The Journal of cell biology, 1995. **131**(6): p. 1435-1452.
17. Onodera, Y., J.-M. Nam, M. Horikawa, H. Shirato, and H. Sabe, *Arf6-driven cell invasion is intrinsically linked to TRAK1-mediated mitochondrial anterograde trafficking to avoid oxidative catastrophe.* Nature communications, 2018. **9**(1): p. 2682.
18. Fei, J., J. Zhao, C. Du, A. Wang, H. Zhang, L. Dai, and J. Li, *One-pot ultrafast self-assembly of autofluorescent polyphenol-based core@ shell nanostructures and their selective antibacterial applications.* ACS nano, 2014. **8**(8): p. 8529-8536.
19. Jean, S.R., D.V. Tulumello, C. Riganti, S.U. Liyanage, A.D. Schimmer, and S.O. Kelley, *Mitochondrial targeting of doxorubicin eliminates nuclear effects associated with cardiotoxicity.* ACS chemical biology, 2015. **10**(9): p. 2007-2015.
20. Wallace, D.C., *Mitochondria and cancer.* Nature Reviews Cancer, 2012. **12**(10): p. 685.
21. Weinberg, S.E. and N.S. Chandel, *Targeting mitochondria metabolism for cancer therapy.* Nature chemical biology, 2015. **11**(1): p. 9.
22. Gilliam, L.A., J.S. Moylan, E.W. Patterson, J.D. Smith, A.S. Wilson, Z. Rabbani, and M.B. Reid, *Doxorubicin acts via mitochondrial ROS to stimulate catabolism in C2C12 myotubes.* American Journal of Physiology-Cell Physiology, 2011. **302**(1): p. C195-C202.
23. Davies, K. and J. Doroshow, *Redox cycling of anthracyclines by cardiac mitochondria. I. Anthracycline radical formation by NADH dehydrogenase.* Journal of Biological Chemistry, 1986. **261**(7): p. 3060-3067.

Appendix 8

8.5. Supporting Information

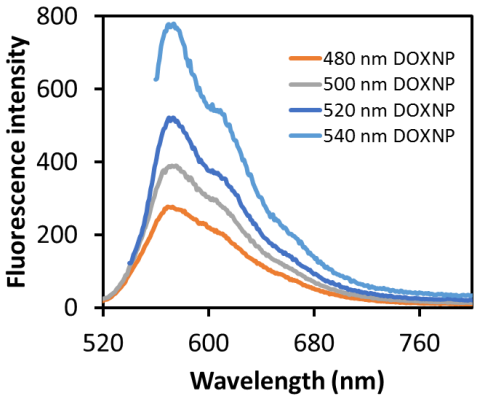

***Figure S1**: Fluorescence emission spectra of DOXNPs after dissolution at different excitation wavelengths*

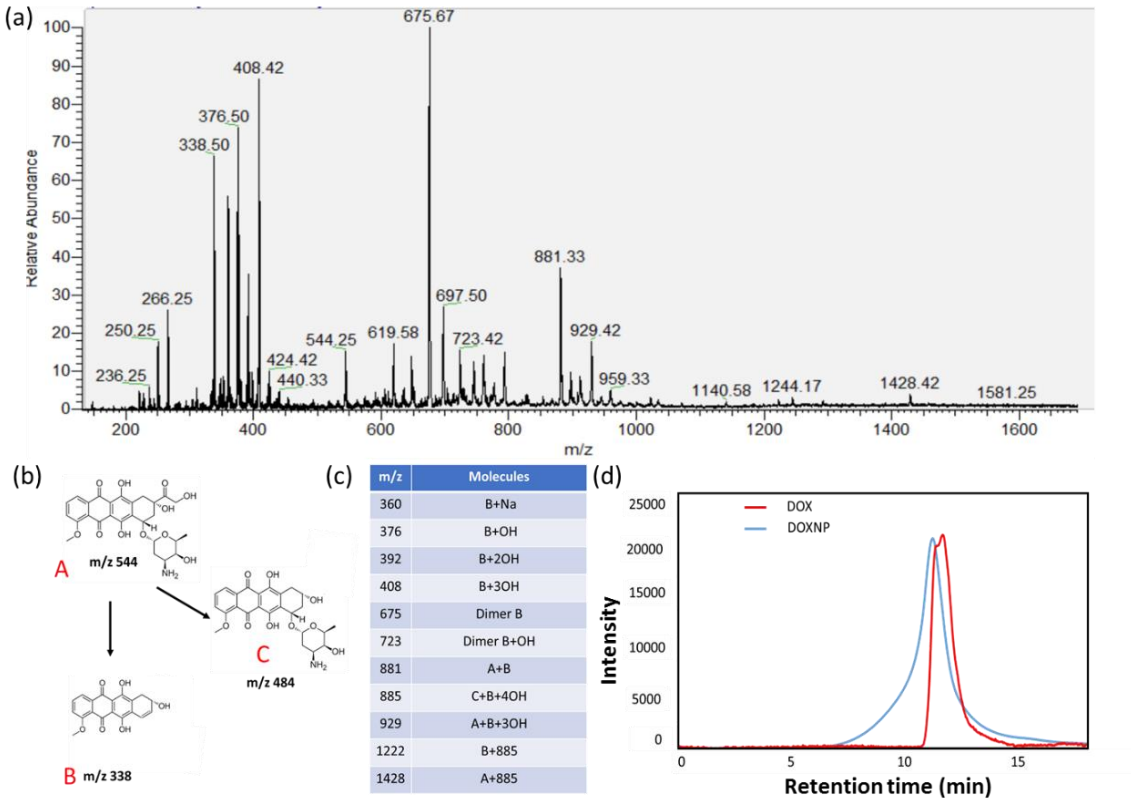

m/z	Molecules
360	B+Na
376	B+OH
392	B+2OH
408	B+3OH
675	Dimer B
723	Dimer B+OH
881	A+B
885	C+B+4OH
929	A+B+3OH
1222	B+885
1428	A+885

***Figure S2:** a) Mass spectra of DOXNP after dissolution, (c) List of possible structures formed due to sonication of doxorubicin and (d) Size exclusion chromatography (SEC) of DOX and DOXNP representing the presence of high molecular weight species.*

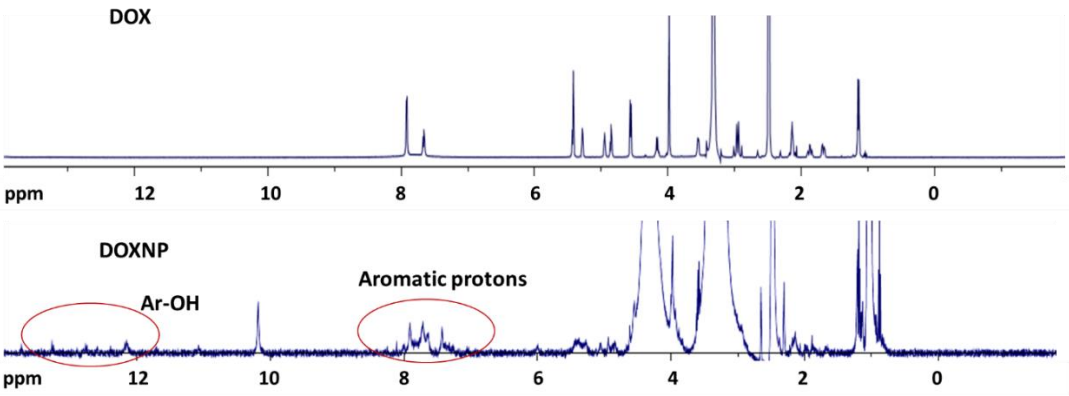

Figure S3: *Proton NMR of DOX and DOXNPs in DMSO.*

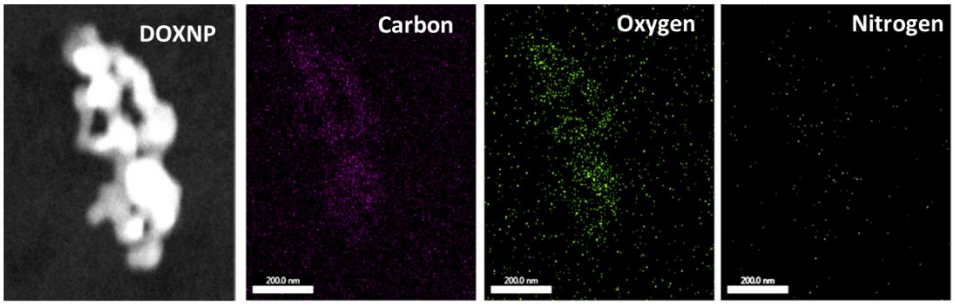

Figure S4: *TEM-EDX elemental mapping of DOXNP where carbon, oxygen and nitrogen were observed.*

(a)

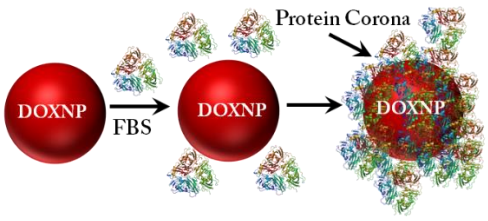

(b)

	Average size (nm)	Standard Deviation
DOXNP in PBS	252	99
DOXNP + 10 % FBS	280	99
DOXNP + 50 % FBS	315	104
DOXNP + 100 % FBS	332	107

(c)

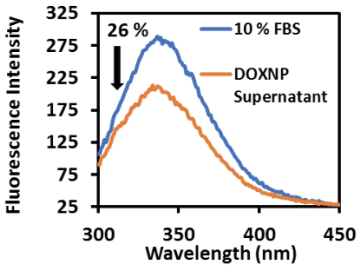

(d)

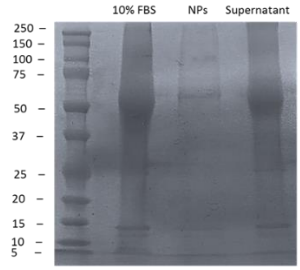

Figure S5: *(a) Schematic summarising the interaction of protein and formation of protein corona on DOXNP after incubation with FBS, (b) Table summarizing the change in average size of DOXNPs after incubation with different FBS concentrations, (c) Fluorescence emission spectra of 10 % FBS protein before and after incubation with DOXNPs and (d) SDS-PAGE analysis of 10 % FBS, washed DOXNPs after incubation with FBS and their supernatant.*

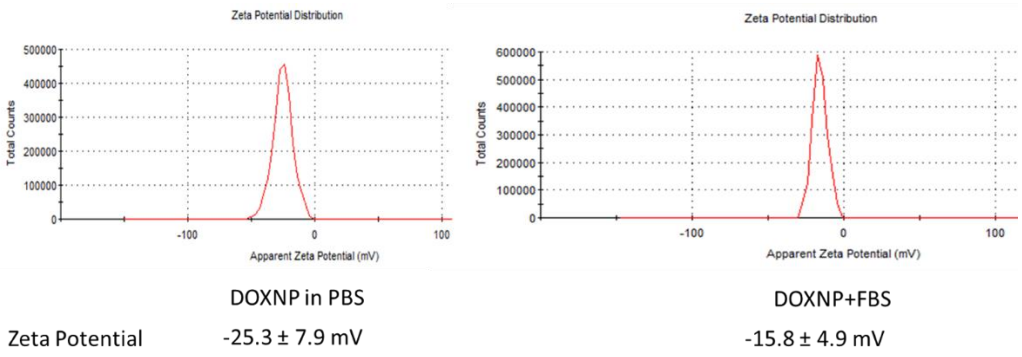

Figure S6: *Zeta potential of DOXNPs in PBS and after incubation with FBS.*

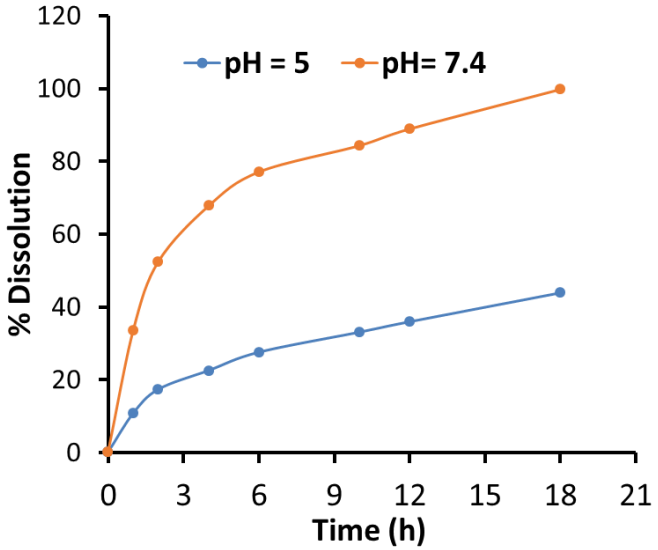

Figure S7: *The dissolution kinetics of DOXNP as a function of time at pH 7.4 and pH 5.*

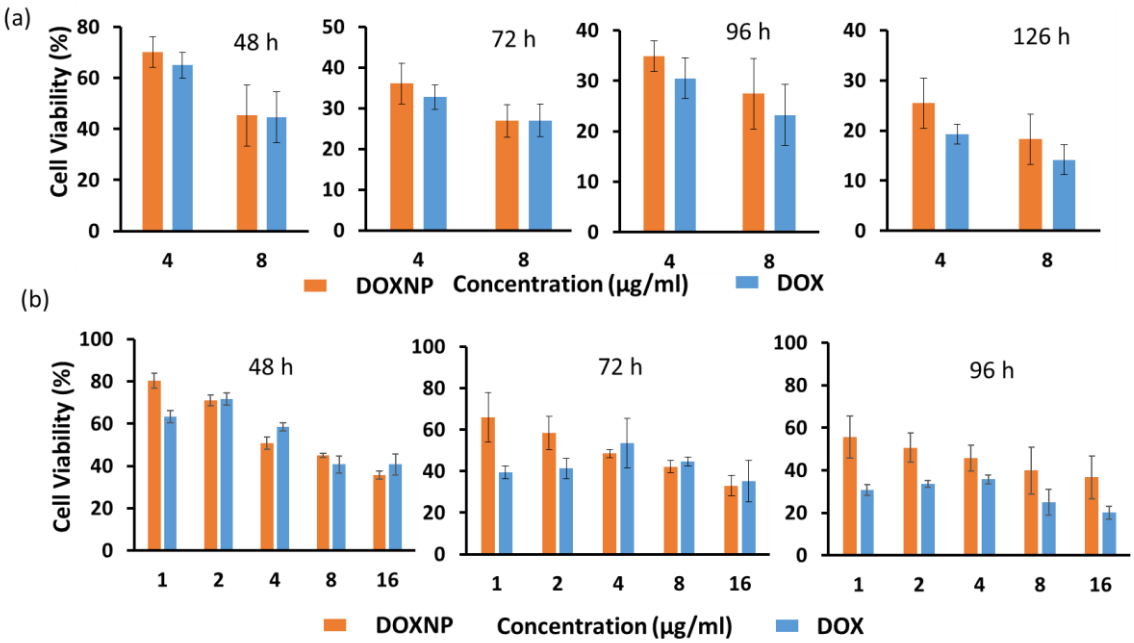

Figure S8: *(a) Comparison of cell viability of DOXNP and free DOX after 48 h, 72 h, 96 h and towards HCC-1143 at different concentrations (b) Comparison of cell viability of DOXNP and free DOX after 48 h, 72 h, 96 h and 126 h towards HCC-1937 cells at different concentrations*

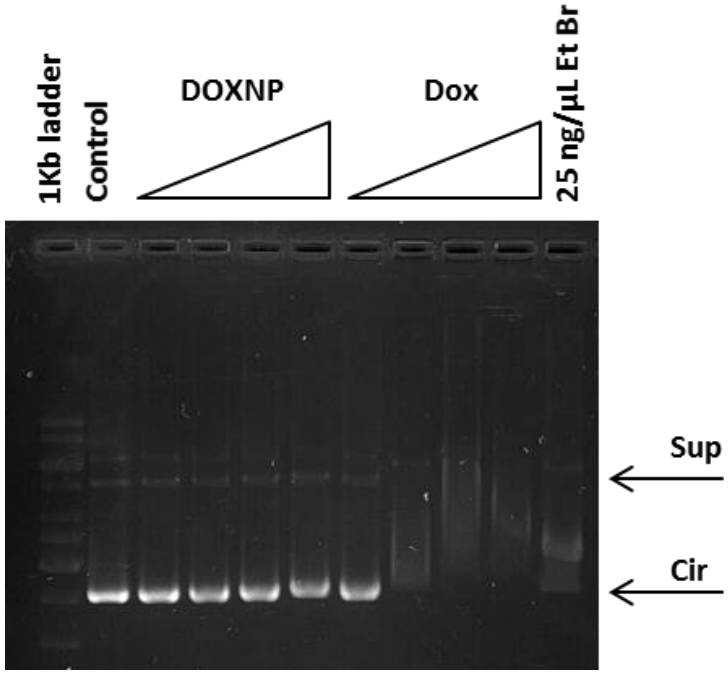

Figure S9: *Interaction of DOXNP (dissolved) and DOX with the DNA. pBluescript DNA plasmid (233 ng) and DOXNP (0.05-25 ng/µL) or DOX (0.05-25 ng/µL) were incubated in 20 µL of 0.5x phosphate buffered saline for 2h at 37 °C. The incubation of plasmid with 25 ng/ µL of ethidium bromide was used as positive control. Samples were run on 1% ethidium bromide-free agarose gel and image was taken after ethidium bromide staining. The arrows indicate the migration of the circular (Cir) and supercoiled (Sup) DNA plasmid*

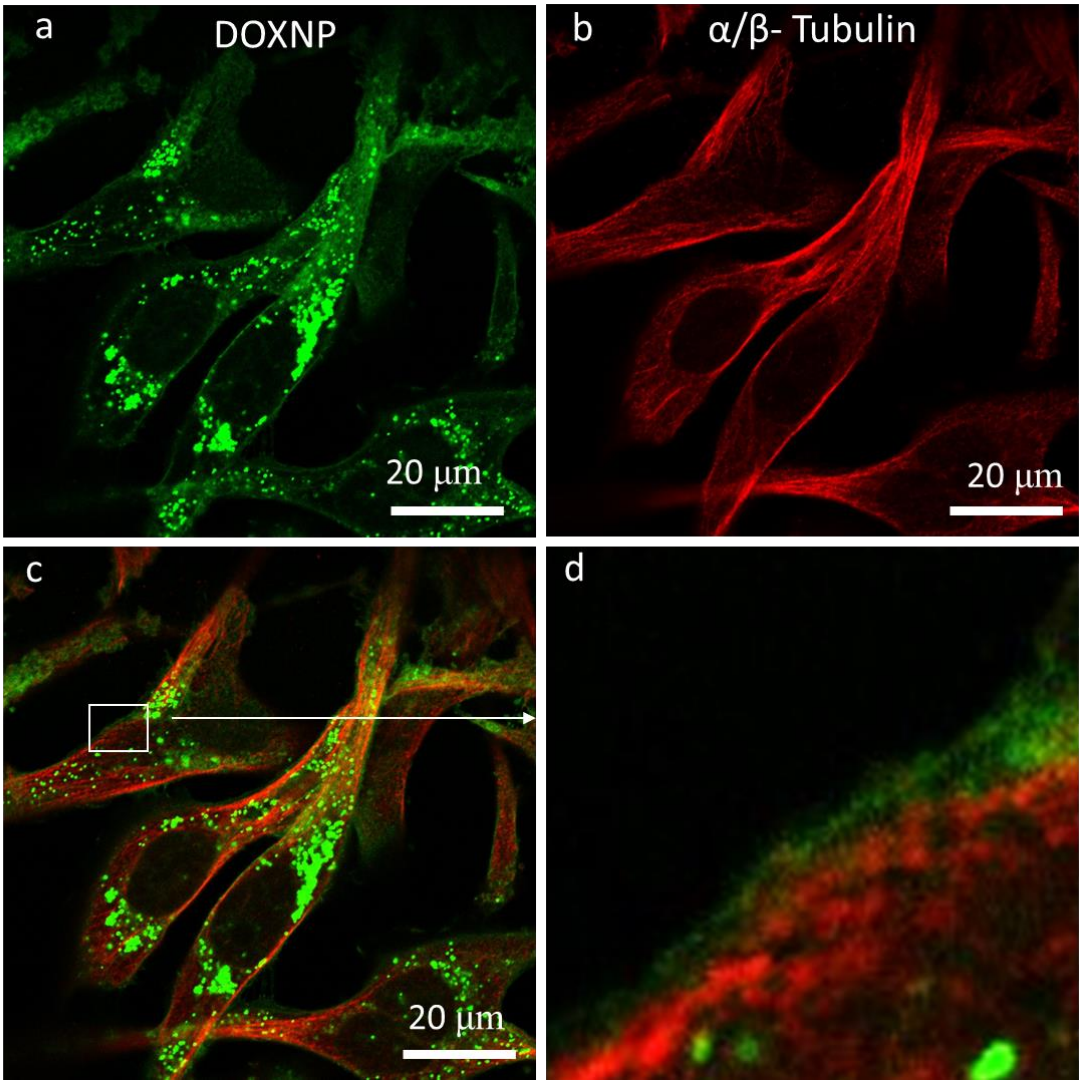

Figure S10: *Confocal microscopy images of the MDA-MB- 231 cells when incubated with DOXNP (Green) where cells were stained with for α/β Tubulin (Red)*

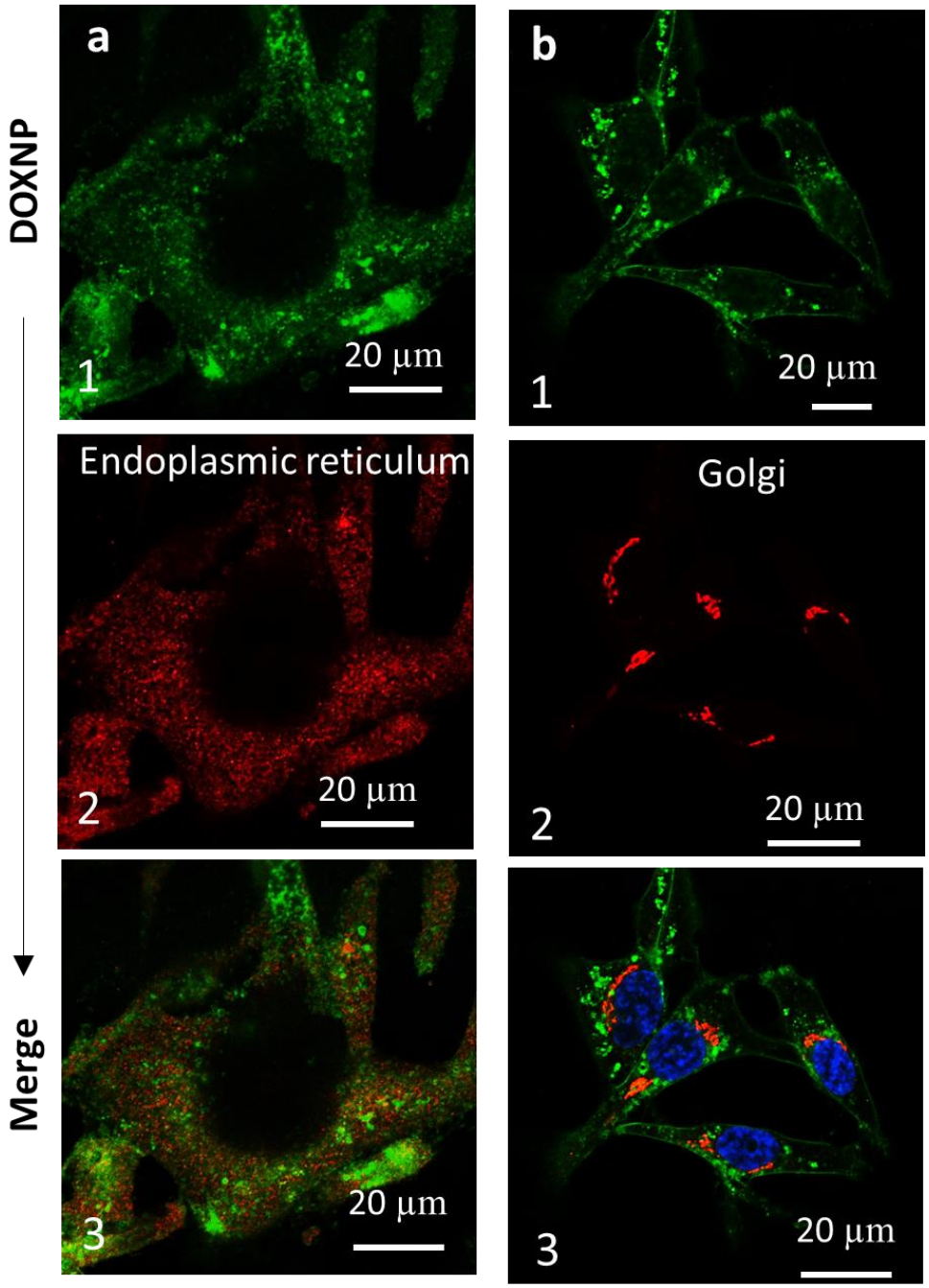

Figure S 11: *Confocal microscopy images of the MDA-MB-231 cells when incubated with DOXNP (Green) where cells were stained with (a) ERp72 – a Endoplasmic reticulum marker (Red), and (b) GM 130- a Golgi Marker (Red), Blue (DAPI-nuclear stain)*

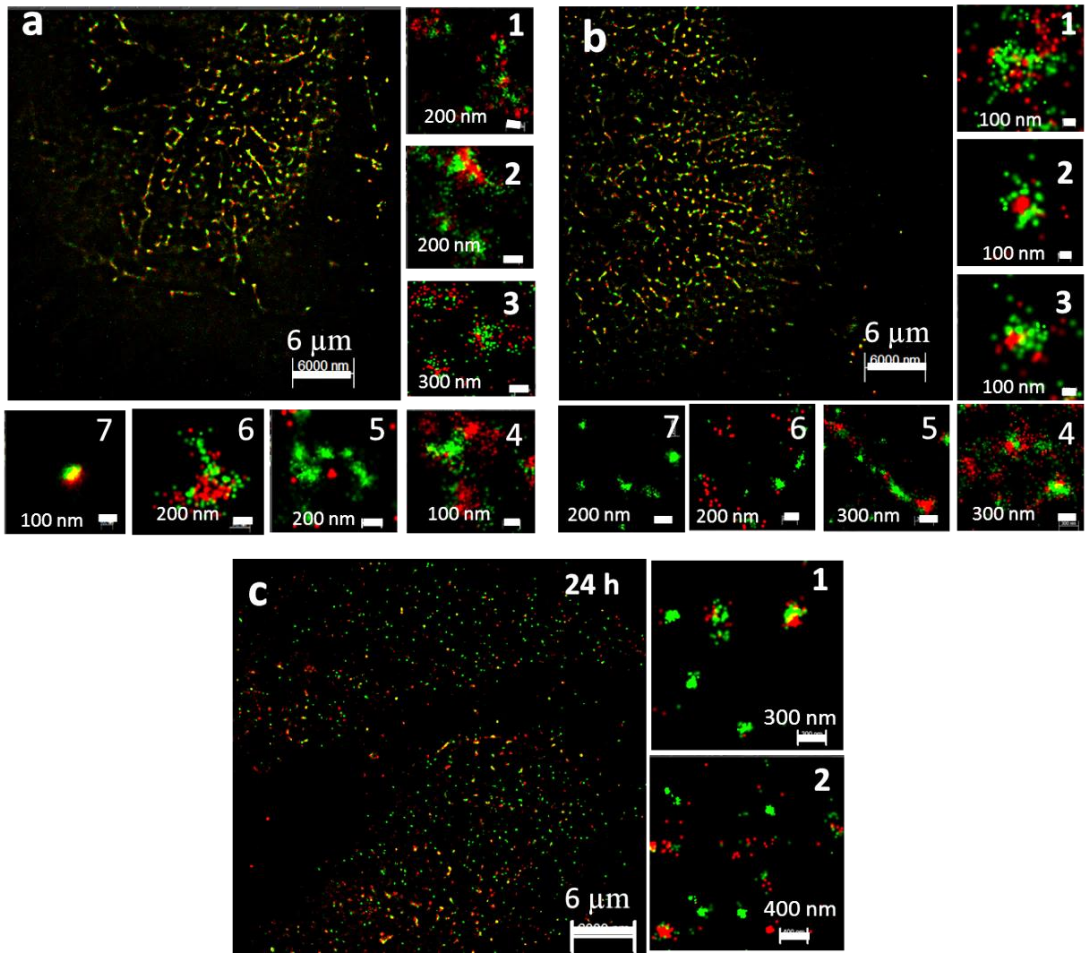

***Figure S12**: Multicolour STORM images of the MDA-MB-231 cells representing DOXNP and (a) Early endosome, (b) Late endosome, (c) Lysosome. The intracellular trafficking of DOXNP and Early endosome, Late endosome, lysosome after 24 h incubation with MDA-MB-231 cells. Figures a1-7, b1-7 and c1-3 are magnified images of the intracellular nano-objects. The red colour illustrated the anti- EEA1, anti-Rab 7 and anti-LAMP1 dual labelled AF 555/AF 647 stained early endosome, late endosome and lysosome respectively; and green colour is due to the AF 488/ AF 647 dual labelled DOXNP.*

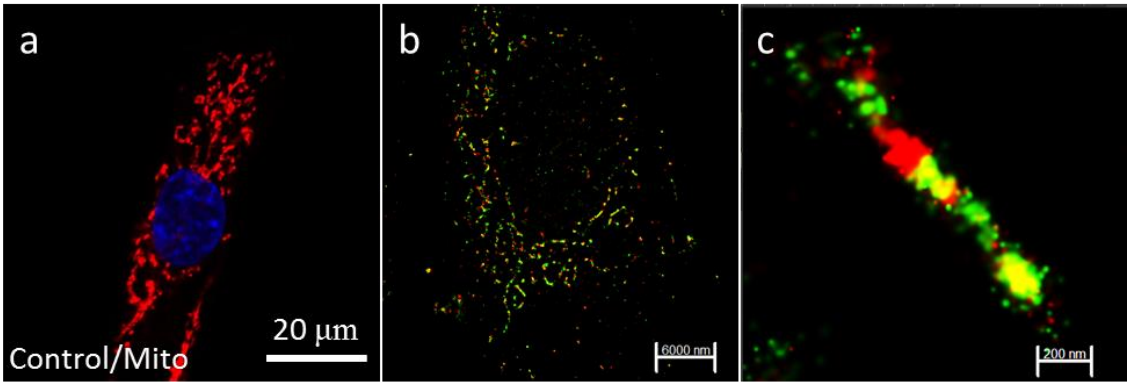

Figure S13: *The arrangement of mitochondria in MDA-MB-231 cells without the addition of DOXNP, (b) STORM image of MDA-MB-231 cells after incubation with DOXNP(green) and staining with TOM20 antibody (Red-mitochonria marker), (c) Magnified STORM image of b.*

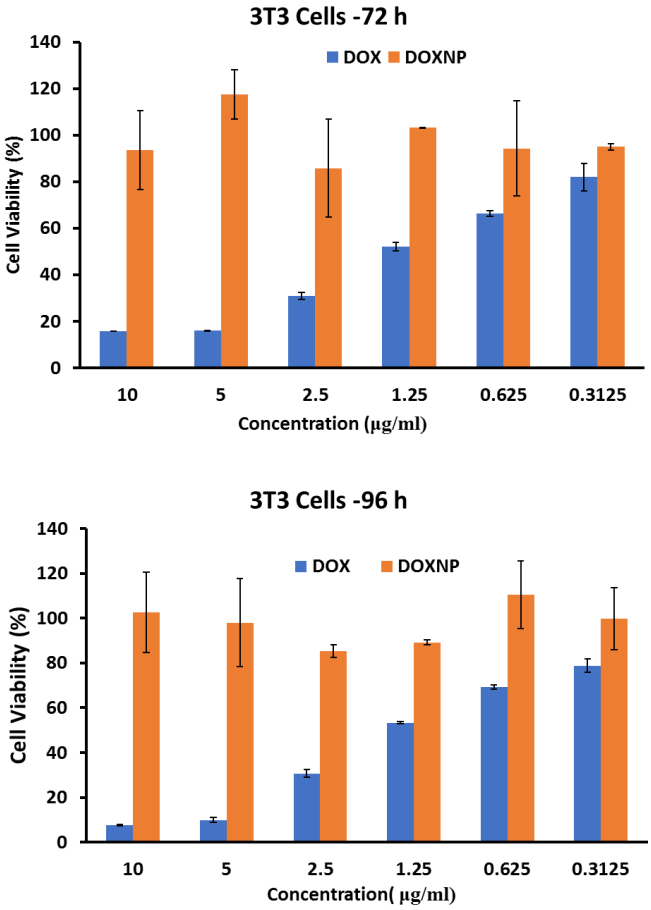

Figure S14: *Comparison of cell viability of DOXNP and free DOX after 72 h and 96 h towards 3T3 Cells at different concentrations*

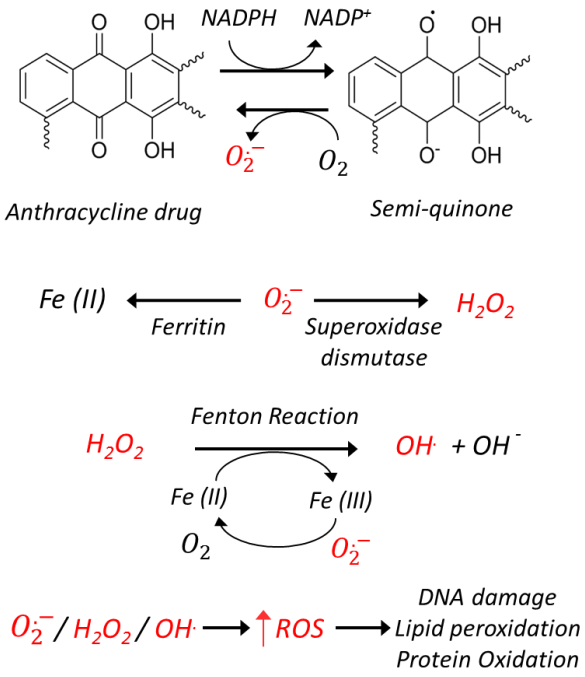

Figure S15: *Schematic representing possible mechanism of ROS generation due to anthracycline drugs.*

Chapter 9

Summary and Concluding Remarks

9.1. Summary

This PhD study demonstrates the ultrasound driven synthesis of bio-functional micro/nanostructures and their applications in cancer therapy. A simple ultrasonic procedure was developed to perform oxidative coupling reactions for the generation of dimers, trimers and oligomers from various aromatic biomolecules namely- simple and complex phenolic molecules, aromatic amino acids and chemotherapeutic drugs. It was demonstrated that acoustic bubble acts as a catalytic binding site not only to perform such reactions but also to trigger the self-assembly of biomolecules to generate nanostructures. In particular, some major conclusions drawn from different chapter are as follows:

1. Chapter 4 has established a general ultrasonic concept for the formation of fluorescent oligomeric species from simple phenolic compounds with new functional properties. It was found that the gas−liquid interface of the cavitation bubble can act as a catalytic binding site even for simple phenolic moieties leading to formation of oligomers provided that experimental conditions are finely controlled. The oligomers formed by 2−6 units of phenol can aggregate together with π-π interaction to form phenolic nanostructures. Ultrasonic frequency, surface activity, and concentration of the solute are the some of the crucial parameters needed to be controlled in order to form oligomers and nanostructures.
2. In Chapter 5 it was demonstrated that ultrasound can be used to perform multiple and consecutive reactions on tannin molecules. The product obtained from tannic acid after sonication i.e., ellagic acid (TAS crystals), assembles and crystallizes into regularly shaped particles. The particle sizes and morphologies can be tuned by changing the ultrasonic parameters and concentration of tannic acid. The study suggests that the radical yield and shear forces can alter the size and morphology of

the particles. TAS particles possess optical properties in a wide range of wavelengths as well as showed significantly higher cytotoxicity and higher radical scavenging activity as compared to that of soluble TA. This study, in nutshell, highlights the importance of using a powerful and green ultrasonic methodology to synthesize EA particles starting from a biomass such as TA.

3. In Chapter 6 computational and experimental approaches demonstrated the role of the acoustic field in the formation of out-of-equilibrium nanoaggregates using a simple amino acid, Tryptophan, as a building block. The collapse of acoustic bubble first triggered the formation of tryptophan dimers and then ultimately acted as a fuel for dissipative self-assembly of tryptophan dimers to form uniform nanostructures with multifarious properties. The characteristic optical and bio-functional properties of synthesized nanoparticles made them a powerful tool for probing the intracellular trafficking of an anti-cancer drug. Correspondingly, the study was extended to phenylalanine in chapter 7 and result obtained were in accordance with chapter 6
4. In Chapter 8 the synthesis of nano-formulation of anticancer drug doxorubicin was demonstrated. The synthesized nanoparticles were composed of the modified dimer of the native drug. Apart from being chemically modified DOXNP were found to be still active in different types of cancer cell lines and were surpassing drug resistance better than that of doxorubicin. A combination of STORM and confocal was used to depict the intracellular trafficking pathway and mechanism of action of DOXNP. The DOXNPs, rather than intercalating with nuclear DNA, were binding with mitochondria where they generate high levels of reaction oxygen species (ROS) and lead to nuclear DNA damage and cell death.

High frequency Ultrasound, therefore, is a very promising technique to perform oxidative coupling reactions without the use of any external agents such as enzymes, metal cross-

linkers, and other toxic agents for the conversion of simple molecules to value-added compounds. In addition, the insight provided in this work paved the way for the ultrasound driven dissipative self-assembly applicable on different biomolecules. This PhD study can be used to modify the existing anti-cancer drugs to generate new drugs and their nano-formulation.